



## **Terms and Conditions of Use of Digitised Theses from Trinity College Library Dublin**

### **Copyright statement**

All material supplied by Trinity College Library is protected by copyright (under the Copyright and Related Rights Act, 2000 as amended) and other relevant Intellectual Property Rights. By accessing and using a Digitised Thesis from Trinity College Library you acknowledge that all Intellectual Property Rights in any Works supplied are the sole and exclusive property of the copyright and/or other IPR holder. Specific copyright holders may not be explicitly identified. Use of materials from other sources within a thesis should not be construed as a claim over them.

A non-exclusive, non-transferable licence is hereby granted to those using or reproducing, in whole or in part, the material for valid purposes, providing the copyright owners are acknowledged using the normal conventions. Where specific permission to use material is required, this is identified and such permission must be sought from the copyright holder or agency cited.

### **Liability statement**

By using a Digitised Thesis, I accept that Trinity College Dublin bears no legal responsibility for the accuracy, legality or comprehensiveness of materials contained within the thesis, and that Trinity College Dublin accepts no liability for indirect, consequential, or incidental, damages or losses arising from use of the thesis for whatever reason. Information located in a thesis may be subject to specific use constraints, details of which may not be explicitly described. It is the responsibility of potential and actual users to be aware of such constraints and to abide by them. By making use of material from a digitised thesis, you accept these copyright and disclaimer provisions. Where it is brought to the attention of Trinity College Library that there may be a breach of copyright or other restraint, it is the policy to withdraw or take down access to a thesis while the issue is being resolved.

### **Access Agreement**

By using a Digitised Thesis from Trinity College Library you are bound by the following Terms & Conditions. Please read them carefully.

I have read and I understand the following statement: All material supplied via a Digitised Thesis from Trinity College Library is protected by copyright and other intellectual property rights, and duplication or sale of all or part of any of a thesis is not permitted, except that material may be duplicated by you for your research use or for educational purposes in electronic or print form providing the copyright owners are acknowledged using the normal conventions. You must obtain permission for any other use. Electronic or print copies may not be offered, whether for sale or otherwise to anyone. This copy has been supplied on the understanding that it is copyright material and that no quotation from the thesis may be published without proper acknowledgement.

# The Fatigue Behaviour of Three-Dimensional Stress Concentrations

by  
Daniel Bellett

A thesis submitted to The University of Dublin in partial fulfilment of the  
requirements for the degree of

**Doctor of Philosophy**

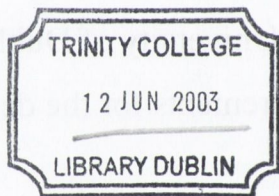
Trinity College Dublin

October 2002

Supervisor  
Professor David Taylor

The Fatigue Behaviour of Three-Dimensional  
Stress Concentrations

by  
Daniel Bolger



Thesis  
~~4364~~  
7163

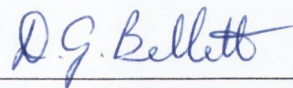
Supervisor  
Professor David Taylor

## Declaration

---

I declare that the present work has not been submitted as an exercise for a degree at any other University. This thesis consists entirely of my own work except where references indicate otherwise.

I agree that the library of the University of Dublin, Trinity College, Dublin, may lend or copy this thesis upon request.



---

Daniel Bellett

# Table of Content

---

<b>DECLARATION .....</b>	<b>IX</b>
<b>ACKNOWLEDGEMENTS .....</b>	<b>X</b>
<b>SUMMARY .....</b>	<b>XI</b>
<b>NOMENCLATURE .....</b>	<b>XIII</b>
<b>CHAPTER 1: INTRODUCTION .....</b>	<b>1</b>
<b>CHAPTER 2: REVIEW OF FATIGUE ASSESSMENT METHODS.....</b>	<b>3</b>
2.1    DEFINITION OF TERMS.....	3
2.2    STRESS BASED FATIGUE ASSESSMENT METHODS .....	4
2.2.1 <i>The stress-life approach</i> .....	4
2.2.2 <i>Critical volume methods</i> .....	5
2.2.2.1    The Peterson and Neuber methods .....	5
2.2.2.2    The critical distance methods [Taylor, 1999] .....	7
2.2.2.2.1    The point and line methods .....	8
2.2.2.2.2    Criteria to define the focus path.....	9
2.2.2.3    The Pluvinage method .....	10
2.2.3 <i>The assessment of welds</i> .....	12
2.2.3.1    Design Codes and Standards .....	12
2.2.3.2    The "hot-spot" or structural stress approach.....	13
2.3    FATIGUE ASSESSMENT METHODS BASED ON LEFM .....	13
2.3.1 <i>The Smith and Miller method</i> .....	13
2.3.2 <i>The crack modelling method (CMM)</i> .....	14
2.4    STRAIN BASED FATIGUE ASSESSMENT METHODS.....	16
2.4.1 <i>The strain-life method</i> .....	16
2.4.1.1    Implementation of the strain-life approach using the Neuber Rule.....	16
2.4.1.2    Mean strain effects.....	18
2.5    CONCLUDING REMARKS.....	19

<b>CHAPTER 3: THE AREA AND VOLUME METHODS .....</b>	<b>20</b>
3.1 THE AREA METHOD.....	20
3.1.1 Which stress component to use.....	20
3.1.2 Determining the critical radius .....	21
3.1.3 Orientation of the critical area for a complex stress concentrations.....	23
3.2 THE VOLUME METHOD .....	24
3.2.1 The critical radius .....	24
3.2.2 Orientation of the critical volume for a complex stress concentrations.....	26
3.3 CONCLUDING REMARKS.....	26
<b>CHAPTER 4: PREVIOUS WORK DONE ON WELDS.....</b>	<b>27</b>
4.1 THE FATIGUE PROPERTIES OF WELDED JOINTS.....	27
4.2 TWO-DIMENSIONAL WELDED GEOMETRIES .....	28
4.3 A THREE-DIMENSIONAL WELDED GEOMETRY (T-SHAPE-B).....	30
4.4 CONCLUDING REMARKS.....	33
<b>CHAPTER 5: DEFINING THE PROBLEM.....</b>	<b>34</b>
5.1 ANOTHER 3-D WELDED GEOMETRY (FILLET-A).....	34
5.2 WELD DATA TAKEN FROM THE LITERATURE.....	37
5.3 THREE-DIMENSIONAL STRESS CONCENTRATIONS IN SOLID COMPONENTS .....	39
5.3.1 Material properties.....	39
5.3.2 The Model-E specimen .....	40
5.3.3 The Model-T specimen.....	42
5.4 CONCLUDING REMARKS.....	44
<b>CHAPTER 6: THE SHAPE EFFECT.....</b>	<b>45</b>
6.1 NON-PROPAGATING CRACKS.....	45
6.2 THE EFFECT OF CRACK SHAPE.....	48
6.2.1 The effect of crack shape on long crack growth.....	48
6.2.2 The effect of crack shape on non-propagating cracks.....	49
6.3 ASSESSMENT OF 3D STRESS CONCENTRATIONS USING A 2D “FOCUS PATH” .....	52
6.4 QUANTIFYING THE CORRECTION FACTOR.....	53
6.4.1 In terms of the elliptical integral, $\Phi$ .....	54
6.4.2 Verification of the correction factor defined in terms of $\Phi$ .....	57
6.5 ESTIMATING THE ACTUAL CRACK SHAPE .....	58

6.5.1	<i>Load sharing criteria</i> .....	62
6.5.2	<i>Application to the Model-T specimen</i> .....	65
6.5.3	<i>Application to the Model-E specimen</i> .....	66
6.5.4	<i>The effect of the growth law constants</i> .....	68
6.5.5	<i>Application of the method without load sharing</i> .....	68
6.5.6	<i>Conclusion</i> .....	69
6.6	APPLICATION OF THE CORRECTION FACTOR.....	70
6.6.1	<i>Model -T</i> .....	70
6.6.2	<i>Model-E</i> .....	71
6.6.3	<i>Fillet-A</i> .....	71
6.6.4	<i>T-shape-B</i> .....	72
6.7	CONCLUDING REMARKS.....	73
<b>CHAPTER 7: THE CONSTRAINT EFFECT .....</b>		<b>74</b>
7.1	CRACK TIP CONSTRAINT IN FRACTURE.....	74
7.1.1	<i>The plastic zone size due to Irwin</i> .....	75
7.1.2	<i>Plastic zone size due to Dugdale</i> .....	76
7.1.3	<i>Plastic zone shape</i> .....	77
7.1.4	<i>The effect of constraint on fracture toughness</i> .....	80
7.2	CRACK TIP CONSTRAINT IN FATIGUE.....	82
7.2.1	<i>The cyclic plastic zone</i> .....	82
7.2.2	<i>The effect of constraint on fatigue crack growth rate</i> .....	84
7.2.3	<i>Crack closure</i> .....	85
7.3	NOTCH TIP CONSTRAINT .....	87
7.4	QUANTIFYING THE DEGREE OF CONSTRAINT .....	87
7.4.1	<i>Using the plastic zone size</i> .....	87
7.4.1.1	<i>The relationship between plastic zone size and <math>a_0</math></i> .....	88
7.4.1.2	<i>Testing <math>\Delta K_{th}</math> in plane stress</i> .....	88
7.4.1.3	<i>Extension to 3-D stress concentrations</i> .....	89
7.4.1.4	<i>The plastic zone sizes for the various specimens</i> .....	90
7.4.2	<i>Elastic parameters</i> .....	91
7.4.2.1	<i>The <math>ps</math> parameter</i> .....	91
7.4.2.2	<i>Elastic strain energy parameter, <math>C_E</math></i> .....	93
7.4.2.3	<i>Von Mises stress parameter, <math>C_{VM}</math></i> .....	94
7.4.3	<i>Application of the elastic parameters</i> .....	95

7.4.3.1	Welded geometries .....	95
7.4.3.2	Model-E .....	97
7.4.3.3	Model-T .....	98
7.4.3.4	Discussion .....	99
7.5	EXPERIMENTAL INVESTIGATIONS OF THE CONSTRAINT EFFECT .....	99
7.5.1	<i>Determining <math>\Delta K_{th}</math> in both plane stress and plane strain</i> .....	99
7.5.1.1	The specimens and material properties .....	99
7.5.1.2	Fatigue tests and results .....	101
7.5.1.2.1	Measured S-N curves .....	101
7.5.1.2.2	Failure surfaces .....	104
7.5.1.2.3	Crack growth rate data .....	105
7.5.1.3	Life Corrected to a crack length of 0.8mm .....	108
7.5.1.4	A check of the degree of constraint .....	111
7.5.1.5	Conclusion .....	112
7.5.2	<i>A notched component in plane stress (Model-J)</i> .....	113
7.5.2.1	The specimen and material properties .....	113
7.5.2.2	Defining the degree of constraint .....	114
7.5.2.2.1	Application of the elastic constraint parameters .....	114
7.5.2.2.2	Elastic plastic finite element analysis .....	115
7.5.2.3	Experimental results .....	115
7.5.2.4	Fatigue analysis results .....	116
7.5.2.5	Discussion and conclusions .....	117
7.6	QUANTIFYING THE EFFECT OF CONSTRAINT .....	118
7.6.1	<i>Method 1</i> .....	118
7.6.2	<i>Method 2</i> .....	120
7.7	CONCLUDING REMARKS .....	122
<b>CHAPTER 8: THE STRESSED VOLUME EFFECT</b> .....		<b>124</b>
8.1	DEFINITION OF TERMS .....	125
8.2	THE CRITICAL DISTANCE METHODS AND THE STRESSED VOLUME EFFECT .....	126
8.3	SIZE EFFECTS IN PLAIN CYCLIC TENSION SPECIMENS .....	128
8.4	A STATISTICAL APPROACH TO THE STRESSED VOLUME EFFECTS .....	130
8.4.1	<i>The Weibull distribution</i> .....	130
8.4.2	<i>Two-parameter and three-parameter distributions</i> .....	131
8.4.3	<i>Volume dependence</i> .....	131



8.4.4	<i>Comparison between specimens</i> .....	132
8.4.5	<i>The effective volume model</i> .....	133
8.4.5.1	Comparison between specimens.....	135
8.4.5.2	Application to size effect data for plain specimens.....	135
8.4.5.2.1	Plain rotating bending specimen.....	135
8.4.5.2.2	Plain cyclic tension specimens .....	137
8.4.5.2.3	Discussion.....	137
8.4.5.3	Extension to notched components .....	139
8.4.5.3.1	Definition of failure .....	140
8.4.5.3.2	Calculation of the effective volume.....	140
8.4.5.3.3	Application to the various specimens.....	142
8.4.5.4	The Weibull modulus .....	145
8.4.5.5	Discussion.....	145
8.5	AN EFFECTIVE VOLUME CORRECTION TO THE CDMs.....	147
8.5.1	<i>The stressed volume correction</i> .....	148
8.5.2	<i>Application to three-dimensional stress concentrations</i> .....	149
8.5.3	<i>Application to the various specimens</i> .....	149
8.5.4	<i>Discussion</i> .....	151
8.6	CONCLUDING REMARKS .....	152
<b>CHAPTER 9: COMBINING THE EFFECTS .....</b>		<b>153</b>
9.1	MODEL-E .....	153
9.2	MODEL-T .....	154
9.3	MODEL-J .....	155
9.4	FILLET-A .....	157
9.5	T-SHAPE-B .....	158
9.6	DISCUSSION.....	159
<b>CHAPTER 10: CONCLUSIONS.....</b>		<b>160</b>
<b>REFERENCES:.....</b>		<b>162</b>
<b>APPENDIX A: EXPERIMENTAL INVESTIGATIONS.....</b>		<b>170</b>
A.1	MATERIAL CHARACTERISATION.....	170
A.1.1	<i>Mechanical properties and the monotonic stress-strain relationship</i> .....	170
A.1.2	<i>The cyclic stress-strain relationship and LCF data</i> .....	172

A.1.3	<i>Chemical properties</i> .....	173
A.1.4	<i>Fatigue properties</i> .....	173
A.1.4.1	Plain specimen fatigue strength in bending .....	173
A.1.4.2	Plain specimen fatigue strength in tension .....	176
A.1.4.3	The threshold stress intensity factor .....	178
A.1.4.4	Determining $\Delta K_{th}$ and $a_0$ .....	179
A.1.4.5	The Smith and Miller diagram .....	182
A.1.5	<i>Stress relieving</i> .....	183
A.1.6	<i>Hardness test</i> .....	184
A.1.7	<i>Microstructure</i> .....	185
A.2	THE FILLET-A SPECIMEN .....	187
A.2.1	<i>The specimen</i> .....	187
A.2.2	<i>Material properties and welding</i> .....	188
A.2.3	<i>Experimental results</i> .....	189
A.2.3.1	Horizontal displacement of the lower clamp .....	191
A.2.4	<i>Stress and fatigue analysis</i> .....	195
A.2.4.1	Mesh refinement .....	195
A.2.4.2	Weld penetration and the gap distance .....	195
A.2.4.3	Modelling of the weld end .....	196
A.2.4.4	Summary of FE models .....	196
A.2.4.5	Selection of the focus path .....	197
A.2.4.6	Summary of the results .....	200
A.2.5	<i>Discussion</i> .....	201
A.3	THE MODEL-E SPECIMEN .....	201
A.3.1	<i>The specimen</i> .....	201
A.3.2	<i>Material properties</i> .....	202
A.3.3	<i>Experimental results</i> .....	203
A.3.4	<i>Stress and fatigue assessments</i> .....	204
A.3.4.1	Selection of the focus path .....	205
A.3.4.2	Summary of results .....	207
A.3.5	<i>Discussion</i> .....	208
A.4	THE MODEL-T SPECIMEN .....	209
A.4.1	<i>The specimen</i> .....	209
A.4.2	<i>Material properties</i> .....	211

A.4.3	<i>Experimental results</i> .....	211
A.4.3.1	Crack shape observation and measurement.....	212
A.4.3.1.1	Crack growth measurements.....	213
A.4.3.1.2	SEM observations of the crack shape.....	214
A.4.4	<i>Stress and fatigue assessments</i> .....	222
A.4.4.1	Direction of the focus path.....	225
A.4.4.2	Summary of results.....	226
A.4.5	<i>Discussion</i> .....	227
A.5	CONCLUDING REMARKS.....	227
<b>APPENDIX B: APPLICATION OF OTHER FATIGUE METHODS.....</b>		<b>228</b>
B.1	THE PLUVINAGE METHOD.....	228
B.2	THE NEUBER AND PETERSON METHODS.....	231
B.3	THE STRAIN LIFE METHOD.....	233
B.3.1	<i>Using an elastic-plastic FEA</i> .....	234
B.3.2	<i>Using the Neuber rule</i> .....	236
B.4	CONCLUDING REMARKS.....	239
<b>APPENDIX C: ANSYS MACROS .....</b>		<b>240</b>
C.1	THE AREA METHOD MACRO .....	240
C.1.1	<i>Methodology</i> .....	240
C.1.2	<i>Running the Area Method macro</i> .....	240
C.1.3	<i>Inputs</i> .....	241
C.2	THE VOLUME METHOD MACRO.....	242
C.2.4	<i>Methodology</i> .....	242
C.2.5	<i>Running the Volume Method macro</i> .....	243
C.2.6	<i>Inputs</i> .....	243
<b>APPENDIX D: APPLICATION OF PM TO ROTATING BENDING DATA....</b>		<b>245</b>
D.1	THE DATA .....	245
D.2	APPLICATION OF THE POINT METHOD.....	248
D.3	DISCUSSION.....	253

## Declaration

---

I declare that the present work has not been submitted as an exercise for a degree at any other University. This thesis consists entirely of my own work except where references indicate otherwise.

I agree that the library of the University of Dublin, Trinity College, Dublin, may lend or copy this thesis upon request.

---

Daniel Bellett

## Acknowledgements

---

I would like to express my heartfelt thanks to my supervisor Prof. David Taylor for his guidance, patience, wisdom and experience, all of which was invaluable to the completion of this project. Sir Isaac Newton was right, it is only by standing on the shoulders of giants that any of us will ever see further. I feel particularly fortunate that our paths have crossed and thank you for creating a great environment in which to work.

I must also acknowledge the contributions made to this work by Stephano Marco, Ezio Mazzeo, Jerome Guillois and Thomas Pircher. Thank you gentlemen, I can honestly say that it was an experience I would gladly repeat.

A special thanks goes to all the people in the Fatigue research group, both past and present. Gerry, Stephano, Ezio, Jerome, Thomas, Susanne, Victor, Luca, Vincenzo and Zep it has been a pleasure.

Thanks to Peter O'Reilly for his help testing and to Tom, Sean and Gabriel for showing me around the workshop.

To all the postgraduates and staff, you know who you are. Thank you. You've made my time at Trinity very memorable indeed.

I also gratefully acknowledge the financial support provided by IDAC Ireland, Enterprise Ireland and Rover Ltd. UK.

Finally, thank to Maryline for putting up with me and to my parents and family for their constant support.

## Summary

---

The fatigue behaviour of complex three-dimensional notched components is a subject of great practical interest to industrial engineers. Unfortunately, the analysis of this type of feature presents problems for most assessment methods, which have been developed on the basis of standard two-dimensional fatigue specimens. This work is essentially an investigation of several factors that are considered important and unique to the assessment of this type of feature.

It has been demonstrated experimentally that the fatigue assessment methods advocated by Taylor [1996; 1999], and indeed most assessment methods, result in conservative predictions for certain three-dimensional stress concentration features. These are typically very localised stress concentrations characterised by high stress gradients in all directions and also stress concentrations characterised by low constraint.

Three possible explanations have been proposed and investigated. These have been termed the *shape effect*, the *constraint effect* and the *stressed volume effect*.

The *shape effect* is based on the observation that if failure is forced to occur at a point or small region, via geometrical constraints, it will have a semi-elliptical crack front. It is proposed that even at the so-called fatigue limit, crack shape can affect the life of a component through the growth of non-propagating cracks. It is shown that a simple correction factor, based on the crack shape, can be applied to account for this.

It is well known that crack tip constraint, or the degree of plane stress, has a considerable effect on fracture. The *constraint effect* is an investigation of the corresponding effect in fatigue. It is shown experimentally that the stress intensity threshold measured in conditions of plane stress is significantly higher than the corresponding value measured in plane strain. It is further demonstrated that fatigue predictions made for stress concentration features characterised by low notch tip constraint result in conservative errors.

The third possible explanation for the conservative errors is referred to as the *stress volume effect*. This idea is based on the fact that the volume of highly stressed material is considerably smaller for localised 3D stress concentrations, when compared to an equivalent two-dimensional notched geometry. Hence, the probability of finding a flaw or crack initiation location in the stressed region is lower. A method to account for this using a Weibull type analysis is proposed. It is shown that if appropriate values of the Weibull modulus are assumed, a stressed volume correction can be made which is self-consistent and makes good sense for the specimens considered here. Unfortunately, this is not enough data to confirm the validity of the approach.

It is shown that, within the framework of the assumptions made and if all of the effects mentioned above are considered, the conservative errors can be accounted for and good predictions can be made for the three-dimensional stress concentrations considered in this work.

# Nomenclature

---

Symbol	Unit	Definition
a	mm	Crack length
a <sub>o</sub>	mm	El Haddad short crack constant
a <sub>p</sub>	mm	Peterson material characteristic length
A		Constant factor in the growth rate equation
AM		Area method or area critical distance method
b		Weibull modulus
C		Ratio of plain specimen fatigue strength to the yield strength
C <sub>E</sub>		Parameter to determine the degree of constraint
C <sub>VM</sub>		Parameter to determine the degree of constraint
CDMs		Critical distance methods
CMM		Crack modelling method
CPZ		Cyclic plastic zone
D	mm	Notch depth
E	GPa	Young's modulus
F		Crack shape or configuration factor
F <sub>assumed</sub>		Assumed crack shape factor
F <sub>actual</sub>		Actual crack shape factor
<i>f<sub>shape correction</sub></i>		Correction factor due to crack shape
<i>f<sub>size correction</sub></i>		Correction factor due to stressed volume effect
K	MPa m <sup>1/2</sup>	Stress intensity factor
K <sub>c</sub>	MPa m <sup>1/2</sup>	Critical stress intensity factor or fracture toughness
K <sub>1c</sub>	MPa m <sup>1/2</sup>	Plane strain critical stress intensity factor or fracture toughness
K <sub>f</sub>		Fatigue notch factor
K <sub>t</sub>		The elastic stress concentration factor
K <sub>e</sub>		Strain concentration factor
K'		Cyclic hardening coefficient
LM		Line method or line critical distance method
MPZ		Monotonic plastic zone
m		Crack growth rate exponent
N		Number of cycles
N <sub>f</sub>		Number of cycles to failure
n'		Cyclic hardening exponent
P	N	Applied point load
P <sub>s</sub>		Probability of survival
PM		Point method or point critical distance method
P <sub>SWT</sub>		Smith, Watson and Topper parameter
ps		Parameter to determine the degree of plane stress
q		Notch sensitivity index
r <sub>c</sub>	mm	Critical distance
U		Closure ratio
UTS	MPa	Ultimate tensile strength
VM		Volume method or volume critical distance method
V <sub>ref</sub>	mm <sup>3</sup>	Reference volume



$V_{\text{eff}}$	$\text{mm}^3$	Effective volume
$V_{\text{crit}}$	$\text{mm}^3$	Critical volume used in the volume method
$v$	$\text{mm}$	Crack face displacement
$Z_I$		Westergaard stress function
$\Delta\sigma_{\text{ave}}$	MPa	Average stress range
$\Delta\sigma_{\text{max}}$	MPa	Maximum value of the 1st principal stress range
$\Delta\sigma_{\text{on}}$	MPa	The notched specimen fatigue strength range
$\Delta\sigma_{\text{o}}$	MPa	The plain specimen fatigue strength range
$\Delta\sigma_{\text{nom}}$	MPa	Nominal stress range
$\Delta\sigma_{\text{ref}}$	MPa	Reference stress for which the $P_s = 37\%$
$\Delta K$	$\text{MPa m}^{1/2}$	Range of the stress intensity factor
$\Delta K_{\text{eff}}$	$\text{MPa m}^{1/2}$	Effective stress intensity factor range
$\Delta K_{\text{th}}$	$\text{MPa m}^{1/2}$	Threshold stress intensity factor range
$\Delta K_{\text{th,a}}$	$\text{MPa m}^{1/2}$	Threshold stress intensity range used in the resistance curve
$\Delta K_I$	$\text{MPa m}^{1/2}$	Mode I stress intensity factor range
$\varepsilon$		Strain
$\varepsilon_f'$		Fatigue ductility coefficient
$\Phi$		Complete elliptical integral of the second kind
$\sigma_{\text{FI}}$	MPa	Stress field intensity (Pluvinage method)
$\sigma_y$	MPa	Stress in the y-direction
$\sigma_{\text{ys}}$	MPa	Yield stress
$\sigma_f'$	MPa	Fatigue strength coefficient
$\rho$	$\text{mm}$	Root radius or the radius in a spherical coordinate system
$\rho^*$	$\text{mm}$	Neuber material characteristic length
$\mu$	MPa	Shear modulus
$\nu$		Poisson's ratio
$2r_y$	$\text{mm}$	Irwin's plastic zone size

# Chapter 1: Introduction

---

The fatigue behaviour of engineering materials is an extremely complex subject. Even after more than 100 years of continuous research, industrial engineers still don't have adequate tools for the fatigue design and assessment of real engineering components. Indeed the notch sensitivity concept, developed by Neuber [1958], Peterson [1959] and others, more than 40 years ago is still the dominant tool used in the high cycle fatigue regime. This is due mostly to the complexity of the problem, but also to the tendency of researchers to reduce the problem to the most fundamental level, or to try and isolate the specific problem of interest to them. Hence, in the body of research about fatigue of notched components, the most common problem studied is the behaviour of very simple two-dimensional notched geometries, subject to constant amplitude, mode one loading, in controlled environmental conditions. This is a very sound scientific approach, however fatigue assessment methods developed in this way are of little practical use until they have been extended and validated to include all complicating factors, such as variable amplitude loading, multi-axial loading, environmental effects, residual stresses, size effects, the analysis of welded joints and complex geometries to name just a few.

The work presented here is centred on the fatigue analysis methods developed by Taylor and co-workers. These include the crack modelling method (CMM) and the critical distance methods (CDMs). A brief discussion of these is given in Chapter 2 along with a review of other common methods used for the analysis of notched components. It has been shown, prior to the commencement of this work, that the CMM and CDMs can be used successfully to predict the behaviour of standard two-dimensional fatigue specimens and various engineering components, in the high cycle fatigue regime. Hence, the initial aim of this project was to extend these methods to include the analysis of welded geometries.

Some previous work on welded geometries had already been undertaken, with mixed results. This is discussed in Chapter 4. Basically, it had been shown that the methods are very successful at predicting the behaviour of two-dimensional welded geometries, however significant conservative errors were observed when predicting the behaviour of a

more three-dimensional welded geometry. That is, a geometry where the failure occurs at the end of a weld bead.

The initial work undertaken in this project was experimental and was done with the purpose of clarifying the conservative predictions observed for the three-dimensional welded geometry mentioned above. The results of these investigations are given briefly in Chapter 5, although full and complete details are presented in Appendix A. Essentially it was concluded that the conservatism is not only limited to 3D welded geometries but can also be observed in certain three-dimensional stress concentration features machined from solid steel. These features are typically very localised stress concentrations where failure is confined to occur from a point or small region and are characterised by high stress gradients in all directions.

From this point forward, the focus of the project moved to understanding and explaining this conservatism, which wasn't seen in the two-dimensional case.

The first approach investigated was to consider a volume implementation of the critical distance methods, which was thought to be more appropriate for the assessment of three-dimensional stress concentrations. This is referred to as the volume method and is discussed in Chapter 3. Unfortunately it was demonstrated that this approach did not significantly decrease the prediction error.

Therefore, three possible explanations, based on the observed differences between two and three-dimensional stress concentrations, were proposed and investigated in parallel. These have been termed the *shape effect*, *constraint effect* and the *stressed volume effect* and are discussed in Chapters 6, 7 and 8 respectively. It is shown in Chapter 9 that if all of these effects are taken into consideration the conservative errors can be explained.

## Chapter 2: Review of fatigue assessment methods

---

In the following, a brief review of the most common methods used for the fatigue assessment of notched components is undertaken. Particular attention is paid to the way in which each of these methods is able to deal with the assessment of complex three-dimensional stress concentrations. But first, some important terms, used throughout this work, are defined.

### 2.1 Definition of terms

#### *Endurance strength*

This term is used to indicate the strength of a component or specimen corresponding to a given number of cycles, which is less than the number of cycles where the *knee* in the stress-life curve occurs. The *knee* is the position on the curve where the slope decreases, so that the curve becomes almost horizontal.

#### *Fatigue limit*

This is a slightly misleading term, but one which is too well established in the engineering terminology to be forgotten. It implies that there is in fact a fatigue limit, below which a component will never fail. Its use here does not imply this. It's simply used to indicate the strength of a component or specimen at its life corresponding to the knee in its stress-life curve, which is assumed to occur somewhere between  $1 \times 10^6$  and  $1 \times 10^7$  cycles. If no knee in the stress-life curve is observed, the term endurance strength is used.

#### *Fatigue strength*

As above this term is used to indicate the strength of a component or specimen at its life corresponding to the knee in its stress-life curve, however, the number of cycles at which this occurs is always stated. Hence this is a slightly more precise term than fatigue limit.

#### *Initiation and propagation life*

In this work it is assumed that the initiation life of a fatigue crack is very short. That is, it is extremely easy to initiate a crack, even if it is very small and confined to a single crystal.

In this way the life of a crack is simply one of propagation life. It should be noted however, that short crack growth behaviour is different to that of long cracks, which is emphasised by the fact that linear elastic fracture mechanics does not provide a valid description of short crack behaviour.

*Shape factor or configuration factor, F*

This is a factor that modifies the stress intensity reference value (i.e. the stress intensity for a through-thickness, two-dimensional centre crack of length  $2a$  in an infinite plate subjected to a uniform tensile stress) to account for other cracked geometries, configuration and loading conditions.

*Stress intensity factor and stress intensity factor range*

This is a measure of the strength, or change in strength, of the singularity in the elastic stress field ahead of a crack given by the standard linear elastic fracture mechanics equation.

*Stress intensity threshold*

This is the stress intensity range for which negligible crack growth can be observed, or the crack growth rate approaches zero. It is considered to be a constant for long cracks. This isn't the case for short cracks, where the threshold approaches zero as the crack length goes to zero. Unless otherwise clarified the stress intensity threshold is always assumed to be the long crack threshold.

## **2.2 Stress based fatigue assessment methods**

### 2.2.1 The stress-life approach

The stress-life approach to the fatigue assessment of notched components is based on the concept that failure is assumed to occur if the maximum stress range at the notch tip exceeds the fatigue strength of a smooth specimen at the same life. This can be expressed mathematically in terms of the elastic stress concentration factor,  $K_t$  as follows:

$$\Delta\sigma_{on} = \frac{\Delta\sigma_o}{K_t} \quad (2-1)$$

Where  $\Delta\sigma_{on}$  is the fatigue strength range of the notched specimen and  $\Delta\sigma_o$  is the fatigue strength range of the smooth specimen. The elastic stress concentration,  $K_t$  is defined as the ratio of the maximum local stress at the notch tip, to the nominal stress.

The method is relatively simple to implement, either through the use of published stress concentration factors [e.g. Peterson, 1953; 1974] or by the use of finite element analysis. The application to complex three-dimensional geometries generally requires the latter. However, one limitation is that it is unable to deal with the class of problems in which there exists a singularity in the elastic stress field. This can occur either through finite element modelling simplifications, for example when a fillet radius is modelled as a sharp corner or in the modelling of cracks. In this case, the elastic stress concentration factor approaches infinity, hence the method would predict a notched fatigue strength of zero, which is clearly incorrect.

The stress-life method is relatively successful at predicting the behaviour of "blunt" stress concentrations, however it becomes increasingly conservative when the amount of plastic deformation at the notch root increases, or as the stress concentration becomes sharper. This was demonstrated clearly by Frost [1959].

## 2.2.2 Critical volume methods

Critical volume theories have been used in the analysis of notches for over 40 years, since the work of, Neuber [1958], Peterson [1959], Siebel and Stieler [1955] and others. The basic idea is to examine stresses not only at the notch tip but also within a discrete volume of material surrounding the notch. It is assumed that fatigue failure will occur if the average cyclic stress within this volume exceeds some given value, usually taken to be the plain specimen fatigue strength.

### 2.2.2.1 The Peterson and Neuber methods

The Peterson and Neuber methods are based on critical volume concepts, as discussed above, but are usually implemented using the "fatigue notch factor",  $K_f$ .

$$K_f = \frac{\text{unnotched bar fatigue strength}}{\text{notched bar fatigue strength}} \quad (2-2)$$

In general,  $K_f$  is less than  $K_t$  and approaches  $K_t$  for large notch-root radii and for higher strength materials. The relationship between the  $K_t$  and  $K_f$  is often described in terms of the notch sensitivity index, which is defined as:

$$q = \frac{K_f - 1}{K_t - 1} \quad (2-3)$$

Hence,  $q$  varies from zero, where there is no notch effect, to unity, where the full effect predicted by elasticity theory is observed. The difference between  $K_f$  and  $K_t$  is a function of both the local notch geometry and the material.

Neuber [1958] proposed that the controlling parameter for the fatigue behaviour of notched components should be the elastic stress averaged in some critical volume surrounding the stress concentration. He simplified this by using the average stress on a line ahead of the notch. He argued that the critical volume or distance should be large enough so that the material is sampled homogeneously, that is to say that there should be more than one grain included, with ideally enough grains to make sure that the behaviour of the material in the critical volume is *typical* of the material as a whole. Based on these ideas, and using the notch root radius,  $\rho$ , as a parameter to characterise the stress field surrounding a notch, Neuber developed the following approximate formula for the notch factor for  $R = -1$  loading:

$$q = \frac{1}{1 + \sqrt{\rho^*/\rho}} \quad \text{or} \quad K_f = 1 + \frac{K_t - 1}{1 + \sqrt{\rho^*/\rho}} \quad (2-4)$$

Where  $\rho^*$  is the characteristic length, or critical distance of the material. This has to be determined empirically and is generally correlated to the ultimate tensile strength of the material.

Peterson [1959] used a similar approach, although he simplified the situation even further by considering only the stress at a point ahead of the stress concentration. He proposed the following:

$$q = \frac{1}{1 + \frac{a_p}{\rho}} \quad \text{or} \quad K_f = 1 + \frac{K_t - 1}{1 + \frac{a_p}{\rho}} \quad (2-5)$$

Where  $a_p$  is another material characteristic length which has to be determined empirically.

Implementation of these methods for complex three-dimensional stress concentrations is usually possible, although it is often difficult to define the nominal stress range, which is needed to determine the elastic stress concentration factor,  $K_t$ , which is in turn required to calculate the notch reduction factor,  $K_f$ . Also, because  $K_f$  is a function of the notch root radius, these methods are unable to deal with the class of problems that are characterised by a singularity in the elastic stress field (i.e. when there is no root radius). Situations where this is important are discussed in Section 2.2.1.

#### 2.2.2.2 The critical distance methods [Taylor, 1999]

The major weakness of the traditional critical-volume methods, discussed above, is that the material characteristic length or critical distance parameter must be determined empirically. This parameter is known to vary considerably from one material to another, and large errors can occur if the critical distance is slightly incorrect. This problem was solved by Taylor [1999] by borrowing a fracture mechanics concept. He pointed out that the critical distance can be determined explicitly for a crack and that if a crack is considered as the limiting case of a sharp notch where the root radius goes to zero, then this distance should be equally valid for notched components. Tanaka [1983] similarly realised this, 16 years earlier, but he failed to appreciate the importance and wide applicability of this approach.

Simplifications, similar to those made by Neuber [1958] and Peterson [1959], can be adopted using this approach. That is, the method can be applied by:

- a) Considering only the stress range at a single point ahead of the stress concentration. This is referred to, by Taylor, as the Point Method (PM).
- b) Considering the average stress range on a line ahead of the stress concentration. This is termed the Line Method (LM).

This approach can also be implemented by considering the average stress in an area or volume surrounding the stress concentration. These are referred to as the Area Method (AM) and Volume Method (VM) and are discussed more fully in Chapter 3.



### 2.2.2.2.1 The point and line methods

A full discussion of the point method and line method will not be included here, as they are reported elsewhere [Taylor, 1999; 2001], [Taylor *et al.*, 2000], [Taylor and Wang, 1999; 2000] and [Wang, 1999], however it is important to note that the critical distance,  $r_c$ , for these methods is calculated to be:

For the Point Method:

$$r_c = \left( \frac{\Delta K_{th}}{\Delta \sigma_o} \right)^2 \left( \frac{1}{2\pi} \right) = \frac{a_o}{2} \quad (2-6)$$

For the Line Method:

$$r_c = \left( \frac{\Delta K_{th}}{\Delta \sigma_o} \right)^2 \left( \frac{2}{\pi} \right) = 2a_o \quad (2-7)$$

Where,  $a_o$  is El Haddad's constant [El Haddad *et al.*, 1980], which is a parameter used in short-crack fracture mechanics and is defined as:

$$a_o = \left( \frac{\Delta K_{th}}{\Delta \sigma_o} \right)^2 \left( \frac{1}{\pi} \right) \quad (2-8)$$

It should be noted that the El Haddad parameter is used only as a convenience, although a slightly confusing one. As defined by El Haddad,  $a_o$  is the geometrical intersection of the two lines on the Kitagawa diagram [Kitagawa and Takahashi, 1976]. As such it is a function of the configuration, or shape factor of the specimen used to construct the Kitagawa diagram. This is not the case here, where it is always defined as per equation 2-8 (this is in fact the  $a_o$  for a centre cracked infinite plate where the configuration factor is equal to one).

Implementation of the point and the line method is extremely simple and is most easily achieved through the use of a linear elastic finite element analysis to determine the stress distribution around the stress-concentration in question. Once this is available, the opening stress, or first principal stress is plotted on a *focus path*, ahead of the stress concentration. The focus path is simply a line, starting at the hotspot and extending into the component, in some direction. The criteria to define the direction of the focus path are discussed below.

However, once the stress-distance data is available, it is a matter of determining if the stress at the critical distance (PM) or the average stress (LM) is greater than the plain specimen fatigue strength. If it is, failure is predicted.

#### 2.2.2.2.2 Criteria to define the focus path

The focus path is chosen to coincide with the direction of fatigue crack propagation. In order to estimate this for any three-dimensional stress concentration, two criteria are needed. These are stated as follows:

- a) The *plane of crack growth* is chosen to be perpendicular to the maximum principal stress at the hotspot. For two-dimensional geometries the plane of crack growth is a line, hence only this criterion required. This is illustrated in Figure 2.1(a), where the focus path coincides with the x-axis.
- b) The direction of the focus path within the plane of crack growth is chosen to be the direction of *minimum crack growth potential*. This is determined by examining the stress field resulting from the stress concentration, without the presence of a crack. Consider the situation shown in Figures 2.1(a) and (b). The problem is to find which angle  $\beta$ , should be chosen in the x-z plane, or the plane of crack growth. If the focus path were chosen to be coincident with the z-axis ( $\beta = 90^\circ$ ), the stresses on this path would be essentially constant and equal to the maximum stress. If it were chosen to be on the x-axis ( $\beta = 0^\circ$ ), the stress distribution would rapidly fall away to the nominal stress. Any other path (between  $\beta = 0^\circ$  and  $90^\circ$ ) will result in an intermediate situation. Hence, the stress distribution in the x-direction will result in much slower crack growth than any other direction in the x-z plane. This is the direction of minimum crack growth potential and is chosen to be the focus path because it is believed that crack growth in this direction will retard growth in all other directions and is thus more representative of the three-dimensional phenomenon. It should be noted that the direction of minimum crack growth potential is simply the direction with the highest stress gradient.

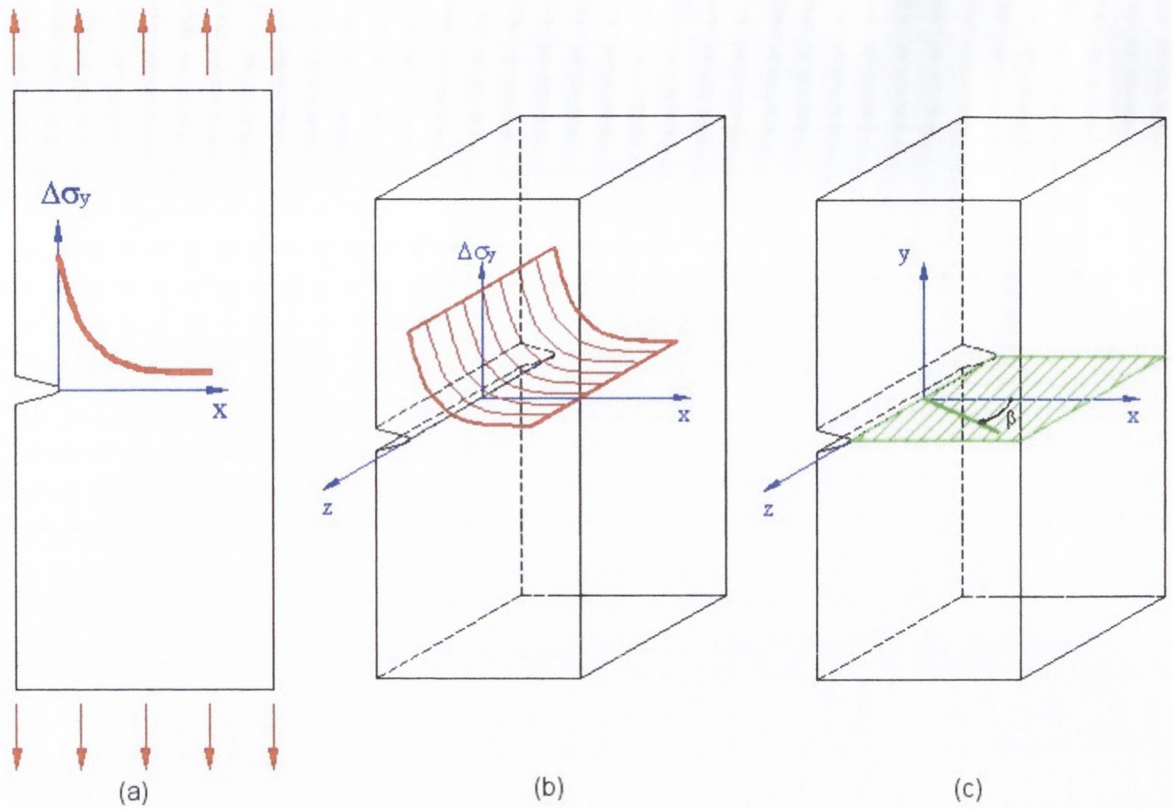


Fig. 2.1 - Choice of the focus path

### 2.2.2.3 The Pluvinage method

The Pluvinage approach [Qyalfku et al., 1999; 2001] is essentially a critical distance method implemented using the elastic-plastic stress distribution and taking into consideration the evolution of the stress gradient.

Figure 2.2, shows a typical elastic-plastic stress distribution ahead of a notch, which can be divided into three distinct regions:

Zone I - the opening stress is nearly constant and/or increasing to a maximum,  $\sigma_m$ .

Zone II - is an intermediate transition zone.

Zone III - there exists a pseudo stress singularity, which can be described by,

$$\sigma_{yy} = \frac{C}{x^\alpha} \quad (2-9)$$

where  $\alpha$  and  $C$  are constants depending on the load and geometry. The distance that corresponds to the beginning of the third zone is referred to as the effective distance,  $x_{ef}$ . This is assumed to be the boundary of the fatigue process zone and also corresponds to the

boundary of plastic relaxation. The stress corresponding to this distance is named the effective stress,  $\sigma_{ef}$ , and is assumed to play the major role in the mechanisms of fatigue.

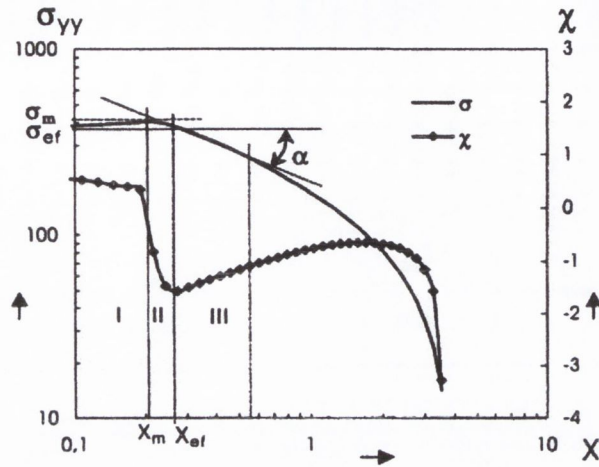


Fig. 2.2 - The elastic-plastic stress distribution and the relative gradient as a function of distance from the notch tip

The relative stress gradient,  $\chi$ , is also shown in the same diagram. This is defined as:

$$\chi = \frac{1}{\sigma(x)} \frac{d\sigma(x)}{dx} \quad (2-10)$$

It can be seen from Figure 2.2 that at the effective distance, the relative stress gradient is a minimum.

Based on the above observations and definitions, the following fatigue assessment criterion has been suggested. In this approach failure is assumed if the value of the stress field intensity,  $\sigma_{FI}$ , described by the equation below, is greater than the smooth specimen fatigue strength.

$$\sigma_{FI} = \frac{1}{x_{ef}} \int_0^{x_{ef}} \sigma_{yy} (1 - \chi x) dx \quad (2-11)$$

This is essentially the average opening stress, on a line of length equal to the effective stress, multiplied by a weight function, which is determined by the relative stress gradient.

A similar approach has also been proposed using a volumetric method. In this case the effective stress is defined as the average of the weighted stress inside the fatigue process volume:

$$\sigma_{FI} = \frac{1}{V_{ef}} \iiint_{V_{ef}} \sigma_{ij}^* dV \quad (2-12)$$

Where the weighted stress is given by:

$$\sigma_{ij}^* = \sigma_{ij} \cdot \varphi(r, \chi) \quad (2-13)$$

And the weight function is defined as:

$$\varphi(r, \chi) = e^{r \cdot \chi / 2} \quad (2-14)$$

In the three-dimensional case the relative stress gradient is:

$$\chi = \frac{1}{\sigma_{ij}} \frac{\delta \sigma_{ij}}{\delta X} \quad (2-15)$$

### 2.2.3 The assessment of welds

There are two schools of thought regarding the fatigue assessment of welded joints. Some people believe that they can be treated exactly the same as solid components and others believe that they cannot. In this work the former is assumed. However, two of the most common methods used almost exclusively for the assessment of welded joints are discussed below.

#### 2.2.3.1 Design Codes and Standards

Design codes and standards such as BSI [1993], are essentially a "nominal stress" approach to fatigue design and are based on a vast quantity of experimental data. They define various detail classes, each of which corresponds to an S-N curve. The S-N curve includes the effect of the weld and local stress concentration at the failure location (usually the weld toe or root).

This approach is well accepted, due to its ease of use and formal codification, but is quite limited. That is, a designer only has a limited number of detail classes into which he must classify every possible geometry. Also, it is often very difficult to define the nominal stress, in a complicated geometry.

### 2.2.3.2 The "hot-spot" or structural stress approach

The structural stress approach to the design of welded joints is similar to the nominal stress approach, however the structural stress is defined as per Figure 2.3 below. It includes the stress raising effects due to structural geometry or local discontinuities but excludes the stress concentrations due to the presence of the weld. A single S-N curve can then be used for the assessment of all welds.

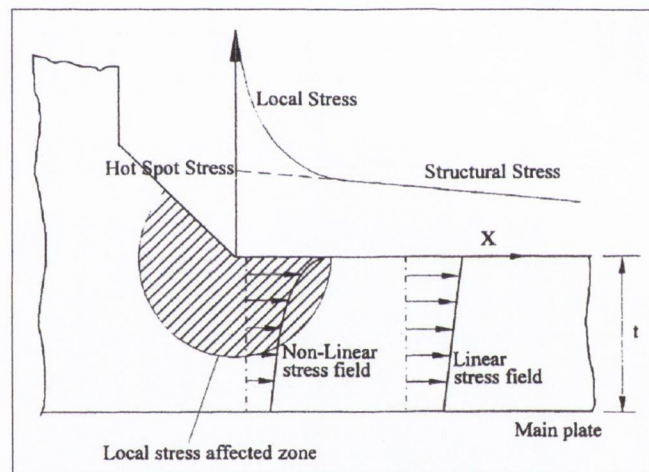


Fig. 2.3 - Definition of structural stress and the hotspot stress

## 2.3 Fatigue assessment methods based on LEFM

### 2.3.1 The Smith and Miller method

Smith and Miller [1978] demonstrated that *sharp* notches could be modelled as cracks using linear elastic fracture mechanics (LEFM). Figure 2.4, often referred to as the Smith and Miller Diagram, is a schematic representation of this. It shows that as the stress concentration of a notched fatigue specimen is increased (by reducing the notch root radius, but keeping the depth constant), experimental results deviate from the prediction made using the stress-life method, where the fatigue strength is given by equation 2-1.

However they subsequently approach the predictions made using LEFM, where the fatigue strength is determined from:

$$\Delta\sigma_{on} = \frac{\Delta K_{th}}{F\sqrt{\pi D}} \quad (2-16)$$

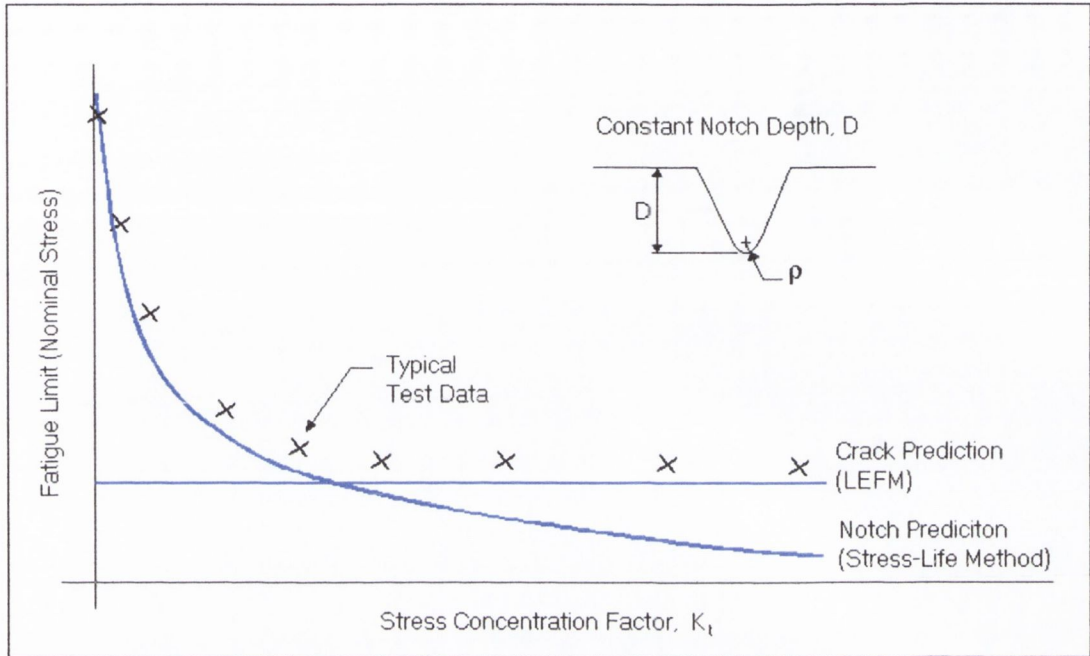


Fig. 2.4 - Schematic representation of the effect of  $K_t$  on the fatigue strength of notched specimens with constant notch depth, showing experimental results and predictions based on: (a) the stress-life method and (b) LEFM

Hence the stress-life method and LEFM can be used together to obtain a good prediction. Which ever of the two methods estimates a higher fatigue strength, will be more accurate.

### 2.3.2 The crack modelling method (CMM)

The Smith and Miller approach works well for a simple geometry, however for more complex shapes, in which it is impossible to define a crack (or notch) depth, equation 2-16 cannot be used.

The Crack-modelling method [Taylor, 1996] is a solution to this problem. It is essentially a method to obtain an equivalent stress intensity range, for any two or three-dimensional stress concentration feature, based on the stress distribution. Figure 2.5 is a schematic

illustration of the concept. Essentially, the elastic stress distribution obtained via finite element analysis, ahead of the stress concentration feature, is compared to the theoretical stress distribution ahead of a centre-crack in an infinite plate. The theoretical curve, obtained via the Westergaard equation [Westergaard, 1939], which best fits the FEA data defines an equivalent stress intensity factor. This can then be compared to the stress intensity threshold range,  $\Delta K_{th}$ , of the material to determine the likelihood of failure, for a given load range. It should be noted however, that like the Smith & Miller method discussed above, the CMM must be used in conjunction with the stress-life method to obtain a good prediction. Which ever of the two methods estimates a higher fatigue strength, will be more accurate.

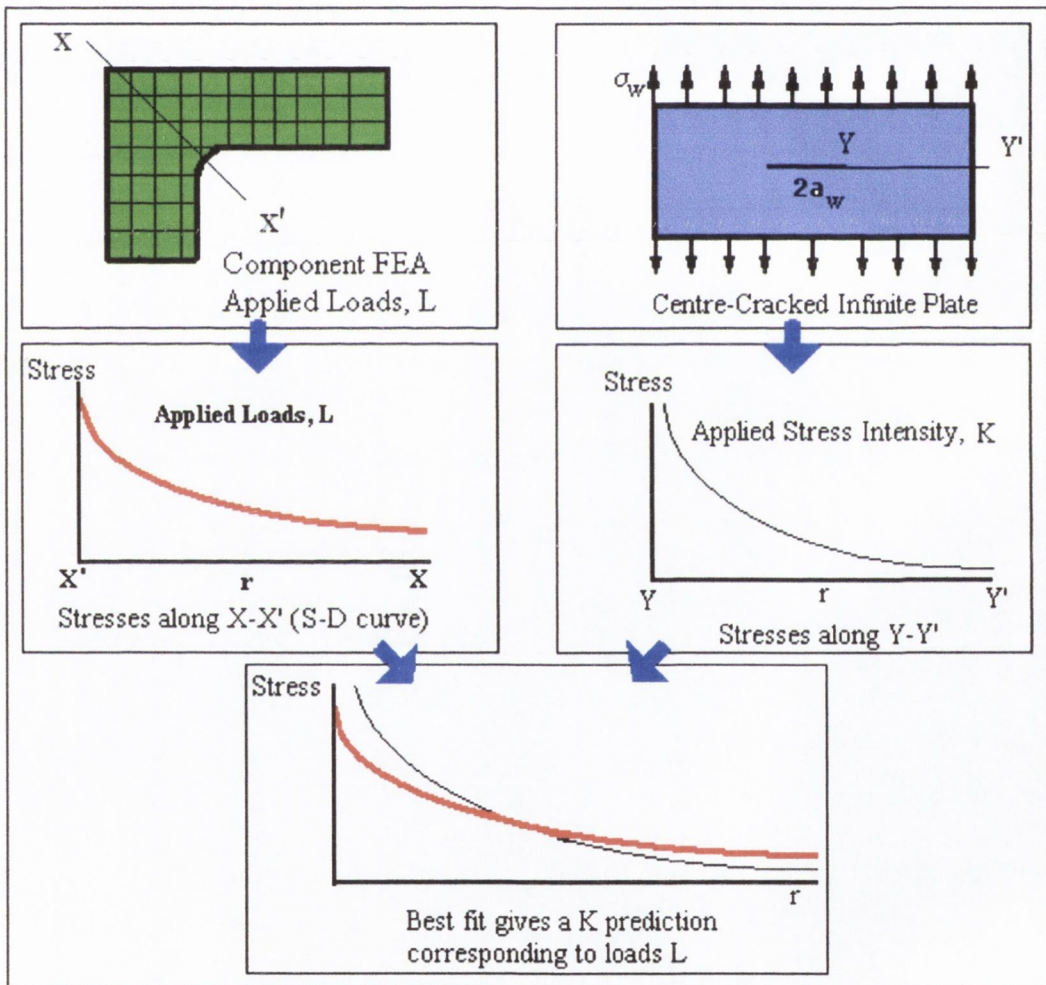


Fig. 2.5 - Schematic illustration of the methodology used in the crack modelling technique

More detailed descriptions of the crack modelling method, together with application of its use have been described elsewhere [Taylor, 1996], [Taylor and Carr, 1999], [Taylor et al., 1997; 1999; 2002], [Taylor and Wang, 2000], [Wang et al., 2000] and [Wang, 1999],



where it has been demonstrated that the CMM, when used in conjunction with the stress-life method, produces accurate predictions for a wide range of materials, notch geometries and actual components, including welded joints.

## **2.4 Strain based fatigue assessment methods**

### **2.4.1 The strain-life method**

In this approach, fatigue behaviour is described in terms of the local notch strain. This is considered important, as the deformation of material at a notch root is often inelastic involving plastic strains.

In order to apply the method it is necessary to have knowledge of the following:

- a) The local stress-strain behaviour of the material at the notch root. This can be obtained via an elastic-plastic finite element analysis or by using various approximations, for example the Neuber rule [Neuber, 1961] or Glinka rule [Molski and Glinka, 1981].
- b) The cyclic stress-strain curve for the material and the strain-life curve, determined from constant strain fatigue testing of smooth specimens.

The strain-life approach is most commonly applied to the low cycle fatigue regime, in which failure generally occurs in less than 10 000 cycles. In this case, the loads are higher and the degree of local, notch-tip plasticity becomes more significant. It can generally be applied to any three-dimensional geometry, especially if an elastic-plastic finite element analysis is used to determine the local strain. However, problems can result in the definition of nominal stress and strain when using the Neuber approximation (see below).

#### **2.4.1.1 Implementation of the strain-life approach using the Neuber Rule**

Neuber [1961] proposed that the geometric mean of the stress and strain concentration factors should remain equal to the elastic stress concentration factor during plastic deformation. That is:

$$K_t = \sqrt{K_\sigma K_\epsilon} \quad (2-17)$$

Where, for cyclic loading

$$K_{\sigma} = \frac{\Delta\sigma}{\Delta\sigma_{nom}} \quad \text{and} \quad K_{\varepsilon} = \frac{\Delta\varepsilon}{\Delta\sigma_{nom}} \quad (2-18)$$

Here,  $\Delta\sigma$  and  $\Delta\varepsilon$  are the local maximum stress and strain range at the notch root respectively. If yielding is constrained to occur locally at the stress concentration and the nominal stress remains elastic, then the nominal strain range will also remain elastic and is given by:

$$\Delta\varepsilon_{nom} = \frac{\Delta\sigma_{nom}}{E} \quad (2-19)$$

Where  $E$  is the Young's modulus of the material. Substitution of equations 2-19 and 2-18 into equation 2-17 results in:

$$\Delta\sigma\Delta\varepsilon = \frac{(K_t\Delta\sigma_{nom})^2}{E} \quad (2-20)$$

Hence, given the elastic stress concentration factor, the nominal applied stress range and the Young's modulus of the material, the relationship between the local stress range and the local strain range is uniquely determined. Also, Topper *et al.* [1969] have proposed the use of the fatigue notch factor  $K_f$  in place of the  $K_t$ , in equation 2-20, for cyclic loading when using Neuber's rule. This was suggested as it was observed to correlate better with experimental observations.

$$\Delta\sigma\Delta\varepsilon = \frac{(K_f\Delta\sigma_{nom})^2}{E} \quad (2-21)$$

Once the local stress-strain relationship at the notch tip is known, it can be used in conjunction with the measured cyclic stress-strain curve of the material to quantify the local strain range experienced at the notch tip. The cyclic stress-strain curve is typically represented by the Ramberg-Osgood relationship.

$$\frac{\Delta\varepsilon}{2} = \frac{\Delta\sigma}{2E} + \left(\frac{\Delta\sigma}{2K'}\right)^{1/n'} \quad (2-22)$$

So the equation for the stabilized hysteresis loop can then be obtained by doubling equation 2-22. Which results in:

$$\Delta\varepsilon = \frac{\Delta\sigma}{E} + 2\left(\frac{\Delta\sigma}{2K'}\right)^{1/n'} \quad (2-23)$$

Intersection of equation 2-23 with equation 2-21 results in:

$$\frac{(\Delta\sigma)^2}{E} + 2\Delta\sigma\left(\frac{\Delta\sigma}{2K'}\right)^{1/n'} = \frac{(K_f\Delta\sigma)^2}{E} \quad (2-24)$$

Figure 2.6 is an illustration of the way in which Neuber's rule is used to determine the actual notch tip stresses and strains for constant amplitude cyclic loading.

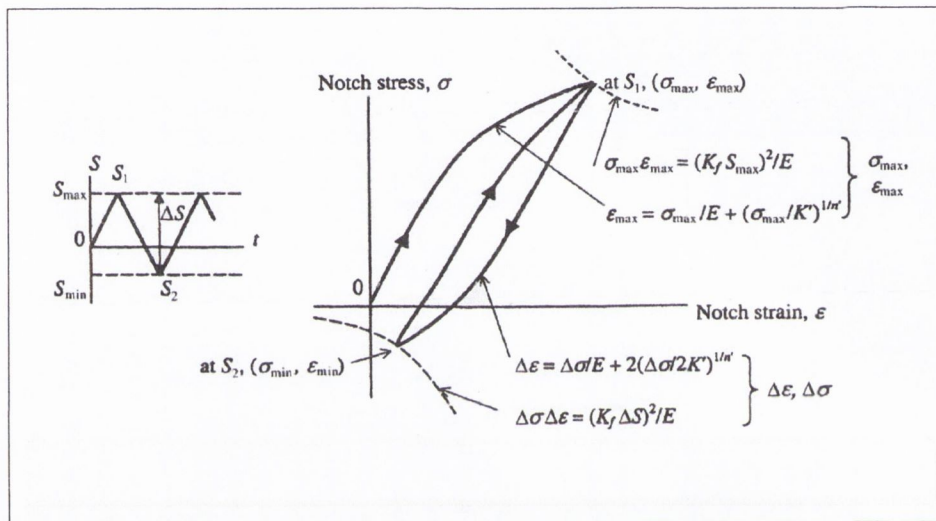


Fig. 2.6 - Illustration of how to determine notch strain using Neuber's rule

#### 2.4.1.2 Mean strain effects

Strain-controlled cycling with a mean strain usually results in a mean stress, which may relax fully or partially with continued cycling. This relaxation is due to the presence of plastic deformation, and therefore, the degree of relaxation depends on the magnitude of the plastic strain amplitude. Mean strain does not usually affect fatigue behaviour unless it results in a non-fully relaxed mean stress. Since there is more mean stress relaxation at higher strain amplitudes due to larger plastic strains, mean stress effect on fatigue life is smaller in the low-cycle fatigue region and larger in the high cycle fatigue region [Stephens *et al.*, 1999].

As discussed in Stephens *et al.* [2001], the parameter suggested by Smith, Watson and Topper can be used to deal with mean stress effects on strain-life fatigue behaviour. This is

most often referred to as the SWT parameter (or  $P_{SWT}$ ) and is described as per equations 2-25 and 2-26 below.

$$P_{SWT} = \sqrt{(\sigma_{amp} + \sigma_{mean}) \varepsilon_{amp} E} \quad (2-25)$$

$$P_{SWT}(N) = \sqrt{(\sigma_f')^2 (2N)^{2b} + E \sigma_f' \varepsilon_f' (2N)^{(b+c)}} \quad (2-26)$$

Equation 2-26 describes the variation of the  $P_{SWT}$  parameter as a function of the number of cycles. It is sometimes referred to as the damage parameter life curve and essentially describes the failure condition. It is obtained by substituting the equations describing the strain-life curve into equation 2-25. The criterion is therefore based on the assumption that quantity defined by equation 2-25 remains constant for a given life.

## 2.5 Concluding remarks

The theories discussed above are the commonly used and accepted methods for the fatigue assessment of notched and welded components. Within the body of this work, only the critical distance methods [Taylor, 1999] and the crack modelling method [Taylor, 1996] are used and discussed, as these theories form the backbone of this work. However, where possible, other methods have been implemented and compared in Appendix B.

## Chapter 3: The area and volume methods

---

This chapter is concerned with the area and volume, critical distance methods and their application to complex three-dimensional stress concentrations. Taylor [1999] showed that if the average stress is evaluated over a semi-circular area of radius  $a_0$  ahead of a crack tip, then the threshold for crack propagation is characterised by an average stress that is slightly larger than the plain specimen fatigue strength. Hence, he suggested using a critical distance or radius of  $a_0$ , for the area method, with the knowledge that the resulting prediction would be slightly conservative.

In the following a more accurate evaluation of the critical radius for the area method, using a semi-circular area ahead of a crack, is presented. The analysis is also extended to a three-dimensional problem, by considering a semi-spherical volume ahead of a crack.

In this work the area and volume methods have been implemented via macros within the ANSYS finite element program. These calculate the average stress via a numerical integration. The methodology and user instructions for these macros are presented in Appendix C.

### 3.1 *The area method*

#### 3.1.1 Which stress component to use

When calculating the critical distances for the point and line methods, the stress ahead of a crack on the zero degree line is considered (see Figure 3.1). Along this line the tangential stress,  $\Delta\sigma_\theta$ , the y-direction stress,  $\Delta\sigma_y$ , and the maximum principal stress,  $\Delta\sigma_1$ , are equivalent. In all other directions this is not true. Hence, when determining the critical radius for the area method, the first thing that must be decided is which of these stress components should be used.

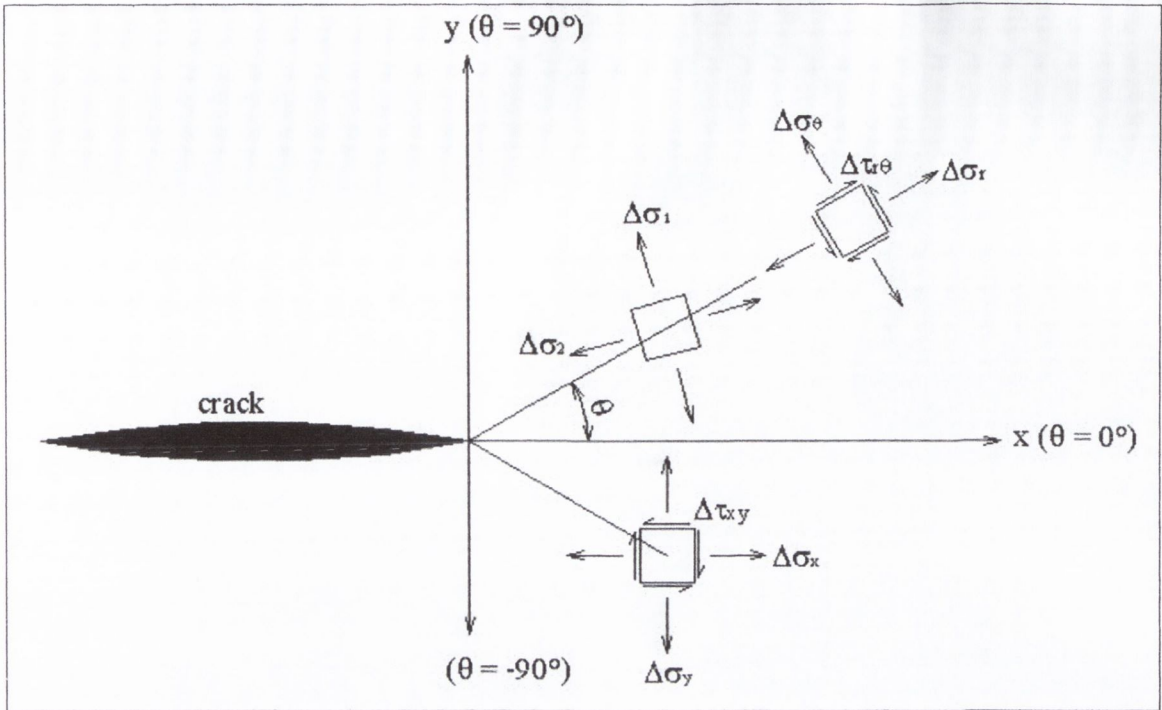


Fig. 3.1 - Stress components ahead of a fatigue crack

The logical approach is to use the stress component responsible for crack growth. However, for mode I loading, crack growth is along the zero degree line, and as all the stress components mentioned above are equivalent on this line, it is not possible to say which one is responsible for crack growth. Therefore, consider a mixed mode loading case, whereby the crack is also loaded by a remote shear stress. In this case it is typical for a propagating crack to change direction in order to follow the direction perpendicular to the maximum principal stress. For this reason it is believed that the maximum principal stress is the most important stress component for the fatigue assessment of notched components and is used in the following to determine the critical distances for the area and volume methods. This is in fact the difference between the result present here and that given by Taylor [1999]. In his derivation of the critical distance for the area method, he considered the stresses ahead of the crack in the y-direction only.

### 3.1.2 Determining the critical radius

As a starting point, consider the elastic stress field surrounding a two-dimensional long crack, which, for cyclic loading, is fully described by the equations below [Irwin, 1957]:

$$\begin{aligned}\Delta\sigma_{\theta}(r, \theta) &= \frac{\Delta K_I}{\sqrt{2\pi r}} \left( \frac{3}{4} \cos \frac{\theta}{2} + \frac{1}{4} \cos \frac{3\theta}{2} \right) \\ \Delta\sigma_r(r, \theta) &= \frac{\Delta K_I}{\sqrt{2\pi r}} \left( \frac{5}{4} \cos \frac{\theta}{2} - \frac{1}{4} \cos \frac{3\theta}{2} \right) \\ \Delta\tau_{r\theta}(r, \theta) &= \frac{\Delta K_I}{\sqrt{2\pi r}} \left( \frac{1}{4} \sin \frac{\theta}{2} + \frac{1}{4} \sin \frac{3\theta}{2} \right)\end{aligned}\quad (3-1)$$

From this, the first principal stress range can be found at any point in the stress field:

$$\Delta\sigma_1(r, \theta) = \frac{\Delta K_I}{\sqrt{2\pi r}} \left( \cos \frac{\theta}{2} + \sqrt{\left( \cos \frac{\theta}{2} \sin \frac{\theta}{2} \right)^2} \right) \quad (3-2)$$

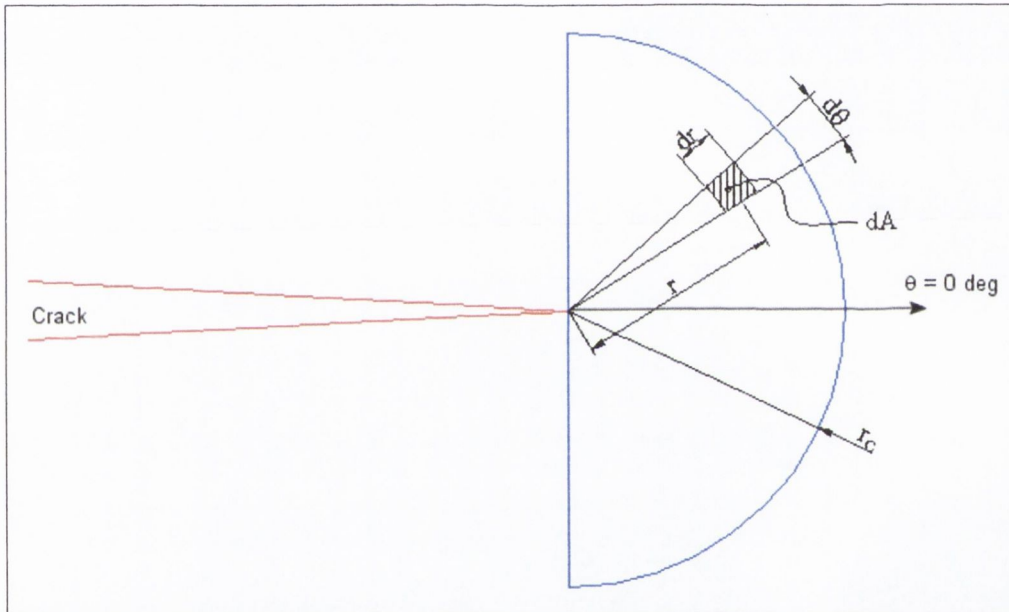


Fig. 3.2 - Calculation of the average first principal stress in a semi-circular area ahead of a crack

Consider a semi-circular area, of radius,  $r_c$ , ahead of the crack tip, as shown in Figure 3.2 above. The average first principal stress,  $\Delta\sigma_{ave}$ , can be found by integration as below.

$$\Delta\sigma_{ave} = \frac{1}{A_{1/2}} \int \Delta\sigma_1(r, \theta) dA_{1/2} = \frac{1}{A_{1/4}} \int_0^{\pi/2} \int_0^{r_c} \Delta\sigma_1(r, \theta) r dr d\theta \quad (3-3)$$

Where,

$$A_{1/4} = \frac{\pi r_c^2}{4} \quad (3-4)$$

The result is,

$$\Delta\sigma_{ave} = \frac{\Delta K_I}{\sqrt{2\pi r_c}} \frac{8}{3\pi} \left( \sqrt{2} + \frac{1}{2} \right) = 0.6482 \frac{\Delta K_I}{\sqrt{r_c}} \quad (3-5)$$

At the threshold condition, where no crack growth is observed,  $\Delta K_I = \Delta K_{th}$ , hence

$$\Delta\sigma_{ave} = 0.6482 \frac{\Delta K_{th}}{\sqrt{r_c}} \quad (3-6)$$

The critical radius for which the average principal stress is equal to the smooth specimen fatigue strength,  $\Delta\sigma_o$ , is given by:

$$r_c = 0.4202 \left( \frac{\Delta K_{th}}{\Delta\sigma_o} \right)^2 \quad (3-7)$$

As per the point and line methods, (see Chapter 2, section 2.2.2.2) the critical distance can be defined in terms of the El Haddad short crack parameter,  $a_o$  [El Haddad *et al.*, 1979].

$$a_o = \frac{1}{\pi} \left( \frac{\Delta K_{th}}{\Delta\sigma_o} \right)^2 \quad (3-8)$$

Hence the critical distance can then be written in terms of  $a_o$ .

$$r_c = 1.32a_o \quad (3-9)$$

### 3.1.3 Orientation of the critical area for a complex stress concentrations

When applying the area method to a complex geometry, the problem arises of how to orientate the critical area. This is demonstrated in Figure 3.3 below. In the work presented here this problem is addressed using the following criteria.

The bisector (or line of symmetry) of the critical area is assumed to coincide with the direction of the focus path, determined as per section 2.2.2.2. Hence the bisector of the critical area is assumed to be perpendicular to the direction of the maximum principal stress at the hot spot.



This implies that the bisector of the critical area is assumed to coincide with the direction of crack propagation.

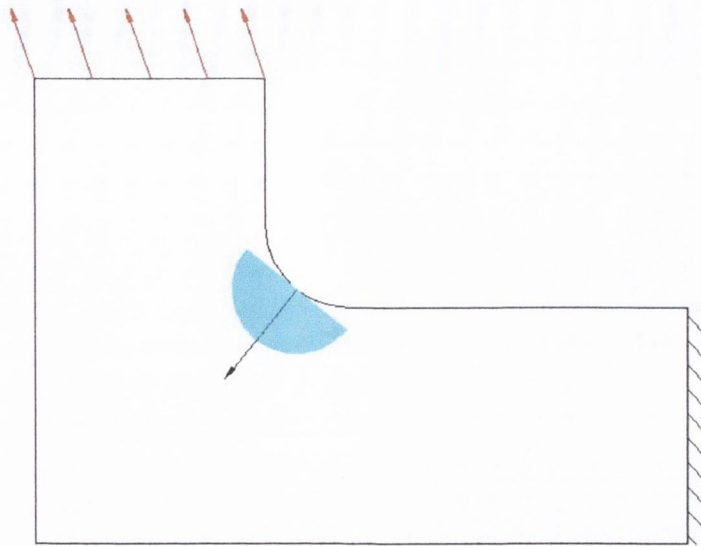


Fig. 3.3 - Application of the area method to a complex geometry

### 3.2 The volume method

#### 3.2.1 The critical radius

The forgoing analysis, for the area method, is two-dimensional and assumes zero stress gradient in the thickness direction, as shown in Figure 3.4(a) below. However, if a spherical critical volume is assumed instead of a cylindrical one (see Figure 3.4(b)) then the stress gradient in all directions can be accounted for.

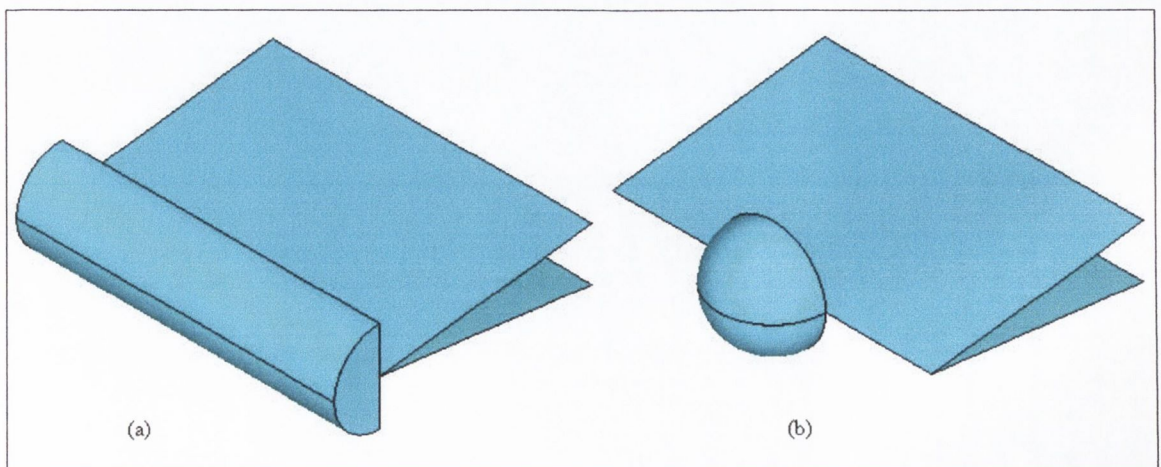


Fig. 3.4 - Possible choice of shapes for the volume method

This is done in a very similar manner as above, except a spherical coordinate system, shown in Figure 3.5 below, is used and the average stress is calculated via a triple integral. Note that in spherical coordinates, the first principal stress range becomes:

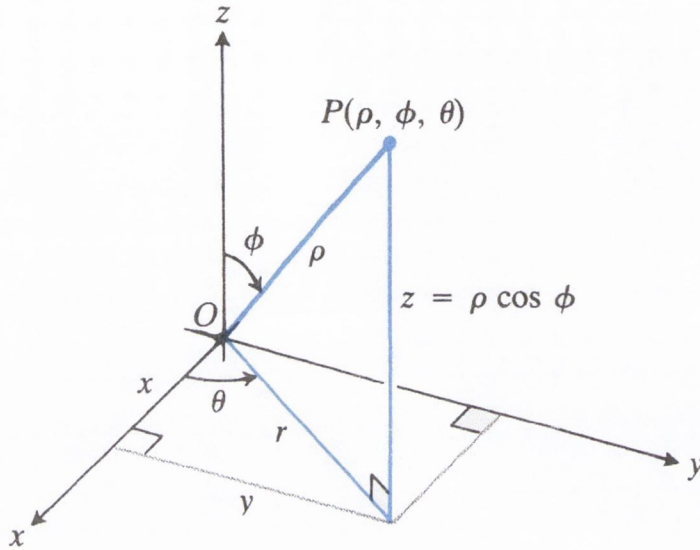


Fig. 3.5 - Definition of spherical coordinate system

$$\Delta\sigma_1(\rho, \phi, \theta) = \frac{\Delta K_I}{\sqrt{2\pi\rho \cos(\phi)}} \left( \cos \frac{\theta}{2} + \sqrt{\left( \cos \frac{\theta}{2} \sin \frac{\theta}{2} \right)^2} \right) \quad (3-10)$$

Hence the average stress is calculated by:

$$\Delta\sigma_{ave, sph} = \frac{1}{V_{1/2}} \int \Delta\sigma_1(\rho, \phi, \theta) dV_{1/2} = \frac{1}{V_{1/8}} \int_0^{\pi/2} \int_0^{\pi/2} \int_0^{\rho_c} \Delta\sigma_1(\rho, \phi, \theta) \rho^2 \sin \phi d\rho d\phi d\theta \quad (3-11)$$

Where,

$$V_{1/8} = \frac{1}{8} \left( \frac{4}{3} \pi \rho_c^3 \right) \quad (3-12)$$

This results in the following:

$$\Delta\sigma_{ave, sph} = 0.699 \frac{\Delta K_I}{\sqrt{\rho_c}} \quad (3-13)$$

Following the procedure outlined above, it can be shown that the critical radius,  $\rho_c$ , where the average stress range is equal to the plain specimen fatigue strength is:

$$\rho_c = 1.54a_o \quad (3-14)$$

### 3.2.2 Orientation of the critical volume for a complex stress concentrations

When applying the volume method to a complex geometry the criteria used to orientate the critical volume is very similar to the one used for the area method, discussed above. That is; the bisector (or line of symmetry) of the critical volume is assumed to coincide with the direction of the focus path, determined as per section 2.2.2.2.2. This implies that the bisector of the critical volume is assumed to coincide with the direction of crack propagation.

### 3.3 *Concluding remarks*

Because the area and volume methods are more spatial versions of the critical distance methods it was expected that they would be more suited to the evaluation of complex three-dimensional stress concentrations when compared to the simpler point and line methods. In particular it was expected that the volume method, as described above, would be useful for the fatigue prediction of localised stress concentrations were the failure occurs from a point or very small region, as it is able to take into account the stress distributions in all three directions. However, as demonstrated in the following chapters, these methods did provide a small increase in accuracy, but in general were a little bit of a disappointment and not really worth the added computational complexity.

## Chapter 4: Previous work done on welds

---

As mentioned in the introduction, the initial aim of this work was to continue the validation of the crack modelling method (CMM) and the critical distance methods (CDMs) for the fatigue assessment of welded joints. This chapter is a brief review of the previous work done on welded joints.

The way in which the CMM and the CDMs are applied to welds is effectively the same method that has been successfully applied to solid parts, using stress data obtained from FEA. In this approach, the stresses are calculated by modelling the weld bead and the parent material as a solid part, with the same values of Young's modulus and Poisson's ratio. The weld bead is generally idealised to have a triangular cross-section with no root-radius at the weld toe. The behaviour of the weld is taken into account, in the fatigue analysis, by using the appropriate material properties for welds. This is discussed in the section below.

### 4.1 *The fatigue properties of welded joints*

In order to determine the fatigue properties of welds, fatigue tests on butt-welded bending specimens (at R-ratio = 0.1), as shown in Figure 4.6, were undertaken [Barrett, 1998; Taylor *et al.*, 2002]. The smooth specimen fatigue strength,  $\Delta\sigma_o$ , was taken to be the fatigue strength of the ground butt-welded specimens: 153 MPa at  $5 \times 10^6$  cycles. The threshold stress intensity range,  $\Delta K_{th}$ , was estimated from the fatigue strength of the notched specimens, as it can be assumed that notches, which are sufficiently sharp, will behave as if they were cracks. Hence,  $\Delta K_{th}$ , was found to be  $6.8 \text{ MPa}\cdot\text{m}^{1/2}$ . The El Haddad short crack parameter,  $a_o$ , was subsequently calculated to be 0.43 mm. All specimens were heat treated in order to relax residual stresses introduced as a result of the welding process.

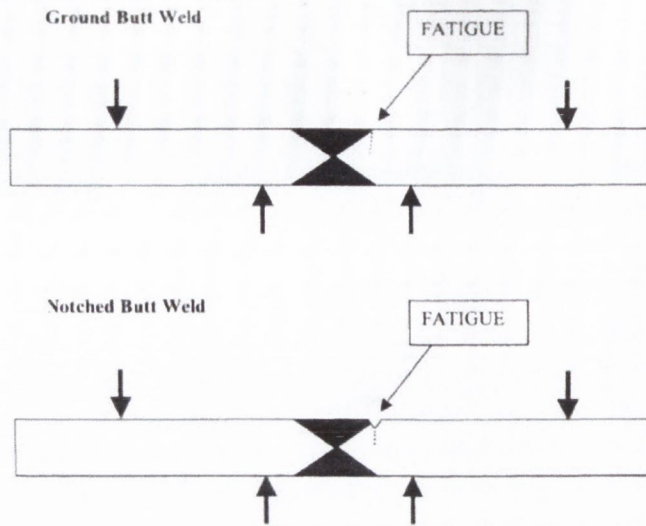


Fig. 4.6 - Determining the material properties for welded steels

#### 4.2 Two-dimensional welded geometries

Considerable work has been undertaken in order to assess the ability of the CMM and the CDMs to predict the fatigue behaviour of two-dimensional welded joints in steel [Barrett, 1998; Taylor et al., 2002; Crupi *et al.*, 2002]. Experimental investigations of the welded geometries shown in Figure 4.7 below, have been undertaken, the results of which are reported by Taylor *et al.* [2002], and are summarised in Table 4.1 below.

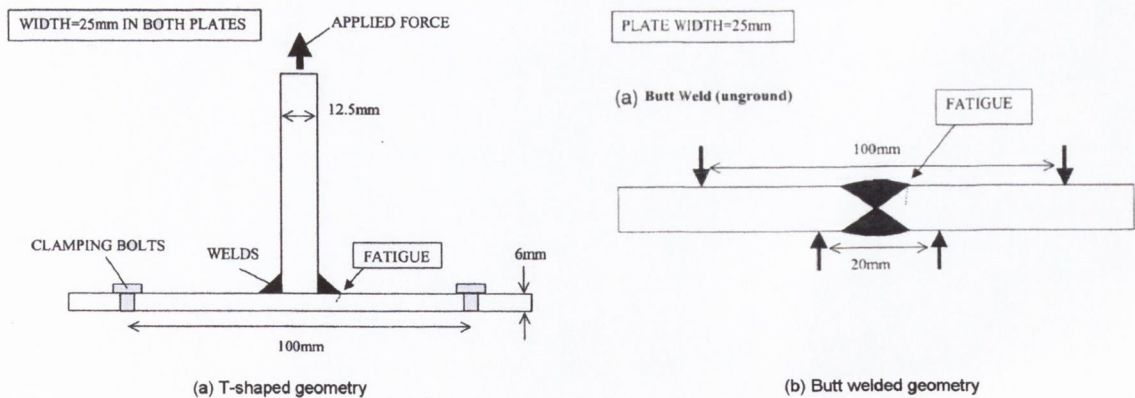


Fig. 4.7 - Two-dimensional welded geometries

Table 4.1 - Results of the investigation of 2D welded geometries

Weld Geometry	Experimental Fatigue limit	Crack modelling method (CMM)	Point Method (PM)	Line Method (LM)	Area Method (AM)
T-shape	2.5 kN	2.53 kN	2.24 kN	2.46 kN	2.09 kN
Butt	140 MPa	102 MPa	131 MPa	138 MPa	129 MPa

In addition, Taylor *et al.* [2002] also examined the effect of finite element mesh density on the prediction errors obtained for the T-shaped specimens shown in Figure 4.7(a). The results of that analysis are summarised in Figure 4.8 which shows the predictions for the fatigue strength using the CMM, PM, LM and AM, as a function of mesh element size. Also shown are the experimental value and the limits of  $\pm 20\%$  error, which is considered to be acceptable for these predictions. It can be seen that the methods give reasonable predictions even for very large element sizes. This is particularly true for the CMM.

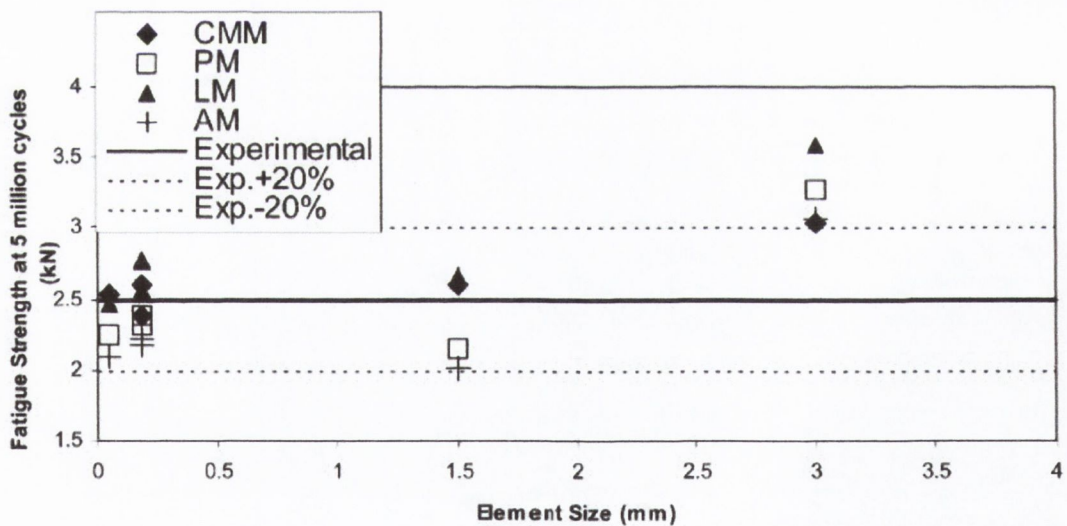


Fig. 4.8 - Results from the CMM and the CDMs for the T-shaped welds as a function of mesh element size

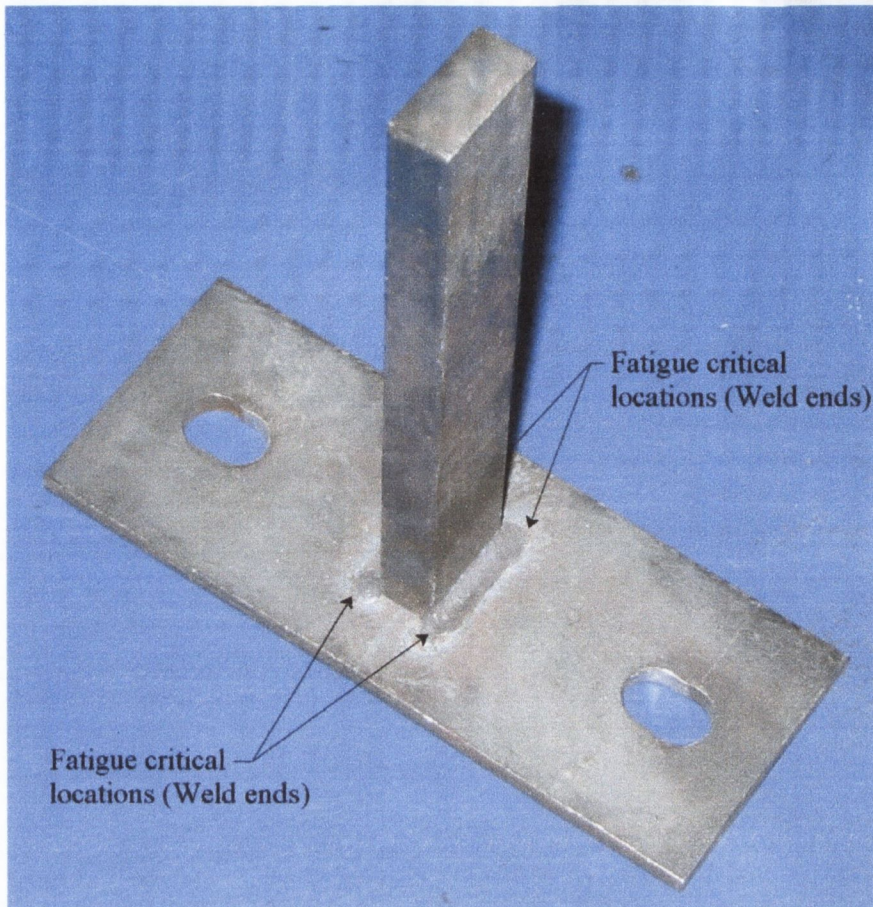
Taylor *et al.* [2002] also showed that these methods could be used to accurately predict data from the literature for non-load-carrying cruciform fillet welds and that the effect of plate thickness, whereby the strength is seen to decrease as the size increases, is similarly accounted for. They also demonstrated that the effect of weld reinforcement angle could be successfully predicted using data from the literature for unground butt welds.

Crupi *et al.* [2002], have recently undertaken a review of fatigue assessment methods for two-dimensional welded geometries in which the CMM and the CDMs were included. They showed that these methods resulted in good predictions when data from the literature for different geometries, dimensions and materials were considered. In particular, they examined cruciform joints in steel; butt welds in AlMg 4.5 Mn aluminium alloy designated AA5083; and T-shaped non-load carrying fillet welded joints made of aluminium alloy AA5083.

Hence, from the above, it can be concluded that the CMM and the CDMs can be used with confidence for the fatigue assessment of two-dimensional welded joints assuming that the correct material parameters are employed.

### **4.3 A Three-dimensional welded geometry (*T-shape-B*)**

After the success obtained for two-dimensional welded joints, it was decided that a more complex three-dimensional case should be investigated. This work was carried out by Lucano [1999]. The geometry that was chosen is shown in Figure 4.9 below and is designated *T-shape-B*. The specimen is similar to the two-dimensional T-shaped geometry discussed above but the width of the base-plate was increased so that the fillet welds were not continuous across the specimen. Fatigue cracks were therefore forced to initiate at the weld end (see Figure 4.9). The base-plate was constrained via two bolts located 100mm apart. A cyclic load was applied at the end of the vertical member in the vertical direction.



*Fig. 4.9 - First three-dimensional welded geometry assessed*

Figure 4.10 shows the S/N data obtained for the T-shape-B welded specimen. A regression line has been drawn through the data using a least-squares fit with the standard equation:

$$N_f = A/(\Delta\sigma)^n \quad (4-15)$$



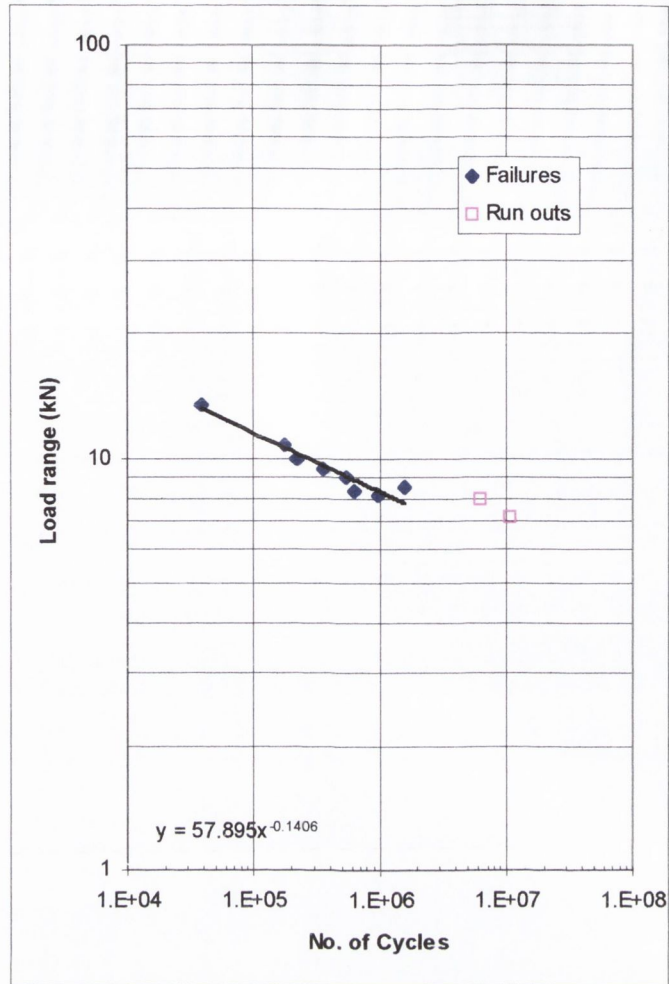


Fig. 4.10 - Experimental results for T-shape-B welded joint, plotted in terms of the applied load range

Using this data the fatigue strength is really only well defined up to a  $2 \times 10^6$  cycles, however the curve is extrapolated to  $5 \times 10^6$  cycles so that the fatigue strength corresponds to this number of cycles at which the material properties are calculated. The fatigue strength of this specimen is therefore calculated to be 6.62 kN at  $5 \times 10^6$  cycles.

Three-dimensional finite element models were made in order to estimate the stress distribution in the specimen. Various geometrical configurations for the weld bead and weld end were investigated and shown to have only a small effect. Table 4.2 is a very brief summary of the results obtained. The error factor is defined as:

$$\text{Error factor} = \frac{\text{actual fatigue strength}}{\text{predicted strength}} \quad (4-16)$$

Hence, an error factor of greater than one indicates a conservative prediction, less than one is non-conservative and an error factor of one indicates a perfect prediction. This is the definition adopted in the remainder of this work.

Table 4.2 - Summary of results from the fatigue assessment of T-shape-B

	<b>Three-dimensional T-shape specimen</b>
<b>Experimental fatigue strength</b>	6.62 kN at $5 \times 10^6$ cycles
<b>Point method</b> <i>(Error factor)</i>	3.75 kN <i>(1.77)</i>
<b>Line method</b> <i>(Error factor)</i>	3.34 kN <i>(1.98)</i>
<b>CMM</b> <i>(Error factor)</i>	4.12 kN <i>(1.61)</i>

#### 4.4 Concluding remarks

From the above it was concluded that the CMM and the CDMs are very useful tools for the fatigue assessment of two-dimensional welded joints. However, a conservative error was encountered when trying to apply these theories to a more three-dimensional geometry. This was the extent of the work done concerning welds, previous to the commencement of this project. The following chapter describes work undertaken in this project, which is essentially a continuation of the above.

## Chapter 5: Defining the problem

---

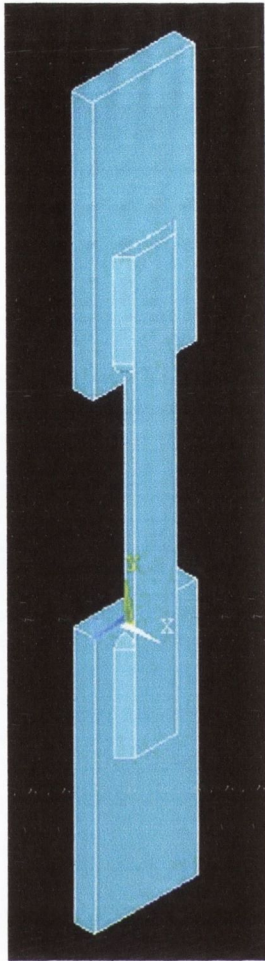
As already stated, the initial aim of this project was to continue the work described in Chapter 4 concerning welded joints. To very briefly summarise, at this point it had been demonstrated that the CMM and the CDMs were very successful at predicting the fatigue behaviour of two-dimensional notched geometries, in both solid components and welded joints. However, problems had been encountered when trying to predict a three-dimensional welded joint where the failure was constrained to occur at the end of a weld bead (T-shape-B).

The starting point was to test another three-dimensional welded geometry and see how successful the methods were for that case. Again large conservative errors were observed. This same conservatism was obtained when trying to predict test data taken from the literature for three-dimensional welded geometries, specifically non-load-carrying *stiffener type* and *flange type* welds. Given this, and knowing that the CMM and the CDMs are very successful at predicting the behaviour of two-dimensional welded geometries, several three-dimensional stress concentrations, machined from solid steel, were designed and tested in order to test the hypothesis that the conservative error was due to the three-dimensional geometry, not the welding.

In the work discussed below, only the results of the experimental work and fatigue analyses are included. A more complete description is presented in Appendix A. In the following it is desirable to focus on the results and the consequences of these in terms of the direction of research, without being bogged down in the details.

### 5.1 Another 3-D welded geometry (*Fillet-A*)

The welded geometry chosen for investigation is shown below in Figure 5.1. It was selected because, like the three-dimensional T-shape specimen discussed above, it was expected that failure would occur at the end of one of the four fillet welds. This specimen is an asymmetric, load-carrying, longitudinal fillet welded attachment and is referred to as *Fillet-A*. This investigation was carried out in collaboration with Stefano Marco [2000].



(a) FEA model



(b) Photo

Fig. 5.1 - Three-dimensional welded specimen (Fillet-A)

The specimens were loaded in tension, by fixing the ends and applying a cyclic load at an R-ratio of 0.1 using a servo-hydraulic testing machine. The stress-life curve obtained is displayed in Figure 5.2. The fatigue strength was determined to be a load range of 8.4 kN at  $5 \times 10^6$  cycles to failure.

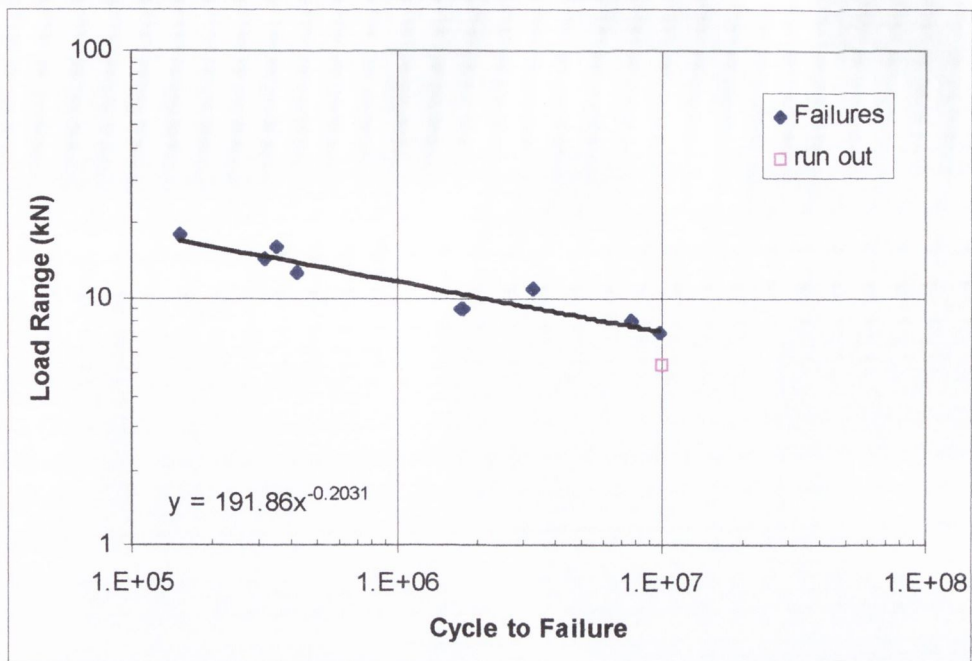


Fig. 5.2 - S-N curve obtained for the Fillet-A specimen

Table 5.1 is a very brief summary of the results from the fatigue analysis of the Fillet-A specimens. It can be seen that large conservative errors, with error factor greater than 2, are observed.

Table 5.1 - Summary of results from the fatigue assessment of Fillet-A

	<b>Fillet-A</b>
<b>Experimental fatigue strength</b>	8.4 kN at $5 \times 10^6$ cycles
<b>Point method</b> (Error factor)	3.78 kN (2.22)
<b>Line method</b> (Error factor)	3.33 kN (2.52)
<b>Area method</b> (Error factor)	3.72 kN (2.26)
<b>Volume method</b> (Error factor)	3.54 kN (2.37)
<b>CMM</b> (Error factor)	4.24 kN (1.98)

Note: Error factor is defined as the ratio of the Experimental fatigue strength to the predicted fatigue strength

## 5.2 Weld Data taken from the literature

In the following the CMM and the CDMs have been tested against data taken from the literature [ESDU, 1976] for longitudinal fillet welded attachments and joints in steels under axial loading. Three specimen geometries have been considered:

- A non-load-carrying, stiffener type, joint - Figure 5.3
- A non-load-carrying, flange type, joint - Figure 5.4
- A non-load-carrying, single sided, stiffener type, joint - Figure 5.5

Three-dimensional finite element models were built in order to obtain the stress distributions. The results of the fatigue analysis are reported in Table 5.2 below. From this it can be seen that the methods produce very conservative predictions of the fatigue strength.

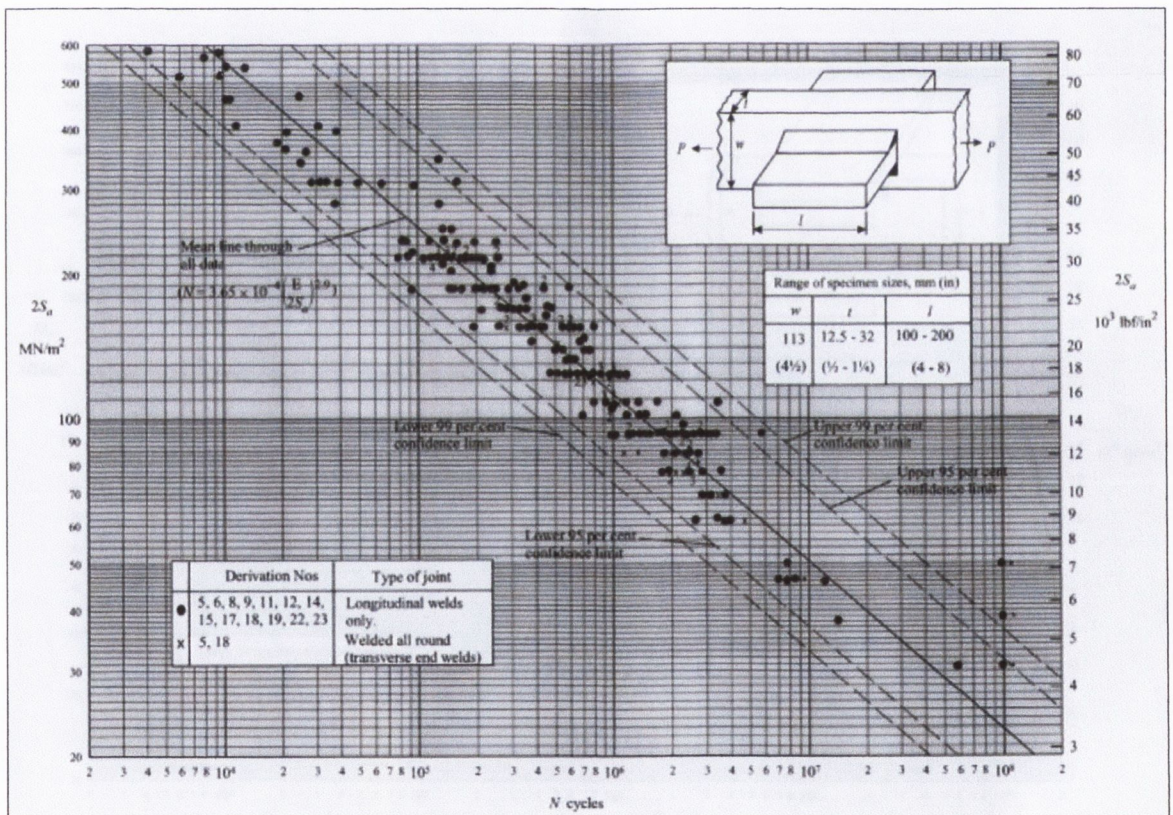


Fig. 5.3 - Non-load-carrying welded joint (Stiffener type)

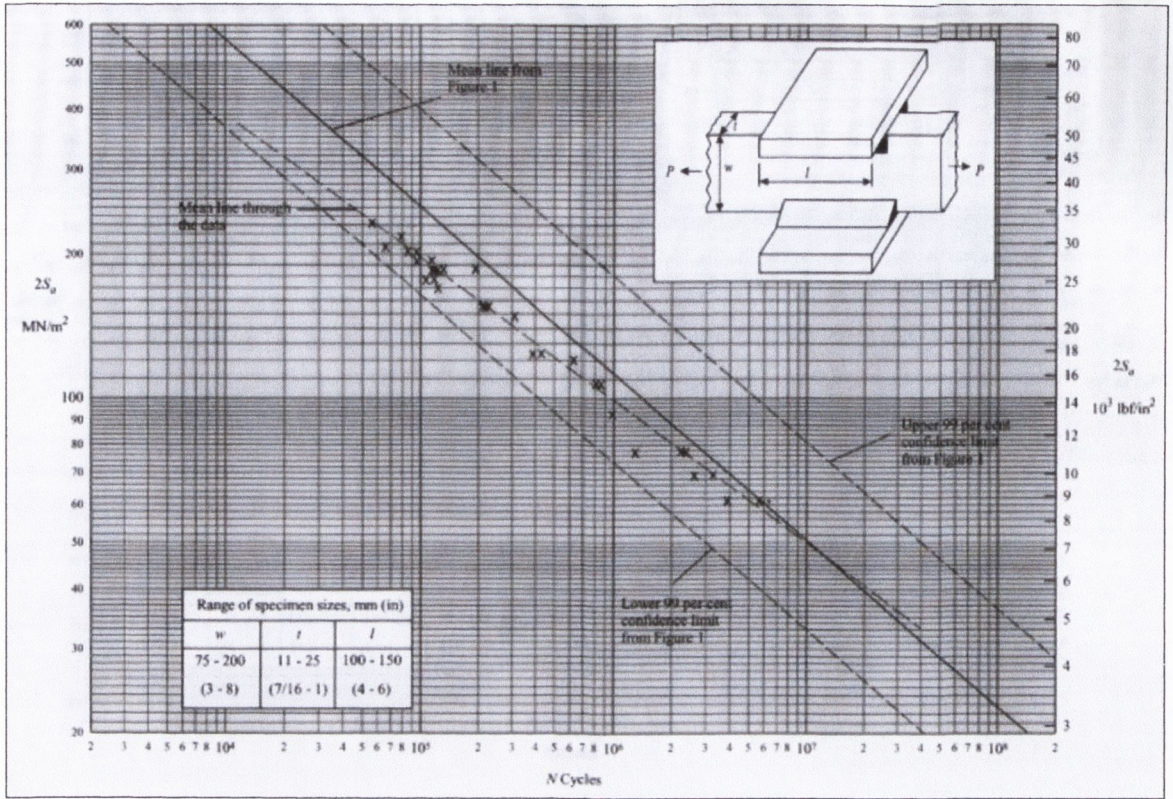


Fig. 5.4 - Non-load-carrying welded joint (Flange type)

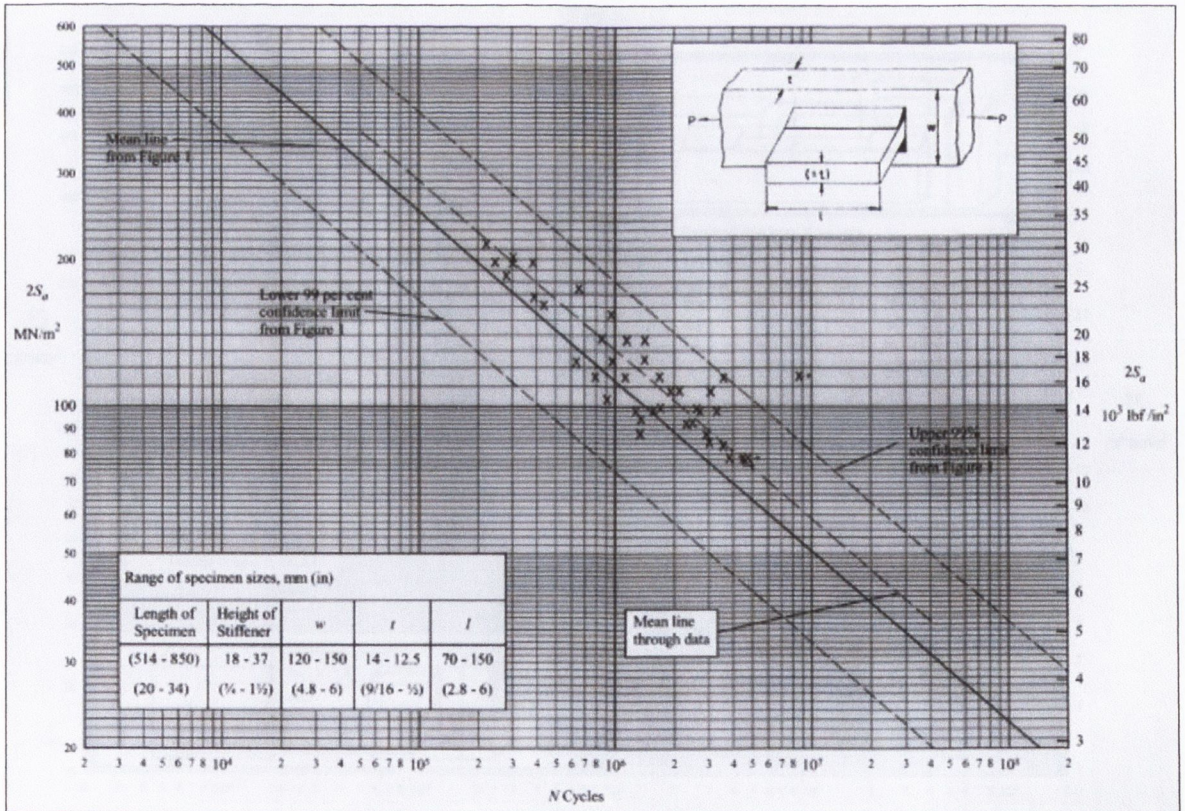


Fig. 5.5 - Non-load-carrying welded joint (Stiffener on one side only)

Table 5.2 - Summary of results for the non-load-carrying welded joints

	Stiffener Type	Flange Type	Stiffener type single
<b>Experimental fatigue strength</b>	64 MPa at $5 \times 10^6$ cycles	62 MPa at $5 \times 10^6$ cycles	72 MPa at $5 \times 10^6$ cycles
<b>Point method</b> (Error factor)	23.1 MPa (2.77)	17.7 MPa (3.62)	54.1 MPa (1.33)
<b>Line method</b> (Error factor)	23.75 MPa (2.69)	15.6 MPa (4.10)	45.8 MPa (1.57)
<b>Area method</b> (Error factor)	24 MPa (2.67)	17.2 MPa (3.72)	45.7 MPa (1.58)
<b>Volume method</b> (Error factor)	31.26 MPa (2.05)	18.16 MPa (3.52)	52.9 MPa (1.36)
<b>CMM</b> (Error factor)	26.34 MPa (2.43)	22.1 MPa (2.89)	53.9 MPa (1.34)

Note: Error factor is defined as the ratio of the *Experimental fatigue strength* to the *predicted fatigue strength*

### 5.3 Three-dimensional stress concentrations in solid components

Based on the above and knowing that the CMM and the CDMs are very successful at predicting the behaviour of two-dimensional welded geometries, it was proposed that the conservative error is due to the three-dimensional geometry, not the welding. In order to test this hypothesis several three-dimensional stress concentrations, machined from solid steel, were designed and tested. These are discussed below

#### 5.3.1 Material properties

The material chosen from which to machine the specimens was a standard, low carbon, structural steel, designated BS 970: 1996: 080A15 (or BS 970: 1955: En2B). A considerable amount of work was done in order to characterise this material. This is discussed in detail in Appendix A. However here, it is sufficient to say that the plain specimen fatigue strength (in bending) was found to be 435 MPa at  $2 \times 10^6$  cycles and the material stress intensity threshold,  $\Delta K_{th}$ , was determined to be  $11 \text{ MPa}\cdot\text{m}^{1/2}$ . Hence the El Haddad parameter,  $a_0$ , was found to be 0.205 mm.



### 5.3.2 The Model-E specimen

The first solid steel specimen investigated is shown in Figure 5.6 below. This specimen has been designated Model-E and the work involving it was done in collaboration with Ezio Mazzeo [2000]. The specimen was loaded in three-point bending at an R-ratio of 0.1.

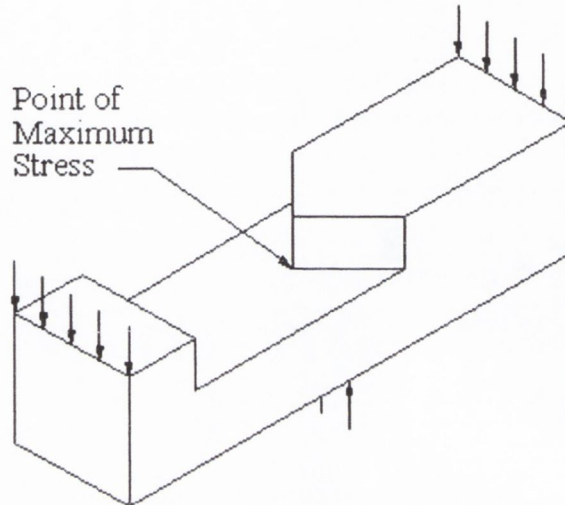


Fig. 5.6 - Schematic of the Model-E specimen

This specimen was chosen for investigation because it shares the following characteristics with the three-dimensional welded specimens:

- The resulting fatigue crack is a non-through crack. In fact, in this case a complex, non-planar fatigue cracks emanated from the stress concentration labelled "*point of maximum stress*" in Figure 5.6.
- There is a significant stress gradient in all directions emanating from the point of maximum stress.
- Thirdly, the failure is constrained to occur from a very small region.

The fatigue strength was determined to be an applied load range of 6.6 kN at  $2 \times 10^6$  cycles. The stress-life curve that was obtained is shown in Figure 5.7 below.

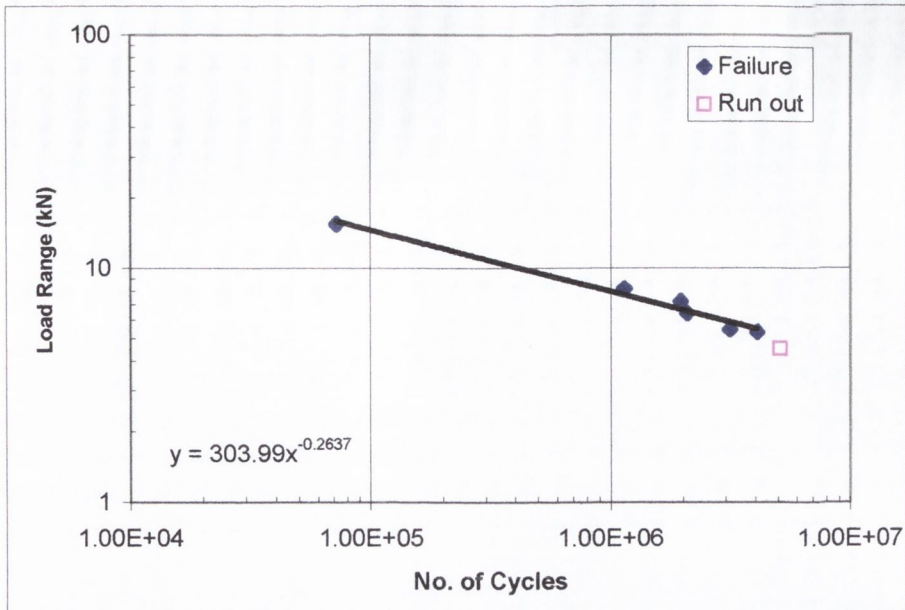


Fig. 5.7 - S-N curve obtained for the Model-E specimen

Two finite element models were built to investigate this geometry. One contained a root radius at the failure location, which was equal to the average measured value of 0.2mm (Model-E2). The other had no root radius (Model-E1). Hence, in this case, a singularity in the elastic stress field existed at the failure location.

Table 5.3 - Summary of results for the Model-E

	Model-E1 ( $\rho=0\text{mm}$ )	Model-E2 ( $\rho = 0.2\text{mm}$ )
<b>Experimental</b>	6.6 kN at $2 \times 10^6$ cycles	
<b>Point method</b> (Error factor)	2.99 kN (2.21)	2.52 kN (2.62)
<b>Line method</b> (Error factor)	3.06 kN (2.16)	3.04 kN (2.17)
<b>Area method</b> (Error factor)	3.35 kN (1.97)	3.14 kN (2.10)
<b>Volume method</b> (Error factor)	3.70 kN (1.78)	4.21 kN (1.57)
<b>CMM</b> (Error factor)	4.56kN (1.47)	3.78 kN (1.75)
<b>Stress-life method</b> (Error factor)		1.25 kN (5.28)

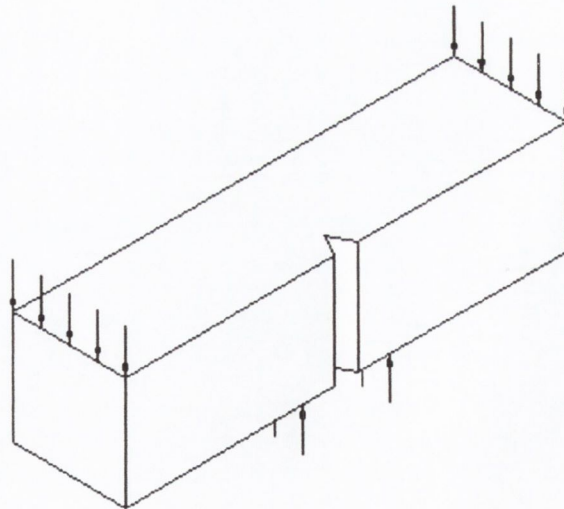
A summary of the results of the fatigue analysis of the Model-E specimen is shown in Table 5.3 above. It can be seen that in all cases significant conservative errors are obtained. Also, as discussed in Appendix A, section A.3.5, the methods for which the lowest

prediction errors are obtained (ie. the volume method (Model-E2) and the CMM (Model-E2)) are believed to be erroneous. Hence, it was concluded that the fatigue assessment methods are not adequate for the assessment of stress concentrations like Model-E.

### 5.3.3 The Model-T specimen

The second solid steel specimen investigated is shown in Figure 5.8 below. This is a sharply notched bar loaded in bending, but the notch is orientated vertically relative to the direction of the applied load so that the fatigue crack is forced to initiate at the top of the specimen, at the notch root. The work on this specimen, which is designated Model-T, was done in collaboration with Thomas Pircher [2001].

This specimen was chosen for investigation because, like the Model-E specimen, the fatigue crack must start from a very specific point or at least a small region, but, in this case, there isn't a high stress gradient in all directions, as the bending gradient is very shallow when compared to the gradient caused by the notch. Also, as discussed in Appendix A, section A.4.3.1, a considerable effort was made to measure the evolution of the crack shape as it grew.



*Fig. 5.8 - Schematic of the Model-T specimen*

The results of the experimental investigation, in the form of the measured stress-life curve, are shown in Figure 5.9 below. The fatigue strength was determined to be a load range of 11.4kN at  $2 \times 10^6$  cycles. Table 5.4 is a summary of the fatigue analysis of this specimen. It

was also shown that fatigue cracks developed at the stress concentration are highly elliptical (i.e.  $a/c \approx 0.2$ ) with the major axis orientated along the notch.

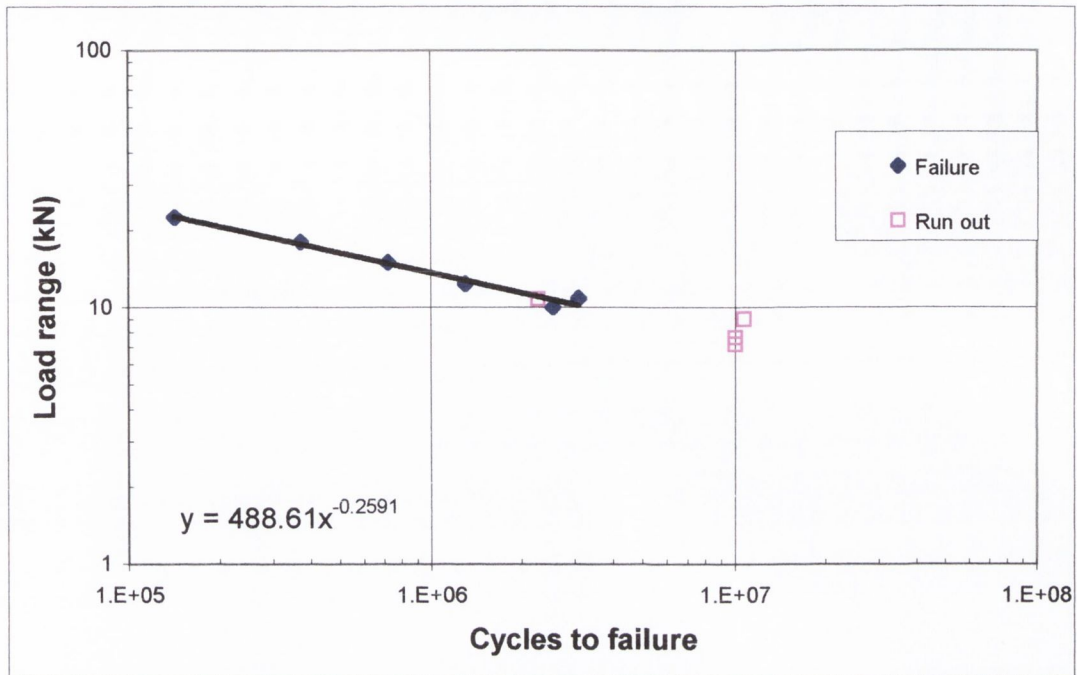


Fig. 5.9 - S/N curve obtained for the Model-T specimen

Table 5.4 - Summary of results for the Model-T

	<b>Model-T</b>
<b>Experimental</b>	11.4 kN at $2 \times 10^6$ cycles
<b>Point method</b> (Error factor)	11.48 kN (0.99)
<b>Line method</b> (Error factor)	13.56 kN (0.84)
<b>Area method</b> (Error factor)	12.72 kN (0.90)
<b>Volume method</b> (Error factor)	13.9 kN (0.82)
<b>CMM</b> (Error factor)	13.64 kN (0.85)
<b>Stress-life method</b> (Error factor)	5.72 kN (1.99)

The prediction for the Model-T specimen are in general quite good, and if anything, slightly non-conservative. Indeed the point method is almost perfect. The line, area and volume methods result in slightly higher predictions with error factors between 0.8 and 0.9. These are still considered acceptable.

## **5.4 Concluding remarks**

From the results outlined above it was concluded that:

- a) The problem, which results in the conservative errors, is not only limited to welded joints, as it was also observed in the Model-E specimen.
- b) Given that good predictions were obtained for the Model-T specimen it was concluded that the problem is limited to geometries in which the failure is constrained to occur from a very localised stress concentration in which there exists large stress gradients in all directions emanating from the hotspot.

Based on this information, three possible reasons as to why the fatigue analysis methods are inadequate were proposed and are discussed separately in the following chapters.

## Chapter 6: The shape effect

---

Methods of high cycle fatigue analysis are generally developed using simple two-dimensional geometries as a base. This is certainly the case for the CMM and the CDMs. Consequently application of these methods to more complex three-dimensional geometries requires additional considerations.

For two-dimensional geometries, whether plane strain or plane stress, a fatigue crack is assumed to extend through the thickness of the specimen. This assumption is not always valid for three-dimensional geometries where the growth of semi-elliptical fatigue cracks, initiated at stress concentrations is extremely common. In the following it is argued that crack shape can affect the life of a component even at its fatigue limit, through the growth of non-propagating cracks. How this is accounted for depends on the analysis method and how it is applied to three-dimensional geometries. The CMM and the CDMs (specifically the point method and the line method) are used below to demonstrate the ideas.

### 6.1 *Non-propagating cracks*

Before continuing, a brief review of the literature concerning the nature and prediction methods of non-propagating cracks will be undertaken. Fenner *et al.* [1951] were the first to observe the phenomena. Earlier work to determine the fatigue strength of notched components was based only on unbroken or completely broken specimens. Fenner and co-workers found that cracks could form at the root of a notch at a stress level that was insufficient to cause the cracks to propagate to complete fracture. This was confirmed by Frost and Dugdale [1957], who showed that a crack formed at the notch root when the nominal stress was very nearly equal to the smooth specimen fatigue limit divided by the appropriate value of  $K_t$  (i.e. the stress predicted by the stress-life method), but the crack did not continue growing until a certain limiting stress level was applied. This behaviour is shown in Figure 6.1 below. Frost [1959] later proposed that this limiting stress (for mild steel at an R-ratio of -1) is governed by the parameter  $\sigma^3 l$ , where  $\sigma$  is the nominal stress and  $l$  is the crack length.

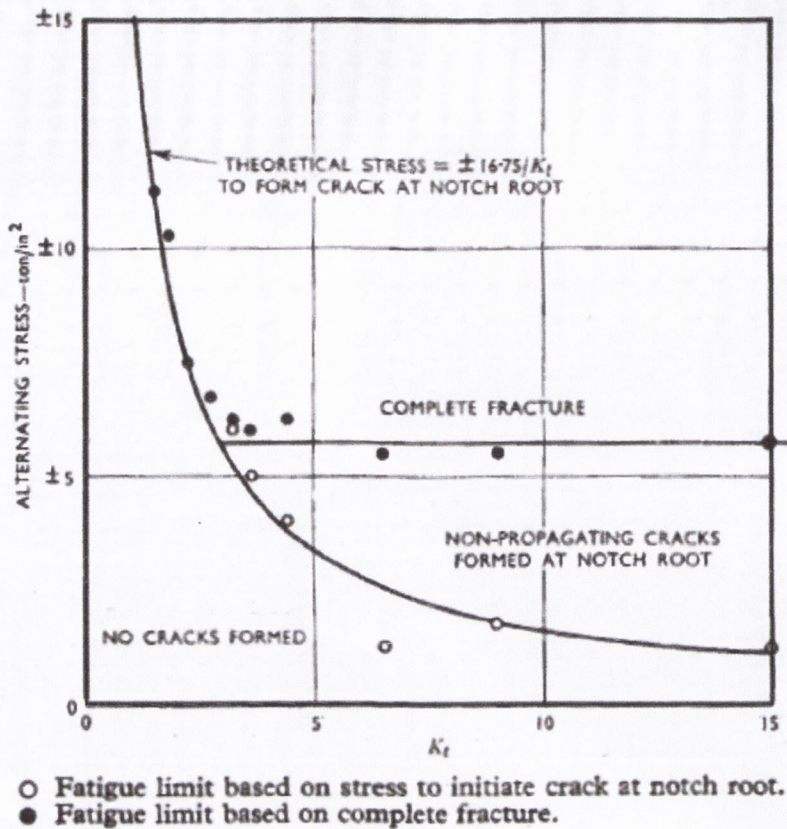


Fig. 6.1 - The Frost diagram

Smith and Miller [1977] subsequently demonstrated that linear elastic fracture mechanics could be used to describe the horizontal line in Figure 6.1 (this is discussed in Chapter 2, section 2.3.1). Hence, Figure 6.1, as modified by Smith and Miller can be used as a mechanism map to describe the conditions under which non-propagating cracks will develop and govern the fatigue behaviour of sharp notches.

An alternative approach to predict the behaviour of non-propagating cracks is the *resistance curve method*, which is based on LEFM modifications, to predict short crack behaviour. Fundamental to the resistance curve approach is the idea that the stress intensity threshold is a function of crack length, which approaches a constant as the crack becomes large, but decreases from the long crack value when the crack is short. This behaviour is observed experimentally and was first modelled by El Haddad *et al* [1979]. They described the threshold as per Equation 6-1, where  $\Delta K_{th}$  is the stress intensity threshold measured for a long crack,  $a$  is the crack length and  $a_0$  is the El Haddad short crack parameter discussed in chapter 2.

$$\Delta K_{th,a} = \sqrt{\frac{a}{a+a_0}} \Delta K_{th} \quad (6-1)$$

The use of the resistance curve is demonstrated in Figure 6.2 below. The curved line describes the variation in the threshold given by equation 6-1. The two almost straight, parallel lines describe the increase in stress intensity of a small crack, growing from a notch, as the crack gets longer. The two lines represent different applied stress levels. The uppermost line, labelled  $\Delta K_2$ , never intersects the resistance curve. Hence, at this stress level the crack will continue to propagate until failure occurs. The lower line, labelled  $\Delta K_1$ , just touches the resistance curve at one point. At this crack length and applied stress level the crack will become non-propagating. Hence, this condition represents the fatigue limit of the component. A lower applied stress level will result in a non-propagating crack of a smaller length.

The El Haddad resistance curve approach has been confirmed to agree well with the experimental data for various metals [El Haddad *et al.*, 1979; Tanaka *et al.*, 1981] and is used below, as it fits nicely with the CDMs.

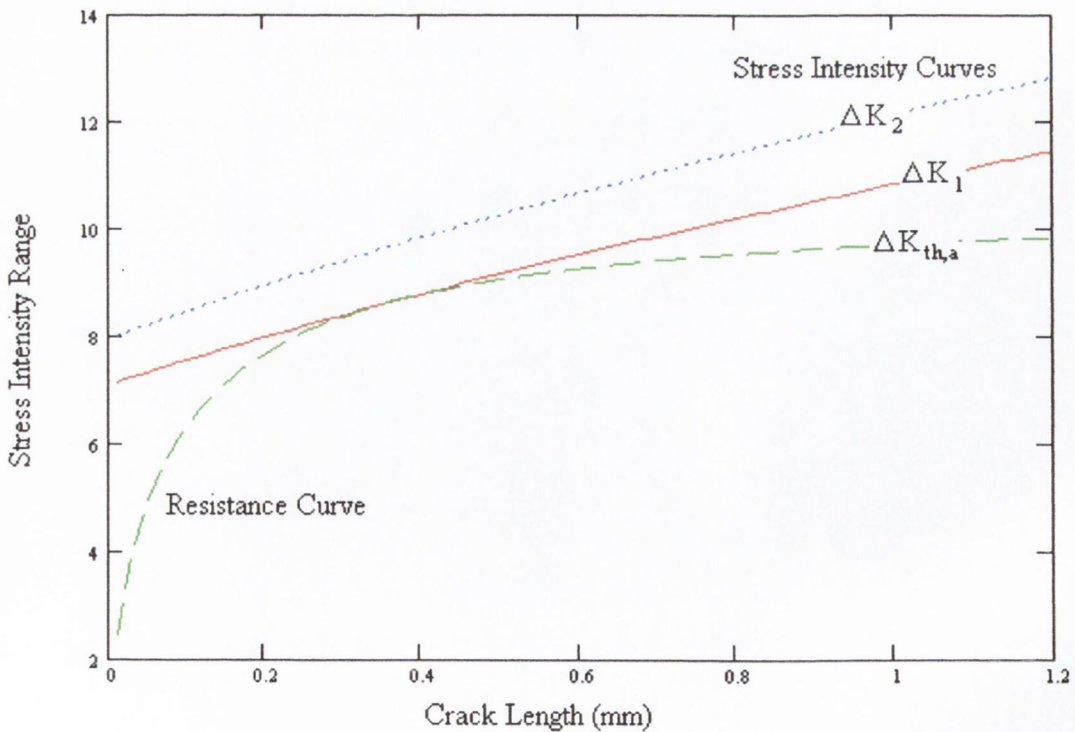


Fig. 6.2 - The El Haddad resistance curve



Tanaka *et al.* have also proposed a slightly different resistance curve approach, which is based on crack closure arguments [Tanaka *et al.*, 1981; Tanaka and Nakai, 1983; 1984; Akiniwa *et al.*, 1997].

## 6.2 The effect of crack shape

As already stated, the idea being investigated in this chapter is how the shape of a crack can affect the fatigue strength of a three-dimensional component where cracks are forced to have a semi-elliptical shape. It is believed that this occurs because the fatigue limit of these components is governed by the growth of non-propagating cracks. Therefore, in the following the effect of crack shape on the growth rate of both long cracks and non-propagating cracks are investigated.

### 6.2.1 The effect of crack shape on long crack growth

From a fracture mechanics point of view, the crack propagation rate of a long crack, above the threshold can be expressed by the Paris equation.

$$\frac{da}{dN} = A(\Delta K)^m \quad (6-2)$$

Where, A and m are experimentally determined material constants. By rearranging and integrating, the number of cycles,  $\Delta N$ , required for a crack to propagate from an initial length,  $a_i$ , to some final length  $a_f$ , can be determined as:

$$\Delta N = \int_{a_i}^{a_f} \frac{1}{A(\Delta K)^m} da \quad (6-3)$$

Using the standard LFM equation for the stress intensity and assuming that the shape factor or configuration factor, F, is independent of crack length, we obtain equation 6-4. The assumption that the configuration factor is independent of crack length is not, strictly speaking, valid. However, as long as the shape factor doesn't change significantly between the limits of crack growth it is a reasonable approximation and adequate for the purpose of qualitatively determining the effect of crack shape on propagation life.

$$\Delta N = \frac{1}{AF^m (\Delta\sigma)^m \pi^{m/2}} \int_{a_i}^{a_f} a^{-m/2} da$$

For m not equal to 2

$$\Delta N = \frac{1}{AF^m (\Delta\sigma)^m \pi^{m/2}} \frac{a_i^{(1-m/2)} - a_f^{(1-m/2)}}{(m/2) - 1} \quad (6-4)$$

Therefore the number of cycles required for a crack to propagate an arbitrary length (at a constant stress range,  $\Delta\sigma$ ) is inversely proportional to the shape factor, F, raised to the power of the growth rate exponent, m:

$$\Delta N \propto \frac{1}{F^m} \quad (6-5)$$

### 6.2.2 The effect of crack shape on non-propagating cracks

In the following the resistance curve, due to El Haddad (see section 6.1), is used in conjunction with equation 6-6 below to qualitatively determine the effect of crack shape on the crack growth rate of non-propagating cracks. Equation 6-6 is a modification of the Paris growth rate equation to account for near threshold behaviour. It can be seen that as the stress intensity approaches the threshold value the crack growth rate approaches zero. This is a common approach to estimating near threshold crack growth rate, however in equation 6-6 the threshold stress intensity range is not the long crack constant, but the relationship developed by El Haddad (equation 6-1) to describe short crack growth and consequently non-propagating cracks.

$$\frac{da}{dN} = A(\Delta K - \Delta K_{th,a})^m \quad (6-6)$$

The material constants A and m, in equation 6-6, must be experimentally determined and the stress intensity range,  $\Delta K$ , of a small crack at the root of a sharp notch can be estimated as per equation 6-7 (assuming again that the shape factor of the crack, F, doesn't change significantly as a function of crack length)

$$\Delta K = F\Delta\sigma\sqrt{\pi(a+D)} \quad (6-7)$$

Figure 6.3 shows the resulting crack growth curve for the case of a small crack growing at  $R=0.1$  at a notch with a depth of 0.75mm and root radius of 0.04mm using a material with a plain specimen fatigue limit of 446MPa, and a long crack stress intensity threshold range of 10.52 MPa.m<sup>1/2</sup> (therefore  $a_0 = 0.017$ mm). The results for a long crack are also shown, in this case the constant, long crack, threshold stress intensity is used in equation 6-6.

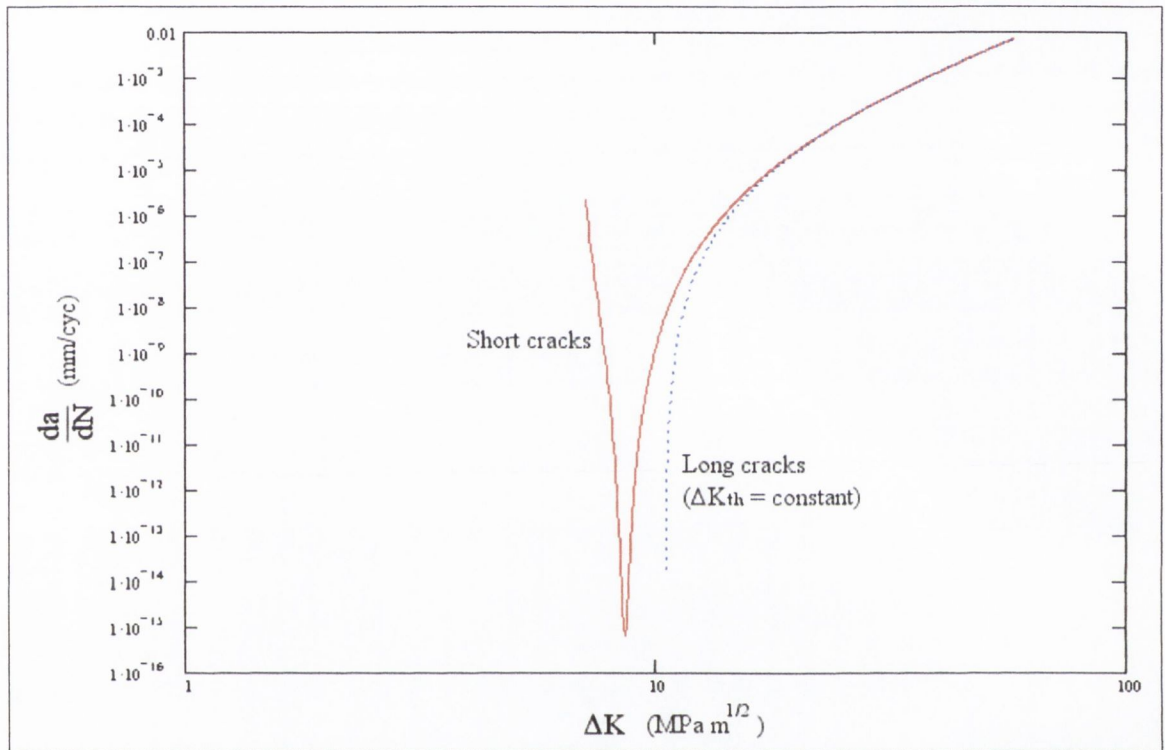


Fig. 6.3 - Crack growth curves, with and without the El Haddad short crack correction

The stress level, for both of the curves above, corresponds to the line labelled  $\Delta K_1$  in the Figure 6.2. It is in fact the stress level at which the maximum non-propagating crack length is formed and is therefore the fatigue limit of the component. The curve for the short crack shows a sharp valley, where the crack growth rate approaches zero. This corresponds to the point (in Figure 6.2) where the stress intensity of the crack is equal to the threshold stress intensity given by the resistance curve or the stress intensity of the maximum non-propagating crack length.

The effect of changing the shape factor (or the shape of the non-propagating crack) in equation 6-7 above is shown in Figure 6.4. It can be seen that increasing the shape factor results in an increased crack growth rate.

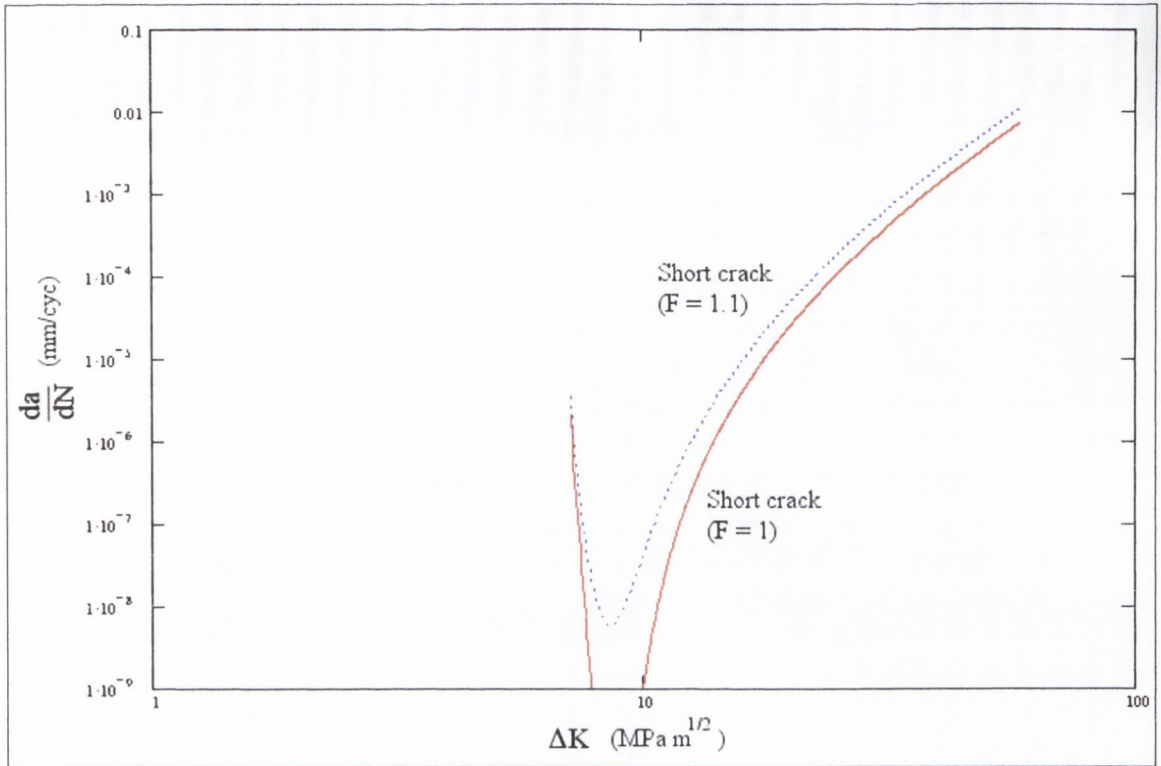


Fig. 6.4 - The effect of crack shape on the growth rate of non-propagating cracks

The relationship between life, applied stress level, and crack shape can be determined by integration of equation 6-6 between a very small crack length (eg. the average grain size) and the maximum non-propagating crack length, determined from the resistance curve. This is shown schematically in Figure 6.5 below for the same situation as described above. It can be seen that as the shape factor increases the permissible applied stress level decreases proportionally (for the same life).

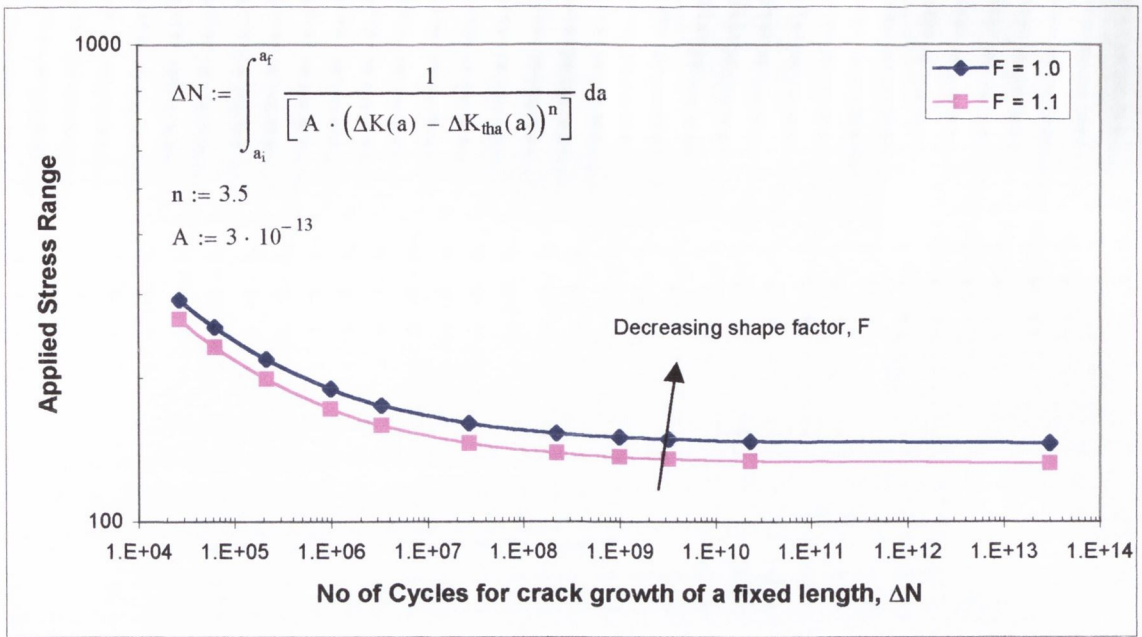


Fig. 6.5 - The effect of crack shape on the predicted stress-life relationship

### 6.3 Assessment of 3D stress concentrations using a 2D “focus path”

Application of the point method and the line method involves evaluating the stress at a point, or the average stress on a line ahead of the stress concentration. Hence, the simplest way of adapting these methods to a three-dimensional geometry is by the use of a two-dimensional *focus path*. The focus path is essentially a line extending from the hotspot in a direction chosen by some criteria on which the stresses can be evaluated (this is discussed in Chapter 2, section 2.2.2.2.2). The analysis is then performed in the same way as per the two-dimensional case.

In 2D, the focus path is a straight line that is thought of as being coincident with the plane of crack growth. Within this plane the crack length is assumed to be constant, or a through thickness crack. Hence, for a three-dimensional stress concentration the use of a focus path is equivalent to making an inherent assumption about the shape of a crack initiated from that stress concentration. This is illustrated schematically in Figure 6.6. Figure 6.6(a) shows the actual stress concentration and loading configuration, Figure 6.6(b) shows the real crack shape, and Figures 6.6(c) and (d) show the crack shape that would be assumed for the choice of two different focus paths (i.e. a straight crack front normal to the focus path).

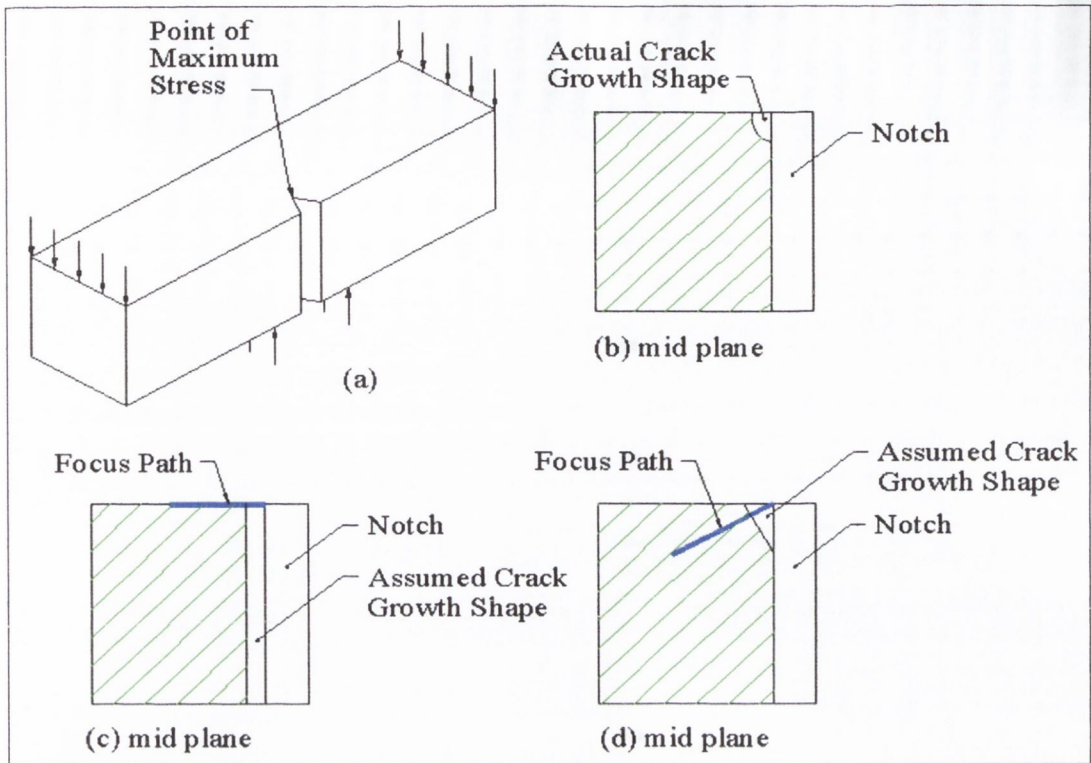


Fig. 6.6 - The problem created by choosing a 2D focus path

#### 6.4 Quantifying the correction factor

The foregoing analysis demonstrates that:

- a) The fatigue limit of sharp, "crack-like" stress concentrations is governed by the growth of non-propagating cracks.
- b) The shape of a non-propagating crack affects its growth rate and consequently its stress-life relationship. As the shape factor increases the permissible applied stress level decreases proportionally (for the same life).
- c) The use of a 2D focus path for a 3D stress concentration results in an inherent assumption about the shape of a crack initiated from a stress concentration.

Consequently, fatigue predictions made using the focus path concept should be multiplied by the correction factor given in equation 6-8, where  $F_{\text{assumed}}$  is the shape factor for the crack assumed by the choice of a focus path and  $F_{\text{actual}}$  is the shape factor of the actual crack.

$$f_{\text{shape correction}} = \frac{F_{\text{assumed}}}{F_{\text{actual}}} = \frac{\Delta K_{\text{assumed}}}{\Delta K_{\text{actual}}} \quad (6-8)$$

This correction factor can be determined by building two finite element models of the component being considered, one including a crack with the assumed shape and the other with a crack of the actual shape. For both cases, the stress intensity range can then be found at the point where the focus path crosses the crack front. It should be noted that, as the correction factor is the ratio of these two stress intensity factors, the modelling of the stress singularity at the crack tip doesn't have to be especially accurate. As long as the FE mesh used in both models is equivalent, any error is cancelled out.

#### 6.4.1 In terms of the elliptical integral, $\Phi$

Given that the error, discussed above, is the result of a difference in crack shape within exactly the same geometry (and loading condition), it can be seen that the correction factor, as defined by equation 6-8, is independent of geometry and load. That is, the correction factor will be exactly the same if the two crack shapes are considered in any geometry. Based on this, a more general expression for the correction factor is determined below using the stress intensity factor for an embedded elliptical crack in an infinite body subjected to uniform tension perpendicular to the crack plane (see Figure 6.7 below).

For this configuration the stress intensity is given by:

$$K = \frac{\sigma\sqrt{\pi a}}{\Phi} \left[ \sin^2 \beta + \left(\frac{a}{c}\right)^2 \cos^2 \beta \right]^{1/4} \quad (6-9)$$

Where  $\Phi$  is the complete elliptical integral of the second kind, and depends on the crack aspect ratio  $a/c$ .

$$\Phi = \int_0^{\pi/2} \left[ 1 - \left(1 - \frac{a^2}{c^2}\right) \sin^2 \phi \right]^{1/2} d\phi \quad (6-10)$$

Values for  $\Phi$  are tabulated in Table 6.1 below. It can be seen that  $\Phi$  varies from 1.0 to 1.571 for  $a/c$  ranging from 0.0, for a very elongated ellipse to 1.0 for a circle.

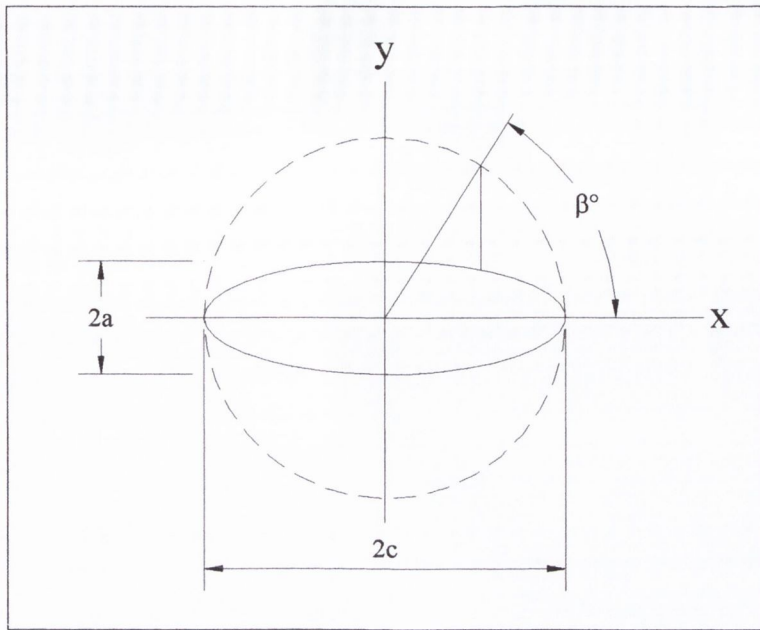


Fig. 6.7 - Elliptical crack parameters

Table 6.1 - Values of the complete elliptical integral of the second kind

$a/c$	0	0.1	0.2	0.3	0.4	0.5	0.6	0.7	0.8	0.9	1.0
$\Phi$	1.0	1.016	1.051	1.097	1.151	1.211	1.277	1.345	1.418	1.493	1.571

Figure 6.8 below shows four possible crack shapes, for which the stress intensity can be determined, at the location labelled point A. If the y-axis coincides with the direction of the focus path, then the case where the width of the elliptical crack goes to infinity is equivalent to a through crack, which in turn is the shape of the crack assumed by the choice of focus path. Hence, if the actual crack shape corresponds to any of the other three shape categories, the correction factor is given in Table 6.2.



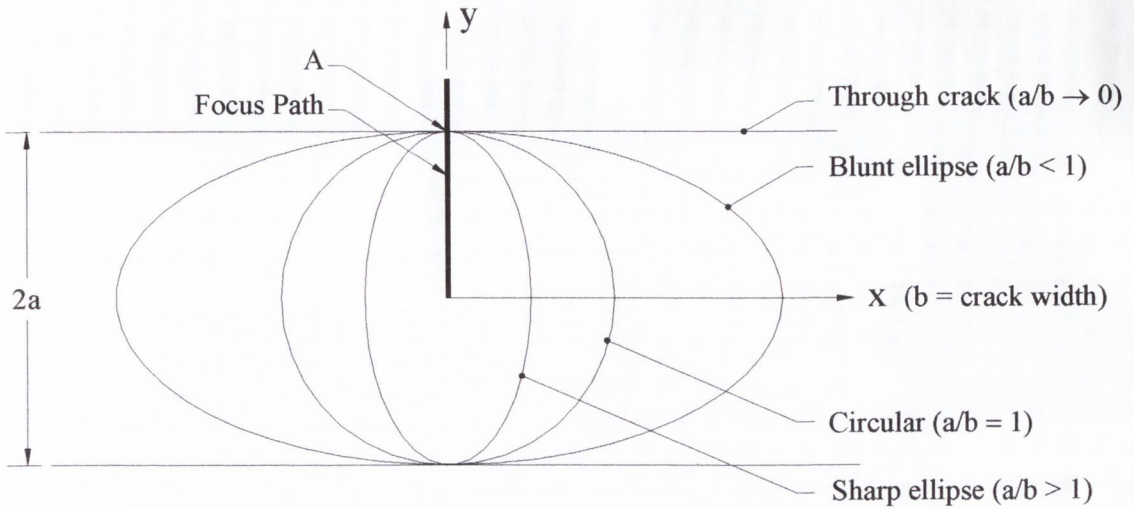


Fig. 6.8 - Possible elliptical crack shape

Table 6.2 - The correction factor for different crack shapes

Through crack	$a/b = 0$	$K = \sigma\sqrt{\pi a}$	
Blunt ellipse	$a/b < 1$	$K = \frac{\sigma\sqrt{\pi a}}{\Phi}$	$f_{shape\ correction} = \Phi_{actual}$
Circular crack	$a/b = 1$	$K = \frac{\sigma\sqrt{\pi a}}{\Phi}$	$f_{shape\ correction} = \Phi_{actual}$
Sharp ellipse	$a/b > 1$	$K = \frac{\sigma\sqrt{\pi a}}{\Phi} \frac{b}{a}$	$f_{shape\ correction} = \frac{a}{b} \Phi_{actual}$

It should be noted that  $\Phi_{actual}$  is the value of the elliptical integral (from Table 6.1) for a crack aspect ratio that is always between 0.0 and 1.0. This is why the correction for the sharp ellipse is different from the other two cases.

It can therefore be seen that the only thing that is needed to determine the correction factor is knowledge or an estimate of the actual crack shape.

#### 6.4.2 Verification of the correction factor defined in terms of $\Phi$

In order to verify if the complete elliptical integral of the second kind,  $\Phi$ , can be used to define the correction factor, two finite element models of the Model-E component were built. One model contained a small, non-planar but circular crack with a shape approximately equal to that seen on the failure surface. The second model contained a through-thickness crack, as would be assumed by the analysis method. These are shown in Figures 6.9 and 6.10 respectively.

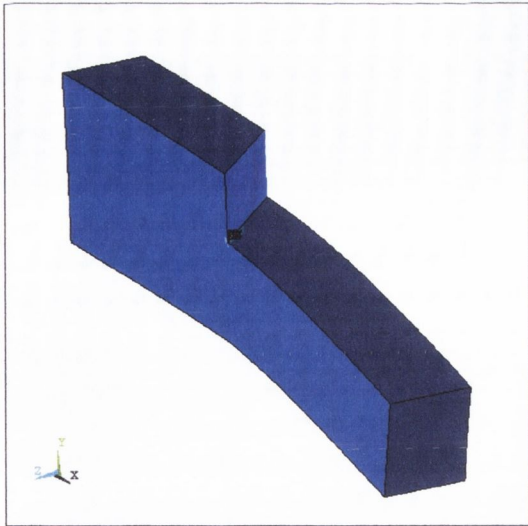
The characteristic crack size used in both models was  $2a_0$ . This has been shown, by Taylor [2002], to be approximately equal to the maximum length of a non-propagating crack, initiated at the root of a sharp, crack-like notch. The stress intensity factor of both cracks was determined at the point on the crack front coincident with the focus path. This was done using a crack face displacement method, which is a standard feature of the ANSYS finite element program.

For this geometry and choice of focus path the correction factor was determined to be:

$$f_{shape\ correction} = \frac{\Delta K_{assumed}}{\Delta K_{actual}} = \frac{F_{assumed}}{F_{actual}} = 1.58 \quad (6-11)$$

With reference to Tables 6.1 and 6.2 above, it can be seen that this is equivalent to the correction factor that would be obtained using the elliptical integral, for a circular crack. That is:

$$f_{shape\ correction} = \Phi_{actual} = 1.571 \quad for \quad \frac{a}{c} = 1 \quad (6-12)$$

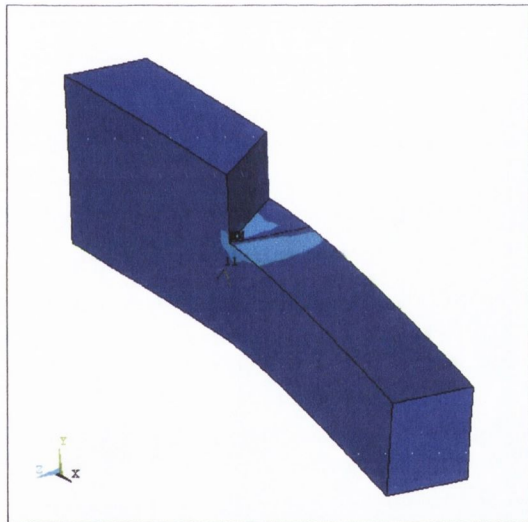


(a) Half model with mid plane symmetry

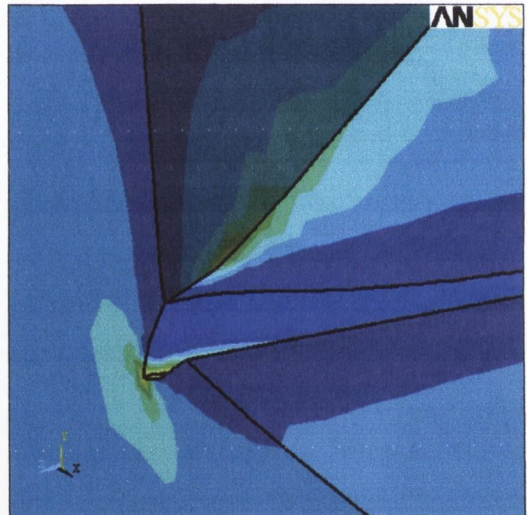


(b) Zoomed view of the crack

Fig. 6.9 - Finite element model including a crack with the correct shape.



(a) Half model – mid plane symmetry



(b) Zoomed view of the crack

Fig. 6.10 - Finite element model including a through-thickness crack.

## 6.5 Estimating the actual crack shape

The correction factor as defined above is all well and good if the *actual* shape of the crack is known. This is generally only the case if a failed component is accessible for examination, and often not even then. Techniques have been developed to predict the shape evolution of fatigue cracks. The approach of Lin and Smith [1997; 1999] is typical. They use a linear elastic three-dimensional finite element analysis to estimate the stress intensity factor along the crack front, and then employ an experimental Paris-type fatigue

crack growth relationship to calculate local crack advances at a few points along the crack front. They subsequently re-create the finite element model for the new crack front and repeat the process. It can be seen that such a method is extremely expensive, in terms of computing resources and time. The method also requires an initial crack shape as an input.

It was therefore decided to try to develop a simple approach to estimate the crack shape, and hence the correction factor describe above, using only the information already available from the stress and fatigue analyses. Unfortunately, the results were not very good, never the less, the approach is illustrated below, via an example, using the Model-T specimen, which is shown in Figure 6.11(a) below.

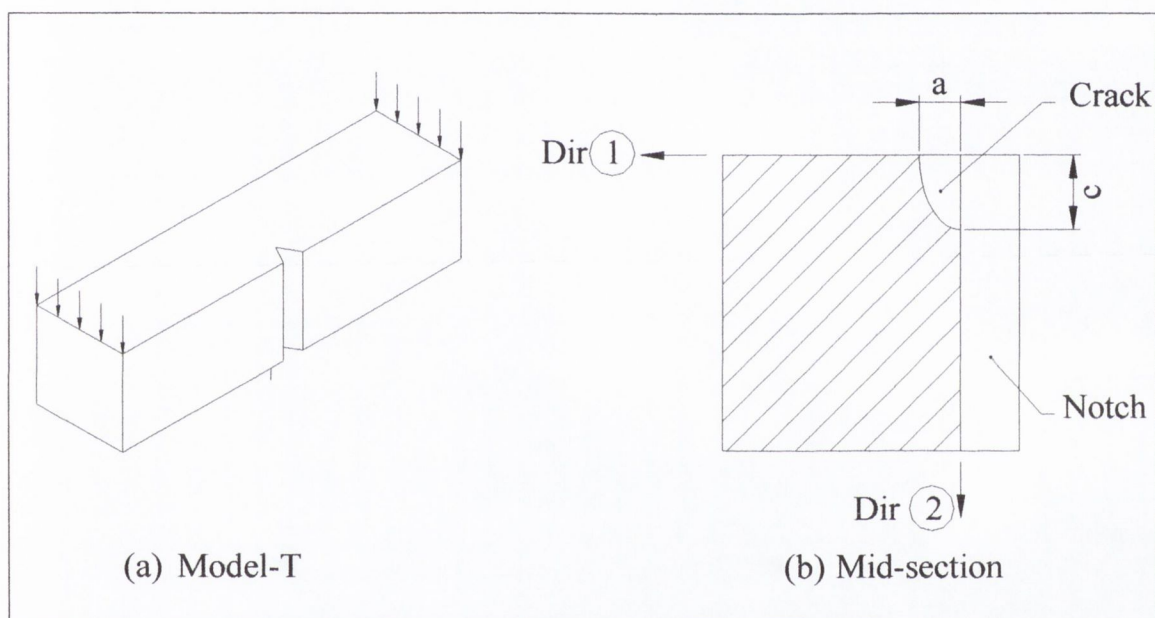


Fig. 6.11 - Estimating crack shape - Model-T

The stress distributions in directions 1 and 2 (as defined in Figure 6.11(b) above) are shown in Figure 6.12. It can be seen that there is a big stress gradient in direction 1, due to the notch and only a very shallow slope in direction 2, due to the bending gradient. If it is assumed that the different stress distributions are the main reason for the different crack lengths in these directions, then we can use this to estimate the crack shape, as follows.

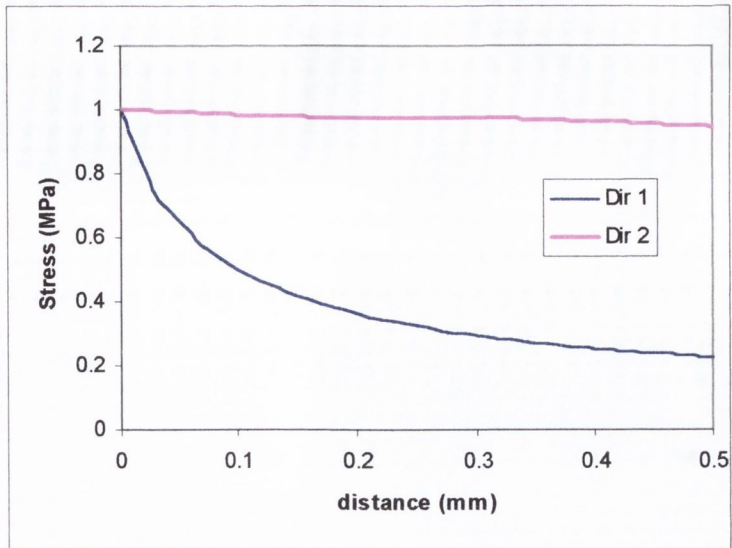
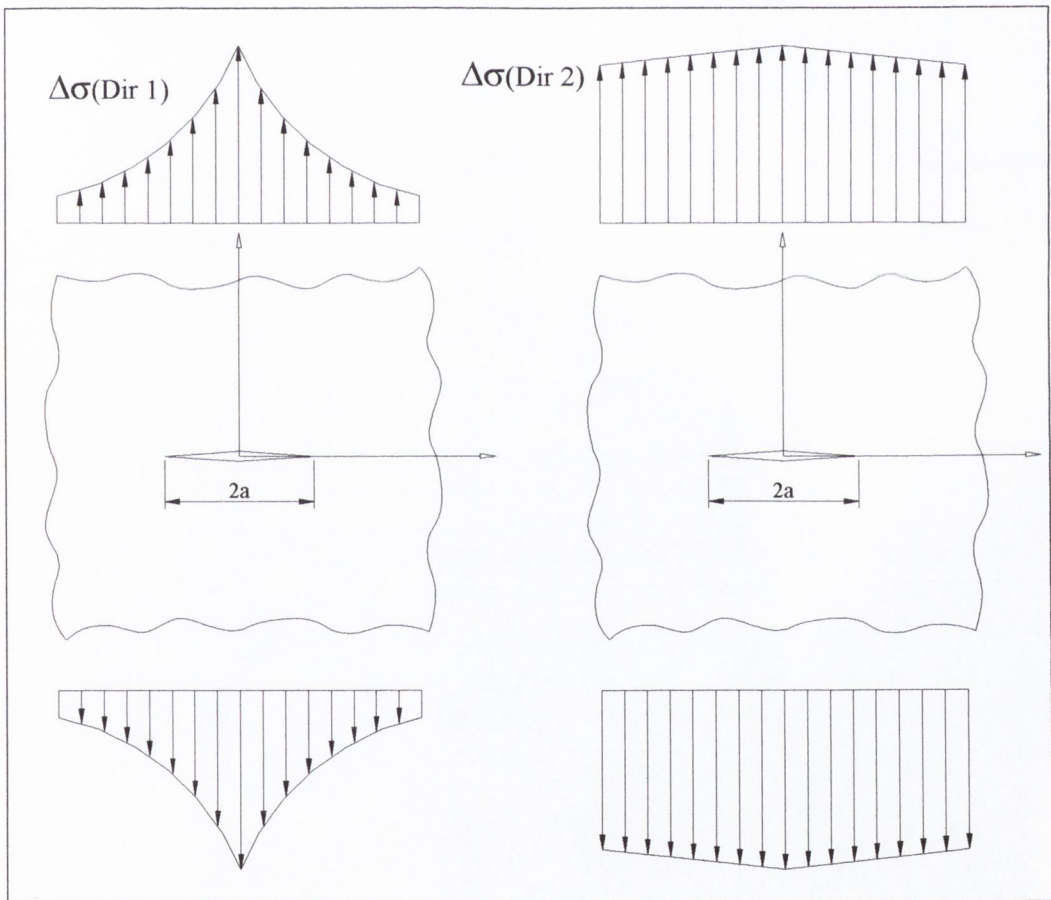


Fig. 6.12 - The stress distributions in directions 1 and 2



(a) Direction 1

(b) Direction 2

Fig. 6.13 - Crack in an infinite plate subjected to different stress distributions

Consider an infinite plate containing a centre crack of length  $2a$  subjected to two different stress distributions, as shown in Figure 6.13 above. The stress distributions are symmetric

versions of those given in Figure 6.12 for the Model-T specimen in directions 1 and 2. Figure 6.13(a) is meant to represent the Model-T crack in direction 1. Direction 2 is represented by Figure 6.13(b).

For both cases the stress intensity factor, as a function of crack length, can be calculated as per the procedure below.

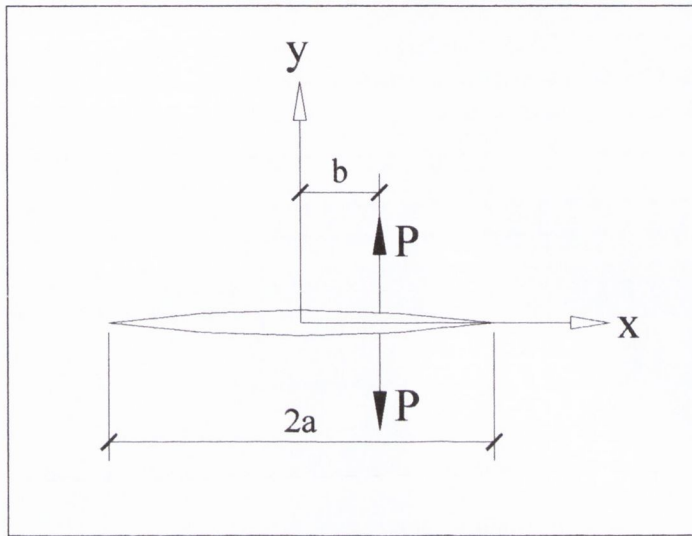


Fig. 6.14 - A crack of length  $2a$ , in an infinite plate, subjected to a pair of concentrated forces,  $P$  at  $x = b$

The Westergaard stress function for a crack subjected to a pair of concentrated forces  $P$ , at a distance  $b$  from the  $y$ -axis (see Figure 6.14), is given by Gdoutos [1999] as:

$$Z_1(z) = \frac{P}{\pi(z-b)} \sqrt{\frac{a^2 - b^2}{z^2 - a^2}} \quad (6-13)$$

The resulting stress intensity is therefore:

$$K_I = \sqrt{2\pi} \lim_{z \rightarrow a} \sqrt{z-a} Z_1(z) = \frac{P}{\sqrt{\pi a}} \sqrt{\frac{a+b}{a-b}} \quad (6-14)$$

This enables us to find the stress intensity caused by any internal pressure distribution, if the distribution can be discretised into individual loads. Then, via the principal of superposition, the stress intensity calculated this way is equivalent to that which would be obtained if the same loads were applied as a remote external load. This is essentially the basis of the crack-line loading method.

For the stress distributions given above, the resulting stress intensity factors, as a function of crack length, are given in Figure 6.15 below. As expected, it can be seen that the stress intensity in direction 2 is always higher than direction 1, for the same crack length.

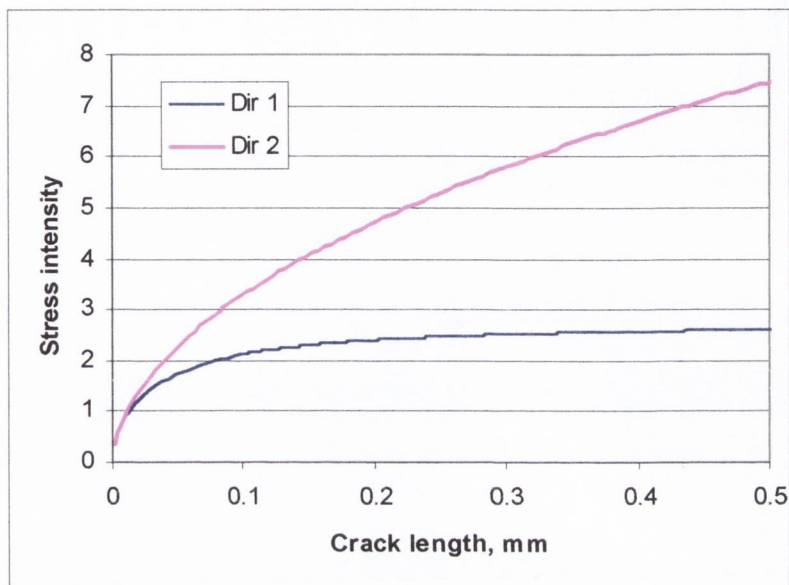


Fig. 6.15 - Stress intensity factor as a function of crack length for both stress distributions

Once the stress intensity factor is known as a function of crack length for both cases, the crack growth rates, at each crack length, can be calculated via the Paris equation (see equation 6-2).

### 6.5.1 Load sharing criteria

The problem is, how to determine the crack lengths, in both directions at the same number of cycles. This is obviously complicated by the fact that in reality the two directions are not independent of each other. The crack will grow fastest in the direction with the highest stress intensity. However, as the crack in that direction gets longer, it becomes more compliant and hence transfers load to the other parts of the crack front. Therefore, if we are only considering two points on the crack front, we must use some criteria to decide the degree of *load sharing*. In the simple approach investigated here, crack face displacement is used. If the displacement at the common point, to both directions, is not the same, load is transferred from the direction with the bigger displacement to the one with the smaller

displacement. In effect, the two directions are considered to behave as two springs in parallel. That is, they must have the same opening displacement and the sum of the load through each side must be equal to the total load.

It is therefore necessary to be able to calculate crack face displacement for any given stress distribution. With reference to Figure 6.14, the crack face displacement of a crack subjected to a pair of concentrated forces  $P$ , at a distance  $b$  from the  $y$ -axis can be determined in terms of the Westergaard stress function (see equation 6-13), via the equation below [Parker, 1981].

$$v = \frac{\chi + 1}{4\mu} \text{Im} \tilde{Z}_1(z) \quad \text{where} \quad \tilde{Z}_1(z) \equiv \int Z_1(z) dz \quad (6-15)$$

Therefore

$$v(x) = \frac{\chi + 1}{4\mu} \text{Im} \left\{ - \text{atan} \left[ \frac{a^2 - bx}{(a^2 - b^2) \sqrt{\frac{x^2 - a^2}{a^2 - b^2}}} \right] \frac{P}{\pi} \right\} \quad (6-16)$$

Where,  $\chi = 3 - 4\nu$  for plain strain and  $\chi = \frac{3 - \nu}{1 - \nu}$  for plane stress,  $\nu$  is Poisson's ratio and  $\mu$  is the shear modulus.

Equation 6-16 is plotted in Figure 6.16 for a crack of length  $2a$  (where  $a = 1$ ), for a pair of point forces applied at  $x = 0.5$ . It can be seen that a singularity exists in the solution at the point of the applied load.



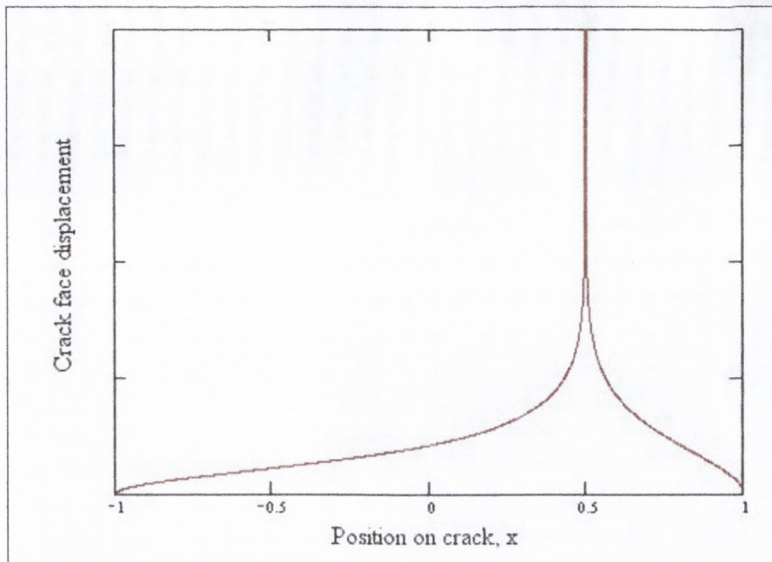


Fig. 6.16 - The crack face displacement profile of a crack subject to a pair of concentrated forces (at  $x = 0.5$ )

At the centre of the crack,  $x = 0$ , equation 6-16 reduces to:

$$v(0) = \frac{\chi + 1}{4\mu} \ln \left\{ \frac{\sqrt{-2a^2 + b^2 - 2a\sqrt{a^2 - b^2}}}{|b|} \right\} \frac{P}{\pi} \quad (6-17)$$

The resulting crack face displacements (at  $x = 0$ ), due to both stress distributions, are shown in Figure 6.17 below.

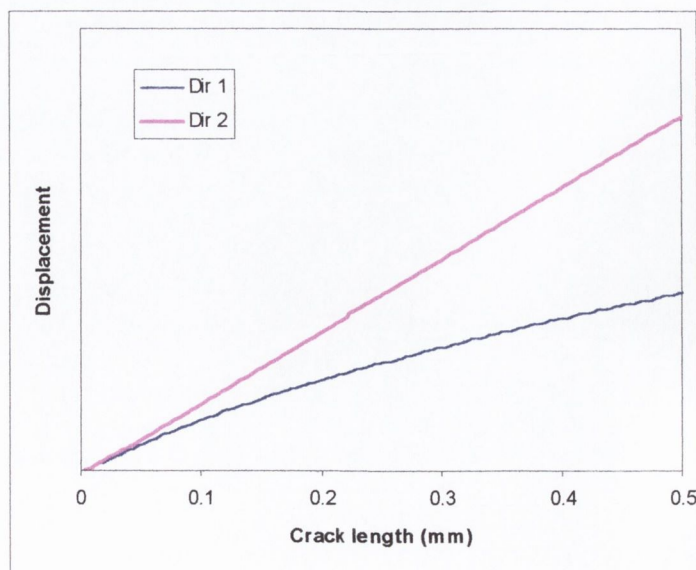


Fig. 6.17 - The crack face displacement (at  $x = 0$ ) for both directions

Once the stress intensity and crack face displacements (at  $x = 0$ ) are available, the crack shape is calculated via the following algorithm, which was implemented as an Excel macro.

1. Assume the crack grows  $\Delta a$  in direction 2 (which has the higher  $\Delta K$  and  $da/dN$ )
2. Using the Paris equation, (equation 6-2), calculate the number of cycles,  $\Delta N$ , needed for this crack extension.
3. Make an initial guess for the change of crack length in direction 1
4. Determine, the stress intensity, the crack face displacement (at  $x = 0$ ), the crack growth rate and the number of cycles needed for this crack extension, via linear interpolation.
5. Using a process of iteration, ensure that the number of cycles needed for crack extension is the same in both directions and the crack face displacement is the same in both directions, by transferring load from one direction to the other and by changing the length of the crack in direction 1.
6. Once the lengths in both directions are known, the crack front is assumed to be an ellipse passing through these points.

### 6.5.2 Application to the Model-T specimen

Using the procedure outlined above, the predicted crack shape for the Model-T specimen is shown in Figure 6.18 below. This was calculated using the following constants for the Paris growth rate equation:  $A = 3 \times 10^{-12}$  and  $m = 3.5$ .

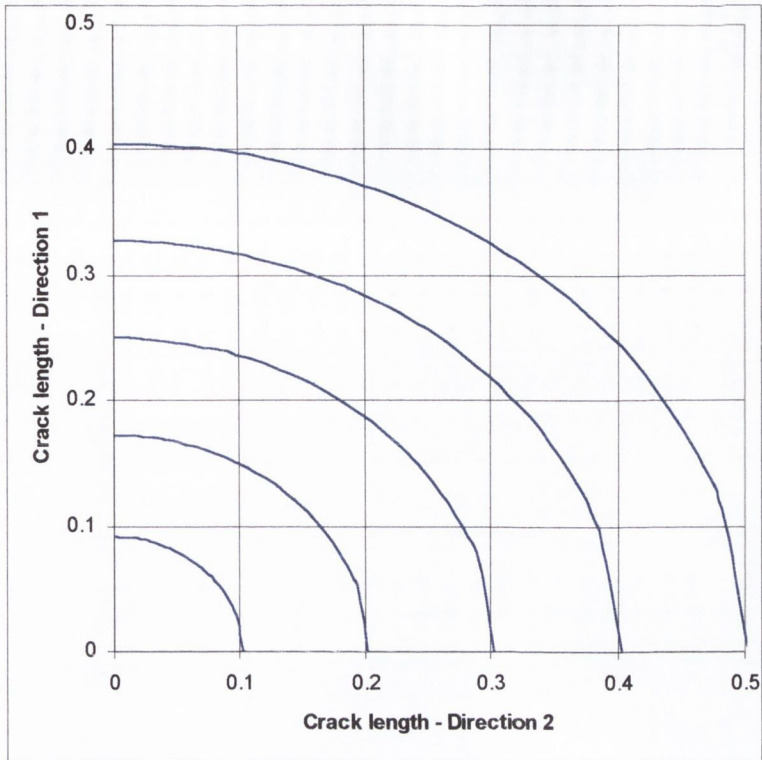


Fig. 6.18 - Predicted crack shape for the Model-T specimen

It can be seen that the method predicts that the crack becomes slightly more elliptical as it gets bigger, but in general remains approximately circular. This is contrary to the experimentally observed shape, which indicates that the elliptical ratio should be approximately 0.2 (see Appendix A, section A.4.3.1).

### 6.5.3 Application to the Model-E specimen

The method was also applied to the Model-E specimen. The directions chosen on which to determine the crack lengths are shown in Figure 6.19 below. The resulting crack shape is shown in Figure 6.20. It can be seen that in this case the crack shape is again approximately circular. However, for this specimen, this is the expected shape.

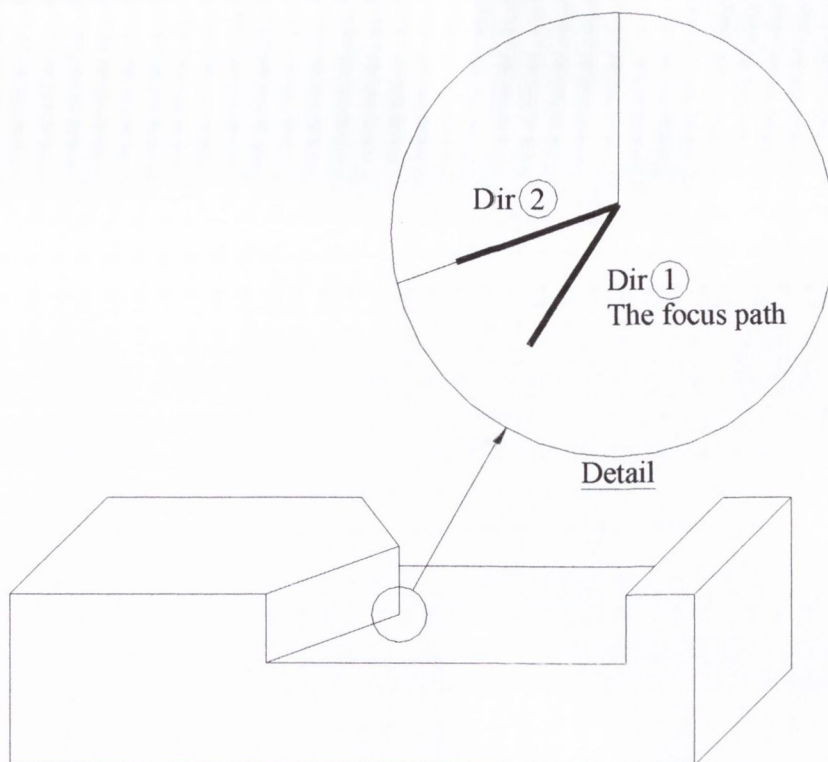


Fig. 6.19 - The two directions chosen for application to the Model-E specimen

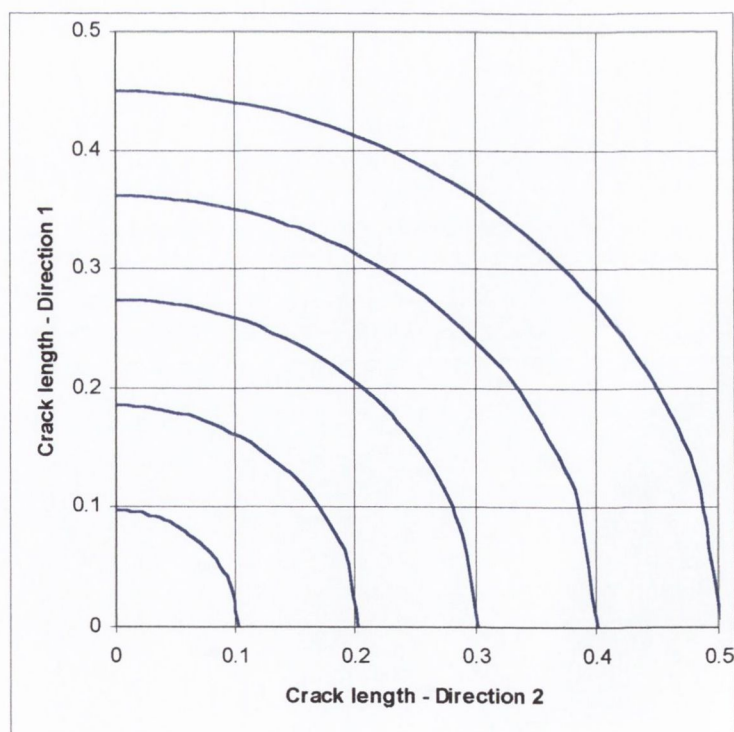


Fig. 6.20 - Predicted crack shape for the Model-E specimen

#### 6.5.4 The effect of the growth law constants

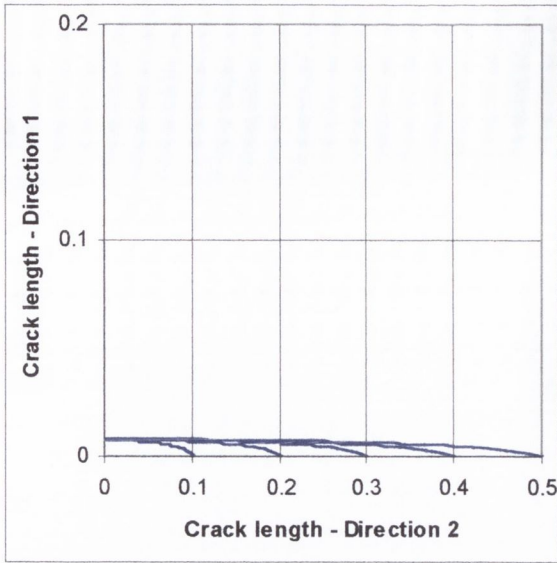
A sensitivity analysis was also conducted to determine the effect of the material constants used in the Paris law growth rate equation (equation 6-2). The results of this are summarised in Table 6.3 below. It can be seen that the crack growth rate exponent,  $m$ , has a small effect on the predicted shape. That is, the crack is predicted to be slightly more elliptical when a higher growth rate exponent is used. The growth rate constant,  $A$ , was observed to have no effect on the predicted shape.

Table 6.3 - Predictions for Model-T and Model-E, for different Paris law constants

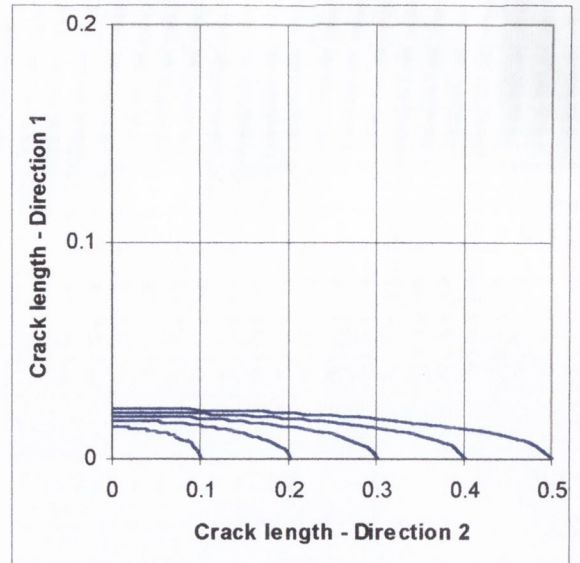
	Model-T			Model-E		
	Dir 2 (mm)	Dir 1 (mm)	$\Phi$	Dir 2 (mm)	Dir 1 (mm)	$\Phi$
$A = 3 \times 10^{-12}$ and $m = 3.5$	0.5025	0.405309	1.423	0.5025	0.449819	1.490
$A = 3 \times 10^{-12}$ and $m = 5$	0.5025	0.394461	1.407	0.5025	0.446757	1.485
$A = 3 \times 10^{-12}$ and $m = 2$	0.5025	0.418463	1.442	0.5025	0.460944	1.507
$A = 3 \times 10^{-6}$ and $m = 3.5$	0.5025	0.404059	1.421	0.5025	0.449819	1.490

#### 6.5.5 Application of the method without load sharing

Because the method, as described above, results in essentially circular crack shapes, even for the Model-T specimen, it was concluded that the load sharing criteria used (see section 6.5.1) is inadequate. It was therefore decided to apply the method without considering any load sharing effect. This obviously results in a more elliptical crack shape, which was hoped could be used as a lower bound for the analysis. The results are shown in Figure 6.21 below. Note that the scale of the vertical axis is different to the scale used previously.



(a) Model-T



(b) Model-E

Fig. 6.21 - Predicted crack shapes assuming no load sharing

In this case, the predicted crack shapes are highly elliptical. The elliptical ratios are:

$$\frac{\text{Dir 1}}{\text{Dir 2}} = 0.016 \quad \text{and} \quad \Phi = 1.00415 \quad \text{for Model-T}$$

$$\frac{\text{Dir 1}}{\text{Dir 2}} = 0.046 \quad \text{and} \quad \Phi = 1.00065 \quad \text{for Model-E}$$

This approach is also obviously wrong, as the shape predicted for the Model-E specimen is far too elliptical. It is also not very useful as a lower bound to the analysis because the elliptical ratios are virtually zero.

### 6.5.6 Conclusion

From the above it is concluded that, although worth investigating, the approach is too simplistic to accurately determine the shape of a fatigue crack, resulting from any given stress concentration. In particular, the load sharing criteria is inadequate. Hence, a step-by-step finite element approach, like that used by Lin and Smith [1997; 1999] is necessary. Unfortunately this couldn't be done within the scope of this project.

## 6.6 Application of the correction factor

As the method investigated above for predicting the crack shape proved to be fruitless, a certain amount of engineering judgement is used below to estimate the actual crack shape for the various specimens for which the crack shape was not measured.

### 6.6.1 Model -T

As already stated, the crack shape for this specimen was measured to be elliptical, with the major axis orientated along the notch (see Appendix A, section A.4.3.1). Furthermore the elliptical ratio was measured to be approximately 0.2, as shown in Figure 6.22 below. This shape makes sense for this specimen and was expected because of the following qualitative arguments. Firstly, as shown in Figure 6.12 above there is a big difference between stress gradients along the top of the specimen and along the notch. Secondly, because the bending gradient along the notch is relatively shallow, cracks can initiate at multiple points over a relatively large distance along the notch. This is quite probable, because as explained in Appendix A, section A.4.4, the hotspot is not at the top surface of the specimen, where simple bending theory would predict. Instead, it is located a very small distance down the notch.

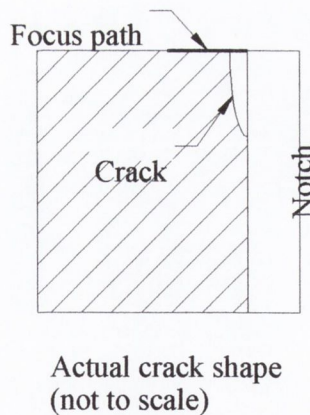


Fig. 6.22 - Crack shapes for the Model-T specimen

With reference to Table 6.1 above the correction factor for the Model-T specimen is 1.051 (for  $a/c = 0.2$ ). Hence, the application of this correction results in an almost negligible change. As discussed in Chapter 5 and Appendix A, the results from the fatigue analysis of

this specimen were very good, without applying any correction. However, even after applying this correction the results will still be good.

### 6.6.2 Model-E

As already stated, it is believed that fatigue cracks emanating from this stress concentration will be approximately circular. Table 6.4 shows the results of the fatigue analysis of the Model-E specimen, before and after the correction factor has been applied, assuming a circular crack (i.e.  $f_{shape\ correction} = 1.58$ ).

Table 6.4 - Fatigue analysis results of Model-E1 with and without the correction factor

	Without correction factor	With correction factor $f_{shape\ correction} = 1.58$
<b>Experimental</b>	6.6 kN at $2 \times 10^6$ cycles	
<b>Point method</b> (Error factor)	2.99 kN (2.21)	4.72 kN (1.40)
<b>Line method</b> (Error factor)	3.06 kN (2.16)	4.83 kN (1.37)

Note: Error factor is defined as the ratio of the Experimental fatigue strength to the predicted fatigue strength

It can be seen that the correction improves the predictions for the CDMs, although conservative errors are still apparent.

### 6.6.3 Fillet-A

Again, it is expected that the actual crack for the Fillet-A specimen will be approximately circular, as it is essentially a corner crack. Therefore, a correction factor of 1.58 is applied. The results are shown in Table 6.5 below.



Table 6.5 - Fatigue analysis results Fillet-A with and without the correction factor

	Without correction factor	With correction factor $F_{shape\ correction} = 1.58$
<b>Experimental</b>	8.4 kN at $5 \times 10^6$ cycles	
<b>Point method</b> (Error factor)	3.78 kN (2.22)	5.97 kN (1.41)
<b>Line method</b> (Error factor)	3.33 kN (2.52)	5.26 kN (1.60)
<b>CMM</b> (Error factor)	4.24 kN (1.98)	6.70 kN (1.25)

Note: Error factor is defined as the ratio of the Experimental fatigue strength to the predicted fatigue strength

As per the Model-E specimen, application of the correction factor results in a considerable improvement, although conservative errors still remain.

#### 6.6.4 T-shape-B

It is quite difficult to estimate the actual crack shape for the T-shape-B welded specimen. If the end of the weld bead is assumed to be a perfectly smooth arc, as it is in the FE model, then the stress gradient in the third direction is quite shallow. Hence, one would predict the actual crack shape to quite a blunt ellipse. However, in reality local irregularities at the weld end could result in higher stress gradients and therefore a higher elliptical ratio. In the following an elliptical ratio of 0.4 is assumed. The resulting correction factor is 1.151. The effect of this correction on the fatigue analysis is shown in the Table below. Again it can be seen that the result is improved, although conservative errors still remain.

Table 6.6 - Fatigue analysis results T-shape-B, with and without the correction factor

	Without correction	With corrections $f_{shape\ correction} \approx 1.151$
<b>Experimental</b>	6.62 kN at $5 \times 10^6$ cycles	
<b>Point method</b> (Error factor)	3.75 kN (1.77)	4.32 kN (1.53)
<b>Line method</b> (Error factor)	3.34 kN (1.98)	3.84 kN (1.72)
<b>CMM</b> (Error factor)	4.12 kN (1.61)	4.74 kN (1.40)

Note: Error factor is defined as the ratio of the Experimental fatigue strength to the predicted fatigue strength

## **6.7 Concluding remarks**

It is argued in this chapter that crack shape can have an effect on the fatigue life of “sharp, crack-like” stress concentrations, for which the fatigue limit is characterised by the growth of non-propagating cracks. In particular, it is shown that fatigue assessment methods which make use of the 2D focus path concept, for complex 3D geometries, make an inherent assumption regarding crack shape and that a simple correction factor, based on the actual crack shape, can be applied to account for this.

A simple approach to estimate the crack shape was investigated. Unfortunately, it was shown that it doesn't work. Hence, engineering judgement was used, where necessary, to make educated guesses for the actual crack shapes and hence the correction factors that should be applied.

It was subsequently shown that the correction considerably improves the predictions for the Model-E, Fillet-A and T-shape-B specimens without greatly affecting the Model-T specimen, for which good predictions were already obtained.

It should be noted that the ideas in this chapter are based on the assumption that non-propagating cracks always exist under certain conditions, at the root of sharp, crack-like stress concentrations. As discussed in section 6.1, this is based on the large body of work, published by very eminent authors, which maintains that this is in fact the case. In effect this faith may be misguided, as the experimental observation of non-propagating cracks, in this work, was found to be much more difficult than expected. In theory they should have been apparent on all of the specimens that didn't fail during testing, but in practice this was not the case.

As discussed in Appendix A, section A.4.3.1, a considerable effort was made to determine the crack shape for the Model-T specimen. This proved to be more difficult than expected because of the small crack lengths involved and the practical problems associated with using methods, like replica tape at 3-D stress concentrations. The most successful way to determine the crack shape was to examine the failure surface under a scanning electron microscope. Unfortunately, this couldn't be done for all of the specimens investigated.

## Chapter 7: The constraint effect

---

In the study of fracture mechanics, it is universally accepted that crack tip constraint strongly influences the fracture toughness of a material. A high degree of *constraint* or *triaxiality* or *hydrostatic stress* at a crack tip, results in a lower energy requirement for fast fracture. This is because the hydrostatic stress state offers less opportunity for the redistribution of high crack tip stress by shear yielding. The difference between fracture toughness values measured in plane stress and plane strain is attributed to this phenomenon.

It is argued in the following, that a similar effect can be observed in fatigue. That is, low crack tip constraint has the affect of increasing the material stress intensity threshold range by effecting crack propagation. The consequence of this is that the critical distance used in the fatigue analysis methods advocated by Taylor should be increased when predicting the behaviour of notched components characterised by low constraint. Two separate experimental investigations, presented below, support this.

### 7.1 Crack tip constraint in fracture

Elasticity theory predicts that the stress at a crack tip is infinite. For a real material this is obviously absurd. In reality, local, small scale yielding occurs at the crack tip as soon as a load is applied. The effect of this is to redistribute high crack tip stresses via shear yielding. This is often referred to as plastic relaxation, which can be thought of as the inverse of constraint. Depending on the stress state the size of the plastic zone varies. For two-dimensional, cracked geometries, the maximum plastic zone size occurs for conditions of plane stress and the minimum size for plane strain. If the plastic zone is large, there will be considerable plastic relaxation and consequently low constraint. The inverse is true if the plastic zone is small.

From the above it is clear that plasticity and constraint are inseparable. Therefore, in the following, methods for predicting the size and shape of the plastic zone ahead of a crack are discussed.

### 7.1.1 The plastic zone size due to Irwin

The simplest approach to estimate the size of the plastic zone ahead of a long crack was proposed by Irwin [1958], by assuming that the shape of the zone would be circular. If the elastic stress distribution ahead of a centre crack in an infinite plate (see Figure 7.1) is considered, the stress in the y-direction, along the x-axis is given by equation 7-1.

$$\sigma_y = \frac{K_I}{\sqrt{2\pi r}} \quad (7-1)$$

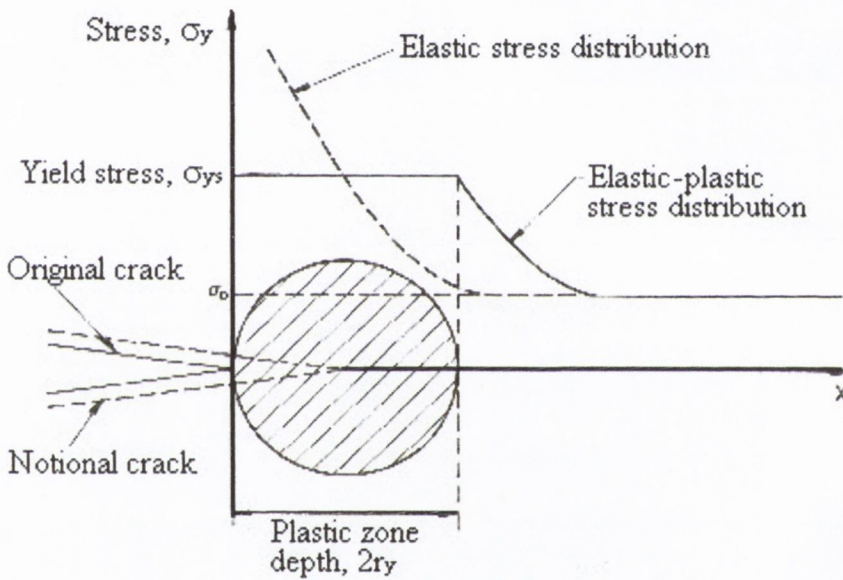


Fig. 7.1 - Plastic zone size due to Irwin

By substituting the yield strength  $\sigma_{ys}$ , for  $\sigma_y$  in equation 7-1, an estimate can be obtained for the distance,  $r_y$ , over which the material is plastically deformed. However, as this simply cuts off the portion of the elastic stress field above  $\sigma_{ys}$ , equilibrium isn't satisfied. Thus the stress distribution, in Figure 7.1 above, must shift to the right, as shown. The actual plastic zone size as estimated by Irwin is  $2r_y$  and is given in equation 7-2 below.

$$2r_y = \frac{1}{\pi} \left( \frac{K_I}{\sigma_{ys}} \right)^2 \quad \text{for plane stress} \quad (7-2)$$

The plane strain plastic zone size is usually taken to be one-third of the plane stress value; therefore:

$$2r_y \cong \frac{1}{3\pi} \left( \frac{K_I}{\sigma_{ys}} \right)^2 \quad \text{for plane strain} \quad (7-3)$$

### 7.1.2 Plastic zone size due to Dugdale

Another model to describe the plastic zone ahead of a crack was formulated by Dugdale [1960], for conditions of plane stress. He did this by modelling the plastic regions extending beyond the physical crack length,  $2c$ , as narrow strips of length  $R$ , which are effectively extensions of the crack (see Figure 7.2 below).

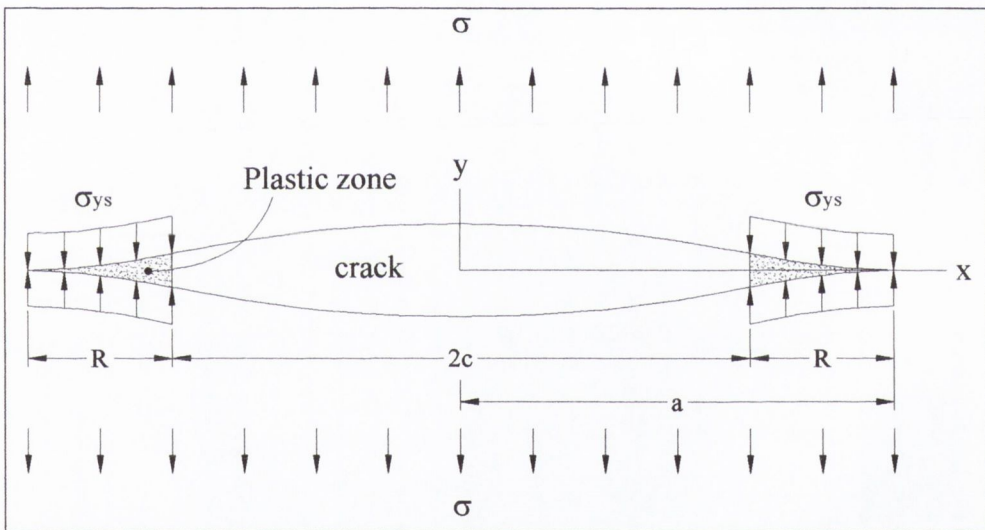


Fig. 7.2 - Schematic of the Dugdale plastic zone strip model

He assumed that there would be an internal pressure, equal to the yield stress acting on these strips over the distance  $R$ , which re-closes the crack to a length of  $2c$ . In this way Dugdale was able to use elastic theory, but eliminated the stress singularity at the end of the physical crack. The plastic zone size he calculated is in close agreement with Irwin's model and is:

$$R \cong \frac{\pi}{8} \left( \frac{K_I}{\sigma_{ys}} \right)^2 \quad \text{for plane stress} \quad (7-4)$$

In order to account for constraint effects under non-plane stress conditions, a constraint factor,  $\alpha$ , is normally adopted (i.e. it is assumed that a constant stress, equal to  $\alpha\sigma_{ys}$  acts on the yielded strips). The lower bound for  $\alpha$  is the plane stress limit ( $\alpha = 1$ ) and the upper bound is the plane strain value, for which  $\alpha$  is usually assumed to be 3.

### 7.1.3 Plastic zone shape

The methods above estimate the plastic zone ahead of a crack by assuming that it will take a specific shape. The following is a method of estimating the shape of the plastic zone, which unfortunately does not yield any information relating to the absolute size of the plastic zone. However it does demonstrate the relative difference in the plastic zone size for conditions of plane stress and plane strain. The concept is to use a yield criterion in conjunction with the equations for the elastic stress distribution ahead of a crack. For example, when considering the Von Mises criterion, it is assumed that yielding occurs when:

$$(\sigma_1 - \sigma_2)^2 + (\sigma_2 - \sigma_3)^2 + (\sigma_1 - \sigma_3)^2 = 2\sigma_{ys}^2 \quad (7-5)$$

Where  $\sigma_1$ ,  $\sigma_2$  and  $\sigma_3$  are the principal stresses. From chapter 3, section 3.1.2, the principal stresses  $\sigma_1$  and  $\sigma_2$  ahead of a centre crack in an infinite plate are found to be:

$$\sigma_1 = \frac{K_I}{\sqrt{2\pi r}} \cos \frac{\theta}{2} \left( 1 + \sin \frac{\theta}{2} \right) \quad (7-6)$$

$$\sigma_2 = \frac{K_I}{\sqrt{2\pi r}} \cos \frac{\theta}{2} \left( 1 - \sin \frac{\theta}{2} \right) \quad (7-7)$$

In conditions of plane stress the third principal stress is equal to zero (i.e.  $\sigma_3 = 0$ ). The Mohr's circle representation of this stress state is shown in Figure 7.3 below. Substituting these equations for the principal stress into the Von Mises yield criterion results in the following:

$$\frac{K_I^2}{\sqrt{2\pi r}} \left( 1 + \frac{3}{2} \sin^2 \theta + \cos \theta \right) = 2\sigma_{ys}^2 \quad (7-8)$$

Rearranging:

$$r(\theta) = \frac{1}{4\pi} \left( \frac{K_I}{\sigma_{ys}} \right)^2 \left( 1 + \frac{3}{2} \sin^2 \theta + \cos \theta \right) \quad (7-9)$$

Equation 7-9 above can be normalised by  $r_y$ , where:

$$r_y = \frac{1}{2\pi} \left( \frac{K_I}{\sigma_{ys}} \right)^2 \quad (7-10)$$

The result is the normalised shape of the plastic zone ahead of a centre cracked infinite plate in plane stress.

$$\left( \frac{r(\theta)}{r_y} \right)_{Pl-Stress} = \frac{1}{2} + \frac{3}{4} \sin^2 \theta + \frac{1}{2} \cos \theta \quad (7-11)$$

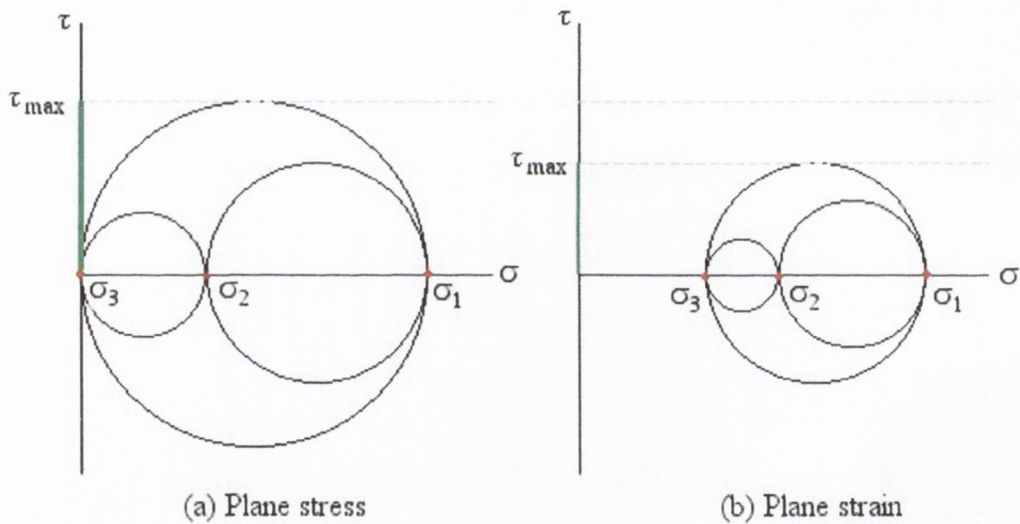
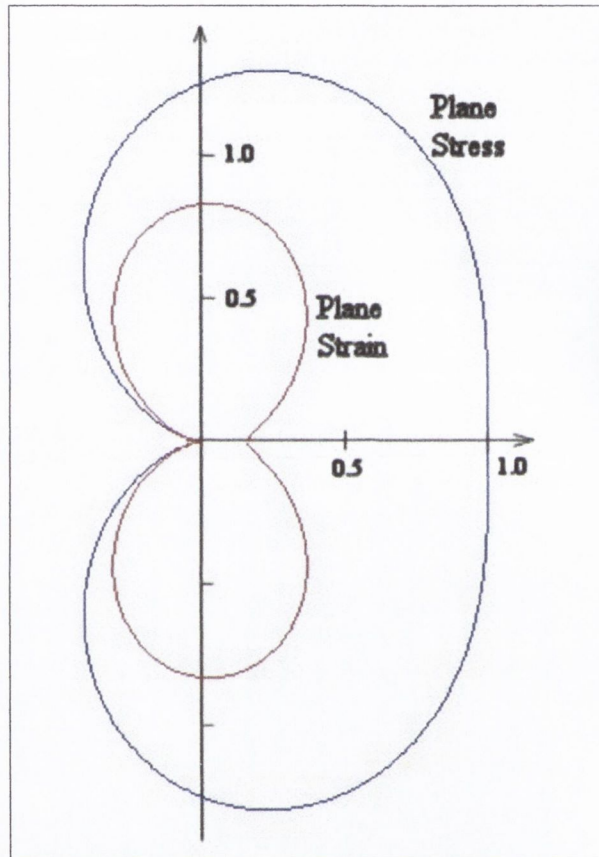


Fig. 7.3 - Mohr's circles for the conditions of plane stress and plane strain in a cracked body

Following exactly the same method, the normalised shape of the plastic zone in plane strain can be determined. In this case the third principal stress is given by  $\sigma_3 = \nu(\sigma_1 + \sigma_2) \neq 0$ , where  $\nu$  is Poisson's ratio. The Mohr's circle representation of this stress state is also shown in Figure 7.3 above. It can be seen that conditions of plane strain result in a lower maximum shear stress when compared to plane stress. Hence, the plastic zone for this case should be smaller. For plane strain the normalised shape of the plastic zone is approximated to be:

$$\left(\frac{r(\theta)}{r_y}\right)_{Pl-Strain} = \frac{3}{4}\sin^2\theta + \frac{1}{2}(1-2\nu)^2(1+\cos\theta) \quad (7-12)$$

A comparison between the normalised plastic zone shape determined in plane stress and plane strain is shown in Figure 7.4 below. It can be seen that, as expected, the plastic zone is much larger for conditions of plane stress.



*Fig. 7.4 - Comparison of the plastic zone in plane stress and plane strain using the method described above*

The ratio of the size of the plastic zones in plane stress and plane strain along the x-axes, for which  $\theta = 0$ , is therefore:

$$\frac{r(\theta = 0^\circ)_{Pl-Strain}}{r(\theta = 0^\circ)_{Pl-Stress}} = 0.11 \quad (7-13)$$



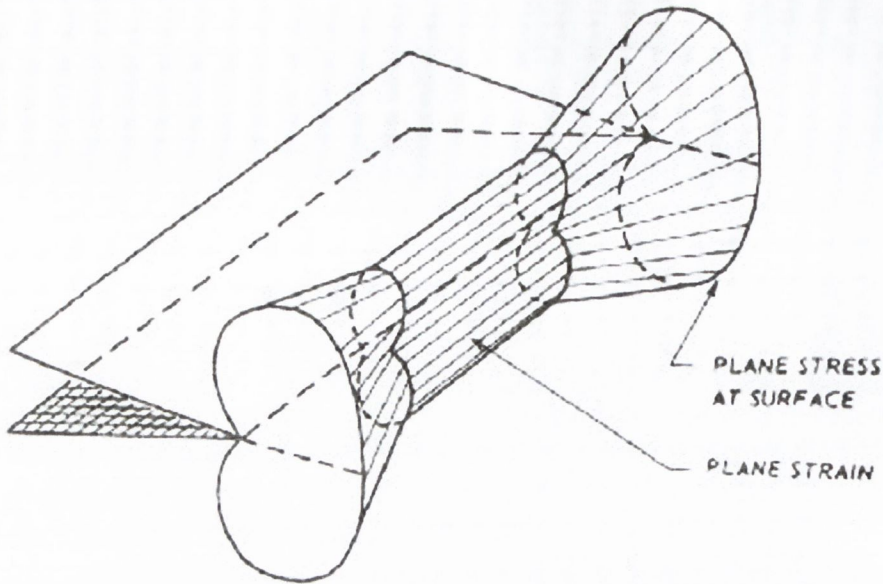


Fig. 7.5 - Schematic of the plastic zone shape for a real situation [Ewalds and Wanhill, 1989]

In a real fracture mechanics specimen, there is an interaction between pure plane stress and pure plane strain states. At the side surface of a cracked plate there is no stress in the thickness direction, so a biaxial condition of plane stress exists. Proceeding inwards, there is an increasing degree of triaxiality, that approaches, and if the specimen is thick enough, may correspond to plane strain. Thus, the plastic zone size and shape varies through the thickness of the plate (see Figure 7.5 above).

#### 7.1.4 The effect of constraint on fracture toughness

The fracture toughness,  $K_{IC}$ , of a material is the critical stress intensity factor at which the crack extends rapidly in an unstable manner without an increase in load. The general relationship between fracture toughness and thickness is shown in Figure 7.6. It can be seen that there are three distinct regions:

##### *The plane strain region*

Occurs when the specimen is relatively thick so that the material is predominantly in plane strain and under maximum constraint. The value of  $K_{IC}$  tends to a constant minimum value, which is referred to as the plane strain fracture toughness  $K_{IC}$ . In this case, the fracture surface is typically flat and perpendicular to the direction of the applied load.

### *The plane stress region*

Occurs when the thickness of the specimen approaches the same size as the plastic zone. The maximum  $K_c$  value is observed at the thickness where there is minimum constraint. This is because more energy is required to push the large plastic zone ahead of the crack. As the material thickness decreases from this value the specimen becomes too thin to support a pure mode I fracture, that is, out-of-plane tearing occurs, hence the fracture toughness decreases. In this region the fracture surface is typically at 45 degrees to the direction of the applied load or has significant *shear lips*.

### *The transitional region*

This is a transition region between the maximum value measured in plane stress and the lower constant value measured in plane strain. In this region the fracture surface is characterised by both flat and slanted fracture surfaces. The percentage of slanted fracture, or shear lips, decreases with increasing thickness.

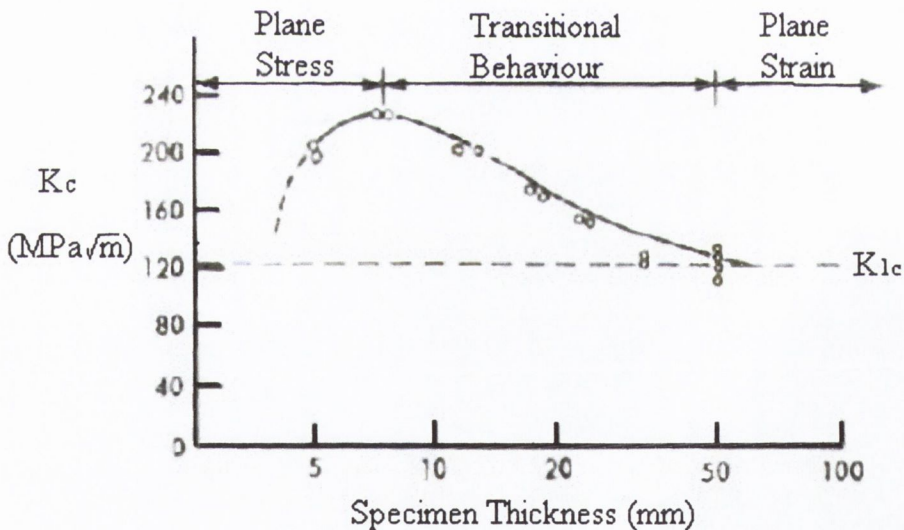


Fig. 7.6 - Variation of  $K_c$  with specimen thickness for a high strength steel [Ewalds and Wanhill, 1989]

As stated above, the fracture toughness,  $K_c$ , approaches a constant minimum value,  $K_{Ic}$  when the thickness of the specimen becomes large compared to the size of the plastic zone. For this reason plane strain fracture toughness,  $K_{Ic}$ , is considered to be a true material property. Guidelines have been developed to ensure that the plane strain fracture toughness

is obtained when measuring the fracture toughness of a material [ASTM, 1974]. These are generally stated in the following form:

$$a \text{ and } t \geq 2.5 \left( \frac{K_{Ic}}{\sigma_{ys}} \right)^2 \quad (7-14)$$

Where  $a$  is the crack length and  $t$  is the specimen thickness. This ensures that the plastic zone of the specimen is approximately 8 times larger than the plane stress plastic zone and 24 times larger than the plane strain plastic zone.

## 7.2 Crack tip constraint in fatigue

The foregoing discussion has all been in relation to fracture, where failure occurs due to a single applied load. In the following, additional factors that should be taken into account when considering the effect of crack tip constraint on fatigue behaviour are considered.

### 7.2.1 The cyclic plastic zone

Sections 7.1.1 and 7.1.2 above describe the plastic zone developed at the tip of a crack as a result of fracture. In terms of fatigue this corresponds to the *monotonic plastic zone* (MPZ) or the plastic zone developed due to the maximum applied load in the loading cycle (point A in Figure 7.7). It's important to realise that this is positive plastic deformation, that is, the material has been permanently *stretched*. However, as the load is reduced to the minimum load (point B in Figure 7.7) the material in the vicinity of the crack tip is plastically deformed in the opposite direction. This results in the formation of a *cyclic plastic zone* (CPZ), in which the direction of plastic straining is reversed every cycle.

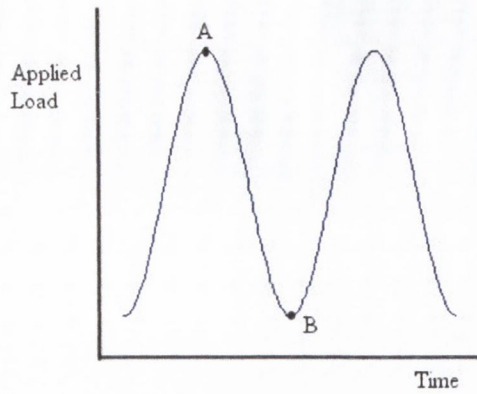
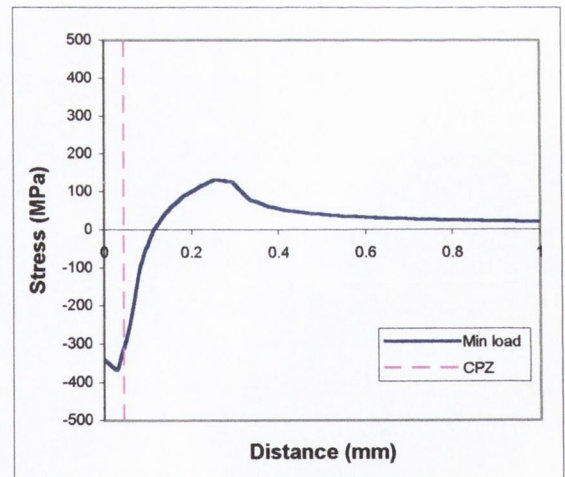
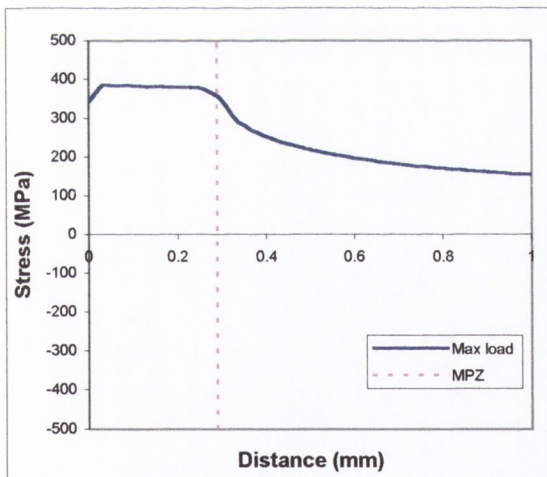


Fig. 7.7 - Loading cycle

Figures 7.8(a) and (b) show the inelastic stress distributions ahead of a crack (in plane stress) for the both the maximum and minimum points in the loading cycle obtained via an elastic-plastic FEA. An elastic-perfectly-plastic material, with a yield strength of 330 MPa was used. The R-ratio was 0.1. The extent of the MPZ and the CPZ can be seen in the figures. An important point to realise is that if a region yields in tension during loading, after unloading a portion of that region is in compression. It stands to reason then, that the size of the CPZ is related to the load ratio. The lower the R-ratio the bigger the CPZ.



(a) The inelastic stress distributions from the **maximum load** showing the extent of the MPZ

(b) The inelastic stress distributions from the **minimum load** showing the extent of the CPZ

Fig. 7.8 - Stress distributions ahead of a crack

The size of the CPZ can be approximated by substituting  $2\sigma_{ys}$  for  $\sigma_{ys}$  and  $\Delta K$  for  $K$  in Irwin's equations for the plastic zone size (equations 7-2 and 7-3). The results are:

$$2r_y |_{cyclic} \cong \frac{1}{\pi} \left( \frac{\Delta K}{2\sigma_{ys}} \right)^2 = \frac{1}{4\pi} \left( \frac{\Delta K}{\sigma_{ys}} \right)^2 \quad \text{for plane stress} \quad (7-15)$$

$$2r_y |_{cyclic} \cong \frac{1}{3\pi} \left( \frac{\Delta K_{th}}{2\sigma_{ys}} \right)^2 = \frac{1}{12\pi} \left( \frac{\Delta K_{th}}{\sigma_{ys}} \right)^2 \quad \text{for plane strain} \quad (7-16)$$

These approximations are valid for R-ratio  $\geq 0$  [Stephens *et al.*, 2001].

## 7.2.2 The effect of constraint on fatigue crack growth rate

In general it is accepted that constraint has an effect on fatigue crack growth. That is, cracks propagate slower in conditions of plane stress. This effect can be observed in standard fatigue specimens, which tend to show bowed crack fronts, where the crack is shortest at the side surfaces of the specimen.

As stated by Guo *et al.* [1999], specimen thickness has been found to considerably influence the fatigue crack growth rate under the same applied stress intensity factor, when the plastic zone size becomes comparable to the thickness. In particular the crack growth rate in thin specimens is found to be lower. An example of this effect is shown in Figure 7.9 below and is most often attributed to the phenomena of crack closure, which is discussed in the section below.

However, as discussed by Knott [1973] other factors must be considered when very thin specimen are investigated. In thin precracked specimen the crack initially propagates on a plane normal to the applied alternating stress. As it grows, the plastic zone at the crack tip becomes larger, until it reaches a critical size, which is related to the sheet thickness. The failure surface then changes to  $45^\circ$  slanting through the thickness and the crack growth rate accelerates markedly. This can be attributed to out-of-plane tearing, or a Mode III type of crack opening, whereby the material immediately above and below the crack tip are displaced laterally out-of-plane. This type of crack propagation is therefore governed by Mode III antiplane strain as opposed to Mode I plane stress.

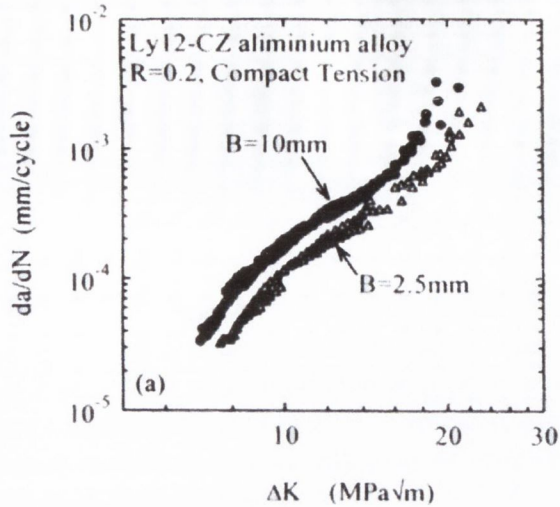


Fig. 7.9 - Fatigue crack growth data for LY12-CZ aluminium for two specimen thicknesses [Guo et al., 1999]

### 7.2.3 Crack closure

The effect of constraint on fatigue crack growth is complicated by the phenomena of crack closure. As the name implies, the effect of closure is to cause the faces of a fatigue crack to come into contact (or the crack to close) in the presence of a tensile far field load, before the crack is fully unloaded. This phenomenon was first observed by Elber [1970] who argued that it is the result of a zone of residual tensile deformation left in the wake of a fatigue crack tip. Subsequent researchers have labelled this *plasticity-induced closure* or *Elber closure* and have also identified other mechanisms responsible for closure. These include, but are not limited to: *Oxide-induced crack closure*, *Roughness-induced crack closure* and *viscous fluid-induced crack closure*.

In the following attention is focused on plasticity-induced closure, as it is expected that this will have a significant effect on the fatigue crack growth in plane stress and plane strain, where the plastic zone size is different. Elber [1970] argued that upon application of constant amplitude cyclic loading during the increasing tensile portion of the load, a plastic zone is formed and that plasticity occurring at the crack tip remains behind as the crack grows. The tensile deformation creates compressive residual stresses which, when the specimen is unloaded, cause the two crack surfaces to contact at a stress level,  $\sigma_{cl}$ , higher

than the minimum stress level,  $\sigma_{\min}$  (see Figure 7.10 below). This effect is usually accounted for by defining an effective stress intensity range,  $\Delta K_{\text{eff}}$  (see Figure 7.10 below).

$$\Delta K_{\text{eff}} = F \Delta \sigma_{\text{eff}} \sqrt{\pi a} \quad (7-17)$$

Alternatively the closure ratio,  $U$ , can be used

$$U = \frac{\Delta K_{\text{eff}}}{\Delta K} = \frac{\Delta \sigma_{\text{eff}}}{\Delta \sigma} = \frac{(\sigma_{\max} - \sigma_{op})}{(\sigma_{\max} - \sigma_{\min})} \quad (7-18)$$

Hence, Elber's crack growth rate equation can be expressed, in terms of the Paris law, as follows:

$$\frac{da}{dN} = A(\Delta K_{\text{eff}})^m = A(U \Delta K)^m \quad (7-19)$$

It is expected that a crack growing in plane stress conditions, in which the plastic zone is approximately three times greater than in plane strain, will experience a higher level of closure. That is, the increased plasticity will result in a higher opening and closing stresses. Consequently the effective stress intensity and fatigue crack growth rate will be lower.

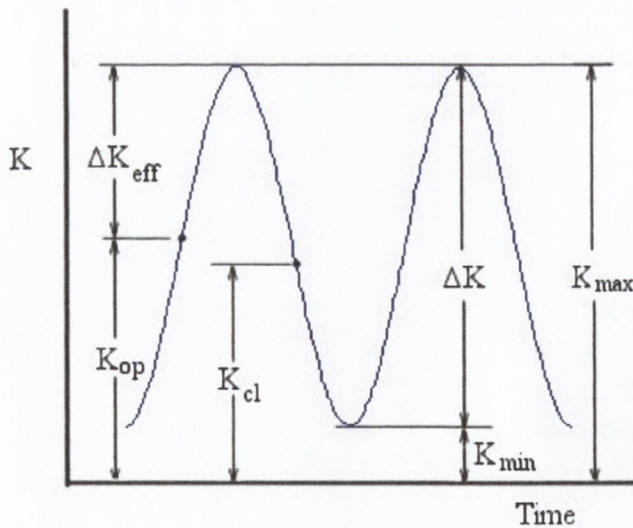


Fig. 7.10 - Schematic representation of opening and effective stress intensity factors

### **7.3 Notch tip constraint**

The foregoing discussion has been limited to the effect of constraint on the behaviour of cracks. However, notches can also be characterised by high or low constraint. For a two-dimensional notched geometry, the size of the plastic zone ahead of the notch will be affected by the thickness of the specimen in a similar manner to that discussed above for cracks. Consequently the degree of constraint will also vary as a function of thickness.

As discussed in the previous chapter, the fatigue limit of sharp, crack-like stress concentrations is characterised by the growth of non-propagating cracks at the root notch. In this case considering crack tip constraint instead of notch tip constraint may be a more relevant approach.

### **7.4 Quantifying the degree of constraint**

Four possible methods to determine the degree of notch tip constraint have been investigated and are presented below.

#### **7.4.1 Using the plastic zone size**

As mentioned above, the usual approach used in fracture to determine if a 2D cracked body experiences conditions of plane stress or plane strain, is to relate the size of the plastic zone ahead of the crack to the thickness of the specimen. The guidelines given in ASTM E 399-74 (see section 7.1.4) to ensure that fracture toughness is measured in plane strain are an example of this. It is generally accepted that if the size of the plastic zone approaches the thickness of the specimen, conditions of pure plane stress are approached. It is believed that this statement is also true for notched components. That is, if the size of the plastic zone ahead of a notch is approximately equal to the thickness of the specimen conditions of plane stress will prevail.



#### 7.4.1.1 The relationship between plastic zone size and $a_o$

In the following a simple relationship between Irwin's equations for the plastic zone,  $2r_p$ , (see section 7.1.1) and the El Haddad short crack parameter,  $a_o$ , is demonstrated. It is known that for most engineering materials the plain specimen fatigue limit is less than the yield stress, or:

$$\Delta\sigma_o < \sigma_{ys} \quad \text{or} \quad \Delta\sigma_o = C\sigma_{ys} \quad (7-20)$$

Where C is a constant, which is less than one (i.e.  $0 > C > 1$ ). Therefore, if a 2-D cracked body is loaded in fatigue at the threshold condition, the monotonic plastic zone can be estimated, using Irwin's equation as:

$$2r_y \cong \frac{1}{\pi} \left( \frac{\Delta K_{th}}{\sigma_{ys}} \right)^2 = a_o \left( \frac{\Delta\sigma_o}{\sigma_{ys}} \right)^2 = C^2 a_o \quad \text{for plane stress} \quad (7-21)$$

$$2r_y \cong \frac{1}{3\pi} \left( \frac{\Delta K_{th}}{\sigma_{ys}} \right)^2 = \frac{a_o}{3} \left( \frac{\Delta\sigma_o}{\sigma_{ys}} \right)^2 = \frac{C^2 a_o}{3} \quad \text{for plane strain} \quad (7-22)$$

Where  $a_o$  is:

$$a_o = \frac{1}{\pi} \left( \frac{\Delta K_{th}}{\Delta\sigma_o} \right)^2 \quad (7-23)$$

It can be seen that, for both stress states, the monotonic plastic zone size,  $2r_y$ , is always smaller than  $a_o$ . Hence, it is proposed that  $a_o$  can be used as a parameter to estimate the degree of constraint, for cracks and crack-like stress concentrations. Specifically, if the thickness of a specimen is the order of  $C^2 a_o$ , then conditions of plane stress will prevail.

#### 7.4.1.2 Testing $\Delta K_{th}$ in plane stress

A consequence of the above is that it is not possible to measure the stress intensity threshold of most engineering materials in plane stress. This is because a two-dimensional cracked specimen with a thickness of approximately  $C^2 a_o$  would be needed. For example, in order to determine  $\Delta K_{th}$  in plane stress for the low carbon steel used in this work ( $a_o \approx 0.2\text{mm}$ ), a 2-D specimen with a thickness of less than 0.2mm would be required. It is clearly not possible to do this type of test. Even if it were possible to obtain specimens thin enough, which still retain their normal material properties, the specimen would be

subjected to out-of-plane tearing (or a  $K_{III}$  failure mode). This explains why the effect of plane stress at threshold conditions is not discussed in the literature.

#### 7.4.1.3 Extension to 3-D stress concentrations

It is proposed that this approach can be extended to a more three-dimensional case by considering the specimen thickness at a small distance ahead of the stress concentration. Consider the longitudinal fillet weld shown in Figure 7.11 below. This is similar to the Fillet-A specimen. The end of the weld bead terminates at the edge of the smaller member and results in failure from that edge. If it is assumed that the stress concentration is *crack-like* then the plastic zone size can be approximated via equations 7-21 and 7-22 described above. It can also be seen from Figure 7.11(c) below, that because the stress concentration occurs at a corner, the effective thickness of the section can be determined as a function of the distance from the corner. For example, if the plastic zone size is estimated to be  $x$  millimetres, then the thickness of the section at a distance of  $x$  millimetres from the corner is  $2x$  millimetres (see Figure 7.11(c)). It can be seen that this relationship is independent of the plastic zone size and depends only on the included angle between the two free edges (i.e.  $90^\circ$  in this case). Furthermore, we know that conditions of plane stress prevail if the thickness of the specimen approaches the plastic zone size.

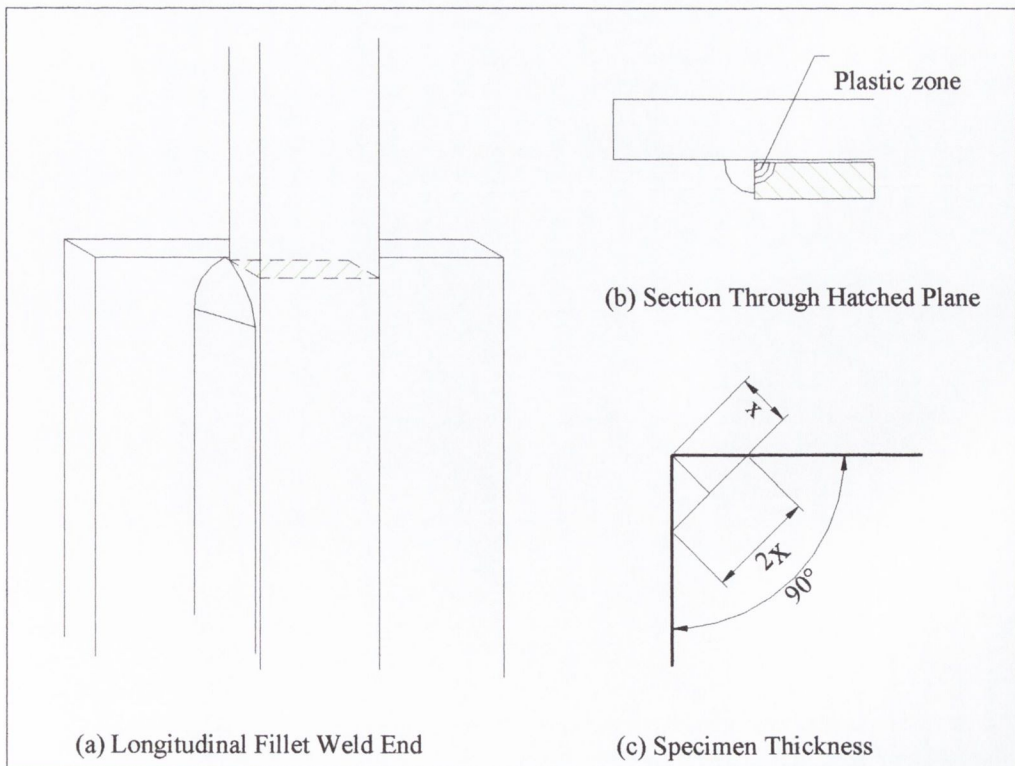


Fig. 7.11 - Failure from the end of a longitudinal fillet weld (Fillet-A)

Hence, the question is, what stress state will prevail if the specimen thickness is twice the size of the plastic zone (at the extent of the plastic zone)? The most likely answer is that stress state will be neither pure plane stress or plane strain.

The argument above can equally be applied to any situation in which failure occurs at a 90° corner. The Model-T specimen is another such case. Therefore, it is proposed that the Fillet-A specimen and the Model-T specimen experience approximately the same degree of notch tip constraint, which is most probably an intermediate stress state that is neither pure plane stress nor pure plane strain.

However, other geometries characterised by a smaller included angle between the free surfaces at the stress concentration feature, will experience conditions of pure plane stress. One such geometry is investigated in section 7.5.2 below. Others can be found, for example, at the intersection of a free surface and a hole, when the axis of the hole is at an acute angle to the free surface. These are often referred to as *knife-edge* stress concentrations.

#### 7.4.1.4 The plastic zone sizes for the various specimens

Elastic-plastic finite element models were built in order to determine the size of the plastic zones at the stress concentration features of the various specimens, discussed in Chapter 5.

The load range applied to the models was the experimentally determined fatigue strengths reported in Chapter 5 at an R-ratio of 0.1. In the case of Model-E and Model-T the measured cyclic stress-strain curve, for the actual material, was used. This is presented in Appendix A. The same curve was used for the Fillet-A specimen, which is in fact correct for the parent metal but is expected to be inaccurate for the weld metal and heat affected zones.

The values of the MPZs and CPZs, measured along the direction of the focus path, are reported in Table 7.1 below.

Table 7.1 - Plastic zone sizes

	MPZ (mm)	CPZ (mm)	$a_0$ (mm)
Model-E	0.74	0.18	0.205
Model-T	0.343	0.0	0.205
Fillet-A	0.46	0.22	0.43

It can be seen that the Model-T specimen has no CPZ, this is believed to be correct as it was checked thoroughly and a similar result was obtained using the Neuber rule (see Appendix B, section B.3.2).

Even though the MPZ for the Model-E specimen is quite large compared to  $a_0$ , the thickness of the specimen at a distance of  $a_0$ , from the hotspot is the full thickness of the specimen. Hence, this specimen is not expected to experience a constraint effect.

It can be seen that the MPZs of the Model-T and Fillet-A specimens are approximately the same as the  $a_0$  value. As discussed above, it is believed that for these specimens experience approximately the same degree of constraint, which is most probably neither pure plane stress nor pure plane strain.

#### 7.4.2 Elastic parameters

In the following, three parameters that depend only on an elastic stress distribution are presented as an alternative means of quantifying the degree of notch tip constraint.

##### 7.4.2.1 The $ps$ parameter

The  $ps$  parameter is a way of quantifying the degree of plane strain or plane stress and consequently the degree of constraint that is present at a stress concentration feature of arbitrary geometry. Figure 7.12 shows two notched bodies. Figure 7.12(a) represents conditions of plane strain. The plane represented by the blue lines (dotted) is the plane of interest. The principal stresses are shown on the plane at the notch tip. In this case the principal stress in the thickness direction is due to the Poisson effect and is equal to  $\sigma_2 = \nu(\sigma_1 + \sigma_3) \neq 0$ , where  $\nu$  is Poisson's ratio. Figure 7.12(b) is a similar diagram that

shows conditions of plane stress. In this case the body is sufficiently thin to relax the stress in the direction perpendicular to the plane, hence  $\sigma_2 = 0$ .

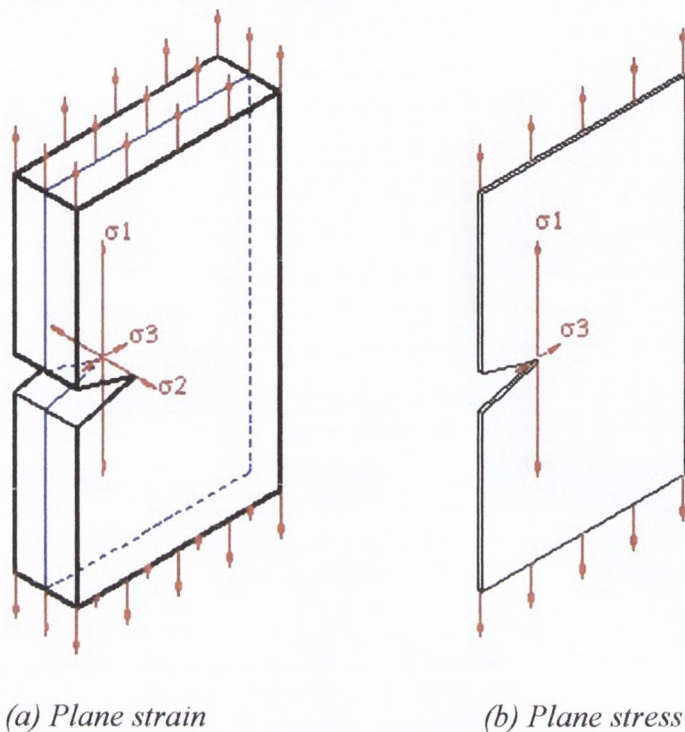


Fig. 7.12 - Plane strain and plane stress conditions for a sharply notched body loaded in uniaxial tension

These stresses are easily found using a finite element analysis. Hence, equation 7-24 can be used to define the degree of plane stress or plane strain for any given geometrical stress concentration.

$$ps = \frac{\Delta\sigma_a}{\nu(\Delta\sigma_b + \Delta\sigma_c)} \tag{7-24}$$

Where:

$\Delta\sigma_a$  - The principal stress range perpendicular to the plane of interest. This is generally the second principal stress,  $\Delta\sigma_2$  as shown in Figure 7.12. For conditions of plane stress  $\Delta\sigma_a = 0$ , in plane strain  $\Delta\sigma_a = \nu(\Delta\sigma_b + \Delta\sigma_c)$

$\Delta\sigma_b$  - The principal stress range in the crack opening direction and in the plane of interest. This is generally the first principal stress,  $\sigma_1$  as shown in Figure 7.12

$\Delta\sigma_c$  - The principal stress in the direction of crack growth. This is generally the third principal stress,  $\sigma_3$  as shown in Figure 7.12

Hence:

$ps = 0$  Implies conditions of pure plane stress, and

$ps = 1$  Implies conditions of pure plane strain.

$ps > 1$  Implies that  $\Delta\sigma_a > \nu(\Delta\sigma_b + \Delta\sigma_c)$ . This may occur if there is an external force applied in the out-of-plane direction.

$ps < 0$  Implies that there is a negative stress in the out-of-plane direction.

#### 7.4.2.2 Elastic strain energy parameter, $C_E$

In the elastic range of a typical engineering material, the elastic strain energy can be divided into two components; strain energy that results in distortion (or distortion energy), and strain energy that does not, (the result of hydrostatic stress). It is generally accepted that for a ductile material, distortion energy results in shear yielding whereas a very large amount of hydrostatic stress can be withstood without plastic deformation. This is the basis of the Von Mises yield criteria. The following is the mathematical realisation of this:

For a given stress state the total strain energy is defined as (in terms of the three principal stresses):

$$U_{tot} = \frac{1}{2E} [\sigma_1^2 + \sigma_2^2 + \sigma_3^2 - 2\nu(\sigma_1\sigma_2 + \sigma_2\sigma_3 + \sigma_1\sigma_3)] \quad (7-25)$$

In order to eliminate the contribution of the hydrostatic stress, an average stress is defined:

$$\sigma_{av} = \frac{\sigma_1 + \sigma_2 + \sigma_3}{3} \quad (7-26)$$

The strain energy due to the average stress is then calculated:

$$U_{\sigma(av)} = \frac{1-2\nu}{6E} [\sigma_1^2 + \sigma_2^2 + \sigma_3^2 + 2(\sigma_1\sigma_2 + \sigma_2\sigma_3 + \sigma_1\sigma_3)] \quad (7-27)$$

Hence the distortion energy is given by:

$$U_d = U_{tot} - U_{\sigma(av)} = \frac{1+\nu}{3E} [\sigma_1^2 + \sigma_2^2 + \sigma_3^2 - (\sigma_1\sigma_2 + \sigma_2\sigma_3 + \sigma_1\sigma_3)] \quad (7-28)$$

It is possible to think of the energy due to the average stress,  $U_{\sigma(av)}$ , as constraint energy. Hence, the total elastic strain energy is the sum of distortion energy and constraint energy. Given this, it is possible to define a parameter to measure constraint as follows:

$$C_E = \frac{U_{\sigma(av)}}{U_{tot}} \quad \text{or} \quad \frac{\Delta U_{\sigma(av)}}{\Delta U_{tot}} \quad (7-29)$$

Using this parameter,  $C_E$ , it is then possible to quantify the degree of constraint for all possible stress states, such that:

- $C_E = 0$      The average stress is zero, consequently  $U_{\sigma(av)} = 0$ . This implies there is no constraint energy.
- $C_E = 1$      This implies  $\sigma_1 = \sigma_2 = \sigma_3$  or pure hydrostatic stress. There is complete constraint.
- $C_E < 0$      Not possible
- $C_E > 1$      Not possible.

#### 7.4.2.3 Von Mises stress parameter, $C_{VM}$

This parameter is very similar to the  $C_E$  parameter but is less intuitive; while at the same time is slightly easier to apply. The parameter is essentially the ratio of Von Mises equivalent stress to the first principal stress and is defined as:

$$C_{VM} = \frac{\Delta\sigma_1 - \Delta\sigma_{VM}}{\Delta\sigma_1} \quad (7-30)$$

It indicates the degree of constraint in terms of Von Mises equivalent stress, (Von Mises stress gives an indication of distortion energy and hence the opposite of constraint).

- $C_{VM} = 0$      Then  $\sigma_{VM} = \sigma_1$ . This implies  $\sigma_2 = \sigma_3 = 0$  or uniaxial tension.
- $C_{VM} = 1$      Then  $\sigma_{VM} = 0$ . This implies  $\sigma_1 = \sigma_2 = \sigma_3$  or hydrostatic stress. There is complete constraint.
- $C_{VM} < 0$      Then  $\sigma_{VM} > \sigma_1$ .

$C_{VM} > 1$  Then  $\sigma_{VM} < \sigma_1$ . This occurs when  $\sigma_1 < 0$  and implies a completely compressive stress state.

### 7.4.3 Application of the elastic parameters

#### 7.4.3.1 Welded geometries

Figures 7.13 to 7.15 below show the application of the three elastic constraint parameters to the following welded geometries:

- Fillet-A (see section 5.1)
- T-shape-A (see section 4.2)
- T-shape-B (see section 4.3)

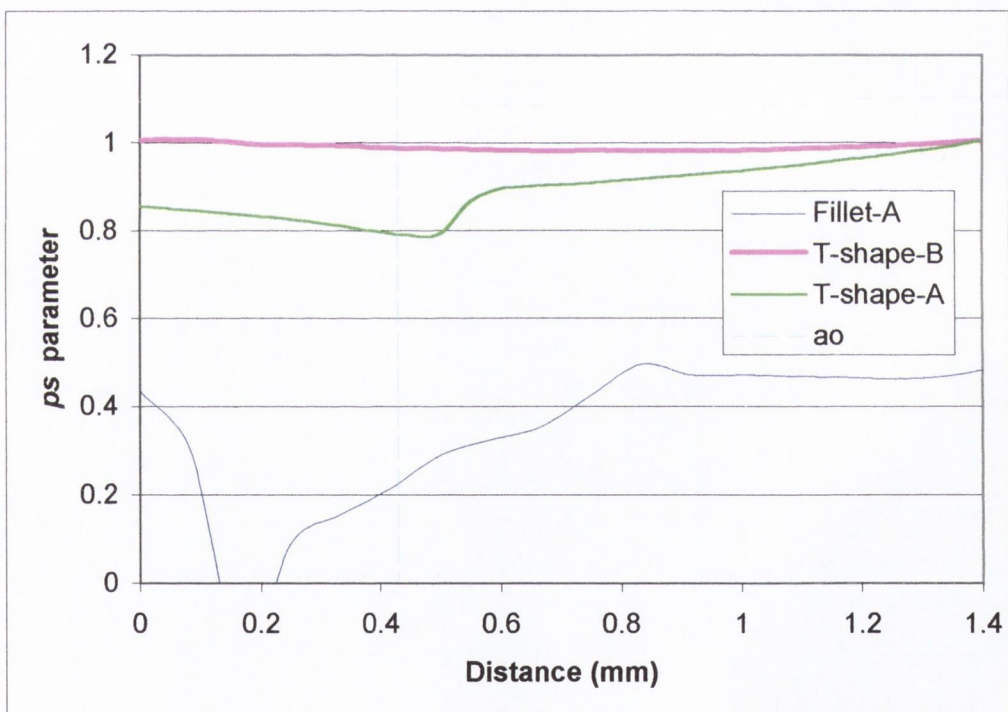


Fig. 7.13 - Application of the  $ps$  parameter to the welded geometries

It can be seen from Figure 7.13 above that the  $ps$  value at the hotspot and also at the distance  $a_0$  along the path is lowest for the Fillet-A specimen and greatest for the T-shape-B specimen.



Unfortunately this parameter is quite sensitive to the direction of the focus path. That is, considerable variations are observed if the direction of the focus path is slightly altered. This was especially a problem for the Fillet-A specimen, which is a very three-dimensional stress concentration. It is also very sensitive to the way in which the end of the weld-bead was modelled for the Fillet-A specimen (ie. as a spherical, triangular or square end, see Appendix A, section A.2.4.3).

Another problem with the  $ps$  parameter is caused by the way finite element programs define principal stresses. That is, the principal stresses are defined using magnitude, not direction. Hence, even in a simple 2-D analysis it is possible for the directions of the principal stress to change along a given path. This makes calculation of the  $ps$  parameter very difficult, especially for complex geometries.

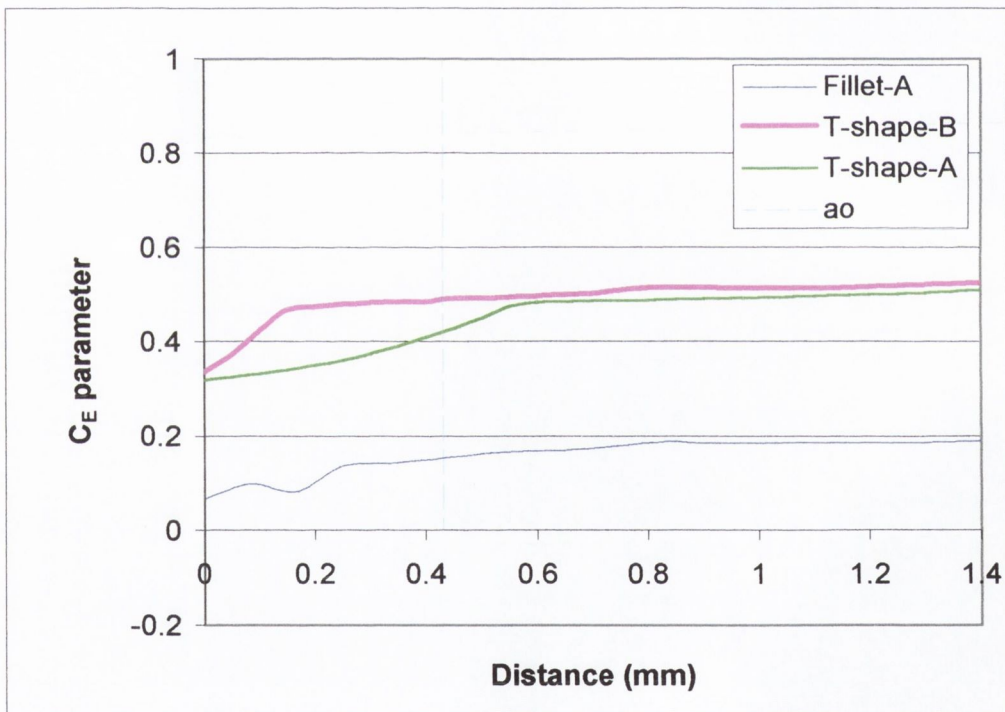


Fig. 7.14 - Application of the  $C_E$  parameter to the welded geometries

Figure 7.14 above shows the application of the  $C_E$  parameter to the three welded geometries. It can be seen that the  $C_E$  parameter shows a similar trend to that exhibited by the  $ps$  parameter. That is, the Fillet-A specimen is less constrained than the T-shaped specimens.

The  $C_E$  parameter takes the whole elastic stress field into account, without regard to the relationship between crack orientation and the stress directions. It therefore represents the total range of possible stress states. The  $ps$  parameter forms a subset within this more general parameter. To make matters more complicated, the position of the  $ps$  subset within  $C_E$  changes depending on the type of geometry being considered. Specifically, this means that a cracked fatigue specimen in plane strain ( $ps = 1$ ) will have higher  $C_E$  values than a plane strain specimen containing a blunt notch. This makes  $C_E$  only really useful as a comparison between similar specimens.

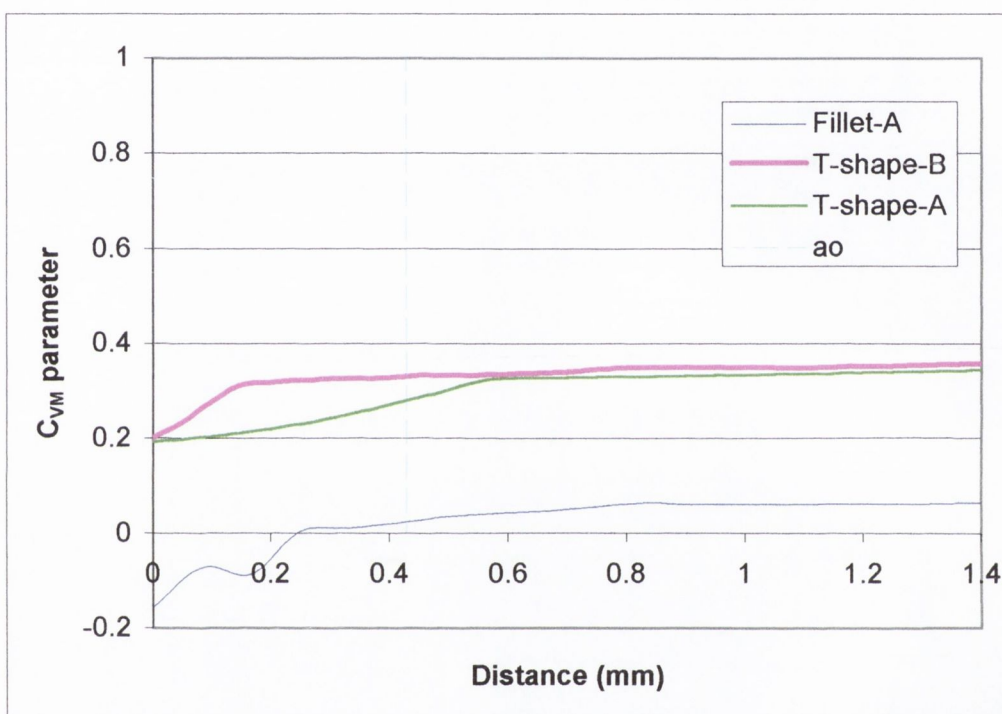


Fig. 7.15 - Application of the  $C_{VM}$  parameter to the welded geometries

Figure 7.15 above shows the application of the  $C_{VM}$  parameter to the three welded geometries. It can be seen that the  $C_{VM}$  parameter shows a very similar trend to that exhibited by the  $ps$  and  $C_E$  parameters. That is, the Fillet-A specimen is less constrained than the T-shaped specimens.

#### 7.4.3.2 Model-E

Table 7.2 summarises the application of the constraint parameters to the Model-E geometry for both FE models (ie. with and without the root radius). It is seen that for the model without the root radius the value for the  $ps$  parameter is very high at both the

hotspot and at  $a_0$ . However the model that includes the root radius shows less constraint especially at the hotspot. This is because the presence of the root radius creates a very thin section directly at the hotspot that relaxes the out-of-plane stress and reduces the constraint. Nevertheless, at a distance of  $a_0$ , the constraint values are similar to the model that doesn't include the root radius.

Table 7.2 - Application of the elastic constraint to Model-E

Model-E	$P_s$	$C_E$	$C_{VM}$
<b>Without root radius</b>			
At hotspot	0.77	0.426	0.285
At $a_0$	1.39	0.555	0.365
<b>With root radius</b>			
At hotspot	0.021	0.136	0.004
At $a_0$	0.809	0.459	0.310

From the above it was concluded that the constraint effect should not be a factor in the fatigue analysis of Model-E.

#### 7.4.3.3 Model-T

Figure 7.16 below shows the application of the elastic constraint parameter to the Model-T specimen (see section 5.3.3). It can be seen that all of the parameters are relatively low.

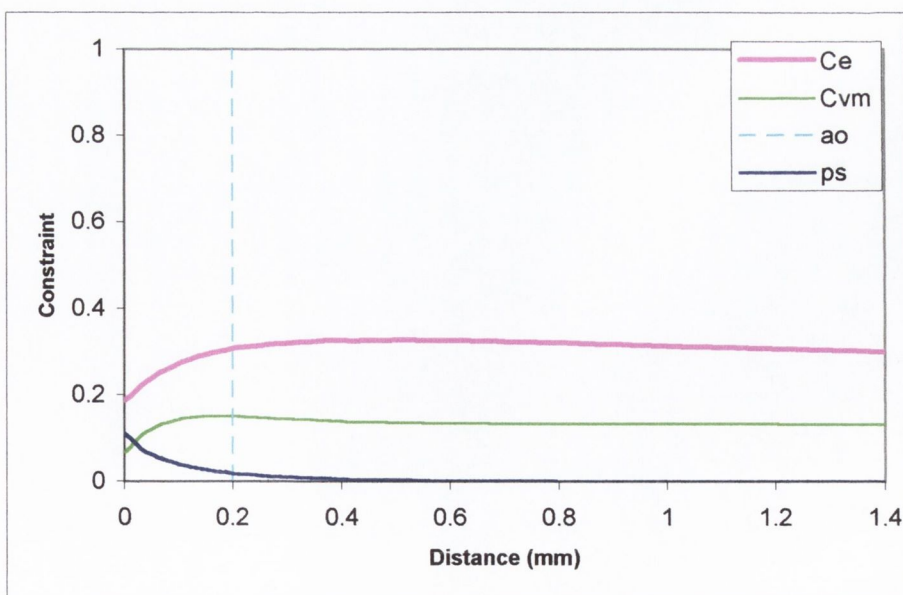


Fig. 7.16 - Application of the elastic constraint parameter to the Model-T specimen

#### 7.4.3.4 Discussion

In general it is considered that the elastic constraint parameters discussed above can give a reasonably good indication of the degree of constraint at a given stress concentration. However each method contains problems and limitations, discussed above, which must be taken into consideration. Also, the fact that these parameters are calculated using only the stress determined along the focus path, is quite limiting. For example, in the case of the Model-T specimen the focus path is chosen to be along the top surface of the specimen (or very close to this, see Appendix A, section A.4.4.1). It is clear that for this path, the degree of constraint will be low, because it is not possible to have a stress at a free surface. It is therefore suggested that the approach discussed above, which is based on the plastic zone size is more useful and reliable.

### **7.5 Experimental investigations of the constraint effect**

Two separate experimental investigations of constraint were undertaken. These are discussed below.

#### 7.5.1 Determining $\Delta K_{th}$ in both plane stress and plane strain

In order to determine, conclusively, if there is any difference in the fatigue stress intensity threshold measured in plane strain and plane stress, a material with a large  $a_0$  value was tested, in which it is possible to obtain a two-dimensional plane stress specimen.

##### 7.5.1.1 The specimens and material properties

Figure 7.17 below shows the two-dimensional, sharply edge-notched, tension specimens that were tested in two different thicknesses (0.5mm and 6mm), to represent plane stress and plane strain conditions. The specimens were 200mm x 50mm with a nominal notch depth of 15mm and an average notch root radius of 0.035mm.

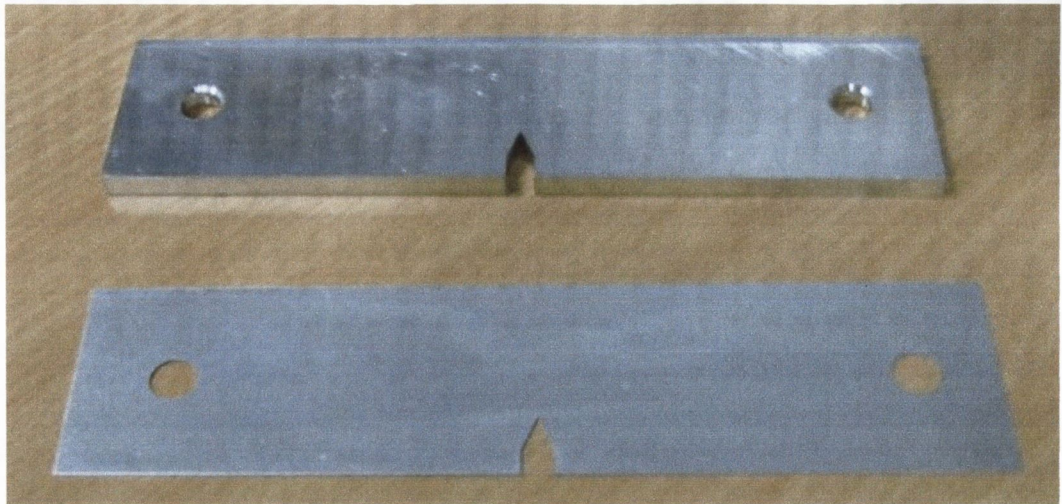


Fig. 7.17 - Sharply notched aluminium specimens; two thicknesses (0.5mm and 6mm)

The material was wrought aluminium specified by BS 1470:1987 [BSI, 1987] as 1050A with a H14 temper. This is 99.5% pure aluminium with mechanical properties as per Table 7.3 below.

Table 7.3 - Mechanical properties of Aluminium 1050A H14

Tensile strength		Elongation on 50 mm				
		Materials thicker than				
Min. (MPa)	Max. (MPa)	0.5mm min. (%)	0.8mm min. (%)	1.3mm min. (%)	2.6mm min. (%)	3.0mm min. (%)
100	135	4	5	6	6	8

Hardness tests were conducted on specimens of the material, taken from both thicknesses, to ensure there were not significant deviations in the mechanical properties. The results are shown in Table 7.4 below. It can be seen that there is almost no difference in hardness. It is therefore assumed that the other mechanical properties will also be the same.

Table 7.4 - Micro-hardness measurements

	Vickers Hardness					Average
0.5mm thickness	44.0	42.8	42.2	43.9	42.3	43.0
6.0mm thickness	44.9	43.6	43.9	39.9	44.8	43.4

### 7.5.1.2 Fatigue tests and results

The specimens were cyclically loaded via an Instron servo-hydraulic testing machine at an R-ratio of 0.1. The clamping arrangement was such that rotation of the specimen ends was constrained.

The initial intention was to determine the stress-life curves for both thicknesses and hence determine the threshold stress intensity ranges by assuming that the behaviour of a sharp notch is crack-like. However, the final crack length obtained for each specimen tested was not constant. This was because visual inspection was the only way in which crack length and hence failure of the specimen could be determined. A reduction of stiffness technique was not viable because the testing machine was not sensitive enough to detect the change in displacement necessary for the method to be reliable. Hence, it was decided that crack growth data could also be measured, from which crack growth rate curves could be obtained and used to correct the crack lengths to a common value. This also allowed determination of the threshold stress intensity ranges via crack growth rate curves.

Crack length data was measured by interrupting the test and using replica tape to take a copy of the specimen surface. The replica was subsequently examined under an optical microscope and the crack length was measured. Using this technique cracks as small as 0.05mm could be observed and measured.

#### 7.5.1.2.1 Measured S-N curves

The results, including the measured crack lengths are reported in Table 7.5 and Table 7.6 below. The S-N curves obtained are shown in Figures 7.18 to 7.20 below.

Table 7.5 - Experimental results 6 mm specimens

Specimen Number	Applied Stress Range [MPa]	Initial Stress Intensity Range [MPa m <sup>1/2</sup> ]	Number of Cycles	Measured Crack Length [mm]
1	No Result			
2	50.983	14.323	1.038E+04	total
3	28.507	7.989	1.507E+05	total
4	27.300	7.683	4.043E+04	1.6
5	18.153	5.079	2.417E+05	1.9
6	12.205	3.350	4.085E+05	1.8
7	21.273	5.955	4.011E+04	1.3
8	9.103	2.563	8.309E+05	1.5
9	7.605	2.133	1.816E+06	2.75
10	6.052	1.687	1.555E+06	0.478
11	21.894	6.031	1.253E+05	0.679
12	5.471	1.530	1.700E+06	0 (run out)

Table 7.6 - Experimental results 0.5 mm specimens

Specimen Number	Applied Stress Range [MPa]	Initial Stress Intensity Range [MPa m <sup>1/2</sup> ]	Number of Cycles	Measured Crack Length [mm]
1	48.776	13.459	5.243E+03	Total
2	26.557	7.365	4.885E+04	Total
3	24.669	6.762	3.709E+04	3.5
4	17.570	4.789	1.552E+05	3.4
5	21.145	5.774	2.679E+04	2
6	11.747	3.223	1.416E+06	5.9
6(a)	9.142	2.496	2.159E+06	0 (run out)
7	15.201	4.149	3.385E+05	2.3
8	21.092	5.724	3.503E+04	2.535
9	9.855	2.683	1.030E+06	0.795
10	9.204	2.502	1.600E+06	0 (run out)
11	16.242	4.407	1.895E+05	2.061
12	9.575	2.614	1.157E+06	1.953

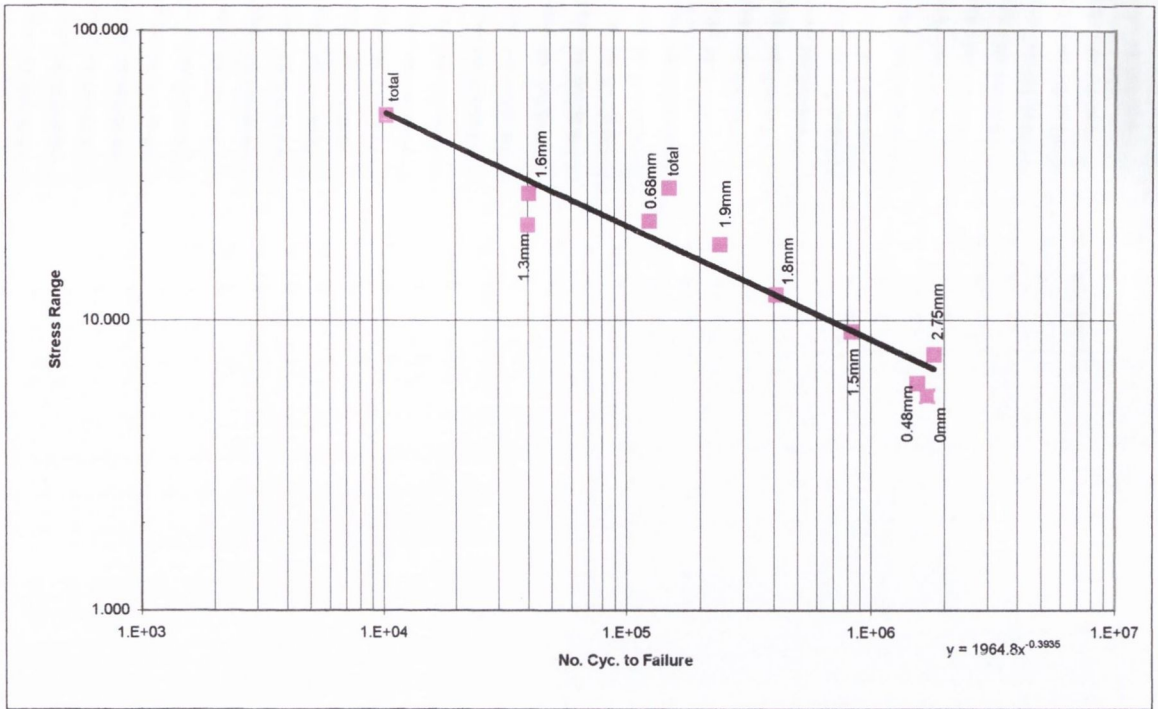


Fig. 7.18 - Measured S-N curves for the 6mm specimens

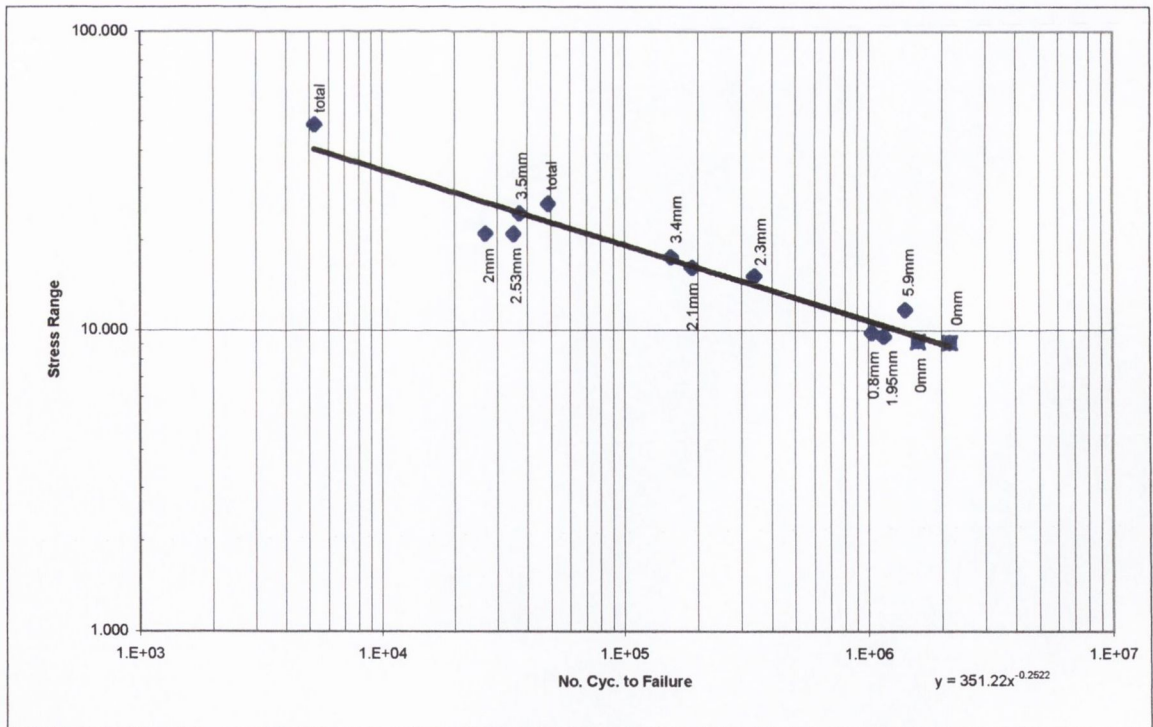


Fig. 7.19 - Measured S-N curve for the 0.5mm specimens



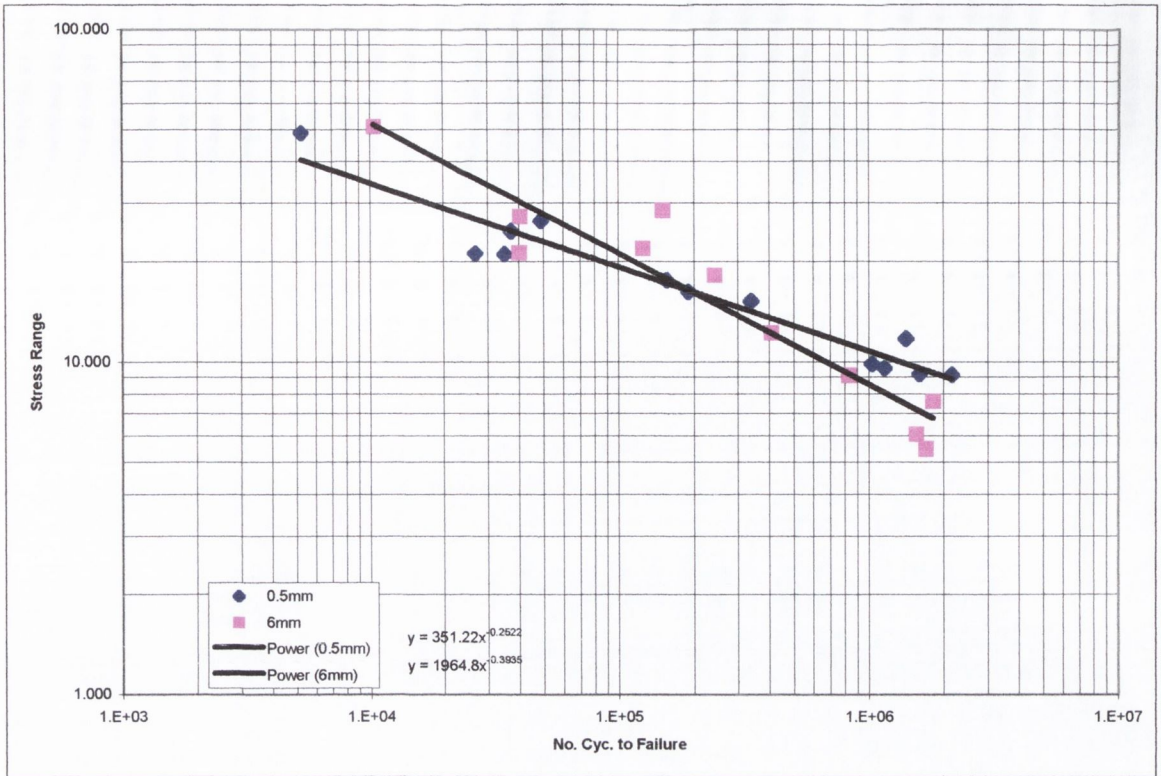


Fig. 7.20 - Both measured S-N curves

From the above, the fatigue strength of these specimens is predicted by drawing regression lines with the standard equation, through the data using least-squares fitting. The fatigue strengths are found to be:

9.04 MPa at  $2 \times 10^6$  cycles for the 0.5mm specimens

6.51 MPa at  $2 \times 10^6$  cycles for the 6mm specimens

#### 7.5.1.2.2 Failure surfaces

The failure surfaces for the two different specimens were observed to be very different. The cracked surface of the thicker, 6mm specimens, were typically flat and perpendicular the direction of the applied load with slightly bowed crack fronts. However, the cracked surfaces in the thin specimens were orientated at 45 degrees to the direction of the applied load.

### 7.5.1.2.3 Crack growth rate data

In order to determine the crack growth rate curves, crack length as a function of the number of cycles was measured for many specimens. Hence, data was obtained at various applied stress levels and crack lengths and therefore at various stress intensity ranges. An example of the data, for Specimen 8 with 0.5mm thickness, is shown in Table 7.7 below.

Table 7.7 - An example of crack growth data for specimen 8 with 0.5mm thickness

Number of Cycles	Crack Length [mm]	Stress Range [MPa]	Shape Factor	Stress Intensity [MPa m <sup>1/2</sup> ]	da/dN [mm/cyc]
1500	0	21.092	1.265	5.711	
10074	0.43	21.092	1.271	5.822	5.015E-05
15015	0.661	21.092	1.274	5.882	4.675E-05
18026	0.884	21.092	1.277	5.939	7.406E-05
21016	1.052	21.092	1.280	5.983	5.619E-05
24029	1.441	21.092	1.285	6.084	1.291E-04
27265	1.609	21.092	1.288	6.128	5.192E-05
32024	2.184	21.092	1.297	6.278	1.208E-04

The shape factor or configuration factor,  $F$ , used to determine the stress intensity factor above, is taken to be [Pickard, 1986]:

$$F = \frac{5}{\sqrt{20 - 13\left(\frac{D+a}{W}\right) - 7\left(\frac{D+a}{W}\right)^2}} \quad (7-31)$$

Where  $D$  is the notch depth,  $a$ , is the crack length and  $W$  is the width of the specimen.

The crack growth rate,  $da/dN$ , was then calculated, via equation 7-32, at each stress intensity level and these points were plotted against  $\Delta K$  on crack growth curves (see Figures 7.21 and 7.22).

$$\frac{da}{dN} \approx \frac{a_i - a_{i-1}}{N_i - N_{i-1}} \quad (7-32)$$

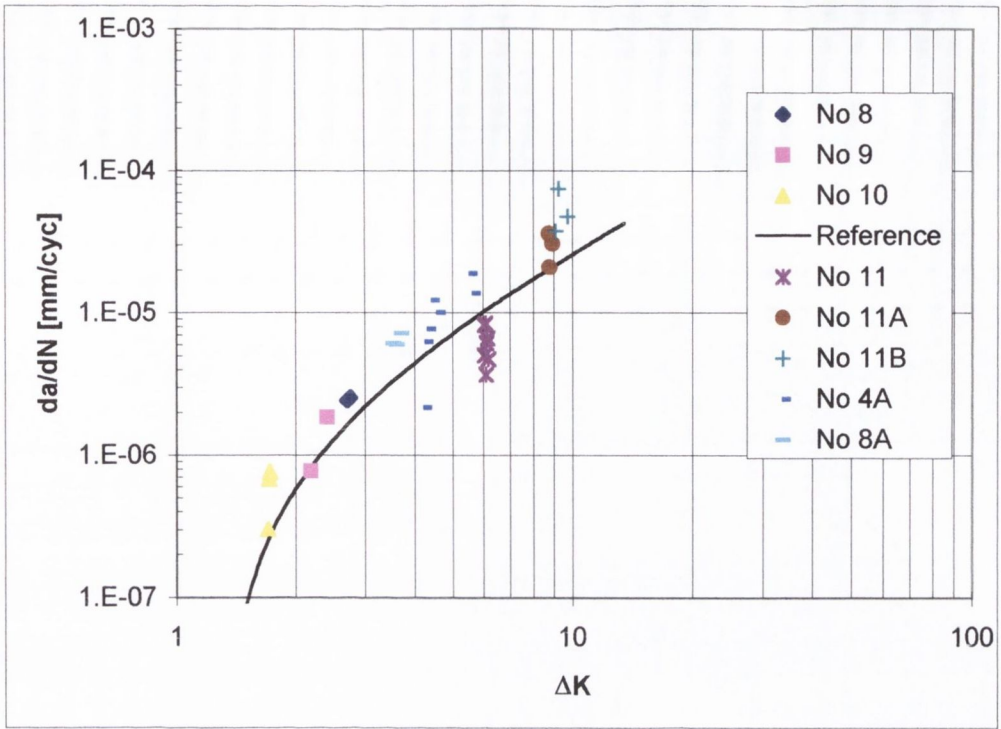


Fig. 7.21 - Crack growth rate curve for the 6mm specimens

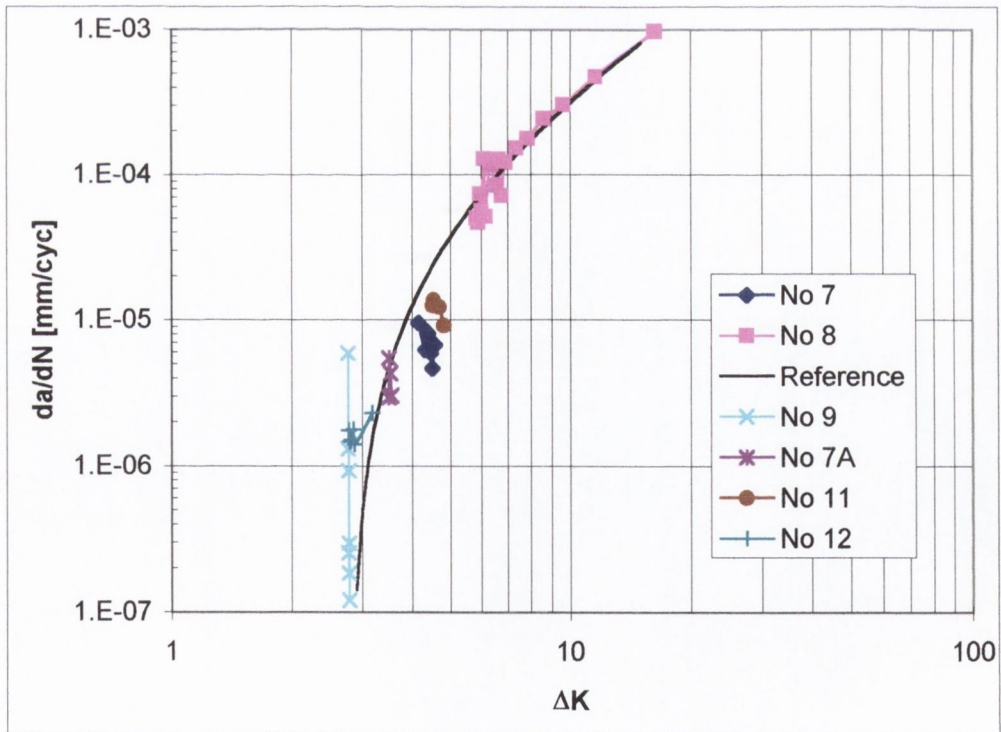


Fig. 7.22 - Crack growth rate curve for the 0.5mm specimens

In addition to the experimental data plotted in Figures 7.21 and 7.22 there is a *reference curve* on each figure. This is a line that is governed by equation 7-33 below.

$$\frac{da}{dN} = A(\Delta K - \Delta K_{th})^m \quad (7-33)$$

Where:

- A Is the crack growth rate constant
- m Is the crack growth rate exponent, and
- $\Delta K_{th}$  Is the threshold stress intensity range, for a long crack

For both thicknesses, the values of A, m, and  $\Delta K_{th}$  have been manually adjusted to obtain a reasonably fit with the experimental data. The values chosen are reported in Table 7.8 below. The reference curves are plotted together in Figure 7.23.

Table 7.8 - Reference curve constants

	A [mm/(cyc. MPa <sup>m</sup> )]	$\Delta K_{th}$ [MPa m <sup>1/2</sup> ]	m
<b>6mm Thickness</b>	1e-6	1.3	1.5
<b>0.5mm Thickness</b>	9e-6	2.8	1.8

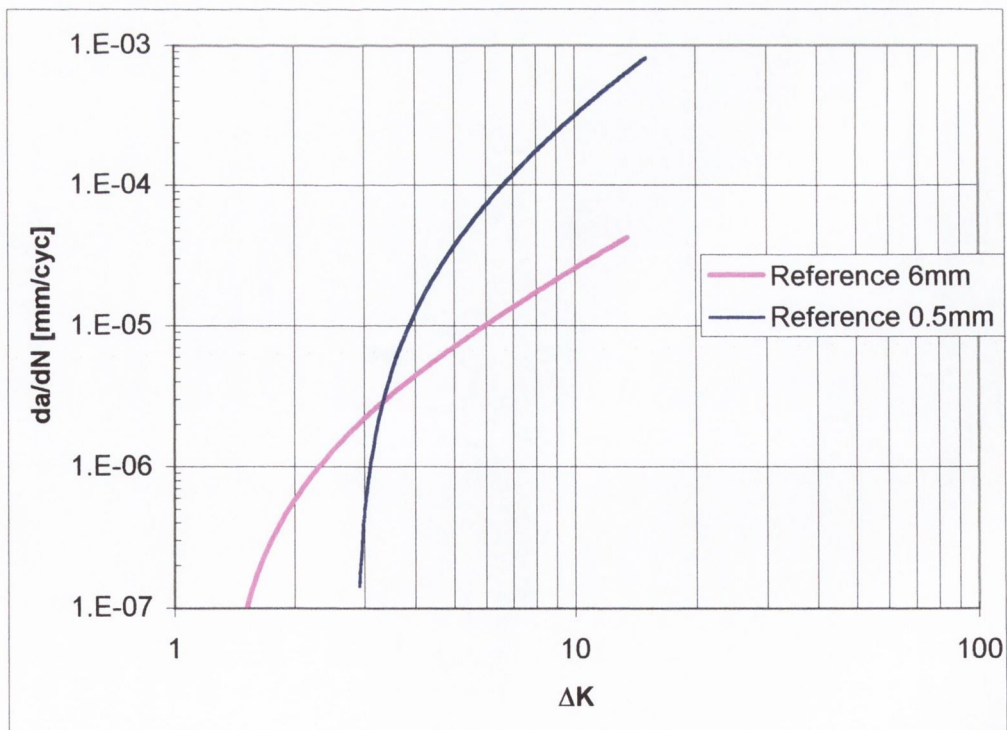


Fig. 7.23 - Comparison of crack growth rate curve

Figure 7.23 clearly demonstrates the difference between the two specimen thicknesses. It can be seen that for low crack growth rates, the curve for the 0.5mm specimens is below the curve for the 6mm specimens. Consequently the 0.5mm specimens have a higher threshold value. However, at approximately  $5.8 \times 10^{-5}$  mm/cycle the curves cross each other. This means that in the Paris or linear region, the thinner specimens have a higher crack growth rate.

As discussed in section 7.2.2, a probable explanation for this behaviour relates to the danger of out-of-plane loadings in thin specimens. That is, small deviations from in-plane loading can cause Mode-III stress intensities which tend to increase the crack growth rate. The fact that the failure surface in the thin specimens was observed to be a  $45^\circ$  to the direction of the applied load supports this. It is therefore suspected that this effect is being observed in the thin specimen and that it is more pronounced at higher stress intensities where the loads are higher. Hence, the near threshold shown in Figure 7.23 is believed to be correct.

#### 7.5.1.3 Life Corrected to a crack length of 0.8mm

These reference curves, discussed above, have then been used below to correct the life of the specimens, measured at various crack lengths, to a common crack length value. In order to do this, a small visual basic program was written which essentially performs a numerical integration of equation 7-33 above. The resistance curve concept whereby the threshold stress intensity range decreases from the usual long crack value, when the crack is short, was also included. The El Haddad approach, discussed in Chapter 6, section 6.1, is used.

For this analysis, a plain specimen fatigue limit,  $\Delta\sigma_0$ , of 50 MPa is assumed. This value is an estimate based solely on the specified UTS of the material. The resulting  $a_0$  values are 0.998mm for the 0.5mm specimens and 0.215mm for the 6mm specimens.

The results of this correction are tabulated in Tables 7.9 and 7.10 below, whereby the life of each specimen is estimated at a crack length of 0.8mm.

Table 7.9 - Life correction to a crack length of 0.8mm for the 6mm specimens

Specimen Number	Applied Stress Range [MPa]	Measured Data		No. of Cycles for 0.8mm Crack Length	
		No. Cycles	Crack Length [mm]	Without R-curve	With R-curve
1	No result				
2	50.983	1.038E+04	total	-2.195E+05	-2.189E+05
3	28.507	1.507E+05	total	-4.501E+05	-4.468E+05
4	27.300	4.043E+04	1.6	-6.370E+03	-5.270E+03
5	18.153	2.417E+05	1.9	1.047E+05	1.096E+05
6	12.205	4.085E+05	1.8	1.146E+05	1.332E+05
7	21.273	4.011E+04	1.3	-6.785E+03	-5.125E+03
8	9.103	8.309E+05	1.5	3.798E+05	4.301E+05
9	7.605	1.816E+06	2.75	-2.517E+05	-1.170E+04
10	6.052	1.555E+06	0.478	2.749E+06	2.256E+06
11	21.894	1.253E+05	0.679	1.364E+05	1.359E+05
12	5.471	1.700E+06	0	1.700E+06	1.700E+06

Table 7.10 - Life correction to a crack length of 0.8mm for the 0.5mm specimens

Specimen Number	Applied Stress Range [MPa]	Measured Data		No. of Cycles for 0.8mm Crack Length	
		No. Cycles	Crack Length [mm]	Without R-curve	With R-curve
1	48.776	5.243E+03	total	-8.527E+03	-8.077E+03
2	26.557	4.885E+04	total	-6.974E+03	-2.874E+03
3	24.669	3.709E+04	3.5	1.820E+04	2.161E+04
4	17.570	1.552E+05	3.4	9.933E+04	1.162E+05
5	21.145	2.679E+04	2	1.203E+04	1.619E+04
6	11.747	1.416E+06	5.9	6.699E+05	1.077E+06
6(a)	9.142	2.159E+06	0	2.159E+06	2.159E+06
7	15.201	3.385E+05	2.3	2.730E+05	3.020E+05
8	21.092	3.503E+04	2.535	1.426E+04	1.962E+04
9	9.855	1.030E+06	0.795	1.030E+06	1.030E+06
10	9.204	1.600E+06	0	1.600E+06	1.600E+06
11	16.242	1.895E+05	2.061	1.479E+05	1.650E+05
12	9.575	1.157E+06	1.953	1.157E+06	1.063E+06

The resulting S-N curves are shown in Figures 7.24 to 7.26 below. Note that only positive values are plotted on the graphs.

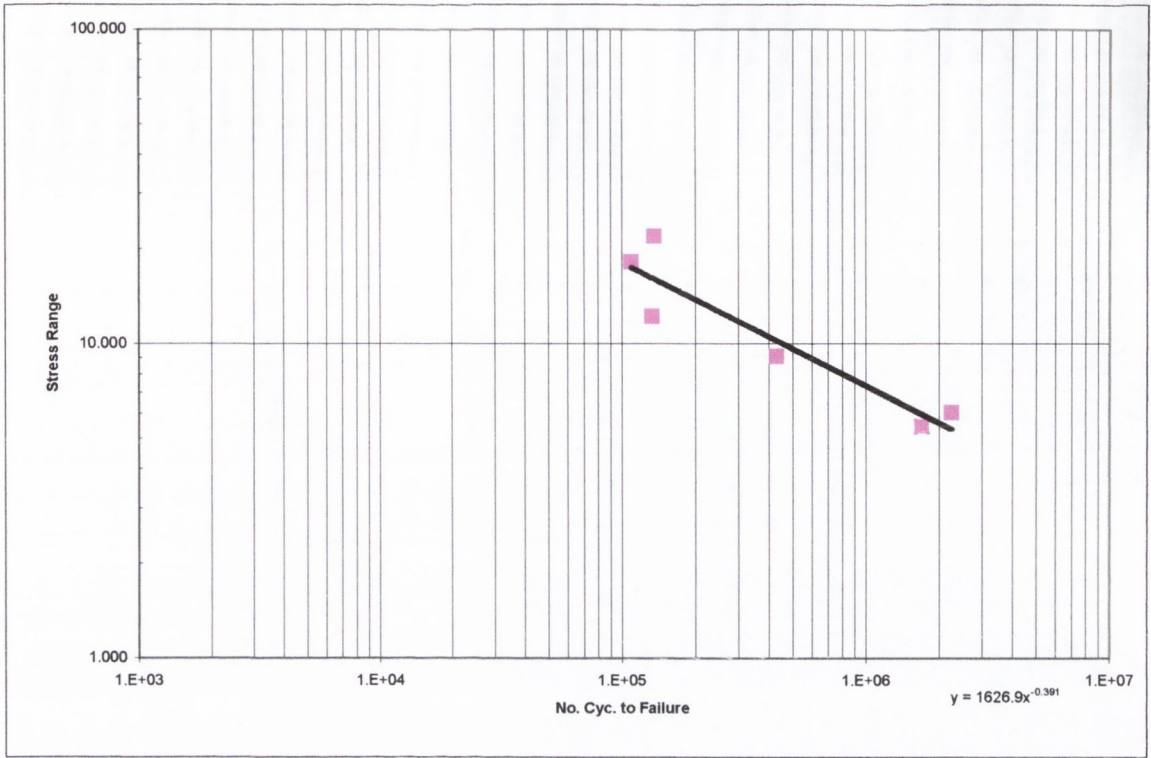


Fig. 7.24 - Modified S-N curve for the 6mm specimens

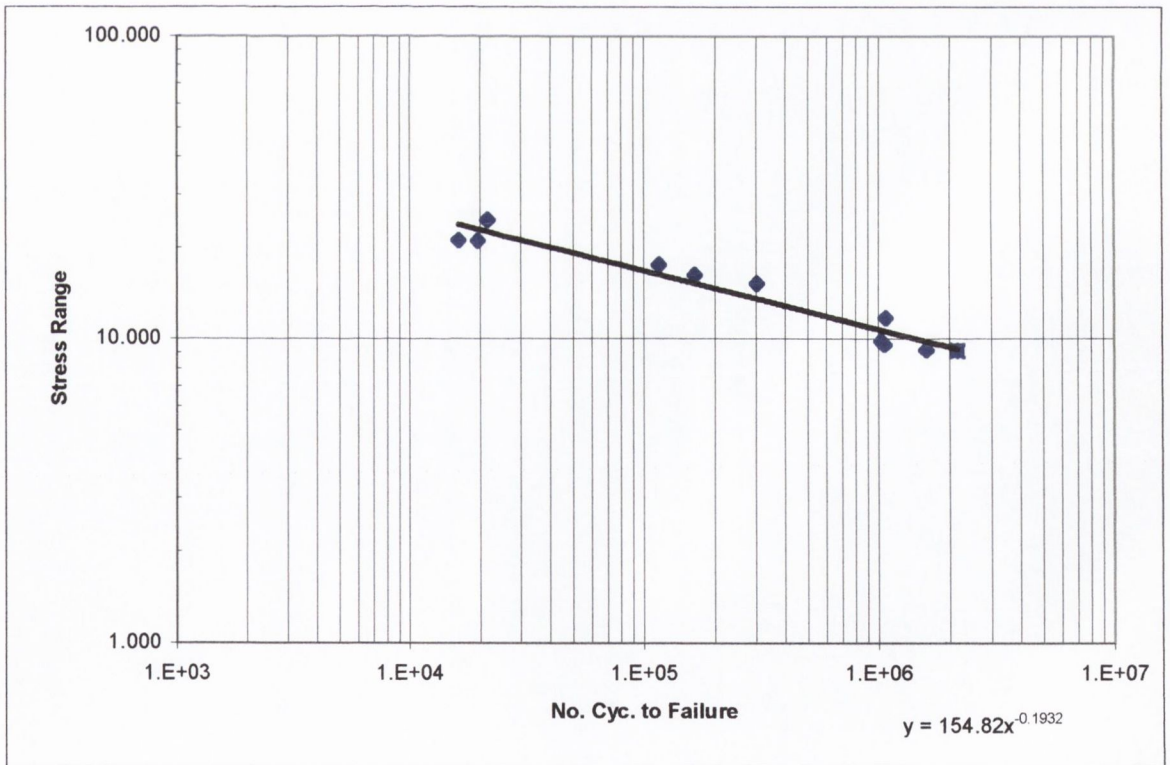


Fig. 7.25 - Modified S-N curve for the 0.5mm specimens

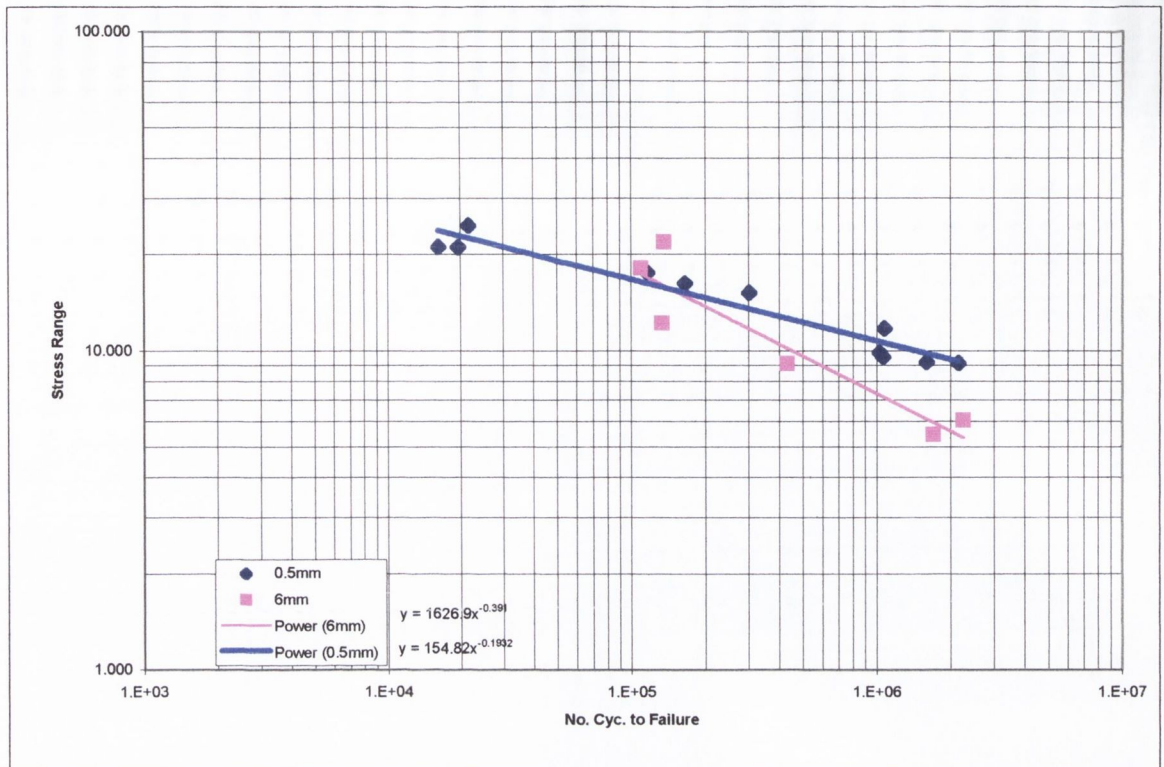


Fig. 7.26 - Both modified S-N curves

From these S-N curves the fatigue strength of these specimens is predicted to be:

9.39 MPa at  $2 \times 10^6$  cycles for the 0.5mm specimens

5.59 MPa at  $2 \times 10^6$  cycles for the 6mm specimens

It should be noted that the number of cycles for a crack to grow 0.8mm is calculated to be negative for several specimens (see Tables 7.9 and 7.10 above). This is a physical impossibility that suggests the calculation method is not very accurate. This is especially a problem for the 6mm specimens as 5 out of the 11 test points are invalid because they have a negative number of cycles to failure.

Regardless, the Modified S-N curves show a bigger difference between the two thicknesses than the Measured S-N curves.

#### 7.5.1.4 A check of the degree of constraint

In order to check that conditions of plane stress and plane strain were actually achieved in the specimens, two elastic-plastic finite element analyses were undertaken. These were



two-dimensional models of the actual notched geometries; one model was in pure plane stress and the other in pure plane strain.

The stress-strain curve of the material was modelled as being bi-linear, where the yield strength was assumed to be 70MPa and the ultimate tensile strength was taken to be 100MPa (as per the minimum published value). The load applied on each of the models was the experimentally determined fatigue load reported above (using the modified S-N curves) that is, 9.39 MPa for the 0.5mm specimens and 5.59 MPa for the 6mm specimens.

The size of the monotonic plastic zone (MPZ) and cyclic plastic zone (CPZ) for each case was determined as per Table 7.11 below. Note that these are the sizes of the plastic zones measured along the notch bisector (or the zero degree line).

*Table 7.11 - Plastic zone sizes*

	MPZ size (mm)	CPZ size (mm)	MPZ / CPZ
Pure plane stress	0.361	0.051	7.08
Pure plane strain	0.057	0.011	5.18

It can be seen that the MPZ for the case of pure plane strain is very small compared to the thickness of the actual specimens (6mm). Therefore it is expected that plane strain conditions are predominate in these specimens. On the other hand the MPZ for the plane stress specimen is approaching the same size as the thickness of the actual plane stress specimen (0.5mm). Hence, this specimen should experience conditions of plane stress.

#### 7.5.1.5 Conclusion

The most important conclusion that can be made from this experimental investigation is that the stress intensity threshold measured in plane stress is higher than that measured in conditions of plane strain. For the material investigated here, the plane stress threshold was measured to be approximately 1.68 time higher than plane strain value, using the S-N curves. When considering the crack growth rate curves this factor was determined to be 2.15.

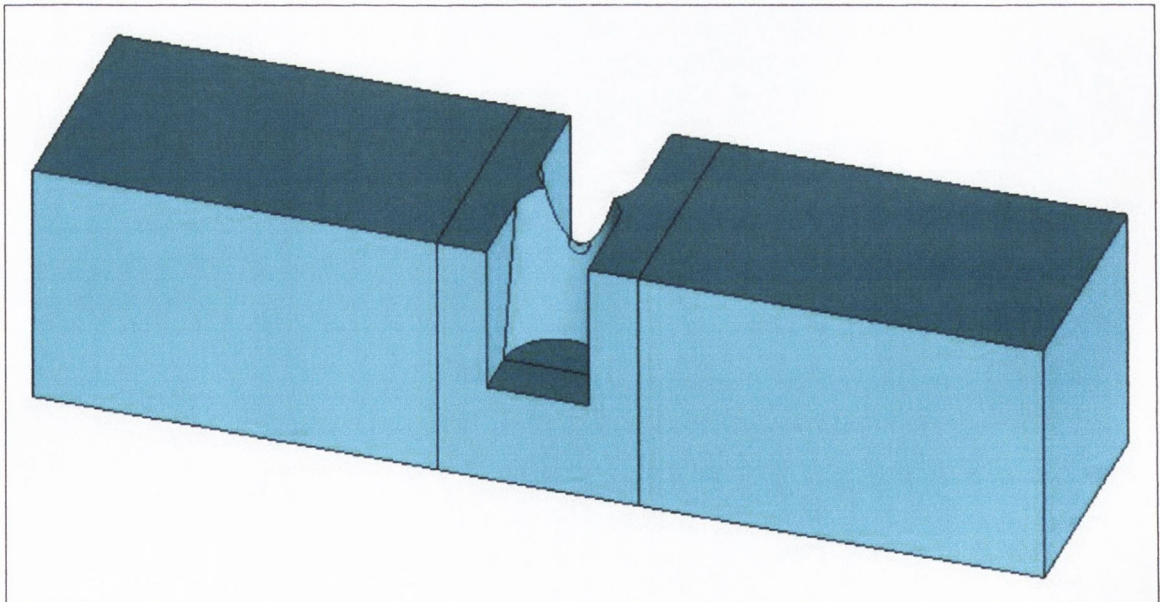
## 7.5.2 A notched component in plane stress (Model-J)

In order to further test the hypothesis that low constraint affects fatigue behaviour and can result in the poor performance of the CMM and CDMs, a notched fatigue specimen in which the crack would grow in predominately plane stress conditions was devised and tested. This was done in calibration with Jerome Guillios [2000].

### 7.5.2.1 The specimen and material properties

The specimen was designated Model-J and is shown in Figures 7.27 and 7.28 below. It was machined from an inch-by-inch mild steel bar and then stress relieved. The specimen was tested in three point bending. Crack growth was in the negative y-direction, starting at the stress concentration feature and propagating through the very thin section.

The specimens were machined from the same material previously used for the Model-E and Model-T specimens. This material is discussed at length in Appendix-A, section A.1. It was determined to have a plain specimen fatigue limit (in bending),  $\Delta\sigma_o$ , of 435 MPa and a material stress intensity threshold range,  $\Delta K_{th}$ , of 11 MPa.m<sup>1/2</sup> at an R-ratio of 0.1. Hence the value of  $a_o$  was found to be 0.205 mm.



*Fig. 7.27 - Three-dimensional view of the Model-J specimen*

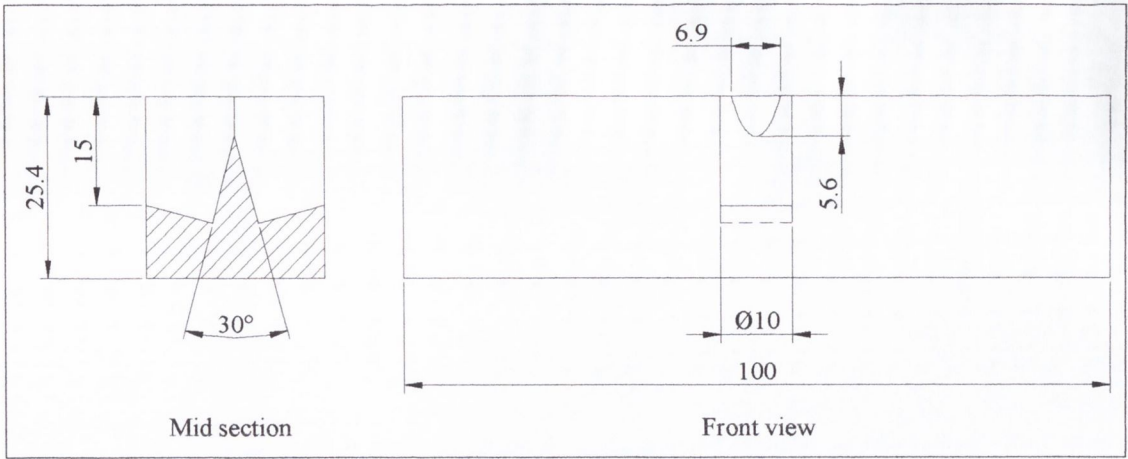


Fig. 7.28 - Dimensions of the Model-J specimen

### 7.5.2.2 Defining the degree of constraint

#### 7.5.2.2.1 Application of the elastic constraint parameters

Before the specimen was tested, a finite element analysis was conducted to determine the degree of constraint using the elastic parameters discussed above (see section 7.4.2). The results of this analysis are reported below in Figure 7.29. It can be seen that all of the parameters indicate a very low constraint factor.

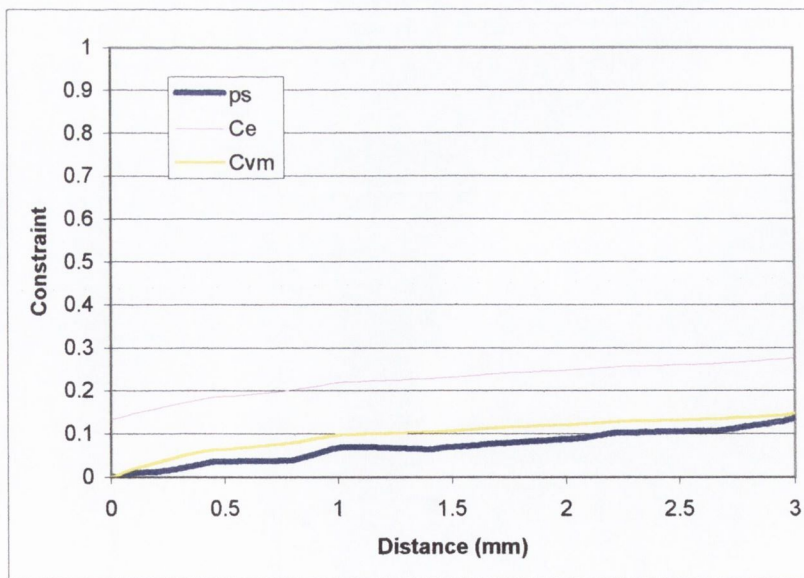


Fig. 7.29 - Elastic constraint parameters applied to the Model-J specimen

#### 7.5.2.2.2 Elastic plastic finite element analysis

In addition, an elastic-plastic finite element analysis of the Model-J specimen has been undertaken to determine the degree of constraint.

The load range applied to the model was the experimentally determined fatigue strength (see section 7.5.2.3 below) at an R-ratio of 0.1. The measured cyclic stress-strain curve, for the actual material, was used. This is presented in Appendix A. The MPZ is determined to be approximately 5.1 mm and the CPZ is 1.36mm. It can be seen from the cross sectional view in Figure 7.28 that, at the extent of the MPZ, the thickness (2.7mm) is considerably less than the size of the plastic zone. Hence, conditions of plane stress will prevail in this specimen.

#### 7.5.2.3 Experimental results

The results of the experimental investigation of the Model-J specimen are reported in Table 7.12 and Figure 7.30 below. From these the fatigue strength was determined to be 3.16 kN at  $2 \times 10^6$  cycles.

*Table 7.12 - Experimental test results - Model-J*

<b>Test No.</b>	<b>R-ratio</b>	<b>Load Range (kN)</b>	<b>No. of cycles</b>	<b>Comment</b>
1	0.101	2.63	2.87E+06	No failure - Test aborted
2	0.103	4.49	6.99E+05	Failure
3	0.094	3.705	1.26E+06	Failure
4	0.113	3.12	1.85E+06	Failure
5	0.089	2.515	4.45E+06	Failure
6	0.102	2.2	5.66E+06	Failure
7	0.105	2.04	9.70E+06	No failure - run out
8	0.098	6.14	2.91E+05	Failure

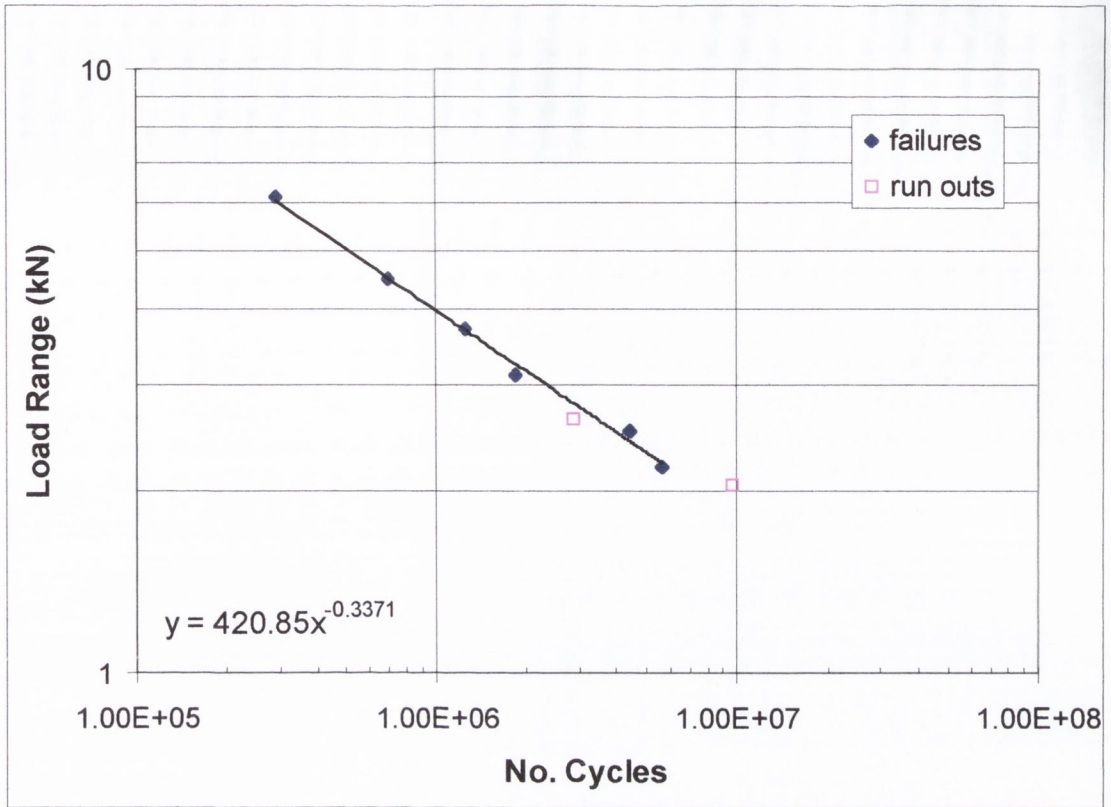


Fig. 7.30 - Experimental results - Model-J

#### 7.5.2.4 Fatigue analysis results

For this specimen the choice of the focus path is logical because the specimen has two planes of symmetry. Hence, the focus path starts at the hot spot and extends down through the centre of the thin cross section shown in Figure 7.28 above.

The results of the fatigue analysis are presented in Table 7.13 below. It can be seen that the errors are conservative and in general quite large, with error factors ranging approximately between 3 and 4.

Table 7.13 - Summary of results from the fatigue assessment of Model-J

	<b>Model-J</b>
<b>Experimental fatigue strength</b>	3.16 kN at $2 \times 10^6$ cycles
<b>Point method</b> (Error factor)	0.97 kN (3.26)
<b>Line method</b> (Error factor)	1.07 kN (2.95)
<b>Area method</b> (Error factor)	1.01 kN (3.13)
<b>CMM</b> (Error factor)	0.766 kN (4.12)
<b>Stress-life method</b> (Error factor)	0.86 kN (3.67)

Note: *Error factor* is defined as the ratio of the *Experimental fatigue strength* to the *predicted fatigue strength*

#### 7.5.2.5 Discussion and conclusions

As discussed in Chapter 2, section 2.3.1, Smith and Miller [1978] showed that stress concentration features can be modelled either as cracks using LEFM or as notches using the stress-life method. Features with a low stress concentration factor,  $K_t$ , fall into the notch category and high stress concentration features are crack-like. For Model-J the result of the crack modelling method and the stress-life method are approximately the same. This implies that on the Smith & Miller diagram (see Figure 2.4) the stress concentration factor of Model-J lies somewhere close to the transition point  $K_t^*$  and is not really notch-like or crack-like.

The results from the experimental investigation of Model-J show the trend that was expected. That is, the CMM and the CDM's were very conservative when predicting fatigue crack growth in the very thin section (or plane stress conditions) of Model-J. It is assumed that this is at least partly due to the effect of low constraint.

## 7.6 Quantifying the effect of constraint

As discussed in section 7.4.1.2 it is not possible to experimentally measure the stress intensity threshold, in conditions of plane stress, for most engineering materials as it would require test specimens which are excessively thin (less than  $a_0$ ). Therefore, we must have some way of estimating it. Two possible ways of doing this are discussed below:

### 7.6.1 Method 1

The first possible approach is to assume that the relationship between the thresholds measured in plane strain,  $\Delta K_{th|plane\ strain}$ , and plane stress,  $\Delta K_{th|plane\ stress}$ , is similar to that which exists for fracture toughness  $K_{Ic}$  and  $K_c$  (see section 7.1.4). This is thought to be worth investigating because the plastic zone size, ahead of a crack, is essentially the same function of stress intensity (or stress intensity range) for both fatigue and fracture. Hence, there is a good probability that similar trends will be observed. This is supported by Knott [1973] who believes that the effect of constraint in fatigue *should* be similar to that in fast fracture, assuming that the fast fracture occurs by ductile (fibrous tearing) mechanisms, because both types of failure are controlled by the level of plastic strain near the crack tip.

Of course, in order to prove that this is indeed the case, experimental investigations of both the  $\Delta K_{th}$  and  $K_c$  must be undertaken for the same material, in plane stress and plane strain. It would have been nice to do this for the aluminium discussed above. Unfortunately it was not possible due to time restrictions and because thicker specimens are needed to determine the plane strain fracture toughness (6mm was the biggest commercially available thickness).

If it is assumed  $K_{th}$  and  $K_c$  will follow the same trends with respect to their behaviour in plane strain and plane stress, it is possible to make some general approximations for the value of  $K_{th}$  in plane stress based on published data for  $K_c$  in plane stress. Figure 7.6 above shows one set of data discussed by Edwalds and Wanhill [1989]. It shows the variation of  $K_c$  with thickness for a high strength steel. It can be seen that  $K_c$  determined in plane stress is approximately 1.8 times the value measured in plane strain.

Another set of data, for aluminium alloy 2219-TB7 is shown in Figure 7.31 below. For this material a similar difference is observed. In this case  $K_{Ic}$  measured in plane stress is approximately 2.3 times higher than the plane strain value.

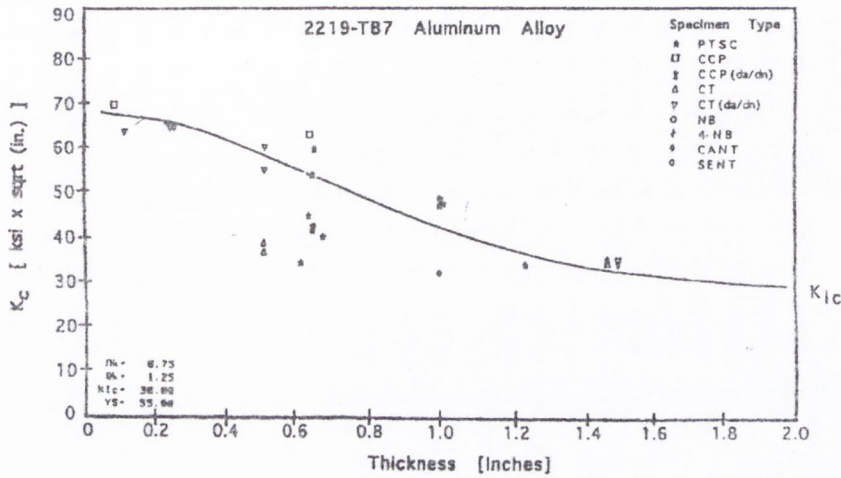


Fig. 7.31 - Variation of fracture toughness with thickness for 2219-TB7 Aluminium Alloy

Another set of data for an aluminium alloy is discussed by Knott [1973] and is shown in Figure 7.32 below. This figure gives toughness in terms of the critical strain energy release rate, which is directly proportional to the square of the critical stress intensity factor,  $K_{Ic}$ . Therefore, for this material the  $K_{Ic}$  value measured in plane stress is approximately 2.96 times higher than the plane strain value.

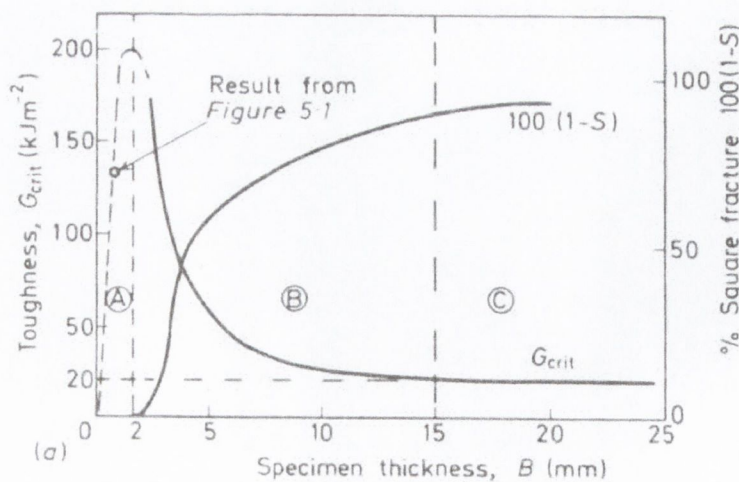


Fig. 7.32 - Variation of toughness with thickness in an Al-Zn-Mg-alloy [Knott, 1973]

All of this data suggests the following very approximate relationship:



$$1.5 \leq \frac{K_c}{K_{1c}} \leq 3 \quad (7-34)$$

The same relationship can be assumed for the threshold stress intensity factor, that is:

$$1.5 \leq \frac{\Delta K_{th} |_{plane\ stress}}{\Delta K_{th} |_{plane\ strain}} \leq 3 \quad (7-35)$$

It can be seen that the results from the experimental investigation discussed in section 7.5 falls within this range. Therefore, this assumption gives us an upper and lower bound for the value of  $\Delta K_{th} |_{plane\ stress}$ , which allows us to make fatigue predictions for components like Model-J which are characterised by low constraint.

Table 7.14 below shows the predictions made with the CDMs and the CMM using this upper and lower bound values for the threshold stress intensity range. It can be seen that predictions are improved, although conservative error are still apparent, even when the upper limit of  $\Delta K_{th} |_{plane\ stress}$  is used.

Table 7.14 - Results of the fatigue analysis of Model-J using different  $\Delta K_{th}$  values

	Plane stain values $\Delta K_{th} = 11 \text{ MPa m}^{1/2}$ $a_o = 0.205\text{mm}$	$\Delta K_{th} _{pstress}=1.5\Delta K_{th} _{pstrain}$ $\Delta K_{th} = 16.5 \text{ MPa m}^{1/2}$ $a_o = 0.458\text{mm}$	$\Delta K_{th} _{pstress}=3\Delta K_{th} _{pstrain}$ $\Delta K_{th} = 33 \text{ MPa m}^{1/2}$ $a_o = 1.832\text{mm}$
<b>Experimental</b>	3.16 kN at $2 \times 10^6$ cycles		
<b>Point method</b> (Error factor)	0.97 kN (3.26)	1.12 kN (2.82)	1.79 kN (1.77)
<b>Line method</b> (Error factor)	1.07 kN (2.95)	1.29 kN (2.45)	2.21 kN (1.43)
<b>CMM</b> (Error factor)	0.766 kN (4.12)	1.15 kN (2.75)	2.30 kN (1.37)
<b>Stress-life meth.</b> (Error factor)	0.86 kN (3.67)	0.86 kN (3.67)	0.86 kN (3.67)

Note: Error factor is defined as the ratio of the Experimental fatigue strength to the predicted fatigue strength

## 7.6.2 Method 2

The second possible approach is to maintain the relationship that exists, in conditions of plane strain, between the monotonic plastic zone size and  $a_o$ , for conditions of plane stress. This relationship is discussed in section 7.4.1.1, where it was shown that for plane strain,

the plastic zone size ahead of a crack is approximately a factor of  $C^2/3$  smaller than  $a_0$ , for any given material. For plane stress this factor is only  $C^2$ , where:

$$C = \frac{\Delta\sigma_o}{\sigma_{ys}} \quad (7-36)$$

Therefore, in order to have the same ratio, of the plastic zone size to  $a_0$ , for both plane strain and plane stress, we must increase the  $a_0$  value, for plane stress, by a factor of 3. This ensures that for both stress states,  $a_0$  is always greater than the plastic zone by approximately a factor of three. Therefore, given the relationship between  $\Delta K_{th}$  and  $a_0$ :

$$\Delta K_{th} |_{plane\ stress} \approx \sqrt{3} \Delta K_{th} |_{plane\ strain} \quad (7-37)$$

This idea is supported by the experimental evidence obtained using the aluminium specimens discussed above, for which the difference between  $\Delta K_{th}$  values, measured in plane stress and plane strain, was between 1.4 and 2.

On the other hand, using this modified value for  $a_0$  in plain stress to obtain fatigue predictions for the Model-J specimen doesn't significantly decrease the prediction error (see Table 7.15) because the Model-J specimen has a relatively low stress gradient when compared to a crack. It is interesting to note that for this specimen the monotonic plastic zone is very large, approximately 5.1 mm, (see section 7.5.2.2.2), hence the relationship between  $a_0$  and the plastic zone size, discussed above, is not maintained for this specimen.

The final column of Table 7.15 below shows the fatigue predictions for the Model-J specimen using values of  $a_0$  and  $\Delta K_{th}$ , which result in good predictions. It can be seen unrealistically large values are required.

Table 7.15 - Results of the fatigue analysis of Model-J using different material properties

	$a_o = 0.205\text{mm}$ $\Delta K_{th} = 11 \text{ MPa m}^{1/2}$	$a_o = 0.615\text{mm}$ $\Delta K_{th} = 19 \text{ MPa m}^{1/2}$	$a_o = 3.94\text{mm}$ $\Delta K_{th} = 48.4 \text{ MPa m}^{1/2}$
<b>Experimental</b>	3.16 kN at $2 \times 10^6$ cycles		
<b>Point method</b> (Error factor)	0.97 kN (3.26)	1.195 kN (2.64)	2.77 kN (1.14)
<b>Line method</b> (Error factor)	1.07 kN (2.95)	1.403 kN (2.25)	3.51 kN (0.90)
<b>CMM</b> (Error factor)	0.766 kN (4.12)	1.10 kN (2.87)	3.37 kN (0.94)
<b>Stress-life method</b> (Error factor)	0.86 kN (3.67)	0.86 kN (3.67)	0.86 kN (3.67)

Note: Error factor is defined as the ratio of the Experimental fatigue strength to the predicted fatigue strength

## 7.7 Concluding remarks

This chapter is essentially an investigation of the effect of constraint on fatigue behaviour. It has been shown that:

- [1] Stress intensity threshold is a function of constraint. That is, the threshold measured in plane stress is higher than the plane strain value. This was confirmed for a material with a large  $a_o$  value, which could be tested in both plane strain and plane stress.
- [2] Fatigue predictions made using the CMM and the CDMs for stress concentrations characterised by low constraint result in conservative errors. This was confirmed by the experimental investigation of the Model-J specimen.
- [3] Furthermore, even if it is accounted for in the most optimistic way, the addition of a correction to account for low constraint still results in conservative error for the Model-J specimen (see section 7.6.1). It is therefore concluded that there are other factors affecting the fatigue behaviour of this specimen. One possibility is the stressed volume effect, which is discussed, in the following chapter.
- [4] Methods to determine the degree of constraint were investigated. The most useful criterion was to relate the plastic zone size to the specimen thickness. Based on this, it is believed that the Model-E specimen will not show a constraint effect.
- [5] It is also believed that the Model-T and Fillet-A specimens will have the same degree of notch tip constraint, which is most probably neither pure plane strain nor pure plane stress. This implies that at least some effect of low constraint should be observed in both cases and consequently a correction should be applied

to both cases. However, as shown in Chapter 5, good fatigue predictions were made for Model-T without any modification to the analysis methods. This was not the case for the Fillet-A specimen where big conservative errors were observed. Hence, the application of any correction factor to the predictions for the Fillet-A specimen will improve the result while the predictions for the Model-T specimen will get worse. However, it is expected that the specimens are predominately in conditions of plane strain. Hence the correction will be small and not greatly affect the results for the Model-T specimen.

## Chapter 8: The Stressed Volume Effect

---

This chapter is an investigation of the third possible explanation for the conservative errors discussed in Chapter 5 and is summarised as follows. Figure 8.1 below shows four different stress concentration features. Figures 8.1(a) and (c) are two-dimensional specimens for which the CMM and the CDMs give good results. Figures 8.1(b) and (d) are examples of three-dimensional stress concentration features which result in conservative predictions. It can be seen that a major difference between these, is that the 3-D features are localised stress concentrations where failure occurs from a point or small region, while in the 2-D case, cracks can initiate at any point along the width of the specimen at the stress concentration feature.

An alternative way of looking at this difference is in terms of stressed volume. In the three-dimensional case the amount of highly stressed material is significantly less when compared to a two-dimensional geometry.

The stressed volume effect is a well-known phenomenon in fatigue. Essentially, fatigue strength is observed to decrease as the amount of highly stressed material is increased. This is qualitatively explained by noting if the amount of stressed material is large, there is a greater probability that it will contain crack initiation sites.

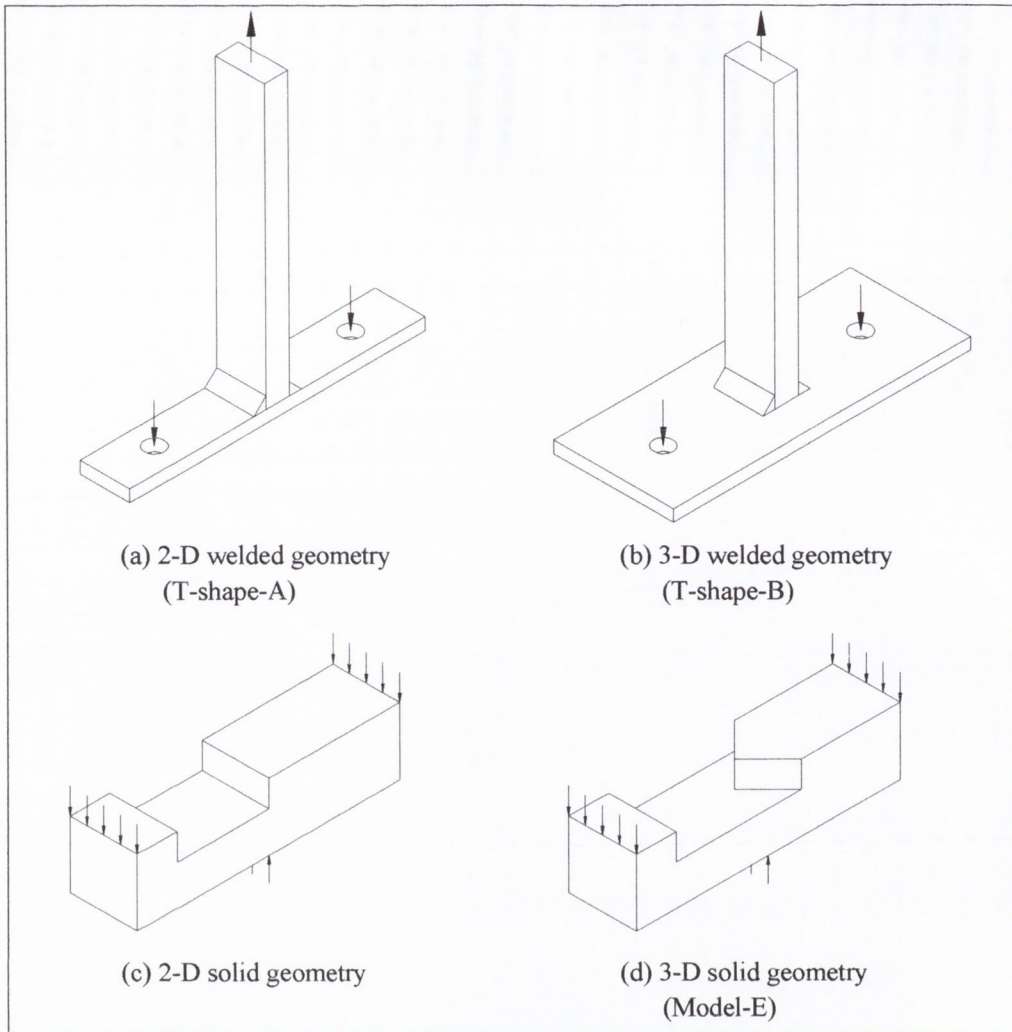


Fig. 8.1 - Illustration of the stressed volume effect

## 8.1 Definition of terms

Before continuing several confusing terms, which are important to the ideas being considered in this chapter are defined.

### Crack initiation sites:

Crack initiation sites are defined as, all locations where fatigue cracks may initiate. These include material flaws and manufacturing defect or can be as simple a grain that is weaker, or preferentially orientated, when compared to other grains. The definition excludes geometrical stress concentrations features (i.e. notches)

### The stressed volume effect:

The stressed volume effect is defined as a reduction in strength due to the fact that there is more stressed material. This could occur by either:

1. A change of scale. For example, the difference observed between geometrically similar specimens, of different size, subjected to a uniform stress distribution (see section 8.3 below).
2. The presence of a stress gradient. For example the reduction in fatigue strength due to the stress gradient at a notch.
3. By a combination of the above. For example the difference observed in the fatigue strength of rotating bending specimens of different diameters. In this case, an increase in diameter results in an overall increase size and at the same time decreases the stress gradient (see Figure 8.7 and Appendix D).

### Size effect:

This term is defined exactly as per the *stressed volume effect*. That is, it implies a reduction in strength due to a greater size of stressed material.

### Stress gradient effect:

This is defined as a *stress volume effect* or *size effect* caused by the presence of a stress gradient.

## **8.2 The critical distance methods and the stressed volume effect**

Do the critical distance methods account for the effect of stressed volume? This is an extremely difficult question to answer. Yet, it is fundamental to the idea being investigated in this chapter.

Indeed this was the original idea of Neuber [1958] who postulated that fatigue strength depends on the average stress acting over an elementary volume of the material ahead of a notch. Hence, in this way stress gradient effect can be accounted for. This is supported by the fact that the critical distance methods, as defined by Taylor [1999] have been shown to successfully predict the fatigue behaviour of a wide range of two-dimensional notched geometries and materials [Taylor and Wang, 2000]. We can therefore say, that the critical

distance methods can predict the stressed volume effect when it is due to a stress gradient caused by the presence of a notch.

Secondly, the CDMs can be used to make predictions for the size effect observed in plain steel rotating specimens. This is done in Appendix D for a large quantity of experimental data, however because the material properties are unknown (specifically  $\Delta K_{th}$  and  $a_o$ ) it is difficult to assess the accuracy of the predictions. It is concluded, on the basis of experience and engineering judgement, that in the majority of cases the point method under-predicts the experimental data. Nevertheless it can at least be stated that CDMs make some sort of correction when a stressed volume effect is caused by both a change in scale and due to the presence of a stress gradient.

Based on this evidence one could be convinced that the critical distance methods do account for stressed volume effects. However, as is always the case, the following arguments demonstrate that the situation is not completely black and white.

In their current form, the CDMs can in no way account for a stressed volume effect due solely to a change of scale. For example, the difference in fatigue strength of different sized, plain specimens, tested in cyclic tension. Compared to the fatigue behaviour of notched components this is a much simpler situation. There is no stress gradient and in general the material behaviour remains elastic. Hence, it can be argued that this is a true size effect and that the difference observed in the fatigue strength is due solely to the statistical distribution of crack initiation sites, or more specifically to the statistical distribution in the *size* and *location* of crack initiation sites within the specimens. This is discussed in greater detail in the following section.

The real problem, when trying to say what the CDMs do and do not account for, is that we don't really understand the underlying mechanisms of the critical distance methods or why they work. It is unlikely that the stressed volume effect is the only mechanism or factor involved in the fatigue behaviour of notched components. The formation of local notch tip plasticity and the growth of non-propagating crack are examples of other factors that should also be taken into consideration. In fact, a recent paper, Taylor [2001] proposed that the CDMs work by specifying the necessary condition for the growth of non-propagating cracks.



A third argument that creates doubt as to whether the CDMs take into account the stressed volume effect, in a complete way, is as follows. In the original work by Neuber [1958] concerning the CDMs, he argued that the critical volume should be large enough so that the material ahead of the notch is sampled homogeneously. That is to say the critical volume must be larger than one grain. If this is not the case the material will be *quantitatively* different. For example, it will not contain grain boundaries and would therefore behave differently to a *typical* material sample. If the critical volume is between one grain and ten grains the situation is not so clear. However, if the volume is greater than approximately ten grains then it can be assumed that conditions of homogeneity will be approached. It can be seen that this argument is different from the probabilistic one, given above, which states that if the amount of stressed material is large, there is a greater probability that it will contain crack initiation sites. It seems logical that the probabilistic argument can only be used IF the stressed volume is big enough to ensure homogeneity. For smaller volumes the whole process of fatigue could be different so it is not wise extrapolate from larger volumes. It is therefore possible that when using CDMs, we look at a volume of material is large enough to ensure homogeneity, but we don't take account of probabilistic effects.

As always, the honest answer to the question posed at the beginning of this section is: we really don't know. Nevertheless the arguments present here create enough doubt to justify investigating other approaches to account for the stressed volume effect. In particular it is thought that an alternative approach or correction could be used in conjunction with the critical distance methods without accounting for the same effect twice.

### **8.3 Size effects in plain cyclic tension specimens**

There is some doubt as to whether a size effect is actually observed in plain specimens loaded in axial tension. On the basis of the data given in Table 8.1 and plotted in Figure 8.2, Heywood [1962] states that the fatigue limit of steels tested in reversed axial loading is *practically* independent of the size of specimen. This is an important point to resolve because if no size effect is observed in plain tension specimens there is little point pursuing a statistical approach to predict size effects.

It is safe to say that if the effect were real it would be less obvious than the corresponding effect observed in plain rotating bending specimens because there is no stress gradient, and would also be a function of the material. Therefore, the position taken in this work is only subtly different from Heywood's. Here it is argued the size effect is real phenomena but for many materials is lost within the experimental scatter.

Table 8.1 - The effect of size on plain steel reversed tension specimens [Heywood, 1962]

Material	UTS (MPa)	Diameter of test section (mm)	Fatigue limit ( $\pm$ MPa)
3.1% Ni, 0.9% Cr (En36)	820.5	3.658	386.1
		9.169	370.9
		12.7	370.9
Mild steel, 0.07% C, 0.2% Mn, 0.2% Si	386.1	4.826	186.8
		4.826	186.8
		4.826	204.1
		8.382	204.1
		14.224	204.1
		24.892	176.5
		24.892	202.7
2.6% Ni, 0.75% Cr, 0.6% Mo, 0.43% C (En26)	972.2	4.826	593.6
		8.382	572.3
		12.7	603.4
		24.892	570.9

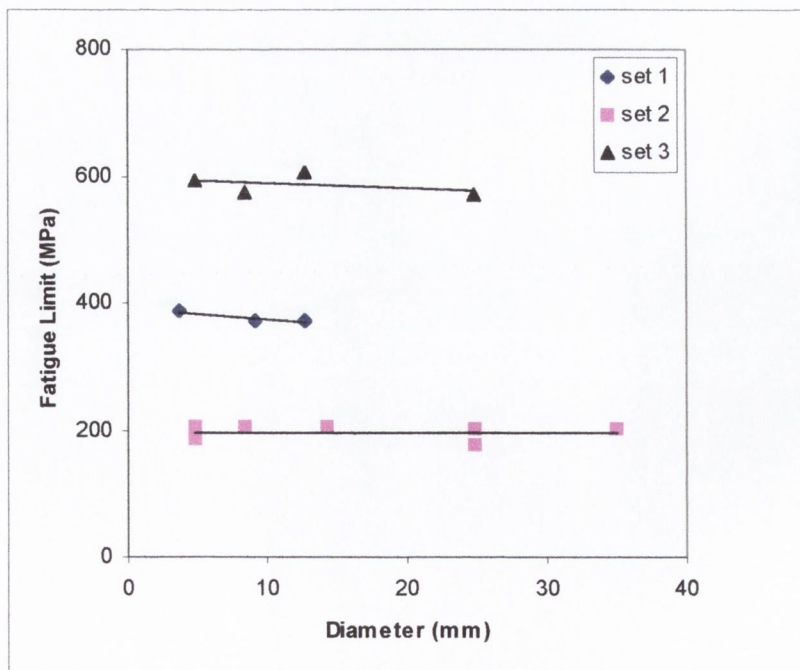


Fig. 8.2 - The effect of size on the plain fatigue strength of steel measured in reversed tension [Heywood, 1962]

## 8.4 A statistical approach to the stressed volume effects

In the following, an alternative approach to predict size effects in fatigue is investigated. It is essentially a statistical approach, which is often used to predict brittle failure in all kinds of engineering materials.

### 8.4.1 The Weibull distribution

The Swedish engineer, Weibull [1951; 1961], developed an approach that can be used to deal with the probability aspects of fatigue. He proposed the following:

$$P_s(V_{ref}) = \exp\left\{-\left(\frac{\Delta\sigma}{\Delta\sigma_{ref}}\right)^b\right\} \quad (8-1)$$

Where  $P_s(V_{ref})$  is the probability of survival, and is defined as the fraction of identical samples, each of volume  $V_{ref}$ , which survive fatigue loading at a stress range of  $\Delta\sigma$ . The quantities,  $\Delta\sigma_{ref}$  and  $b$  are experimentally determined material constants.

Equation 8-1 is plotted in Figure 8.3 below. It can be seen that when the applied stress range,  $\Delta\sigma$ , is equal to zero the probability of survival is one, that is all samples survive. As  $\Delta\sigma$  approaches  $\Delta\sigma_{ref}$  samples begin to fail. When  $\Delta\sigma$  is equal to  $\Delta\sigma_{ref}$  the probability of survival is equal to 37% and as  $\Delta\sigma$  goes to infinity, virtually all samples fail.

Therefore  $\Delta\sigma_{ref}$  is simply the applied stress range which allows 37% of specimens to survive and the constant  $b$  is referred to as the Weibull modulus, which tells how rapidly the fatigue limit falls as  $\Delta\sigma$  approaches  $\Delta\sigma_{ref}$ . Figure 8.3 shows the Weibull distributions for three different values of the Weibull modulus. The lower the modulus, the greater the variability in the fatigue strength and conversely, a material with a high Weibull modulus has a well-defined fatigue strength.

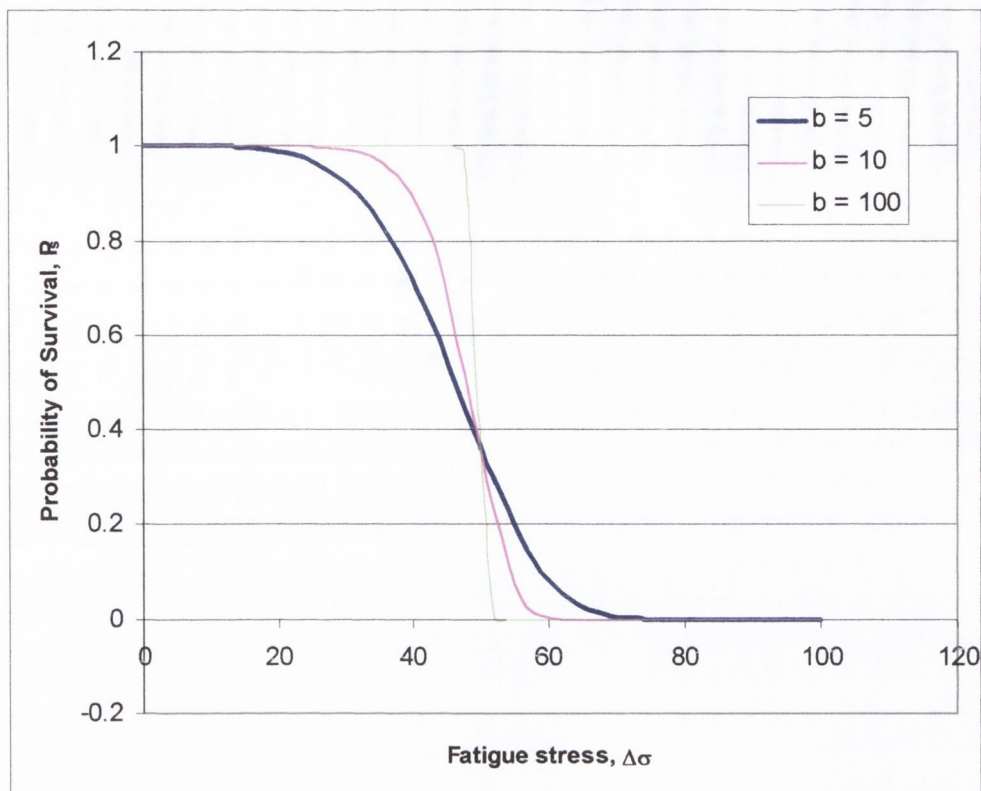


Fig. 8.3 - The Weibull cumulative probability distribution for various Weibull modulus values and  $\Delta\sigma_{ref} = 50$

#### 8.4.2 Two-parameter and three-parameter distributions

The Weibull distribution discussed above is often referred to as a two-parameter Weibull distribution. Three-parameter Weibull distributions also exist, in which a third parameter is used to define the minimum stress range (other than zero). Equation 8-1 then becomes:

$$P_s(V_{ref}) = \exp\left\{-\left(\frac{\Delta\sigma - \Delta\sigma_{min}}{\Delta\sigma_{ref} - \Delta\sigma_{min}}\right)^b\right\} \quad (8-2)$$

#### 8.4.3 Volume dependence

The forgoing discussion is related to how the probability of survival depends on the applied stress range, but it also depends on volume. This was formulated by Weibull in the following way.

If the probability of one sample, of volume  $V_{ref}$ , surviving a stress range  $\Delta\sigma$  is  $P_s(V_{ref})$ , then the probability of  $n$  similar samples all surviving the same stress is  $\{P_s(V_{ref})\}^n$ . If all of the  $n$  samples were then joined together to form one sample with volume  $V=nV_{ref}$  then its probability of survival would also be  $\{P_s(V_{ref})\}^n$ . Therefore, the probability of survival of a specimen with volume  $V$ , is:

$$P_s(V) = \{P_s(V_{ref})\}^n = \{P_s(V_{ref})\}^{V/V_{ref}} \quad (8-3)$$

This is equivalent to

$$\ln P_s(V) = \frac{V}{V_{ref}} \ln P_s(V_{ref}) \quad (8-4)$$

By rearranging and substitution of Equation 8-1

$$P_s(V) = \exp\left\{\frac{V}{V_{ref}} \ln P_s(V_{ref})\right\} = \exp\left\{-\frac{V}{V_{ref}} \left(\frac{\Delta\sigma}{\Delta\sigma_{ref}}\right)^b\right\} \quad (8-5)$$

#### 8.4.4 Comparison between specimens

Equation 8-5 above, allows us to make a comparison between specimens of different size (but with uniform stress distributions). It is possible to show that for a constant probability of failure:

$$\frac{\Delta\sigma_1}{\Delta\sigma_2} = \left(\frac{V_2}{V_1}\right)^{1/b} \quad (8-6)$$

Figure 8.4 below shows a graphical representation of equation 8-6. That is, it shows the predicted relationship that exists between the fatigue strength of two specimens of different volume, in terms of the Weibull modulus. It can be seen that the only way to achieve a big change in stress is to have a small Weibull modulus.

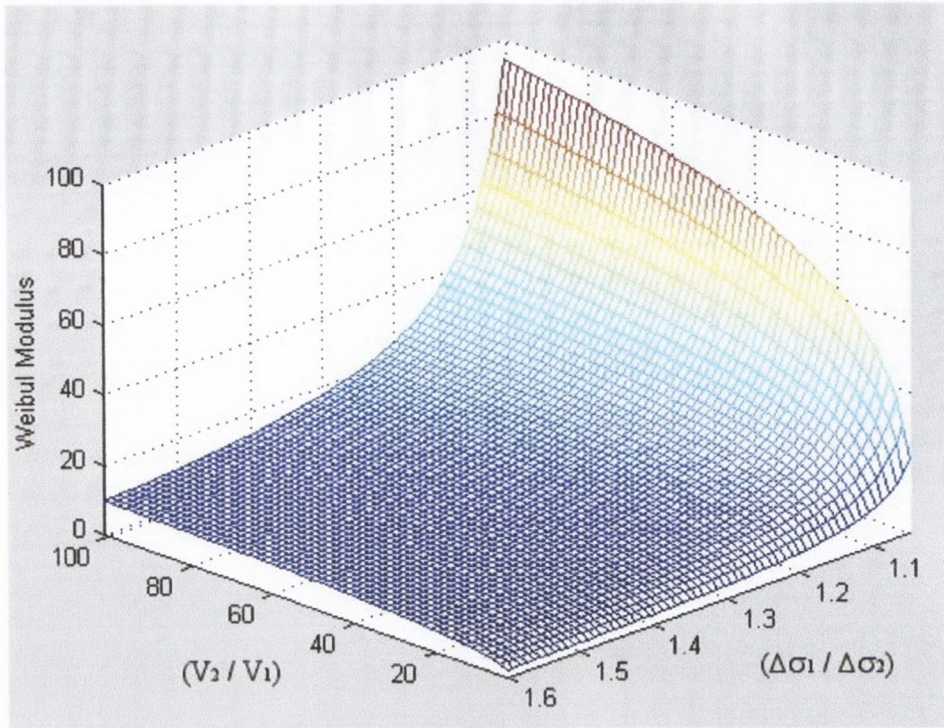


Fig. 8.4 - A graphical representation of equation 8-6

#### 8.4.5 The effective volume model

The ideas discussed above, are only really useful for un-notched tension specimens in which the total volume of the specimen is subjected to a constant stress. *Effective volume models* [Fischer *et al.*, 2002; Trantina and Johnson, 1983] are a way of dealing with more general cases. In these the probability of survival is calculated as a function of the volume, which is effectively being fatigued. Hence, the probability of survival, using a two-parameter Weibull distribution, is given by:

$$P_s = \exp \left\{ - \int_V \left( \frac{\Delta \sigma(x, y, z)}{\Delta \sigma_{ref}} \right)^b dV \right\} \quad (8-7)$$

Or, alternatively

$$P_s = \exp \left\{ - V_{eff} \left( \frac{\Delta \sigma_{max}}{\Delta \sigma_{ref}} \right)^b \right\} \quad (8-8)$$

Where

$$V_{eff} = \int_V \left( \frac{\Delta\sigma(x, y, z)}{\Delta\sigma_{max}} \right)^b dV \quad (8-9)$$

In tension fatigue specimens with no stress concentrations, the *effective volume*,  $V_{eff}$  is equal to the volume of the specimen,  $V$ . All other stress states result in the effective volume being less than the volume of the specimen (i.e.  $V_{eff} < V$ ). The *effective volume* is therefore the volume of the specimen that is effectively being fatigued at the maximum stress range,  $\Delta\sigma_{max}$ .

Alternatively, it can be assumed that it is only the surface area of the specimen, which is important. This is reasonable given that fatigue cracks usually initiate at the surface of a specimen. In this case, the integration in equations 8-7 and 8-9 is done over the specimen area and the model is referred to as an *effective area* model.

An analytical example of the application of this approach is given by Fischer *et al.* [2002]. They showed that if a three-point bending fatigue specimen with a constant rectangular cross-section, is considered, as shown in Figure 8.5 below, the stress state as a function of the  $x$ ,  $y$  and  $z$  coordinates is given by:

$$\Delta\sigma(x, y, z) = \frac{4zy}{hl} \Delta\sigma_{max} \quad (8-10)$$

From equation 8-10, the effective volume,  $V_{eff}$ , is therefore:

$$V_{eff} = \int_V \left( \frac{4zy}{hl} \right)^b dV = 4 \int_0^{l/2} \int_0^{h/2} \int_0^{w/2} \left( \frac{4zy}{hl} \right)^b dx dy dz = \frac{whl}{2(b+1)^2} \quad (8-11)$$

Hence, for a specimen where  $w = 25.4\text{mm}$ ,  $h = 15\text{mm}$  and  $l = 200\text{mm}$  and the Weibull modulus is assumed to be 14, the effective volume would be calculated to be  $169\text{mm}^3$ .

It should be noted that this analysis assumes that the maximum bending stress is the controlling stress component and effectively ignores any contribution of shear stress, which has a different stress gradient. This may not be a wise approach, especially when considering a plain specimen which is initiation controlled.

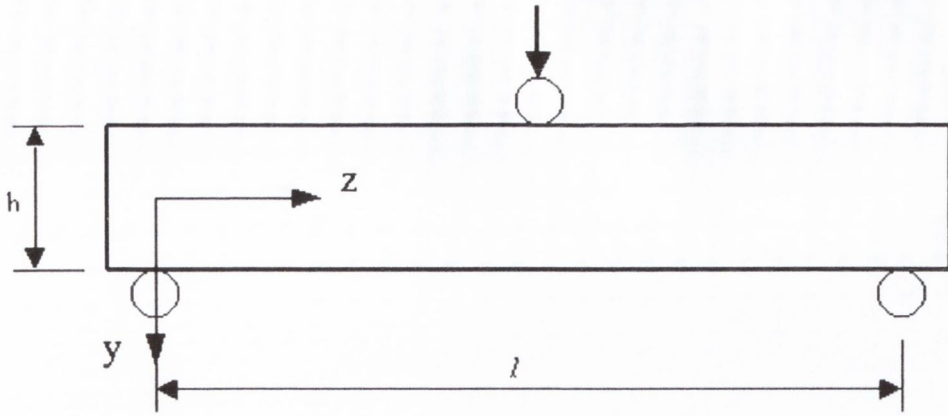


Fig. 8.5 - Example specimen for the effective volume integration showing the definition of the coordinate system. Note that the origin of the coordinate system is located on the half width ( $w$ ) of the specimen

#### 8.4.5.1 Comparison between specimens

The effective volume method gives us more flexibility to make comparisons between specimens. Using this approach the relationship between the fatigue strengths of two specimens with different size, geometry or stress distributions, for the same probability of survival, is given by:

$$\frac{\Delta\sigma_{\max,1}}{\Delta\sigma_{\max,2}} = \left( \frac{V_{eff,2}}{V_{eff,1}} \right)^{1/b} \quad (8-12)$$

#### 8.4.5.2 Application to size effect data for plain specimens

##### 8.4.5.2.1 Plain rotating bending specimen

In the following the way in which the effective volume model is used to predict the size effect observed in the fatigue strength of plain rotating bending specimens is demonstrated.

A rotating bending specimen with both rectangular and cylindrical coordinate systems is shown in Figure 8.6 below. For this loading condition the stress function is given by:

$$\Delta\sigma(x, y, z) = \Delta\sigma_{\max} \frac{y}{R} = \Delta\sigma_{\max} \frac{\rho \sin \theta}{R} \quad (8-13)$$



The effective volume is calculated by substituting equation 8-13 into equation 8-9, so that:

$$V_{eff} = \frac{4R^2 \pi L}{(b+2)} \int_0^{\pi/2} \sin^b(\theta) \quad (8-14)$$

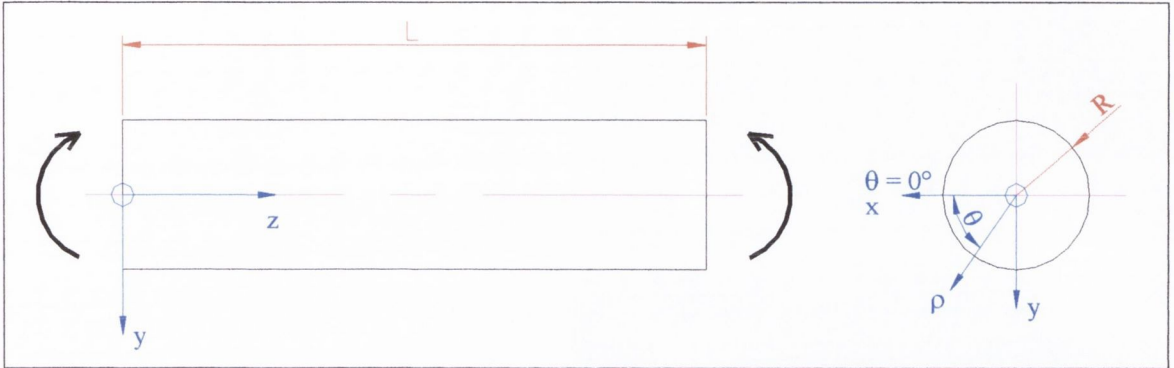


Fig. 8.6 - Rotating bending specimen

However, it must be remembered that this is a *rotating* bending specimen, hence every point on the surface of the specimen is fatigued once per cycle. The stress function above doesn't represent this, as it assumes reversed bending. Hence, a better stress function would be:

$$\Delta\sigma(x, y, z) = \Delta\sigma_{max} \frac{\rho}{R} \quad (8-15)$$

In this case the effective volume is calculated to be:

$$V_{eff} = \frac{2R^2 \pi L}{(b+2)} \quad (8-16)$$

Therefore the ratio of effective volumes between similar specimens but with different diameters is given by:

$$\frac{V_{eff,1}}{V_{eff,2}} = \frac{2R_1^2 \pi L}{(b+2)} \frac{(b+2)}{2R_2^2 \pi L} = \left( \frac{R_1}{R_2} \right)^2 \quad (8-17)$$

With reference to section 8.4.5.1 above, the ratio of fatigue strength of two specimens with different diameters, but the same probability of survival can be calculated as follows:

$$\frac{\Delta\sigma_{\max,1}}{\Delta\sigma_{\max,2}} = \left( \frac{V_{\text{eff},2}}{V_{\text{eff},1}} \right)^{1/b} = \left( \frac{R_2}{R_1} \right)^{2/b} \quad (8-18)$$

#### 8.4.5.2.2 Plain cyclic tension specimens

The effective volume of a cylindrical cyclic tension specimen is simply the volume of the specimen gauge length. Therefore the ratio of effective volumes between similar specimens but with different diameters is given by:

$$\frac{V_{\text{eff},1}}{V_{\text{eff},2}} = \frac{\pi R_1^2 L}{\pi R_2^2 L} = \left( \frac{R_1}{R_2} \right)^2 \quad (8-19)$$

With reference to section 8.4.5.1 above, the ratio of fatigue strength of two specimens with different diameters, but the same probability of survival can be calculated as follows:

$$\frac{\Delta\sigma_{\max,1}}{\Delta\sigma_{\max,2}} = \left( \frac{V_{\text{eff},2}}{V_{\text{eff},1}} \right)^{1/b} = \left( \frac{R_2}{R_1} \right)^{2/b} \quad (8-20)$$

#### 8.4.5.2.3 Discussion

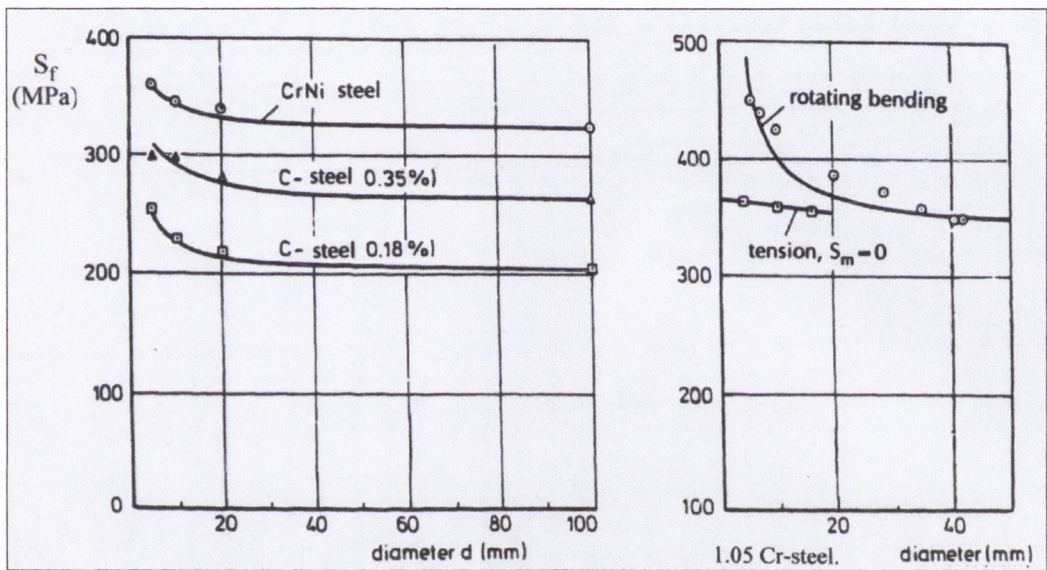
It can be seen that exactly the same relationship is predicted for both plain rotating bending specimens and plain cyclic tension specimens. As already stated the size effect observed in cyclic bending is significantly different to that which is observed in tension. It is therefore apparent that the same relationship will not predict both effects.

This is highlighted in Figure 8.8 below, which shows the application of equation 8-20 to the size effect data given in Figure 8.7(b) below. It has been done for both the cyclic tension data and the reversed bending data (Figures 8.8(a) and (c) respectively). It can be seen that to achieve a reasonably good fit for the tensile data a Weibull modulus of approximately 100 is needed. However when the approach is applied to the rotating bending data, a Weibull modulus of roughly 18 results in a good fit.

Therefore, it appears that the effective volume method is not entirely self-consistent in this respect. However, as usual there are other factors that have not been considered here which may be relevant. For example, when deriving the ratio of effective volumes above, for both

the tension and bending specimens, it was assumed that different sized specimens would have the same length. This may not be an accurate assumption.

Also, it is very probable that surface yielding is a factor in the fatigue behaviour plain rotating bending specimens. This will result in a reduction in maximum stress. Hence, it is possible that predicting the behaviour of plain specimens is not a good way to test the theory. Regardless of this, the approach is investigated further in the following section by considering how it could be applied to notched components.

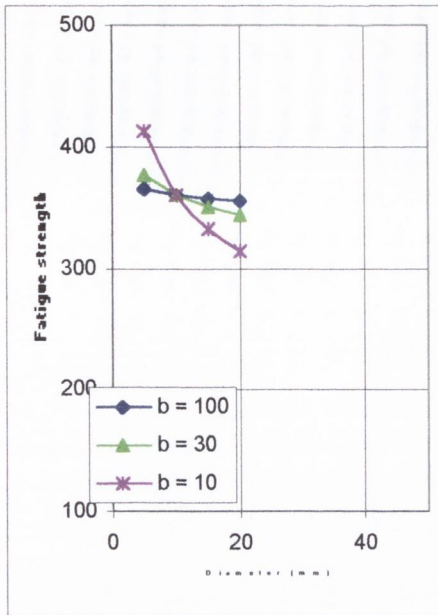


(a) Rotating bending

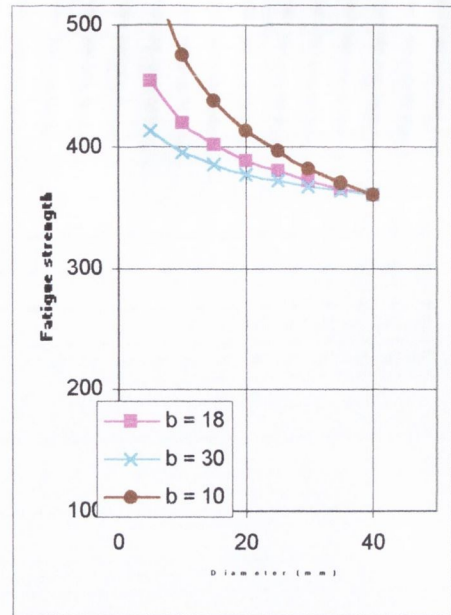
(b) Rotating bending & cyclic tension

Fig. 8.7 - Size effect on the fatigue limit of different types of steel in bending and tension

[Schijve, 2001]



(a) Cyclic tension



(b) Rotating bending

Fig. 8.8 - Application of the effective volume model to the size effect data given in Figure 8.7(b) above

#### 8.4.5.3 Extension to notched components

If the stressed volume effect is the primary mechanism at work in the fatigue behaviour of notched components, then the effective volume method described above should be able to predict the fatigue strength of this type of feature. If this is true then it implies that the effective volume method can be used as a stand-alone fatigue criterion for the assessment of notched components. It can essentially be thought of as the stress-life method, because it is based on the maximum stress, but it includes a correction to account for the effect of stressed volume.

However, as discussed above, the stressed volume effect is certainly not the only mechanism involved and it is unlikely that it is the primary mechanism governing the fatigue behaviour of notches. Nevertheless, in the following, the idea is investigated in terms of how it can be applied to notched components and is applied to the 3-D specimens considered throughout this work. However, it is impossible, within the scope of this project to prove whether the approach is valid or too simplistic to predict the behaviour of all notched components.

#### 8.4.5.3.1 Definition of failure

The definition of failure for this method can be a little confusing. Essentially a notched component is predicted to fail if it has the same *probability of survival* as the plain specimen. The notched specimen in question can be compared directly to the plain specimen, via the equation 8-12 repeated below, which ensures that the two different geometries have the same probability of survival. The failure criterion can therefore be stated as: Failure is predicted if:

$$\Delta\sigma_{\max | \text{notched}} \geq \left( \frac{V_{\text{eff} | \text{plain}}}{V_{\text{eff} | \text{notched}}} \right)^{1/b} \Delta\sigma_{\max | \text{plain}} \quad (8-21)$$

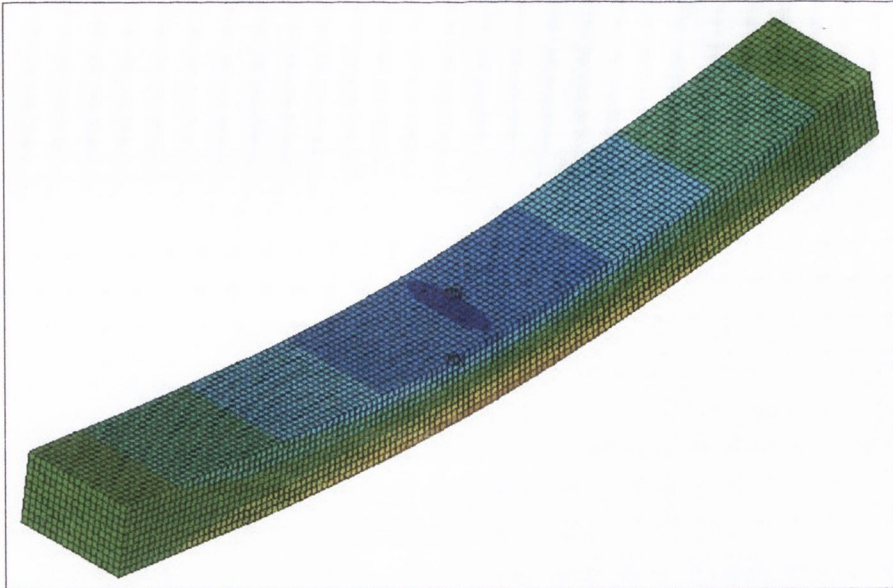
#### 8.4.5.3.2 Calculation of the effective volume

In section 8.4.5 above the effective volume is calculated *analytically* for the simple case of a plain specimen with a rectangular cross-section tested in three-point bending. For a more complicated geometry the effective volume can be calculated via a numerical integration based on finite element stress data. In this case the effective volume is given by:

$$V_{\text{eff}} = \sum_{i=1}^{\text{No. of elements}} \left( \frac{\Delta\sigma_i}{\Delta\sigma_{\max}} \right)^b V_i \quad (8-22)$$

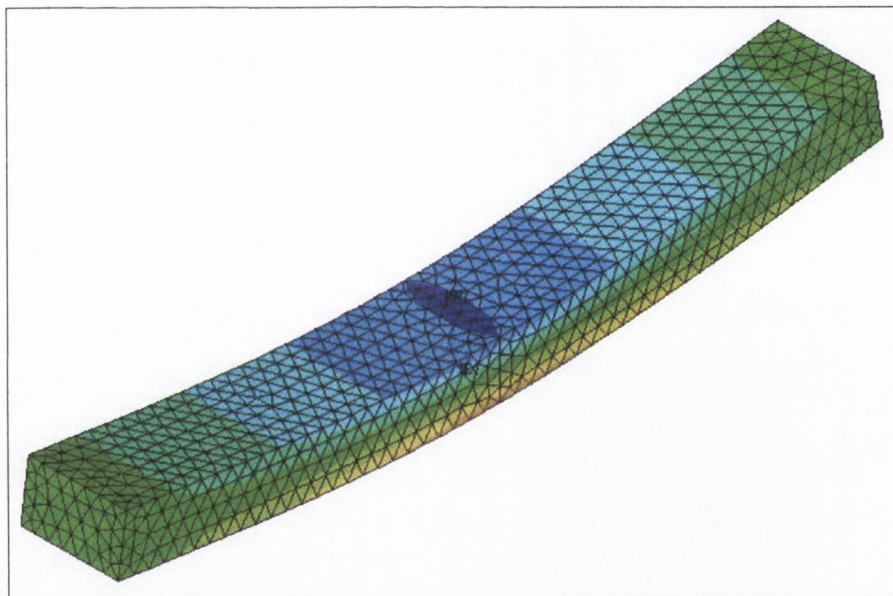
Where  $\Delta\sigma_i$  and  $V_i$  are the element stress range and volume of element number  $i$ .  $\Delta\sigma_{\max}$  is the stress range of the most stressed element and  $b$  is the Weibull modulus.

In order to prove the numerical procedure is reliable, FE models of a rectangular beam loaded in three-point bending were built and the numerical result was compared to the analytical one (see equation 8-11). This was done for three different FE meshes and various values of the Weibull modulus. The different FE meshes are described in Figure 8.9 below. The dimensions of the rectangular bar considered were 200 x 25.4 x 15 mm.



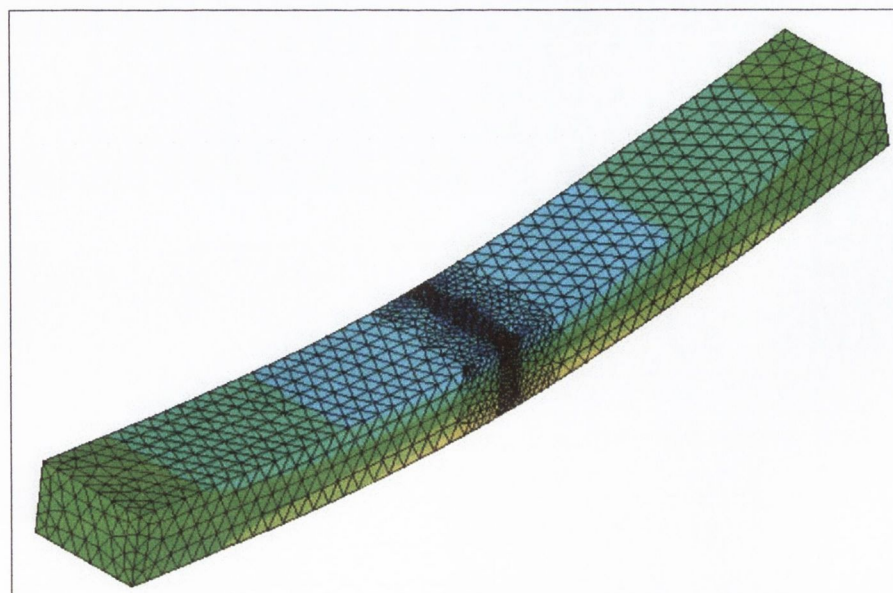
Mesh 1

- 22780 elements.
- 1st order bricks
- 10 elements through the thickness
- Very uniform mesh



Mesh 2

- 8950 elements.
- 2nd order Tets
- Approx. 4 elements through the thickness
- Relatively uniform mesh



Mesh 3

- 36620 elements.
- 2nd order Tets
- Equivalent to Mesh 2 accept the centre section has been refined

Fig. 8.9 - Different FE meshes examined

Table 8.2 shows the comparison between the effective volumes determined using the three different FE meshes and the analytical result. It can be seen that Mesh 3 gives the best result and Mesh 1 the worst. It can also be seen that the numerical result for the effective volume becomes increasingly worse as the Weibull modulus is increased. This is because the numerical error is raised to the power of the Weibull modulus.

Also shown in Table 8.2 is the *prediction error* that would result if the effective volume, calculated numerically were used in a fatigue analysis instead of the analytical one. The error is calculated as:

$$Error = \left( \frac{V_{eff} |_{analytical}}{V_{eff} |_{FEA}} \right)^{1/b} \quad (8-23)$$

Table 8.2 - The effective volume of a beam loaded in three-point bending

Weibull modulus, b		Analytical (eq 8-11)	Mesh 1	Mesh 2	Mesh 3
1	$V_{eff}$	9525	10747.26	10368.33	9779.22
	<i>Error</i>		0.886	0.919	0.974
10	$V_{eff}$	314.87	872.71	507.08	369.59
	<i>Error</i>		0.903	0.953	0.984
30	$V_{eff}$	39.65	352.64	92.21	67.15
	<i>Error</i>		0.930	0.972	0.983
60	$V_{eff}$	10.24	206.01	28.54	24.98
	<i>Error</i>		0.951	0.983	0.985
100	$V_{eff}$	3.73	133.64	11.84	12.15
	<i>Error</i>		0.965	0.989	0.988

It can be seen that the prediction error is in fact very good, even for very large values of the Weibull modulus. This is because unlike the effective volume, the prediction error is not a strong function of the Weibull modulus. It is therefore concluded that the numerical procedure, outlined above, can be used.

#### 8.4.5.3.3 Application to the various specimens

In the following the method is applied to the various 3-D specimens discussed throughout this work. This has been done for various values of the Weibull modulus. A sample

calculation for the Model-E specimen, using a Weibull modulus of 1 is given below. A full summary of the results is given in Table 8.3 below.

In order to determine the effective volume of the plain specimen the dimensions must be know. These are given below for both the solid steel and welded plain bending specimens:

Dimensions of the welded plain bending specimens: 12.7 x 25.4 x 100 mm

Dimensions of the solid steel, plain bending specimens: 15 x 25.4 x 100 mm

The solid steel plain bending specimen fatigue strength: 435 MPa at  $2 \times 10^6$  cycles

The welded plain bending specimen fatigue strength: 153 MPa at  $5 \times 10^6$  cycles

The effective volume for a beam loaded in three point bending is given by:

$$V_{eff} |_{plain} = \frac{whl}{2(b+1)^2} = 1058 mm^3 \quad \text{for the solid steel specimen and } b = 5$$

The effective volume of the Model-E specimen was determine via the numerical procedure to be (see Table 8.3):

$$V_{eff} |_{Model-E} = 4.01 \times 10^{-3} mm^3 \quad \text{for } b = 5$$

The correction due to the different effective volumes is given as:

$$Volume \text{ correction} = \left( \frac{V_{eff} |_{plain}}{V_{eff} |_{Model-E}} \right)^{1/b} = \left( \frac{1058}{4.01 \times 10^{-3}} \right)^{1/5} = 12.14$$

Therefore the predicted maximum stress that should occurs at the stress concentration feature of the Model-E specimen at its fatigue limit is:

$$\text{Predicted max stress} = \left( \frac{V_{eff} |_{plain}}{V_{eff} |_{Model-E}} \right)^{1/b} \Delta \sigma_{max} |_{plain} = 12.14 \times 435 = 5280.9 MPa$$

The maximum stress at the Model-E stress concentration, determined via FEA, at the experimentally determined fatigue load is equal to 1814 MPa. Therefore the error factor is determined to be:



$$\text{error factor} = \frac{\text{Actual maximum stress}}{\text{Predicted maximum stress}} = \frac{1814 \text{ MPa}}{5280.9 \text{ MPa}} = 0.344$$

Table 8.3 - The effective volume of a beam loaded in three-point bending

Weibull modulus, b		Model-E ( $\Delta\sigma_{\max} = 1814 \text{ MPa}$ )	Model-T ( $\Delta\sigma_{\max} = 867 \text{ MPa}$ )	Model-J ( $\Delta\sigma_{\max} = 1174 \text{ MPa}$ )	Fillet-A	T-shape-B
5	Effective Vol. $V_{\text{eff}}$	$4.01 \times 10^{-3}$	0.093	$4.93 \times 10^{-2}$	$2.28 \times 10^{-3}$	0.19
	Vol. correction	12.14	6.47	7.35	13.14	5.43
	Predicted max stress	5280.9	2816.29	3197.25	2010.42	830.79
	(Error factor)	(0.344)	(0.308)	(0.367)		
10	Effective Vol. $V_{\text{eff}}$	$1.04 \times 10^{-4}$	$3.95 \times 10^{-3}$	$3.51 \times 10^{-3}$	$1.14 \times 10^{-4}$	$3.20 \times 10^{-3}$
	Vol. correction	4.45	3.09	3.13	4.33	3.11
	Predicted max stress	1935.75	1344.73	1361.55	662.49	475.83
	(Error factor)	(0.937)	(0.645)	(0.862)		
30	Effective Vol. $V_{\text{eff}}$	$8.54 \times 10^{-6}$	$2.78 \times 10^{-4}$	$1.98 \times 10^{-4}$	$7.43 \times 10^{-5}$	$3.05 \times 10^{-4}$
	Vol. correction	1.67	1.49	1.50	1.54	1.47
	Predicted max stress	726.45	646.07	652.5	235.62	224.91
	(Error factor)	(2.497)	(1.342)	(1.799)		
60	Effective Vol. $V_{\text{eff}}$	$4.73 \times 10^{-6}$	$6.93 \times 10^{-5}$	$5.58 \times 10^{-5}$	$6.87 \times 10^{-5}$	$1.46 \times 10^{-4}$
	Vol. correction	1.28	1.22	1.22	1.22	1.20
	Predicted max stress	556.8	530.46	530.7	186.66	183.6
	(Error factor)	(3.258)	(1.634)	(2.212)		
100	Effective Vol. $V_{\text{eff}}$	$3.56 \times 10^{-6}$	$2.56 \times 10^{-5}$	$2.80 \times 10^{-5}$	$6.79 \times 10^{-5}$	$1.04 \times 10^{-4}$
	Vol. correction	1.15	1.12	1.13	1.11	1.11
	Predicted max stress	500.25	489.92	491.55	169.83	169.83
	(Error factor)	(3.626)	(1.770)	(2.388)		

It is not possible to define the error factor for the welded specimens (i.e. Fillet-A and T-shape-B), because the stress concentration features in these cases were modelled in the FEA as sharp corners with no root radius. Hence, the maximum stress at these locations calculated using an elastic analysis is infinite.

It can be seen for the other three specimens that a Weibull modulus of between 10 and 30 will result in error factors of one. In fact, Table 8.4 below shows values for the Weibull modulus result in perfect predictions:

*Table 8.4 - The effective volume of a beam loaded in three-point bending*

	Weibull modulus (b) need for a perfect prediction
Model-E	10.5
Model-T	16.9
Model-J	11.7

This is quite a good result as it can be seen that values for the three specimens are approximately the same. Hence, choosing the single 'best' value of b will result in small errors all round.

#### 8.4.5.4 The Weibull modulus

As mentioned in section 8.4.1 above, the Weibull modulus is essentially an experimentally determined constant. Furthermore, it is thought of as being a material constant, but only within the framework of a particular approach. This means that for a given material the Weibull modulus used in conjunction with the effective volume method should be constant. However if an alternative approaches is used with the same material, for example the effective area method, mentioned above, then the Weibull modulus will not necessarily be the same.

#### 8.4.5.5 Discussion

As already stated, the foregoing analysis can be described as an effective volume correction to the stress-life method. It has been included here, because it is a very interesting approach to the problem of stressed volume and because the way in which the

effective volume is defined is quite elegant. However, it is essentially a stand-a-lone fatigue criterion. Above it has been applied to:

- A) The size effect observed in a series of published data for plain rotating steel bending specimens and a set of data using the same steel showing the effect of size on the plain fatigue strength measured in reversed tension (see section 8.4.5.2.3). It was shown that the method is not self-consistent because very different values of the Weibull modulus are needed to predict the two effects.
- B) The fatigue behaviour of the 3-D stress concentrations discussed throughout this work (see section 8.4.5.3.3). In this case a Weibull modulus of between 10 and 17 resulted in the best fit with the experimental data.

This is by no means is an extensive or conclusive study, but it is suspected that the criterion is not going to prove particularly useful for the fatigue prediction of notched components. Hence, the concept has been investigated no further. Also, as the focus of this project is on the CDMs and the CMM, we are more interested in developing a stressed volume correction for these, than exploring an entirely different concept.

Unfortunately the effective volume method is not compatible with the critical distance methods. This is because the effective volume method is based on the maximum stress, while the critical distance methods consider the average stress inside a critical volume surrounding the stress concentration (or a simplification of this).

It is tempting however to say that we can use the same volume correction determine above in conjunction with the CDMs. However, consider the situation shown in Figure 8.10 below, which demonstrates the application of the volume, critical distance method to two different notched geometries. Failure is assumed if the average stress is greater than the plain specimen fatigue strength.

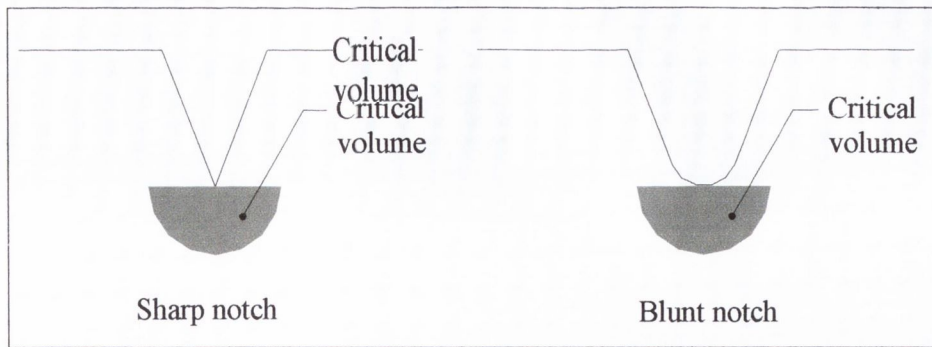


Fig. 8.10 - Application of the volume method to two different notched geometries

However if equation 8-9 is used to determine the critical volumes for both of these notches, it will result in different effective volumes and therefore predict that we should apply a correction to the CDMs. This is not a desirable situation because we know that the CDMs predict the behaviour of two-dimensional notched components well.

### 8.5 An effective volume correction to the CDMs

In the following a simple approach is investigated in order to make an effective volume correction, which can be applied to the critical distance methods [Taylor, 1999]. This is again based on the Weibull distribution, however before continuing the following two terms must be defined:

#### Critical volume:

The term critical volume is defined as the volume ahead of a stress concentration in which the average stress is calculated in order to apply the volume method (i.e. the volume, critical distance method). This is discussed in Chapter 3.

#### Effective volume:

The term effective volume is used, as above, to mean the volume of a specimen that is effectively being fatigued.

The idea is to use the *critical volume* to be the *effective volume*. Figure 8.11 below demonstrated the application of this to two-dimensional notched geometries of different width. It can be seen that the *critical volume* or the semi-cylindrical volume at the notch tip is greater if the width of the specimen is greater. If the average stress in each of these

volumes were the same, then the CDMs would predict that they would have the same fatigue strength. However, because the volume of stressed material is not equivalent, the probability of failure in both cases is not equivalent either.

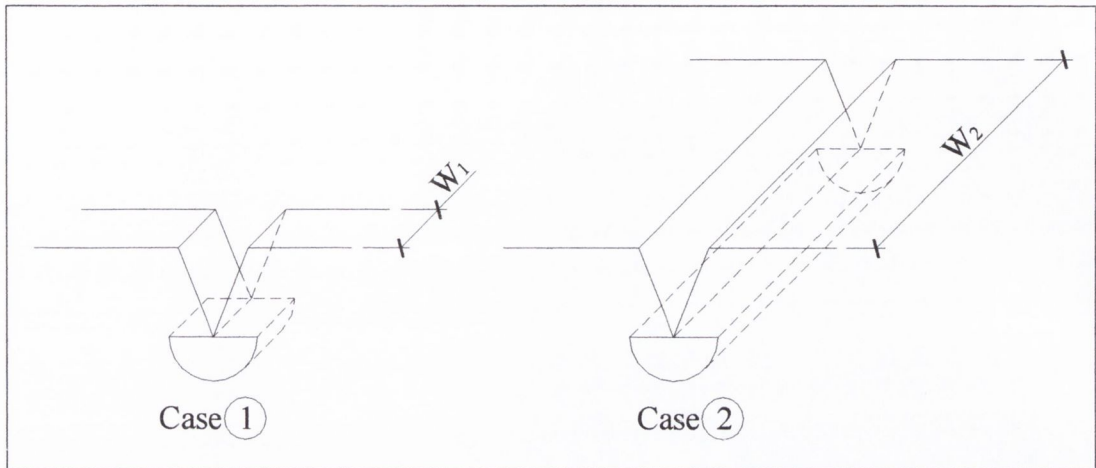


Fig. 8.11 - The change in stressed volumes for a 2-D notched component caused by a change of width

Hence, the thinner specimen is effectively stronger than the wider one by a factor of:

$$\left( \frac{V_{crit,2}}{V_{crit,1}} \right)^{1/b} = \left( \frac{W_2}{W_1} \right)^{1/b} \quad (8-24)$$

### 8.5.1 The stressed volume correction

In the work discussed here we are essentially interested in determining the difference between two-dimensional and three-dimensional notched geometries. Hence, following the logic above, it can be seen that if the CDMs are used to define failure, but the critical volumes are not equal then the geometry with the smaller critical volume should be multiplied by the following correction. In most cases the three-dimensional stress concentration has the smaller critical volume. Therefore the correction is:

$$f_{volume\ correction} = \left( \frac{V_{crit\ |2D}}{V_{crit\ |3D}} \right)^{1/b} \quad (8-25)$$

Where b is the Weibull modulus, applicable to this analysis method.

### 8.5.2 Application to three-dimensional stress concentrations

In order to apply this to localised three-dimensional stress concentrations, consider the two different ways, discussed in Chapter 3, to define the shape of the critical volume to be used for the application of the critical volume method. The first is a semi-cylindrical shape (Figure 8.12 (a)), which is the logical choice for a 2-D geometry or a geometry with a constant cross-section like Figure 8.1(a) and (c). The second is a semi-spherical shape (Figure 8.12 (b)) which is more applicable to very concentrated or localised stress concentration like Figure 8.1 (b) and (d). It was also shown in Chapter 3 that if the first principal stress is used, the critical radii are  $1.32a_0$  for the semi-cylinder and  $1.54a_0$  for the semi-sphere. The volumes for these shapes are reported in Table 8.5 below.

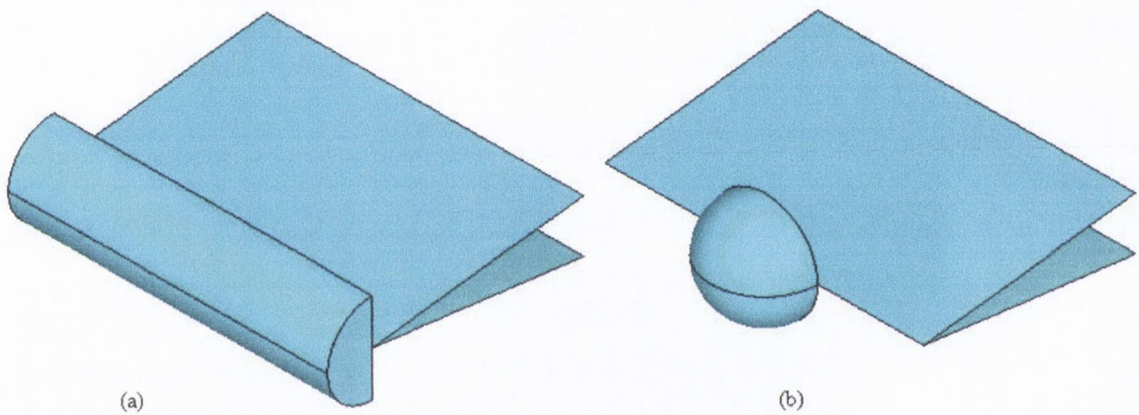


Fig. 8.12 - Two possible choices for the shape of the volume ahead of a stress concentration used in the volume method

Table 8.5 - Volumes of the semi-cylinder and semi-sphere

Semi-cylinder	Semi-Sphere
Critical radius = $1.32a_0$	Critical radius = $1.54a_0$
Volume = $\frac{1}{2}(\pi r_c^2)W = 2.737Wa_0^2$	Volume = $\frac{1}{2} \times \frac{4}{3}(\pi r_c^3) = 7.649a_0^3$

Note: W = the width of the specimen

### 8.5.3 Application to the various specimens

Table 8.6 below shows the critical volumes used for each of the three-dimensional specimens. Note that the specimens do not have the same critical volume.

- The critical volume for the Model-E specimen is simply the semi-spherical volume.
- In the case of the Model-J specimen, the specimen is so thin the majority of the semi-spherical volume is outside of the specimen.
- For the Model-T specimen, it seems wrong to use a semi-spherical volume. This is because we know that the stress gradient along the notch is quite shallow, making this specimen more similar to a 2D notch. Therefore, the effective volume has been calculated by assuming it will be a semi-cylindrical shape. The length of the cylinder has been estimated by taking the distance along the notch where the stress is greater than the plain specimen fatigue strength (i.e.  $\Delta\sigma > \Delta\sigma_0$ ). This results in a semi-cylindrical shape with a length of 5.1mm.
- A similar procedure was used to calculate the length of the semi-cylindrical volume used for the T-shape-B welded specimen. In this case the length is approximately 1.5mm.
- For the Fillet-A welded specimen, the critical volume is one quarter of a sphere, because in this case failure occurs from a corner.

Table 8.6 - The critical volumes used for each of the 3-D specimens investigated

		Critical volume	
	Shape	Size	
2D notched specimen	Semi-cylinder	$2.737Wa_o^2 = 2.737 \times 25.4 \times 0.205^2 = 2.922mm^3$	<u>Solid steel</u>
		$2.737Wa_o^2 = 2.737 \times 25.4 \times 0.43^2 = 12.854mm^3$	<u>Welds</u>
Model-E	Semi-sphere	$7.649a_o^3 = 7.649 \times 0.205^3 = 0.0659mm^3$	
Model-T	Semi-cylinder	$2.737Wa_o^2 = 2.737 \times 5.1 \times 0.205^2 = 0.5866mm^3$	
Model-J	Part-sphere	$0.00269mm^3$	
Fillet-A	1/4-sphere	$7.649a_o^3 / 2 = 7.649 \times 0.43^3 / 2 = 0.3041mm^3$	
T-shape-B	Semi-cylinder	$2.737Wa_o^2 = 2.737 \times 1.5 \times 0.43^2 = 0.7591mm^3$	

Note:  $a_o = 0.205mm$  for the solid steel specimens and  $0.43mm$  for the welded specimens

The effective volume corrections when compared to a 2D notched geometry with a width of 25.4mm are shown below in Table 8.7, for various values of the Weibull modulus.

Table 8.7 - The effective volume of a beam loaded in three-point bending

Weibull modulus, b	The effective volume correction, $f_{volume\ correction}$				
	Model-E	Model-T	Model-J	Fillet-A	T-shape-B
1	44.340	4.981	1086.245	42.269	16.935
10	1.461	1.174	2.012	1.454	1.327
15	1.288	1.112	1.594	1.284	1.208
20	1.209	1.084	1.418	1.205	1.152
30	1.135	1.055	1.262	1.133	1.099
60	1.065	1.027	1.124	1.064	1.048
100	1.039	1.016	1.072	1.038	1.029

It can be seen that the correction factor quickly approaches 1 as the Weibull modulus increases.

#### 8.5.4 Discussion

If we were to speculate and assume that Weibull modulus to be approximately 20, then it can be seen that an almost negligible correction is made for the Model-T specimens while a correction of between 1.124 and 1.418 are made for the remaining specimens. This would appear to make a lot of sense. Also, there is no reason to assume that the two materials considered (i.e. solid steel and welded steel) should have the same Weibull modulus. In fact it is more logical to assume that, due to the nature of welding, the welded material will have a lower Weibull modulus.

As already stated the Weibull modulus is an empirically determined material constant, but only within the framework of a particular analysis method. Therefore, there is no possibility of obtaining a value from the literature. To put it bluntly, there is simply not enough data considered above to make a concrete conclusion.

In the following chapter, stressed volume corrections based on this approach are applied to the various 3D specimens discussed throughout this work. The Weibull modulus is assumed to be 20 for the solid steel specimen and 10 for the welded specimens. As already



stated there is not enough data to say if these are realistic values. Nevertheless it is shown that, in general, good predictions are made if these values for the Weibull modulus are used.

## **8.6 Concluding Remarks**

Two different approaches, both based on a Weibull type analysis have been investigated to describe the probabilistic aspect, or stressed volume effects observed in fatigue data. It was shown that both methods could be used to predict the fatigue behaviour of notched components, if appropriate values of the Weibull modulus are used. The problem is that we have no way of determining if those values are actually realistic.

Another reason for caution regarding the forgoing analysis relates to the scatter in the experimental data. It has been shown that reducing the size of the stressed volume of a fatigue specimen has the effect of increasing the mean life. However, it is expected that the dispersion of the experimental data will also increase. This is not reflected in all of the experimental data obtained in this work, particularly for the Model-J specimen (see Figure 7.30), in which the scatter is extremely low. Hence, this tends to indicate that, for this specimen, the explanation for the bad predictions should probably be sought elsewhere. Nevertheless, the stress volume effect is applied to all specimens in the following chapter. It is concluded that more work needs to be done in this area.

## Chapter 9: Combining the Effects

The purpose of this section is to look at the big picture and to tie together the results from the preceding three chapters in which the various effect were considered separately. Therefore, the following is a brief summary of the application of all three effects to the three-dimensional specimens considered throughout this work.

### 9.1 Model-E

It is believed that the Model-E specimen is affected by the shape effect and the stressed volume effect only. If the actual fatigue crack is assumed to be circular in shape than the correction due to the shape effect is:

$$f_{shape\ correction} = 1.58$$

As discussed in Section 8.5.4 and Table 8.7 of the previous chapter, if the Weibull modulus is assumed to be 20, then the correction due to the size effect is:

$$f_{size\ correction} = 1.288$$

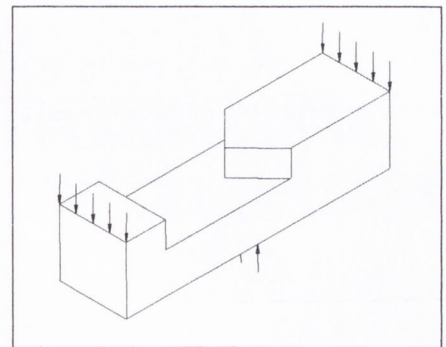


Fig. 9.1 - Model-E

Table 9.1 below show the results of the fatigue analyses for this specimen, with and without the application of these correction factors. It can be seen that results are very good, with error factors very close to one, if these correction are considered.

Table 9.1 - Fatigue analysis results of Model-E1 with and without the correction factors

	Without correction	With corrections $f_{shape\ correction} = 1.58$ $f_{size\ correction} = 1.288$
<b>Experimental</b>	6.6 kN at $2 \times 10^6$ cycles	
<b>Point method</b> (Error factor)	2.99 kN (2.21)	6.08 kN (1.09)
<b>Line method</b> (Error factor)	3.06 kN (2.16)	6.23 kN (1.06)

Note: Error factor is defined as the ratio of the Experimental fatigue strength to the predicted fatigue strength

## 9.2 Model-T

As discussed in Chapter 5, good results were obtained for the Model-T specimen without the application of any correction. It is therefore believed that this specimen is not greatly affected by any of the three factors investigated.

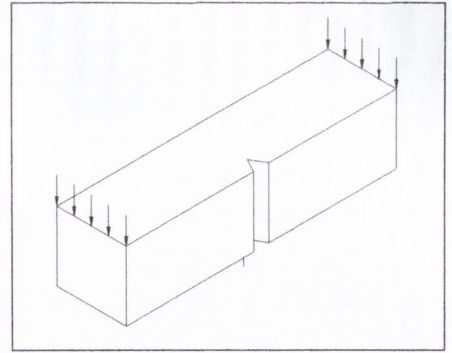


Fig. 9.2 - Model-T

It was shown experimentally that the actual crack shape for this specimen is highly elliptical. Hence, the shape correction factor was determined to be:

$$f_{\text{shape correction}} = 1.051$$

As discussed in Section 8.5.4 and Table 8.7 of the previous chapter, if the Weibull modulus is assumed to be 20, then the correction due to the stressed volume effect is also very low:

$$f_{\text{size correction}} = 1.084$$

In terms of the constraint effect this specimen is quite problematic. As discussed in Chapter 7, it is believed that the stress state at the failure location is neither pure plane stress nor plane strain. Hence, some effect of low constraint should be observed. However having said that, it is expected that the stress state will be predominately plane strain. Hence, it is believed that the correction for low constraint will be small and not greatly affect the results for the Model-T specimen.

As there is no reliable way of quantifying the constraint effect for this specimen, Table 9.2 below demonstrated the application of the shape and stressed volume corrections only. It can be seen that the application of any correction factor, no matter how small, makes the predictions worse.

Table 9.2 - Fatigue analysis results Model-T with and without the correction factors

	Without correction	With corrections $f_{shape\ correction} = 1.051$ $f_{size\ correction} = 1.084$
<b>Experimental</b>		11.4 kN at $2 \times 10^6$ cycles
<b>Point method</b> (Error factor)	11.48 kN (0.99)	13.08 kN (0.87)
<b>Line method</b> (Error factor)	13.56 kN (0.84)	15.44 kN (0.74)
<b>CMM</b> (Error factor)	13.64 kN (0.85)	15.54 kN (0.73)

Note: Error factor is defined as the ratio of the Experimental fatigue strength to the predicted fatigue strength

### 9.3 Model-J

In this case, the thickness of the section, at the failure location, is small compared to the plastic zone size. Hence, the stress state is expected to approach conditions of plane stress. Therefore, it is believed that the Model-J specimen is affected by the constraint and stressed volume effects only.

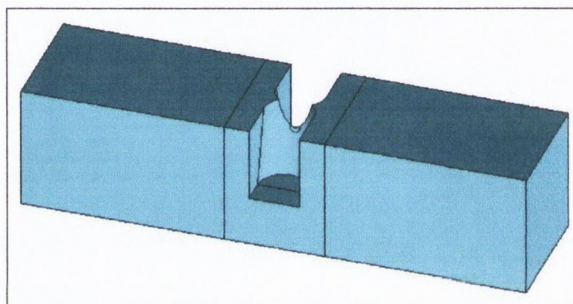


Fig. 9.3 - Model-J

As discussed in Section 8.5.4 and Table 8.7 of the previous chapter, if the Weibull modulus is assumed to be 20, then the correction due to the stressed volume effect is:

$$f_{size\ correction} = 1.418$$

As discussed in Chapter 7, section 7.6.1, one way to account for the effect of constraint was two assume that the relationship between the threshold measured in plane strain and plane stress is similar to that which exists for fracture toughness. This lead to an upper and lower bound for the threshold, which could be used to estimate the effect of constraint in fatigue. In the following both the upper and lower bounds are considered. The results are presented in Tables 9.3 and 9.4 below. It can be seen that if the upper bound is considered the point method still contains a slight conservative error, but in general the results are quite good. If the lower bound for the constraint correction in used, conservative errors, which are quite large, are still apparent.

Table 9.3 - Fatigue analysis results Model-J with and without the correction factors, using the **UPPER bound** for the correction due to constraint

	Without correction	With the correction due to constraint $\Delta K_{th pstress}=3\Delta K_{th pstrain}$	With both corrections $f_{size\ correction} = 1.418$
<b>Experimental</b>	3.16 kN at $2 \times 10^6$ cycles		
<b>Point method</b> (Error factor)	0.97 kN (3.26)	1.79 kN (1.77)	2.54 kN (1.24)
<b>Line method</b> (Error factor)	1.07 kN (2.95)	2.21 kN (1.43)	3.13 kN (1.01)
<b>CMM</b> (Error factor)	0.766 kN (4.12)	2.30 kN (1.37)	3.26 kN (0.97)

Note: Error factor is defined as the ratio of the Experimental fatigue strength to the predicted fatigue strength

Table 9.4 - Fatigue analysis results Model-J with and without the correction factors, using the **LOWER bound** for the correction due to constraint

	Without correction	With the correction due to constraint $\Delta K_{th pstress}=1.5\Delta K_{th pstrain}$	With both corrections $f_{size\ correction} = 1.418$
<b>Experimental</b>	3.16 kN at $2 \times 10^6$ cycles		
<b>Point method</b> (Error factor)	0.97 kN (3.26)	1.12 kN (2.82)	1.59 kN (1.98)
<b>Line method</b> (Error factor)	1.07 kN (2.95)	1.29 kN (2.45)	1.83 kN (1.73)
<b>CMM</b> (Error factor)	0.766 kN (4.12)	1.15 kN (2.75)	1.63 kN (1.94)

Note: Error factor is defined as the ratio of the Experimental fatigue strength to the predicted fatigue strength

If it is assumed that the upper bound values are more appropriate for this specimen and this material, it can be seen that the errors are acceptable. Alternatively, it is possible to achieve acceptable errors by using a constraint correction that is within the expected range.

## 9.4 Fillet-A

It is expected that the main factors affecting the Fillet-A specimen are the shape effect and the stressed volume effect.

If the shape of the actual crack is assumed to be circular, the shape correction is:

$$f_{\text{shape correction}} = 1.58$$

As discussed in Section 8.5.4 and Table 8.7 of the previous chapter, if the Weibull modulus, for the welded material is assumed to be 10, then the correction due to the stressed volume effect is:

$$f_{\text{size correction}} = 1.454$$

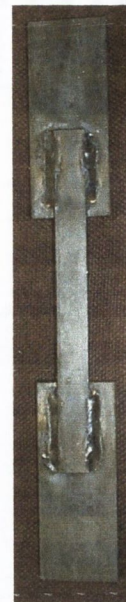


Fig. 9.4 - Fillet-A

In terms of the constraint effect the comments made above with respect to the Model-T specimen are also valid here.

Table 9.5 below shows the application of the shape and stressed volume corrections to the Fillet-A specimen. It can be seen that these corrections result in very good predictions with error factors approximately equal to one.

Table 9.5 - Fatigue analysis results Fillet-A with and without the correction factors

	Without correction	With corrections $f_{\text{shape correction}} = 1.58$ $f_{\text{size correction}} = 1.454$
<b>Experimental</b>	8.4 kN at $5 \times 10^6$ cycles	
<b>Point method</b> (Error factor)	3.78 kN (2.22)	8.68 kN (0.96)
<b>Line method</b> (Error factor)	3.33 kN (2.52)	7.65 kN (1.09)
<b>CMM</b> (Error factor)	4.24 kN (1.98)	9.74 kN (0.86)

Note: Error factor is defined as the ratio of the Experimental fatigue strength to the predicted fatigue strength

## 9.5 T-shape-B

It is expected that the T-shape-B welded specimen will be affected by both the shape and stressed volume effects, while the constraint effect is not expected to be significant.

If the elliptical ratio of the actual fatigue crack is assumed to be 0.4, then the correction factor due to crack shape is:

$$f_{\text{shape correction}} = 1.151$$

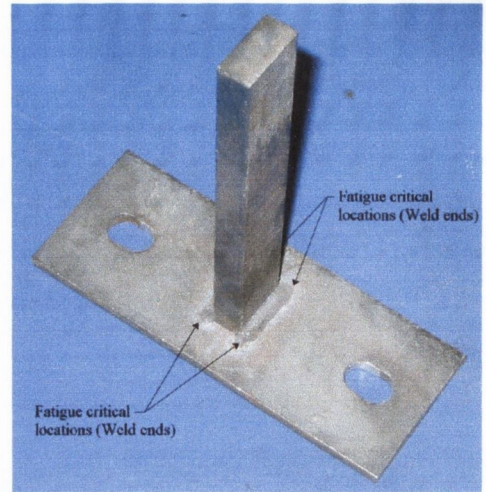


Fig. 9.5 - T-shape-B

As discussed in Section 8.5.4 and Table 8.7 of the previous chapter, if the Weibull modulus, for the welded material is assumed to be 10, then the correction due to the stressed volume effect is:

$$f_{\text{size correction}} = 1.327$$

Table 9.6 below shows the results of the fatigue analyses of this specimen with and without the application of the corrections. It can be seen the addition of the correction factors results in acceptable predictions, with error factors ranging between 1.05 and 1.29.

Table 9.6 - Summary of results from the fatigue assessment of T-shape-B

	Without correction	With corrections $f_{\text{shape correction}} = 1.151$ $f_{\text{size correction}} = 1.327$
<b>Experimental</b>	6.62 kN at $5 \times 10^6$ cycles	
<b>Point method</b> (Error)	3.75 kN (1.77)	5.73 kN (1.15)
<b>Line method</b> (Error)	3.34 kN (1.98)	5.10 kN (1.29)
<b>CMM</b> (Error)	4.12 kN (1.61)	6.29 kN (1.05)

Note: Error factor is defined as the ratio of the Experimental fatigue strength to the predicted fatigue strength

## 9.6 Discussion

It can be seen that the corrections given above are in general successful at explaining the conservative errors originally obtained using the CDMs and the CMM alone.

It should be noted however that these results have been presented in the most flattering light possible. This is due to the nature of the assumptions and educated guesses that have had to be made along the way. The most noteworthy of these include:

- The method used to estimate crack shape. In all cases except the Model-T specimen, crack shape was estimated base on engineering judgement alone.
- The method used to predict the constraint effect. In the above, the biggest correction, which is still within the realm of possibility, was used.
- The value of the Weibull modulus used to predict the stressed volume effect. As already stated this is an experimentally determined material constant. Even though the values used above make a great deal of sense, it must be acknowledged that there is not enough data considered to make any concrete conclusions about the accuracy of the stressed volume correction.



## Chapter 10: Conclusions

---

1. Normal fatigue assessment methods are not able to predict the fatigue behaviour of three-dimensional stress concentration features in which the failure is constrained to occur from a very localised stress concentration, characterised by large stress gradients in all directions emanating from the hotspot. This was shown to be the case for the CDMs and the CMM discussed in the body of this work and the other fatigue assessment methods used in Appendix B, which include the traditional Peterson and Neuber approaches. In particular, all of these fatigue assessment methods result in conservative errors. This has been demonstrated experimentally for both welded geometries and a specimen machined from solid steel.
2. A partial explanation for this is related to the fact that fatigue cracks resulting from this type of stress concentration typically have an elliptical shape. It is proposed that crack shape can have an effect on the fatigue life of sharp, crack-like stress concentrations, for which the fatigue strength is characterised by the growth of non-propagating cracks. In particular, it is shown that fatigue assessment methods which make use of the 2D focus path concept make an inherent assumption regarding crack shape and that a simple correction factor, based on the actual crack shape, can be applied to account for this. It is demonstrated that this correction improves the predictions for the 3D specimens considered here, however conservative errors still remain.
3. It was also demonstrated that normal fatigue assessment methods are unable to predict the behaviour of stress concentration features characterised by low notch tip constraint. Again, significant conservative errors are obtained. It is believed that this is analogous to the effect of constraint observed in fracture mechanics, whereby the fracture toughness measured in plane stress is found to be much higher than the corresponding value determined in plane strain. It was subsequently shown experimentally, using a material with a large  $a_0$  value, that the stress intensity threshold is also a function of constraint. That is, the threshold measured in plane stress is higher than the plane strain value. It can be seen that this has a direct

impact on the CDMs and the CMM, which both make use of this parameter. It was proposed that this could be accounted for by assuming that the relationship between the threshold measured in plane strain and plane stress is similar to that which exists for fracture toughness. It was demonstrated that even if this is done in the most optimistic way, conservative errors are still apparent.

4. Methods to determine the degree of constraint were investigated. The most useful criterion was to relate the plastic zone size to the specimen thickness. Based on this, it is believed that most three-dimensional stress concentrations are not affected by a constraint effect, although other geometries, characterised by very thin sections, like knife-edge stress concentrations, will be affected.
5. A third possible effect has been investigated which may explain the conservative errors that remain even after the application of the corrections discussed above. It is proposed that a geometry characterised by a small volume of highly stressed material will have a lower probability of failure and consequently appear stronger. A correction factor, based on a Weibull type analysis has been proposed, which can be applied to the CDMs. It is shown that if reasonable values of the Weibull modulus are assumed (i.e. values within the expected range) then sensible corrections can be made for the 3D specimen considered. Unfortunately, the validity of this analysis is unproven.
6. It was also demonstrated that for these types of stress concentrations the volume and area implementation of the critical distance methods does not result in a significant improvement over the simpler point and line methods. It is concluded that the slight increase in accuracy is not worth the additional computational complexity.

## References:

---

**Akiniwa, Y., Tanaka, K. and Zhang, L., (1997)**, Prediction of fatigue thresholds of notched components based on resistance-curve method, in *Fatigue '96, Proceedings of the Sixth International Fatigue Congress*, eds. G. Lütjering and H. Nowack, Pergamon, Oxford, pp. 449-454.

**Ashby, M. F. and Jones, D. R. H., (1986)**, *Engineering materials 2: an introduction to microstructures, processing and design*, Pergamon Press, England.

**ASTM, (1974)**, Standard methods of test for plane-strain fracture toughness of metallic materials, ASTM Designation: E 399 - 74.

**ASTM, (1991)**, Standard practice for statistical analysis of linear or linearized stress-life (S-N) and strain-life (e-N) fatigue data, ASTM Designation: E 739 - 91.

**Barrett, N., (1998)**, Failure analysis of simple weld geometries: crack modelling method, M. Sc. Thesis, Department of mechanical and manufacturing engineering, University of Dublin, Trinity College, Ireland.

**Boller, C. H. R. and Seeger, T., (1987)**, *Materials science monographs, 42B: Materials data for cyclic loading - Part B: Low-alloy steels*, Elsevier, Oxford.

**BSI, (1987)**, British standard specification for wrought aluminium and aluminium alloys for general engineering purposes: plate, sheet and strip, BS 1470: 1987.

**BSI, (1993)**, Code of practice for fatigue design and assessment of steel structures, BS 7608: 1993.

**Crupi, G., Crupi, V., Guglielmino, E. and Taylor, D., (2002)**, Fatigue assessment of welded joints by different approaches, In: *Fatigue 2002, Proceedings of the eighth international fatigue congress*, Stockholm, Sweden.

**Dowling, N.E., (1993),** *Mechanical Behavior of Materials - Engineering Methods for Deformation, Fracture and Fatigue*, Prentice-Hall Inc, New Jersey.

**Dugdale, D. S., (1960),** Yielding of steel sheets containing slits, *J. Mech. Phys. Solids*, Vol. 8, pp. 100.

**Ewalds, H. L. and Wanhill, R.J.H, (1989),** Fracture mechanics, DUM.

**Elber, W., (1970),** Fatigue crack closure under cyclic tension, *Engineering Fracture Mechanics*, Vol. 2, pp. 37-45.

**El Haddad, M. H., Smith, K. N. and Topper, T. H., (1979),** Fatigue crack propagation of short cracks, *Journal of Engineering Materials and Technology*, Vol. 101, pp. 42-45.

**El Haddad, M. H., Topper, T. H. and Smith, K. N., (1979),** Prediction of non propagating cracks, *Engineering Fracture Mechanics*, Vol. 11, pp. 573-584.

**El Haddad, M. H., Dowling, N. E., Topper, T. H. and Smith, K. N., (1980),** J integral applications for short fatigue cracks at notches, *Int. J. Fatigue*, Vol. 16, No. 1, pp. 15-30.

**ESDU 76007, (1976),** Fatigue strength of longitudinal fillet welded attachments and joints in steels under axial loading, *Engineering science data unit*.

**Farahmand B., Bockrath G. and Glassco J., (1997),** *Fatigue and fracture mechanics of high risk parts: Application of LEFM & FMDM Theory*, Chapman & Hill.

**Fenner, A. J., Owen, N. B. and Phillips, C. E., (1951),** *Engineering, Lond.*, Vol. 171, pp. 637.

**Fischer, H., Rentzsch, W. and Marx, R., (2002),** A modified size effect model for brittle non-metallic materials, *Engineering Fracture Mechanics*, Vol. 69, pp. 781-791.

**Frost, N. E. and Dugdale, D. S., (1957),** *J. Mech. Phys. Solids*, Vol. 5, pp. 182.

**Frost, N. E., (1959)**, A relation between the critical alternating propagation stress and crack length for mild steel, *Proc. Instn. Mech. Engrs.*, Vol. 173, No. 35, pp. 811-827.

**Guillois, J., (2000)**, *Fatigue failure in a plane stress component*, Université Joseph Fourier, DESS Modélisation et Simulation en Mécanique, France.

**Gdoutos, E. E., (1990)**, *Fracture mechanics criteria and applications*, Kluwer Academic Publishers, The Netherlands.

**Guo, W., Wang, C. H. and Rose, L. R. F., (1999)**, The influence of cross-sectional thickness on fatigue crack growth, *Fatigue Fract. Engng. Mater. Struct.*, Vol. 22, pp. 437-444.

**Heywood, R. B., (1962)**, *Designing against fatigue*, Chapman and Hall Ltd, London.

**Irwin, G. R. J., (1957)**, *Appl. Mech. Tran. ASME*, Vol. 24, pp.361.

**Irwin, G. R. J., (1958)**, Fracture, *In: Handbuch der Physik*, 6, Springer-Verlag, Heidelberg, pp. 551-590.

**Kitagawa, H. and Takahashi, S., (1976)**, Applicability of fracture mechanics to very small cracks or the cracks in the early stage, *Proceedings of the second international conference on mechanical behaviour of materials*, Boston, pp. 627-613.

**Knott, J. F., (1973)**, *Fundamentals of fracture mechanics*, Butterworths, London.

**Lin, X.B. and Smith, R. A., (1997)**, Shape growth simulation of surface cracks in tension fatigued round bars, *Int. J. Fatigue*, Vol. 19, No. 6, pp. 461-469.

**Lin, X.B. and Smith, R. A., (1999)**, Shape evolution of surface cracks in fatigued round bars with a semicircular circumferential notch, *Int. J. Fatigue*, Vol. 21, pp. 965-973.

- Lucano, G., (1998)**, Undergraduate thesis, Dipartimento di meccanica, Politecnico de Torino, Turin, Italy.
- Marco, S., (2000)**, Fatigue failure in welded components: a study of two innovative methods, Undergraduate Thesis, Dipartimento di meccanica, Politecnico di Torino, Italy.
- Mazzeo, E., (2000)**, Applications of new methods for fatigue life prediction. The shape effect in stress concentrators, Undergraduate Thesis, Dipartimento di meccanica, Politecnico di Torino, Italy.
- Miller, K. J., (1993)**, The two thresholds of fatigue behaviour, *Fatigue Fract. Engng Mater. Struct.*, Vol. 16, No. 9, pp. 931-929.
- Molski, K. and Glinka, G., (1981)**, A method of elastic-plastic stress and strain calculations at a notch root, *Mat. Sci. Eng.*, Vol. 50, pp. 93.
- Neuber, H., (1958)**, *Kerbspannungstehre*, Springer, Berlin; *Translation Theory of notch stresses*, U.S. Office of Technical Services, Washington, DC, 1961.
- Neuber, H., (1961)**, Theory of stress concentration for shear-strained prismatical bodies with arbitrary nonlinear stress strain laws, *Trans. ASME, J. Appl. Mech.*, Vol. 28, 1961, pp. 544.
- Parker, A. P., (1981)**, *The mechanics of fracture and fatigue*, E. & F. N. Spon Ltd, London.
- Partanen, T. and Niemi, E., (1996)**, Hot spot stress approach to fatigue strength analysis of welded components: fatigue test data for steel plate thicknesses up to 10 mm, *Fatigue Fract. Engng Mater. Struct.*, Vol. 19, No. 6, pp. 709-722.
- Peterson, R. E., (1959)**, Notch sensitivity. In *Metal fatigue* (Eds. Sines, G. and Waisman, J.L.), McGraw Hill, New York, pp. 293-306.
- Peterson, R. E., (1974)**, *Stress concentration factors*, New York, John Wiley.

**Pickard A. C., (1986)**, *The application of 3-Dimensional finite element methods to fracture mechanics and fatigue life prediction*, Engineering materials advisory services Ltd., London.

**Pircher, T., (2001)**, The shape factor effect in new methods for fatigue life predictions, Undergraduate Thesis, Dipartimento di meccanica, Politecnico di Torino, Italy.

**Pluvinage, G., (1998)**, Fatigue and fracture emanating from a notch; the use of the notch stress intensity factor, *Nuclear Engineering and Design*, Vol. 185, pp. 173-184.

**Qylafku, G., Azari, Z., Kadi, N., Gjonaj, M. and Pluvinage, G., (1999)**, Application of a new model proposal for fatigue life prediction on notches and key-seats, *Int. J. Fatigue*, Vol. 21, pp. 753-760.

**Qilafku, G., Kadi, N., Dobranski, J., Azari, Z., Gjonaj, M. and Pluvinage, G., (2001)**, Fatigue of specimens subjected to combined loading. Role of hydrostatic pressure, *Int. J. Fatigue*, Vol. 23, pp. 689-701.

**Schijve, J., (2001)**, *Fatigue of structures and materials*, Kluwer Academic Publishers, The Netherlands.

**Siebel, E. and Stieler, M., (1955)**, Dissimilar stress distributions and cyclic loading, *Z. Ver. Deutsch. Ing.*, Vol. 97, 121-131.

**Smith, R. A. and Miller, K. J., (1978)**, Prediction of fatigue regimes in notched components, *Int. J. Mech. Sci.*, Vol. 20, pp. 201-206.

**Stephens, R. I., Fatemi, A., Stephens, R. R. and Fuchs, H. O., (2000)**, *Metal fatigue in engineering: second edition*, John Willey & Sons, Inc., New York.

**Tanaka, K., Nakai, Y. and Yamashita, M., (1981)**, Fatigue growth threshold of small cracks, *Int. J. Fract.*, Vol. 17, pp. 519-533.

**Tanaka, K., (1983)**, Engineering formulae for fatigue strength reduction due to crack-like notches, *Int. Journ. of Fracture*, Vol. 22, R39-R45.

**Tanaka, K. and Nakai, Y., (1983)**, Propagation and non-propagation of short fatigue cracks at a sharp notch, *Fatigue of Engineering Materials and Structures*, Vol. 6, No.4, pp. 315-327.

**Tanaka, K. and Nakai, Y., (1984)**, Mechanics of growth threshold of small fatigue cracks, In: *Fatigue crack growth threshold concepts*, (Eds, Davidson, D. and Suresh, S.), TMS-AIME, New York, USA.

**Taylor, D., (1996)**, Crack modelling: a technique for the fatigue design of components, *Engineering Failure Analysis*, Vol. 3, No. 2, pp. 129-136.

**Taylor, D., (1999)**, Geometrical effects in fatigue: a unifying theoretical model, *Int. J. Fatigue*, Vol. 21, pp. 413-420.

**Taylor, D., (2001)**, A mechanistic approach to critical-distance methods in notch fatigue, *Fatigue Fract. Engng. Mater. Struct.*, Vol. 24, pp. 215-224.

**Taylor, D, Barrett, N, and Lucano, G, (2002)**, Some new methods for predicting fatigue in welded joint, *Int. J. Fatigue*, Vol. 24, pp. 509-518.

**Taylor D., Bologna P. and Bel Knani, K., (2000)**, Prediction of Fatigue Failure Location on a Component Using a Critical Distance Method, *Int.J.Fatigue*, Vol. 22, pp. 735-742.

**Taylor, D. and Carr, A. J., (1999)**, The crack-modelling technique: optimisation of parameters, *Fatigue Fract. Engng. Mater. Struct.*, Vol. 22, pp. 41-50.

**Taylor D., Ciepalowicz A.J., Rogers P. and Devlukia J., (1997)**, Prediction of fatigue failure in a crankshaft using the technique of crack modelling, *Fatigue Fract. Engng. Mater. Struct.*, Vol. 20, No. 1, pp.13-21.



**Taylor, D., Hughes, M. and Allen, D., (1996)**, Notch fatigue behaviour in cast irons explained using a fracture mechanics approach, *Int. J. Fatigue*, Vol. 18, No. 7, pp. 439-445.

**Taylor, D. and Lawless, S., (1996)**, Prediction of fatigue behaviour in stress-concentrators of arbitrary geometry, *Engineering Fracture Mechanics* Vol. 53, No. 6, pp. 929-939.

**Taylor, D. and O'Donnell, M., (1994)**, Notch geometry effects in fatigue: A conservative design approach, *Engineering Failure Analysis*, Vol. 1, No. 4, pp. 275-287.

**Taylor, D. and Wang G., (1999)**, A critical distance theory which unifies the prediction of fatigue limits, small cracks and notches, *Proc. Fatigue '99*, China, publ.Higher Education Press (China) and EMAS (UK), Vol. 1, pp.579-584.

**Taylor D. and Wang G., (1999)**, Component design: the interface between threshold and endurance limit, *ASTM STP 1372 "Fatigue crack growth thresholds, endurance limits and design"*, Eds Newman, Piascik, ASTM.

**Taylor D. and Wang G., (2000)**, The validation of some methods of notch fatigue analysis, *Fatigue Fract. Engng. Mater. Struct.*, Vol. 23, pp. 387-394.

**Taylor D., Zhou W., Ciepalowicz A.J., Devlukia J., (1999)**, Mixed-Mode fatigue from stress concentrations: an approach based on equivalent stress intensity, *Int. J. Fatigue*, Vol. 21, pp. 173-178.

**Topper, T. H., Wetzell, R. M. and Morrow, J. D., (1969)**, Neuber's rule applied to fatigue of notched specimens, *J. Materials, JMSLA*, Vol. 4, No.1, pp. 200.

**Trantina, G. G. and Johnson, C. A., (1983)**, Probabilistic defect size analysis using fatigue and cyclic crack growth rate data, In: *Probabilistic fracture mechanics and fatigue methods: applications for structural design and maintenance*, ASTM STP 798, Bloom, J and Ekvall, J. C., Eds., pp. 67-78.

**Wang G., Taylor D., Bouquin B., Devlukia J. and Ciepalowicz A., (2000)**, Prediction of fatigue failure in a camshaft using the crack-modelling method, *Engineering Failure Analysis*, Vol. 7, pp. 189-197.

**Wang G. (1999)**, Prediction of fatigue failure in engineering components using the finite element method, PhD Thesis, University of Dublin, Trinity College.

**Weibull, W., (1951)**, A statistical distribution function of wide applicability, *Journal of Applied Mechanics*, Vol. 73, pp 293.

**Weibull, W., (1961)**, *Fatigue testing and analysis of results*, Pergamon Press, London.

**Westergaard, H. M., (1939)**, Bearing pressures and cracks, *J. Appl. Mech. A*, pp. 49-53.

# Appendix A: Experimental Investigations

---

The purpose of this appendix is to provide full details of the experimental investigations and fatigue analyses undertaken in this project. Only a brief outline of this work is included in the body of the text, so as not to distract from the line of thought being considered. Because of this there is a small amount of repetition. This is regretted however it is considered necessary.

## **A.1 Material characterisation**

Much of the experimental work undertaken throughout this project was done using the same structural steel. That is BS970: 1996: 080A15 (or previously BS970: 1955: En2B). Considerable work was undertaken to properly characterise this material. This is discussed below.

### A.1.1 Mechanical properties and the monotonic stress-strain relationship

A series of tensile tests were conducted on the steel in order to determine its mechanical properties and monotonic stress-strain relationship. Figures A.1(a) and (b) below show the measured load-displacement curves, (c) and (d) show the resulting engineering stress-strain relationship and the true stress-strain relationship is given in Figures A.1(e) and (f).

From this the average mechanical properties were determined to be the following:

Ultimate tensile strength, UTS	410	MPa
Yield strength, $\sigma_{ys}$	290	MPa
Young's modulus, E	210	GPa
Assumed Poisson's ratio, $\nu$	0.3	

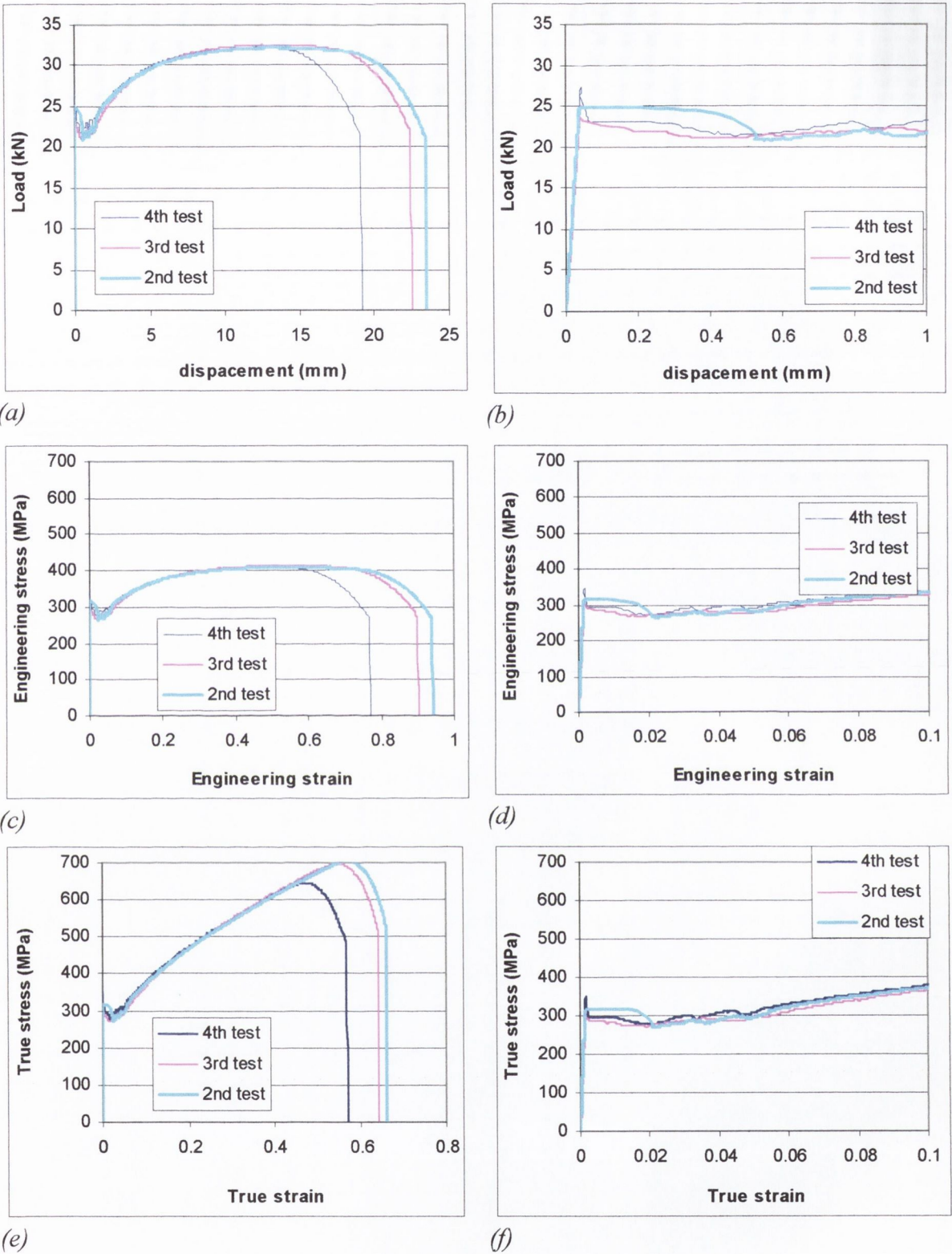


Fig. A.1 - Results of the tensile tests

The true stress ( $\sigma_{true}$ ) and strain ( $\epsilon_{true}$ ) are calculated via the standard equations

$$\sigma_{true} = \sigma_{eng} (1 + \epsilon_{eng}) \quad \text{and} \quad \epsilon_{true} = \ln(1 + \epsilon_{eng}) \quad (A-1)$$

Where,  $\sigma_{eng}$  and  $\epsilon_{eng}$  are the engineering stress and strain respectively.

### A.1.2 The cyclic stress-strain relationship and LCF data

Strain controlled tests were performed on the material by the Gaydon Research Centre, Gaydon, England, which is part of the Landrover group. Figure A.2(a) below shows the measured cyclic stress-strain relationship. Figure A.2(a) is a comparison between the cyclic and monotonic curves. It can be seen that the material cyclically hardens.

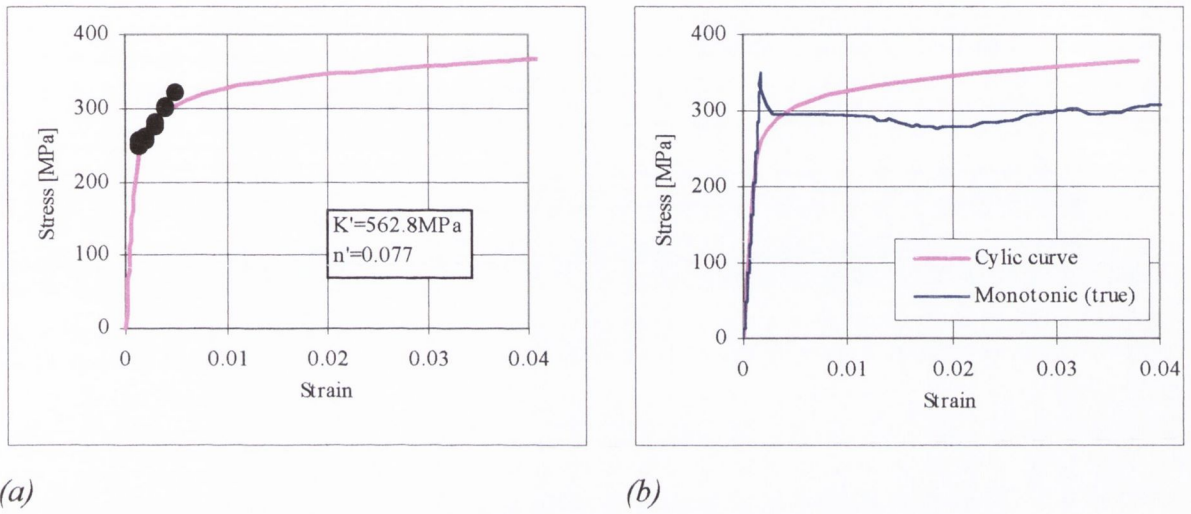


Fig. A.2 - Cyclic stress-strain curve

In order to apply the strain-life method, low cyclic fatigue (LCF) data was also determined by the Gaydon Research Centre. Figure A.3 below shows the resulting strain-life curve, on which the relevant LCF parameters are shown.

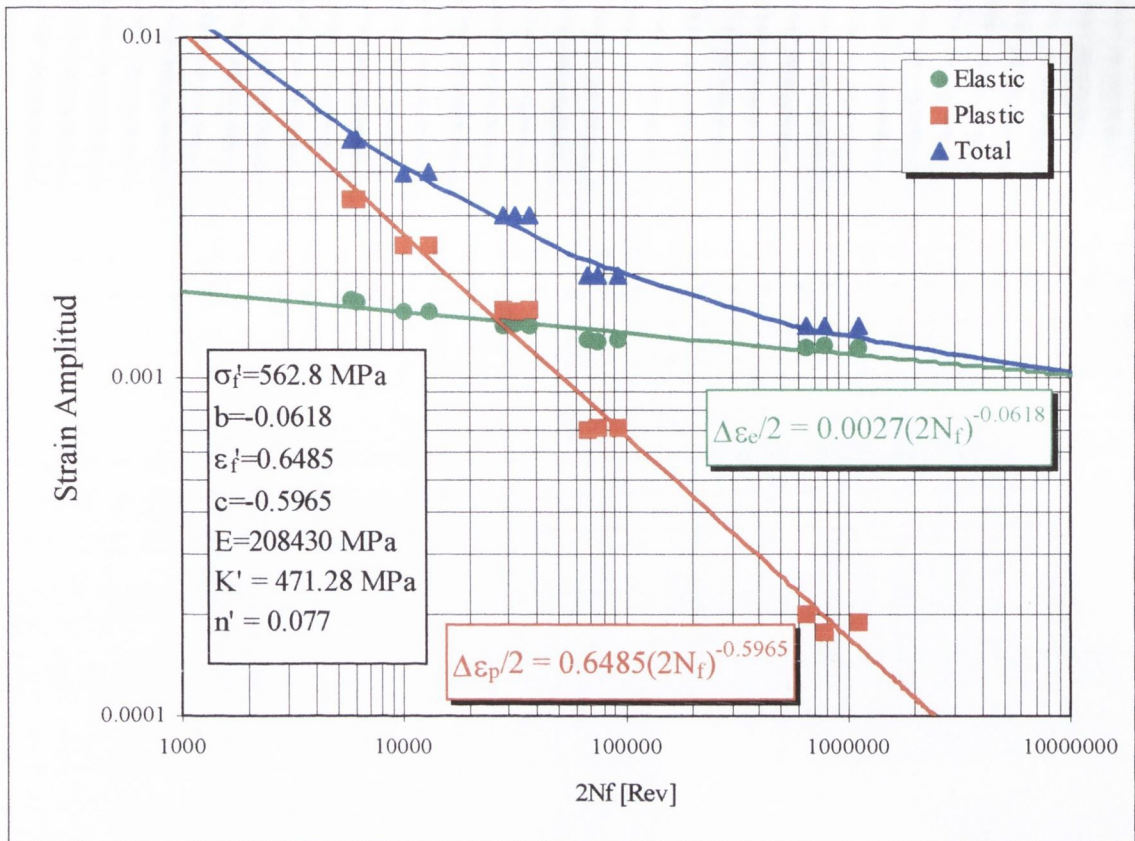


Fig. A.3 - Measured strain-life curve

### A.1.3 Chemical properties

The chemical composition of the material was obtained from a chemical analysis carried out at the TWI Institute, Cambridge, The UK.

Element (wt %)											
C	Si	Mn	P	S	Cr	Mo	Ni	Al	As	B	Co
0.12	0.18	0.57	0.012	0.009	0.079	0.024	0.12	0.004	0.016	0.0003	0.013

### A.1.4 Fatigue properties

#### A.1.4.1 Plain specimen fatigue strength in bending

In order to determine the plain fatigue strength in bending, specimens were machined from inch-by-inch bar. The material at the top and bottom of the section was removed in such a

way as to obtain an inch-by-half inch section with a length of 100 mm, as shown below (Figure A.4).

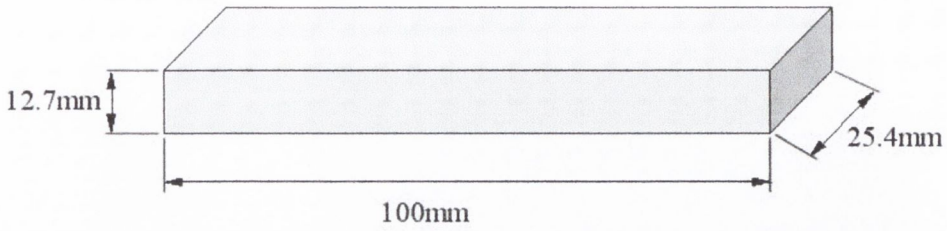


Fig. A.4 - The plain bending specimen

The specimens were tested in three-point-bending at an R-ratio of 0.1. The applied stress range was calculated using the standard elastic bending equations shown below:

$$\left. \begin{aligned}
 M &= \frac{L l}{4} \\
 \sigma &= \frac{M y}{I} \\
 \text{and therefore } \Delta\sigma &= \Delta L \frac{l y}{4 I}
 \end{aligned} \right\} \quad (A-2)$$

Each specimen was individually measured after machining, to account for small variations in size. Hence, slightly different moments of inertia,  $I$ , were determined for each specimen.

The results of the fatigue tests are summarised in Table A.1 below. The ensuing S-N curve is shown Figure A.5.

Table A.1 - Test results for plain bending specimen

Test No	Elastic stress range (MPa)	No. of cycles	Comment
1	435	5.51E+06	No Failure
2	517.1	3.93E+05	Failure
3	488.7	4.68E+05	Failure
4	322.25	1.00E+07	No Failure
5	440	3.40E+05	No Failure
6	402	1.16E+07	No Failure
7	440	6.77E+05	Failure
8	431	2.50E+06	No Failure

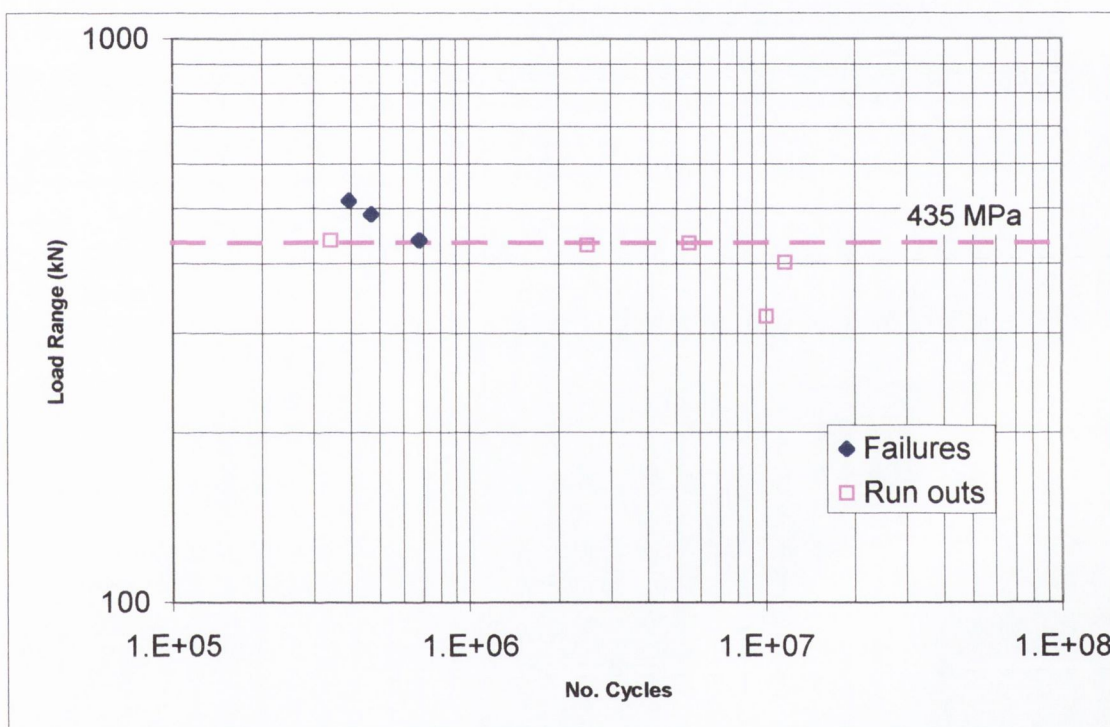


Fig. A.5 - S-N curve for the plain specimen loaded in bending

It can be seen from the above that failure data points are quite scarce. This was because it was very difficult to get failures, as the slope of the curve, in the region between  $1 \times 10^6$  and  $1 \times 10^7$  cycles, is so shallow. Nevertheless the plain specimen fatigue strength (in bending) was determined to be approximately 435 MPa at  $2 \times 10^6$  cycles for an R-ratio of 0.1. At first sight it is possible to assume that this is an error, because it is higher than the ultimate tensile strength of the material (410 MPa, see section A.1.1). However there are two factors that contribute to this. Firstly, as discussed in section A.1.2, the material cyclically hardens. Hence, during the experiments, the specimens were observed to plastically

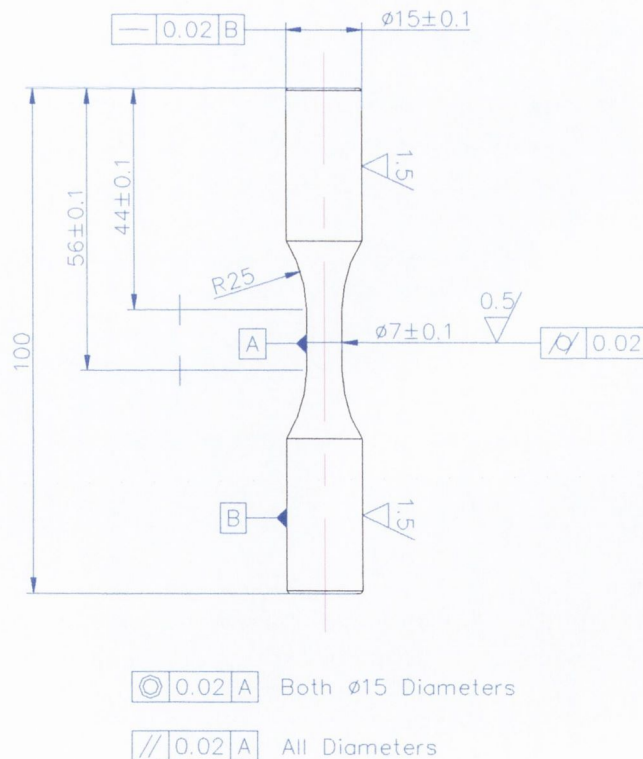


deform, or bend on application of the first several loading cycles and then continue to cycle in an elastic manner. The second contributing factor is that the specimens were loaded in bending, with a relatively thin cross section. Hence the resulting bending gradient creates a stressed volume, or size effect, which causes the fatigue strength determined in bending to be greater than the corresponding value determined in tension.

In order to examine this effect, and also because there was some doubt about the validity of the value determined in bending, the plain specimen fatigue strength was also determined in tension. This is discussed in the section below.

#### A.1.4.2 Plain specimen fatigue strength in tension

The plain specimen fatigue strength for this material was also determined in tension at an R-ratio of 0.1. Hourglass specimens, machined from inch-by-inch bar were used and are shown in Figure A.6 below.



*Fig. A.6 - Tension plain specimen fatigue specimens*

The results are summarised in Table A.2 and illustrated in the S-N curve below (Figure A.7). Also plotted on the S-N curve is the fatigue limit determined in bending.

Table A.2 - Test results for plain tension specimen

Specimen	Elastic stress range (MPa)	No. of Cycles	Comment
1	420.95	9.50E+01	Failure
2	227.36	2.00E+06	No Failure
3	328.70	4.65E+06	No Failure
4	375.48	1.27E+06	Failure
5	389.77	2.18E+02	Failure
6	381.97	3.87E+02	Failure
7	374.18	3.78E+02	Failure
8	374.18	6.49E+02	Failure
9	353.39	1.26E+07	No Failure
10	374.18	1.19E+06	Failure
11	385.87	4.37E+03	Failure
12	363.78	1.23E+06	Failure
13	378.33	5.62E+03	Failure

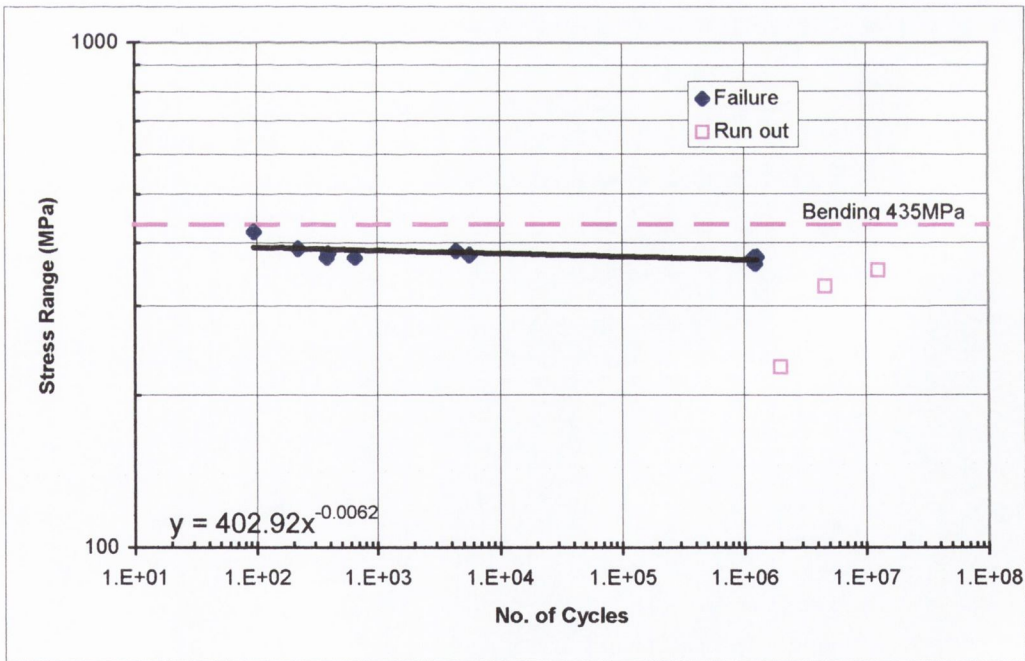


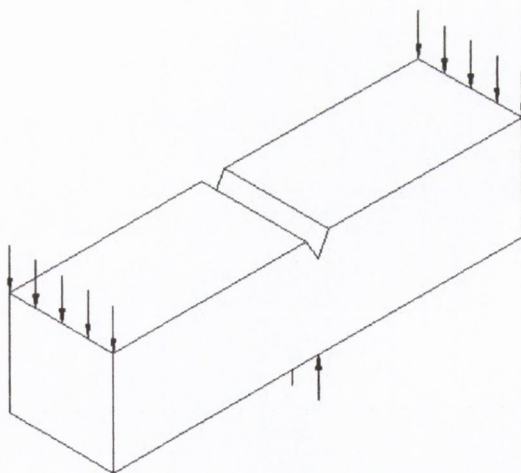
Fig. A.7 - S-N curve for the plain specimens loaded in tension

The plain specimen fatigue strength (in tension) was determined to be approximately 370 MPa at  $2 \times 10^6$  cycles for an R-ratio of 0.1.

It can be seen that the curve is characterised by a very shallow slope, which made testing difficult, as only a very small difference in stress results in a big change in life. Again, this resulted in a limited number of data points in the 1 to 10 million range. However, as expected the fatigue strength, in this case, is less than the value determined in bending and also less than the ultimate tensile strength.

#### A.1.4.3 The threshold stress intensity factor

In order to estimate the threshold stress intensity factor,  $\Delta K_{th}$ , for this material, sharply notched specimens, as shown in Figure A.8 below, were tested.  $\Delta K_{th}$  is then estimated from the notched specimen fatigue strength. This is the usual approach used to determine  $\Delta K_{th}$  throughout this work and is based on the ideas expressed by the Smith & Miller diagram (see Chapter 2, section 2.3.1). The specimens were made from inch-by-inch bar. A notch with a depth of 5mm, a nominal root radius of 0.25mm and an included angle of 45 degrees was machined across the top. The specimens were loaded in three-point bending as shown in Figure A.8 and the length of the specimens was 100mm (i.e. the distance between reaction points).



*Fig. A.8 - Sharply notched specimen used to determine the threshold stress intensity range*

The test results are summarised in Table A.3 below. The resulting S-N curve is shown in Figure A.9.

Table A.3 - Test results for the sharply notched bending specimen

Test No.	Elastic stress range* (MPa)	No. of cycles	Comment
1	187.8	4.40E+04	Failure
2	146	1.38E+05	Failure
3	112.2	1.63E+06	Failure
4	101.7	9.23E+06	Run out
5	108.7	5.00E+05	Failure
6	108.14	3.70E+05	Failure
7	104.63	4.57E+05	Failure
8	94	6.59E+05	Failure
9	86.13	3.50E+06	Run out

\* The stress range is the maximum elastic bending stress calculated using the gross section

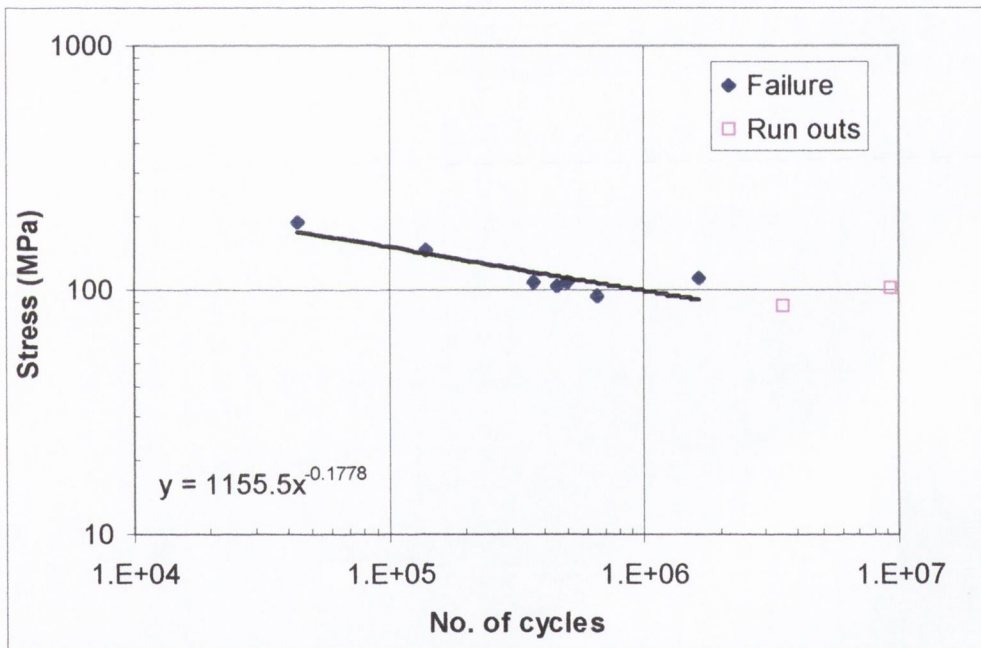


Fig. A.9 - S-N curve for the sharply notched bending specimen

The fatigue strength of this specimen is determined to be 88 MPa at  $2 \times 10^6$  cycles for an R-ratio of 0.1.

#### A.1.4.4 Determining $\Delta K_{th}$ and $a_0$

Because the plain specimen fatigue strength has been determined in both bending and tension, two different sets of values for  $\Delta K_{th}$  and  $a_0$  are determined below (see Table A.4). This raises the question of which values should be used in the fatigue analyses. Within the

body of this report, the values calculated using the plain specimen fatigue strength in bending are used. This is because this was the value determined first and because it can be argued that it is more correct to use these because the sharply notched specimen was also tested in bending. However, within this appendix both sets of material properties are used. It is shown that there is in fact very little difference between the fatigue predictions made using the two different sets of values. This is because the effect of increasing the critical distance is to some extent, cancelled by the effect of decreasing the plain specimen fatigue limit.

The results from testing of the smooth and notched specimens, are summarised below:

$\Delta\sigma_o _{\text{bending}} \cong 435 \text{ MPa}$	at $2 \times 10^6$ cycles	- Plain specimen fatigue strength in bending
$\Delta\sigma_o _{\text{tension}} \cong 355 \text{ MPa}$	at $2 \times 10^6$ cycles	- Plain specimen fatigue strength in tension
$\Delta\sigma_{\text{on}} \cong 88 \text{ MPa}$	at $2 \times 10^6$ cycles	- Fatigue strength of the sharply notched specimen

The stress intensity threshold,  $\Delta K_{th}$  and  $a_o$  are calculated by using El Haddad's equation. This is in the form:

$$\Delta K_{th} = F \Delta\sigma \sqrt{\pi(D + a_o)} \quad (\text{A-3})$$

Where  $D$  is the depth of the notch and  $F$  the configuration or shape factor. It is assumed that:

For the plain or smooth specimens:  $F = 1$ ,  $D = 0 \text{ mm}$  and  $\Delta\sigma = \Delta\sigma_o$

For the notched specimen:  $D = 5 \text{ mm}$  and  $\Delta\sigma = \Delta\sigma_{\text{on}}$

For the notched specimens the configuration or shape factor,  $F$ , was assumed to follow the relationship shown in equation A-4 below. This has been taken from Pickard [1986] and applies to an edge cracked specimen loaded in 3-point bending.

$$F = 1.09 - 0.865 \left( \frac{a}{W} \right) + 2.05 \left( \frac{a}{W} \right)^2 - 1.775 \left( \frac{a}{W} \right)^3 + 0.9125 \left( \frac{a}{W} \right)^4 \quad (\text{A-4})$$

Where  $a$  is the crack length and  $W$  is the width of the specimen. This equation is based on finite element results and is valid for the following geometrical conditions:

$$\frac{L}{W} = 4 \quad \text{and} \quad \frac{a}{W} \leq 1.2 \quad (\text{A-5})$$

For the notched specimen, where  $a = D$ , these requirements are satisfied as:

$$\frac{L}{W} \cong 3.984 \quad \text{and} \quad \frac{D}{W} \cong 0.398 \leq 1.2 \quad (\text{A-6})$$

Hence the configuration factor is found to be:

$$F \cong 0.9816 \quad (\text{A-7})$$

Using the plain specimen fatigue strength determined in **BENDING**, a system of equations is defined as:

$$\begin{cases} \Delta K_{th} |_{bending} = 435 \sqrt{\pi(a_o |_{bending})} \text{ MPa m}^{1/2} \\ \Delta K_{th} |_{bending} = 0.9816 \times 88 \sqrt{\pi(0.005 + (a_o |_{bending}))} \text{ MPa m}^{1/2} \end{cases} \quad (\text{A-8})$$

The results are:

$$\begin{aligned} \Delta K_{th} |_{bending} &\cong 11.046 \text{ MPa m}^{1/2} \\ a_o |_{bending} &\cong 0.205 \text{ mm} \end{aligned} \quad (\text{A-9})$$

Using the plain specimen fatigue strength determined in **TENSION**, a system of equations is defined as:

$$\begin{cases} \Delta K_{th} |_{tension} = 370 \sqrt{\pi(a_o |_{tension})} \text{ MPa m}^{1/2} \\ \Delta K_{th} |_{tension} = 0.9816 \times 88 \sqrt{\pi(0.005 + (a_o |_{tension}))} \text{ MPa m}^{1/2} \end{cases} \quad (\text{A-10})$$

The results are:

$$\begin{aligned} \Delta K_{th} |_{tension} &\cong 11.13 \text{ MPa m}^{1/2} \\ a_o |_{tension} &\cong 0.288 \text{ mm} \end{aligned} \quad (\text{A-11})$$

The resulting two sets of material properties are summarised in Table A.4.

*Table A.4 - Summary of fatigue material properties*

	$\Delta K_{th}$ (MPa m <sup>1/2</sup> )	$\Delta\sigma_o$ (MPa)	$a_o$ (mm)
Bending	11.046	435	0.205
Tension	11.13	370	0.288

It should be noted that  $\Delta K_{th}$  could have been determined directly from the equation below, as in this case the notch depth,  $D$ , is much greater than  $a_o$ . Hence, no short crack effect is observed and the use of El Haddad's equation is unnecessary.

$$\Delta K_{th} = F\Delta\sigma_{on}\sqrt{\pi D} \quad (A-12)$$

#### A.1.4.5 The Smith and Miller diagram

Once the material properties are known, specifically, the plain specimen fatigue strength and the threshold stress intensity factor, it is possible to plot the Smith and Miller diagram for this steel (see Figure A.10 below). The dotted line on the figure indicates the stress concentration factor of the notched specimen used to determine the threshold stress intensity factor (see section A.1.4.4). It can be seen that the notch is in fact crack-like and justifies the use of this specimen to determine the threshold stress intensity factor.

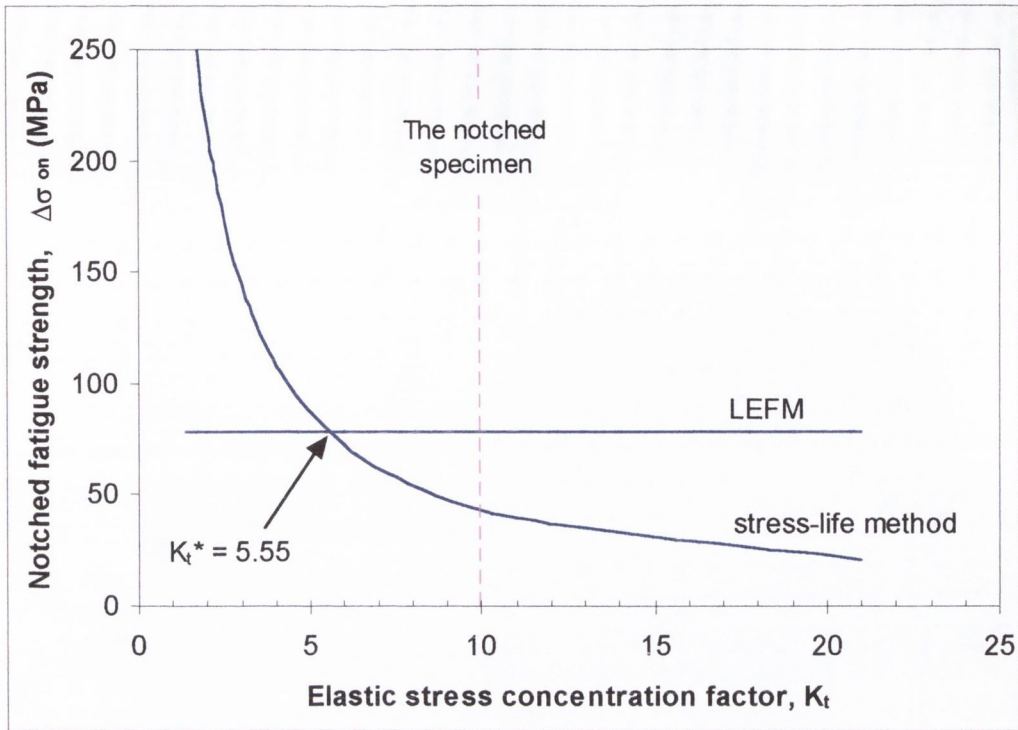


Fig. A.10 - The Smith and Miller diagram

#### A.1.5 Stress relieving

Specimens were heat treated in order to relax residual stresses introduced as a result of machining or welding processes. This was considered especially important for the welded specimens.

In order to stress relieve this steel, specimens were heated slowly to 600°C in a furnace and left at that temperature for 4 hours. After which, the furnace was turned off and the specimens left to cool slowly inside the furnace. The Figure A.11 below shows that this should result in around 85% relief



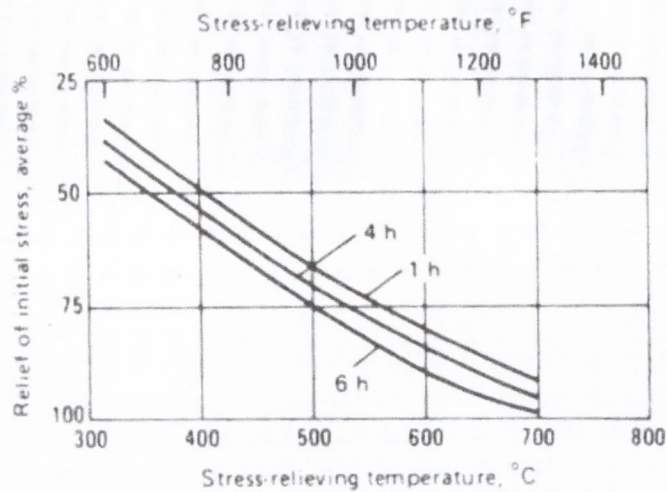


Fig. A.11 - The effect of stress relief on mild carbon steel

### A.1.6 Hardness test

A series of micro hardness tests were conducted on the steel. The purpose of this was to further characterise the material and also to examine the effect of the stress relief process discussed above. Hence, tests were conducted before and after stress relieving.

A micro-hardness testing machine was used to indent highly polished material samples, with a load of 300mg using a diamond pyramid indenter. Both longitudinal and transverse sections (relative to the material rolling direction) were tested. The testing machine automatically calculated the Vicker hardness value,  $H_v$ , which is defined as the load divided by the total surface area of the *indent* [Ashby and Jones, 1986]. The results are reported in Tables A.5 and A.6 below.

Table A.5 - Micro-Vickers hardness values for the non-stress relieved material

Non-stress relieved steel						
		Tests $H_v$				
		1	2	3	4	Average
Section	Transverse	125.3	128.5	132.2	128.6	128.6
	Longitudinal	127.8	129.4	127.2	130.9	128.8

The same experiment was carried out on the stress relieved steel, to determine if the stress relief process affected the hardness of the material and consequently the other material properties.

*Table A.6 - Micro-Vickers hardness values for the stress relieved material*

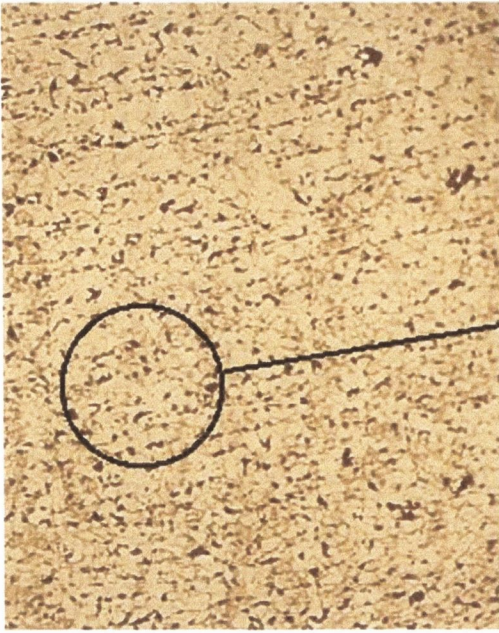
Stress relieved steel						
		Tests H <sub>v</sub>				
		1	2	3	4	Average
Section	Transverse	124.9	127.7	128.5	123.8	126.2
	Longitudinal	132.9	130.3	129.1	129.8	130.5

From the above it was concluded that there was no significant difference in the hardness measured for the stress-relieved and not-relieved material. Hence it was assumed that the stress relief process did not affect the material properties.

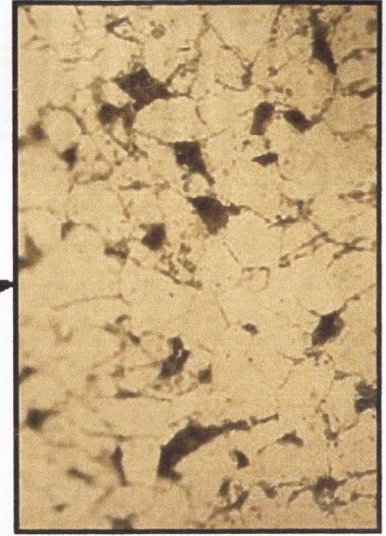
### A.1.7 Microstructure

Figures A.12 and A.13 below show the microstructure of the steel in both the longitudinal and transverse sections (relative to the rolling direction) for two different magnifications. These samples were polished to a roughness of 0.06µm with a diamond suspension mixture. Following this, the polished surfaces were exposed to a weak hydrochloric acid solution, in order to etch the surface and make the grain boundaries visible.

It can be seen that the grains are slightly elongated, due to the effect of rolling, in the longitudinal section, whereas a more uniform structure is observed in the transverse section.

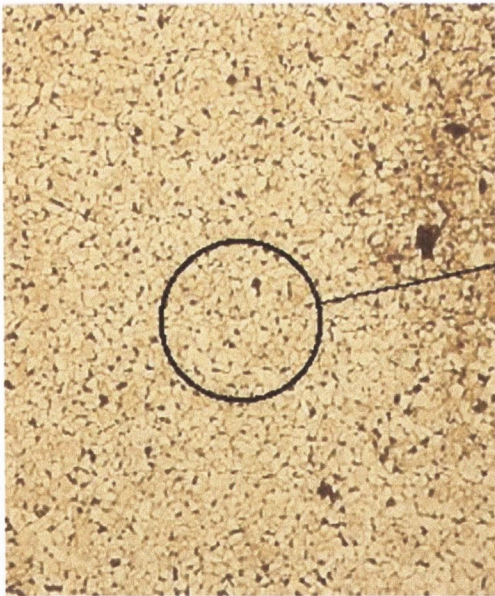


*100 x magnification*

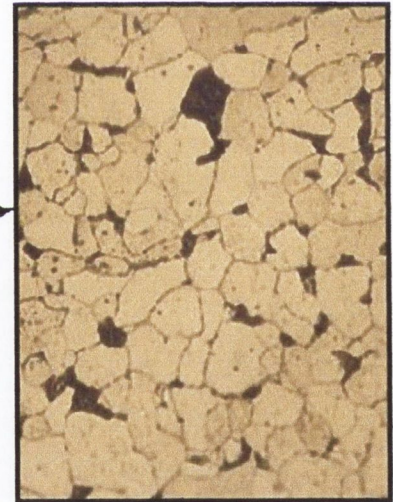


*500 x magnification*

*Fig. A.12 - Microstructure in the longitudinal direction*



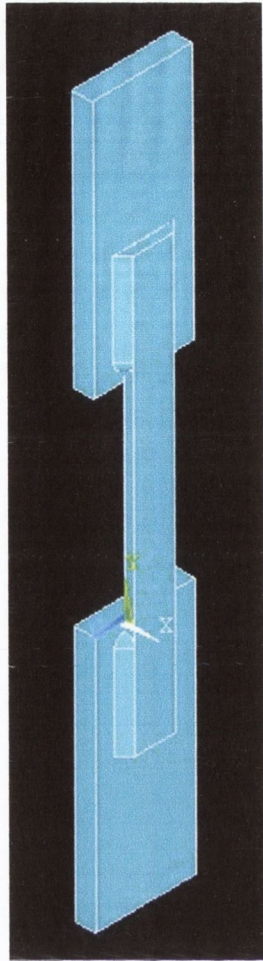
*100 x magnification*



*500 x magnification*

*Fig. A.13 - Microstructure in the transverse direction*





(a) FEA model



(b) Photo

Fig. A.15 - The three-dimensional welded specimen (Fillet-A)

### A.2.2 Material properties and welding

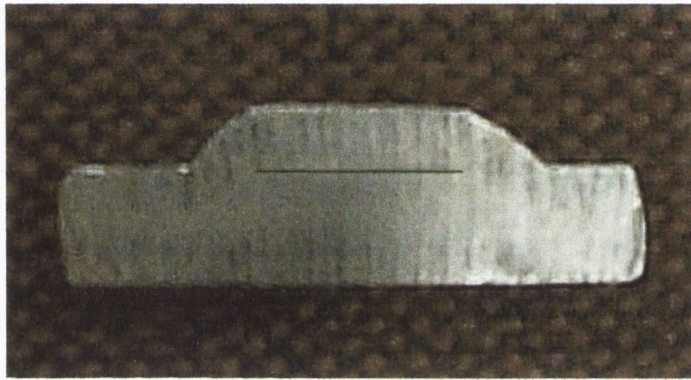
The parent material used to make the Fillet-A specimens was the structural steel discussed in section A.1 above. However, for the fatigue analysis the properties for welded carbon steel, as discussed in Chapter 4, section 4.1, were used. These are summarised below:

The plain specimen fatigue strength, $\Delta\sigma_o$	153 MPa at $5 \times 10^6$ cycles
The threshold stress intensity factor, $\Delta K_{th}$	$6.8 \text{ MPa}\cdot\text{m}^{1/2}$
The El Haddad parameter, $a_o$	0.43 mm

The quality of welding was considered to be good; no undercut, lack of fusion, voids or other discontinuities were encountered, at least in the fatigue critical locations. All of the welding was done by the same operator, using a manual arc welding procedure, with

covered electrodes (class ASME SFA - 5.1, diameter 0.32mm, 138 Amps). A welding jig was also used in order to keep the plates in the correct position during welding

Figure A.16 below shows a transverse cross-section of an actual welded specimen. It can be seen that the penetration of the weld into the narrow plate is almost insignificant. This is evident because the gap between the narrow plate and the wide plate extends in the horizontal direction for a length that is almost equivalent to the width of the narrow plate itself.



*Fig. A.16 - A transverse section of the Fillet-A specimen*

### A.2.3 Experimental results

The specimens were loaded in tension, by fixing the ends and applying a cyclic load at an R-ratio of 0.1 using a servo-hydraulic testing machine. Table A.7 below is a summary of the results obtained.

Table A.7 - Test results, Fillet-A

Specimen No.	R-ratio	Load range [kN]	Horizontal displacement [mm]	No. of cycles	Crack location
1	0.1	18	0.24	152173	Thin plate
2	0.1	5.4	0.07	1E+07	Not failed
3	0.1	9	0.12	1791791	Thin plate
4	0.1	9	0.12	1748717	Thin plate
5	0.1	7.2	0.10	9858009	Wide plate
6	0.1	16.2	0.22	351695	Thin plate
7	0.1	8.1	0.11	7708867	Wide plate
8	0.1	14.4	0.19	316573	Thin plate
9	0.1	12.6	0.17	415489	Thin plate
10	0.1	10.8	0.14	3295745	Wide plate

The final column of Table A.7 indicates that the fatigue cracks didn't always occur in the thin plate, as shown in Figure A.17. Three specimens failed via fatigue crack growth in the wide plate as illustrated in Figure A.18 below. This was investigated via a stress analysis of both ends of the weld bead. It was seen that failure was only slightly more likely to occur in the thin plate than in the wide plate. In fact, the point method predicted the fatigue strength at the wide plate to be only approximately 15% greater than in the thin plate.

Regardless of this, all failures were considered when plotting the S-N curve below. Also, the focus of the stress analysis discussed below is centred on predicting failure in the thin plate.

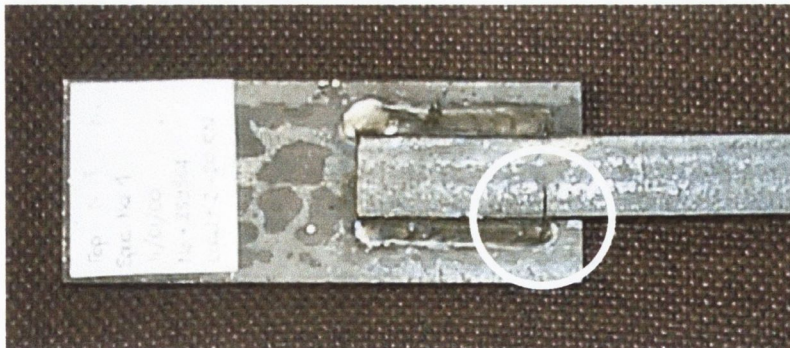


Fig. A.17 - Failure in the thin plate

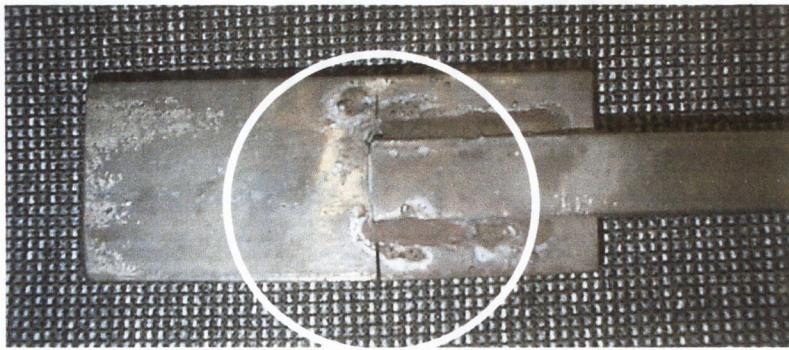


Fig. A.18 - Failure in the wide plate

The resulting stress-life curve is displayed in Figure A.19 below. The fatigue strength was determined to be a load range of 8.4 kN at  $5 \times 10^6$  cycles to failure.

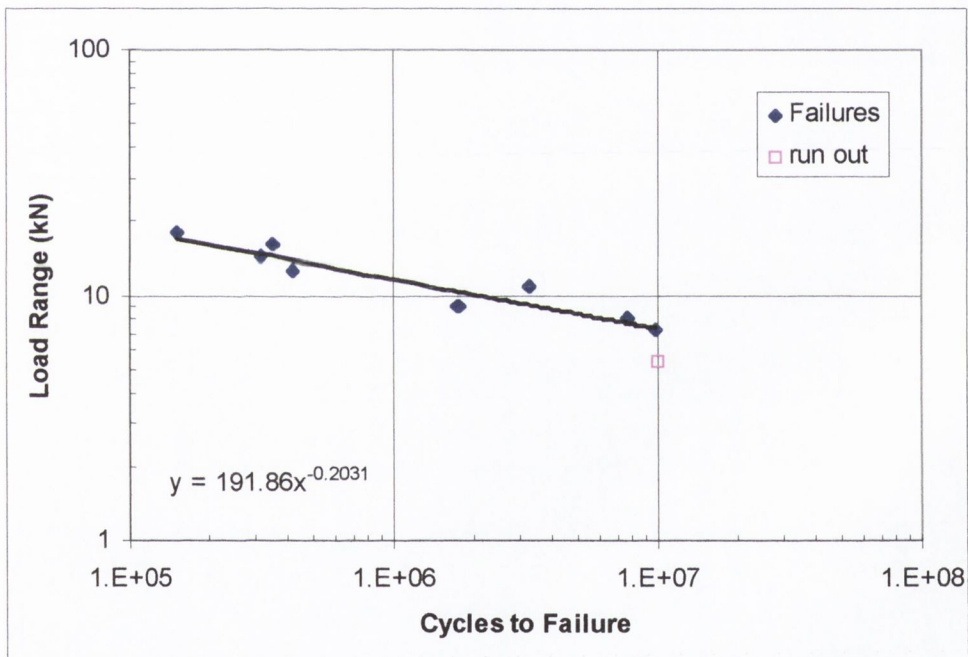


Fig. A.19 - S/N curve obtained for the Fillet-A specimen

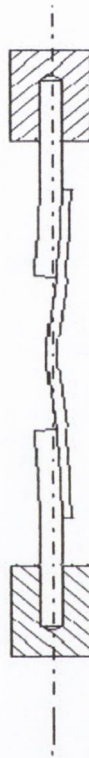
### A.2.3.1 Horizontal displacement of the lower clamp

As a consequence of the asymmetrical nature of the Fillet-A specimen, application of the load resulted in considerable horizontal displacement of the bottom clamp on the Instron testing machine. Figure A.20 shows a schematic of the deflected shape caused by application of the load. It can be seen that if left unrestrained the ends of the specimen would rotate. However the clamping arrangement is such that the specimen ends are not



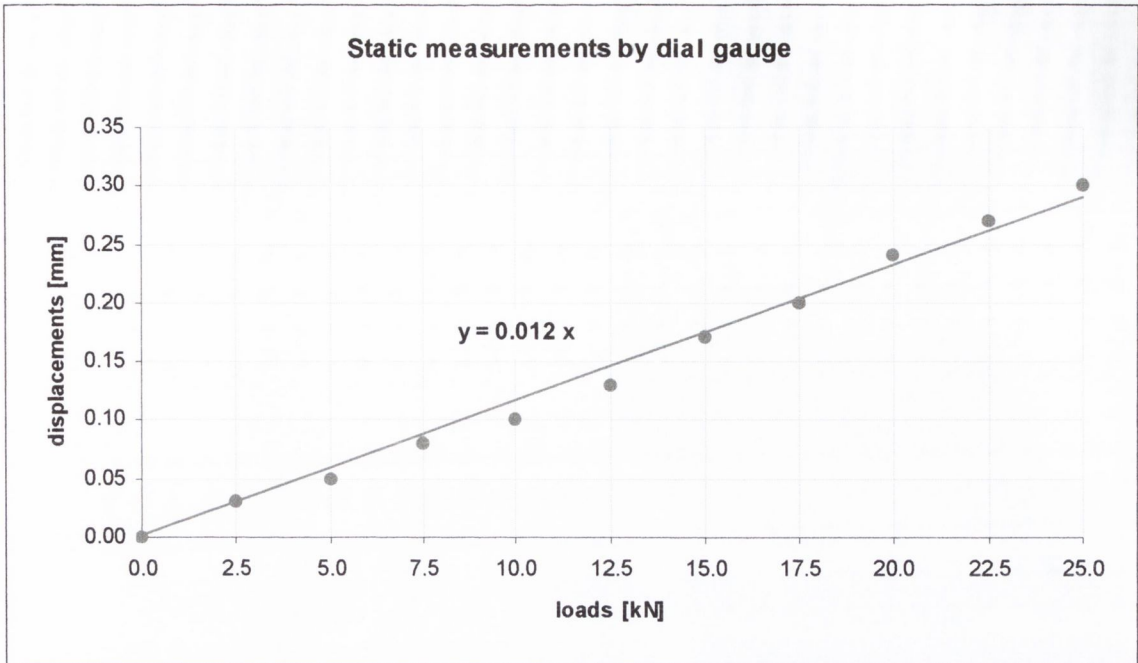
allowed to rotate, hence a bending moment is developed at the ends of the specimen, which results in a lateral load being applied to the clamps. The bottom clamp on the testing machine is attached to the hydraulic actuator and is evidently characterized by a lower lateral stiffness than the top clamp, which is attached to the crosshead of the machine.

As the horizontal movement of the bottom clamp was considerable it was thought that this might have an effect on the stress analysis of the component. In order to account for this, the displacement was measured and applied as a boundary condition to the finite element models.



*Fig. A.20 - Schematic of the Fillet-A specimen and deflected shape caused by application of the load*

The displacement was measured, using an analogue dial gauge, for both static and dynamic loads. Figure A.21 shows the horizontal displacement measured as a function of the applied static load. It can be seen that an approximately linear relationship exists.



*Fig. A.21 - Measurement of lower clamp displacement in static conditions*

The next step was to measure the horizontal displacements under dynamic loads. This was done for two different load cycles ( $\Delta L=9\text{kN}$  and  $\Delta L=18\text{kN}$  at R-ratio=0.1) at a range of frequencies. The results of this investigation are shown in Figures A.22 and A.23 below. It can be seen that the displacements are relatively independent of frequency for both load cycles and approximately equal to the values obtained under static loads. This meant that it was possible to use only the displacements obtained under static loads.

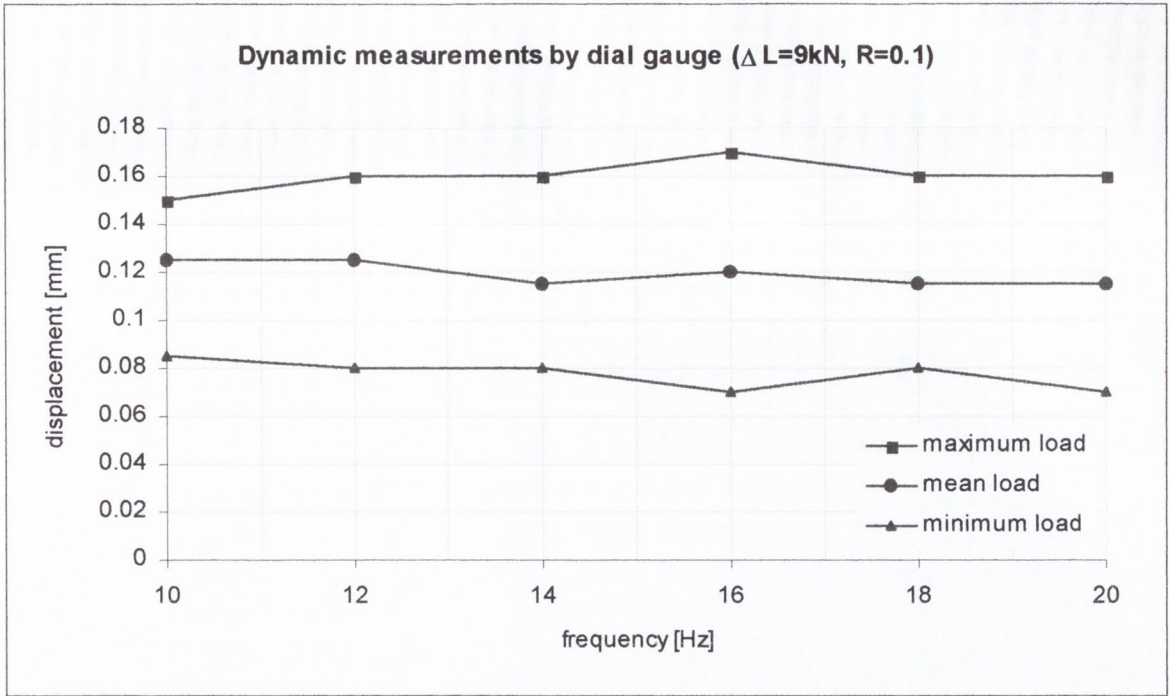


Fig. A.22 - Measurement of lower clamp displacement for a load range of 9kN at various frequencies

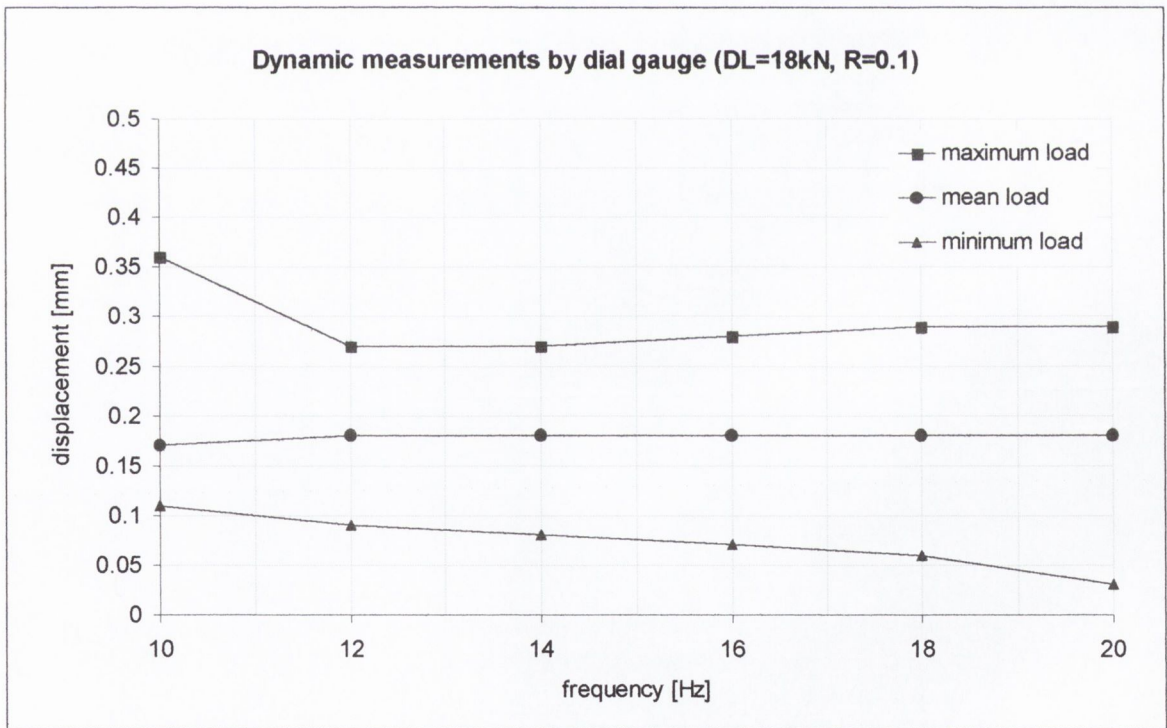


Fig. A.23 - Measurement of lower clamp displacement for a load range of 18kN at various frequencies

## A.2.4 Stress and fatigue analysis

This section describes the work undertaken to determine the stress distribution within the Fillet-A specimen and the subsequent fatigue analyses. In all models, the parent material, heat affected zone (HAZ) and the weld bead were modelled as a single solid component with the same material properties. For an elastic analysis, this implies the same Young's modulus and Poisson's ratio. It is expected that for the above, these values will not be significantly different.

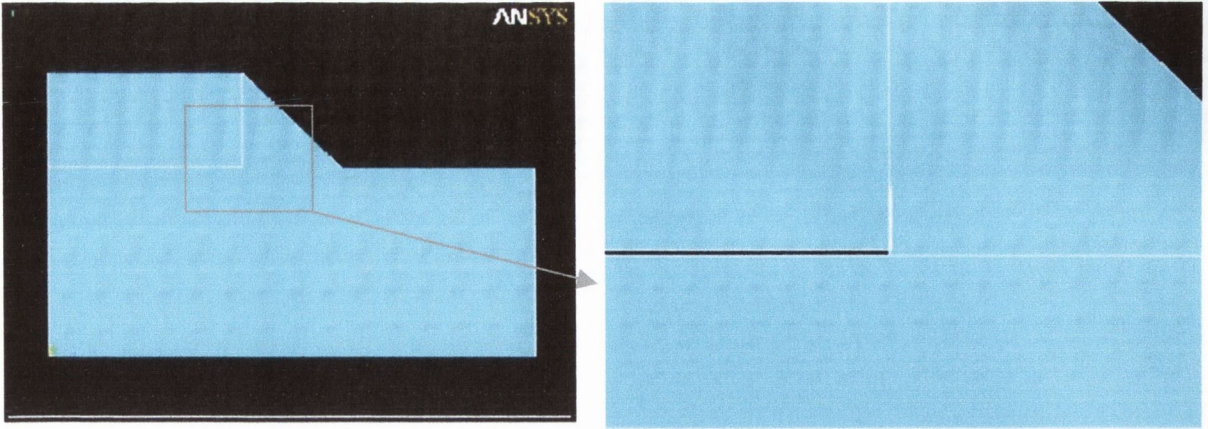
Where possible the double symmetry of the geometry and loads was exploited, so that a quarter model was created. In order to investigate the effect of the horizontal movement of the bottom clamp discussed in section A.2.3.1 above, a half model, utilising the vertical plane of symmetry was used.

### A.2.4.1 Mesh refinement

The FE mesh size was refined at the fillet weld end, where it joined the thin plate. The criterion suggested by Wang [1999] was used to define the mesh size. That is, in order to obtain an accurate prediction for the point method, 5 elements were included within a distance of  $a_0$  from the hotspot.

### A.2.4.2 Weld penetration and the gap distance

Figure A.24(a) below shows a typical cross-section through one of the finite element models (note that only half the cross-section is shown due to the plane of symmetry on the left). The weld bead is assumed to be triangular in cross-section and there is no root radius at the weld toe. The detail on the right demonstrates the way in which the weld bead joins the two plates. Note that there is no weld penetration, as was observed in the real specimens and that the gap between the plates is assumed to be rectangular.



(a) Half the cross-section (due to the plane of symmetry on the left)

(b) Detail

Fig. A.24 - Cross-section through the model

#### A.2.4.3 Modelling of the weld end

The end of the weld was modelled using three different shapes; a convex shape, a concave shape and a squared-off shape. These are shown in Table A.8. In all cases there is no root radius at the termination of the weld end. It should be noted that this is the most fatigue critical location and modelling it like this results in a singular point in the elastic stress field.

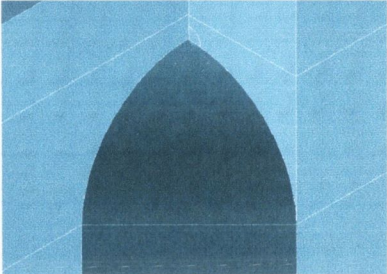

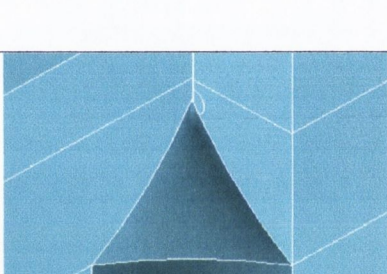
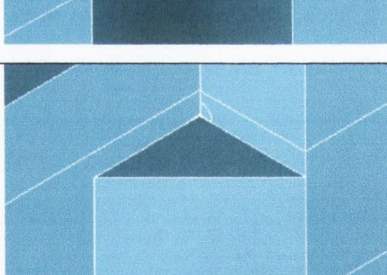
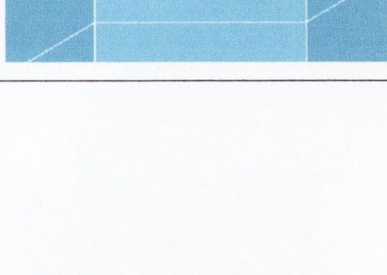
#### A.2.4.4 Summary of FE models

Five, linear elastic, three-dimensional finite element models of the Fillet-A specimen are discussed below. These were built in order to determine the effect of:

- The shape of the weld end, which is the most critical fatigue location.
- The gap between the thin and the wide plates
- The horizontal displacement of the lower end of the specimen when it was loaded on the test machine (see section A.2.3.1 above).

These models are summarised in Table A.8.

Table A.8 - Summary of finite element models investigated for the Fillet-A specimen

Model name	Description	Weld end shape
Fillet-A 1.1	Quarter model 0.05mm gap between plates	
Fillet-A 1.2	Quarter model 0.25mm gap between plates	
Fillet-A 1.3	Half model 0.05mm gap between plates Horizontal displacement included (see section A.2.3.1)	
Fillet-A 2	Quarter model 0.05mm gap between plates	
Fillet-A 3	Quarter model 0.05mm gap between plates	

#### A.2.4.5 Selection of the focus path

For all models, the focus path was determined as per the criteria given in Chapter 2, section 2.2.2.2.2. That is, the focus path is chosen to be the direction of minimum crack growth potential, in the plane perpendicular to the maximum principal stress at the hotspot. Table A.9 lists the direction cosines, which define the vectors normal to the assumed planes of crack growth for each of the FE models (i.e. the direction of the first principal stress at the hotspot). Figure A.25 below shows the orientation of this plane for Model: Fillet-A1.1.

Table A.9 - Direction cosines of the vector normal to the assumed plane of crack growth

	X cosine	Y cosine	Z cosine
<b>ModelA1.1</b>	0.42960	0.77678	-0.46049
<b>ModelA1.2</b>	0.42653	0.77832	-0.46075
<b>ModelA1.3</b>	0.41912	0.71832	-0.55529
<b>ModelA2</b>	0.60010	0.77472	-0.19922
<b>ModelA3</b>	0.37656	0.83578	-0.39959

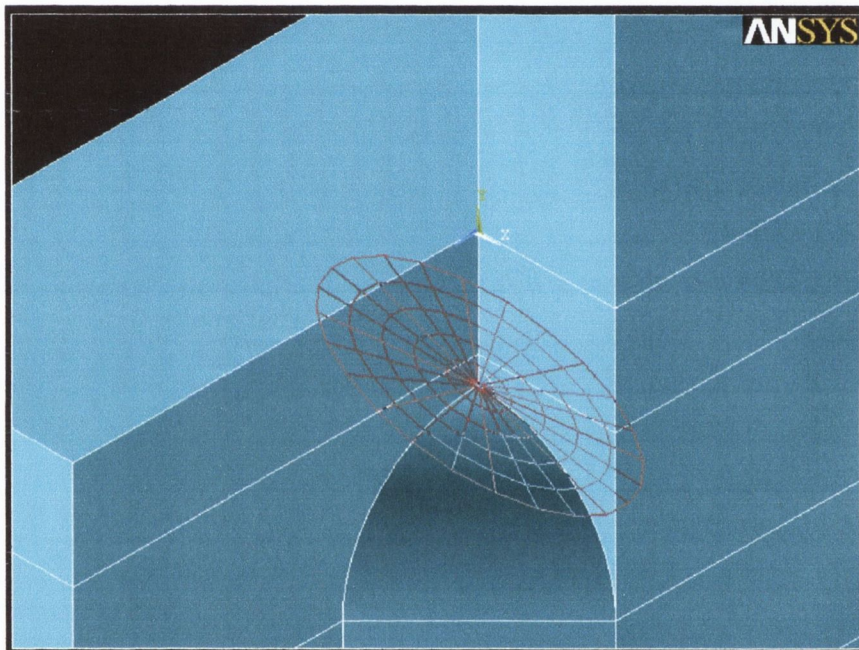


Fig. A.25 - The plane perpendicular to the 1st principal stress at the hotspot

In order to determine the focus path, within the plane of crack growth, the stress-distance curves for various directions in the plane are compared. Figure A.26 is a top view of the Fillet-A models, which shows how the direction within the plane of crack growth is defined. That is, the direction where theta equals zero, coincides with the interface of the two plates.

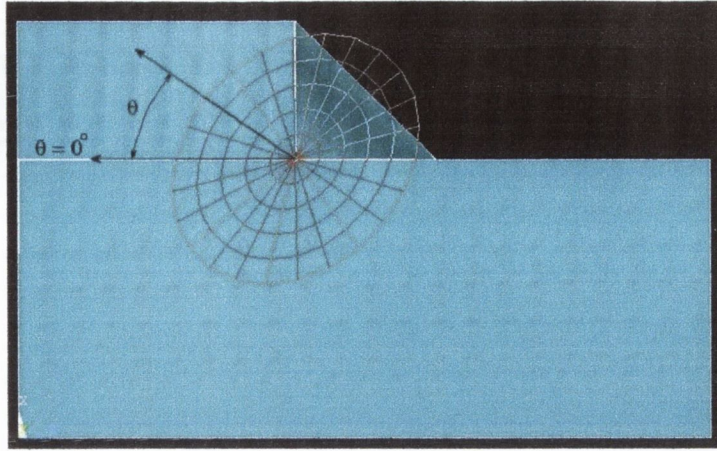


Fig. A.26 - Top view of the Fillet-A specimen, showing the definition of the angle  $\theta$ , within the plane of crack growth

The stress-distance curves for various angles of theta, within the plane of crack growth are compared in Figure A.27 below. The distance corresponding to the critical distance of the point method (i.e.  $a_0/2$ ) is also highlighted. Ignoring the  $\theta = 90^\circ$  curve, which is suffering from some numerical instability, it can be seen that the direction with the steepest stress gradient is  $\theta = 0^\circ$ . Hence, this is chosen as the focus path, as it represents the direction of minimum crack growth potential.

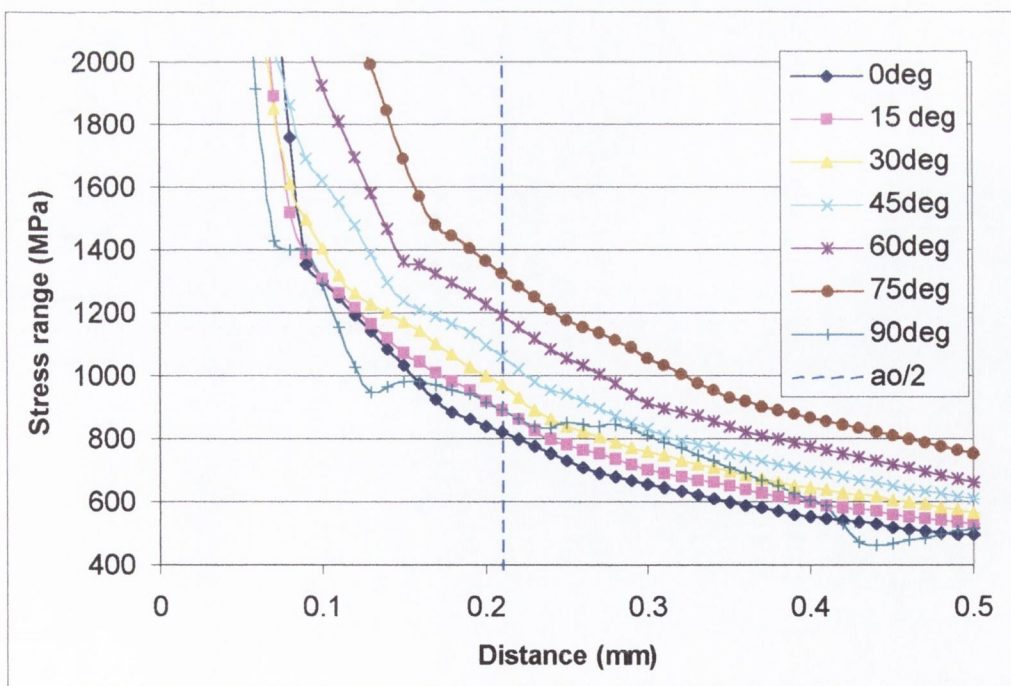


Fig. A.27 - Stress - distance curves for the various angles in the plane of crack growth, for the Fillet-A1.1 model



#### A.2.4.6 Summary of the results

Table A.10 shows the results of the fatigue analyses for the Fillet-A1.1 model, for the various paths, in the assumed plane of crack growth. It can be seen that the fatigue predictions for all the critical distance methods and the CMM are extremely conservative, with error factors greater than 2. However the results for the focus path (i.e. the 0° path) are the least conservative.

For the remainder of the models, only the results for the point method, the line method and the CMM (for the focus path) are presented below (see Table A.11). This is believed to be adequate to demonstrate the effect on the fatigue predictions of the variations modifications being considered in each model.

Table A.10 - Summary of results for the Fillet-A1.1 model

	0 deg	15 deg	30 deg	45 deg	60 deg	75 deg	90 deg
<b>Experimental</b>	8.4 kN at $5 \times 10^6$ cycles						
<b>Point Method</b> (Error factor)	3.78 kN (2.22)	3.49 kN (2.41)	3.21 kN (2.62)	2.93 kN (2.87)	2.61 kN (3.22)	2.34 kN (3.59)	3.49 kN (2.41)
<b>Line Method</b> (Error factor)	3.33 kN (2.52)	3.29 kN (2.55)	3.17 kN (2.65)	2.95 kN (2.85)	2.69 kN (3.12)	2.37 kN (3.54)	3.45 kN (2.43)
<b>Area Method</b> (Error factor)	3.72 kN (2.26)						
<b>Volume Method</b> (Error factor)	3.54 kN (2.37)						
<b>CMM</b> (Error factor)	4.24 kN (1.98)	3.89 kN (2.16)	3.62 kN (2.32)	3.56 kN (2.36)	3.31 kN (2.54)	2.73 kN (3.08)	4.03 kN (2.08)

Note: Error factor is defined as the ratio of the Experimental fatigue strength to the predicted fatigue strength

Table A.11 - Comparison of results for different models (on the zero degree path in the plane perpendicular to the first principal stress at the hotspot)

	<b>Fillet-A1.1</b>	<b>Fillet-A1.2</b> (Bigger gap)	<b>Fillet-A1.3</b> (Horiz. Disp)	<b>Fillet-A2</b> (Concave end)	<b>Fillet-A3</b> (Squared-off end)
<b>Experimental</b>	8.4 kN at $5 \times 10^6$ cycles				
<b>Point Method</b> (Error factor)	3.78 kN (2.22)	3.89 kN (2.16)	2.76 kN (3.04)	2.96 kN (2.84)	3.81 kN (2.20)
<b>Line Method</b> (Error factor)	3.33 kN (2.52)	3.78 kN (2.22)	2.22 kN (3.78)	2.62 kN (3.21)	3.38 kN (2.49)
<b>CMM</b> (Error factor)	4.24 kN (1.98)	4.20 kN (2.00)	3.15 kN (2.67)	3.23 kN (2.60)	4.17 kN (2.01)

Note: Error factor is defined as the ratio of the Experimental fatigue strength to the predicted fatigue strength

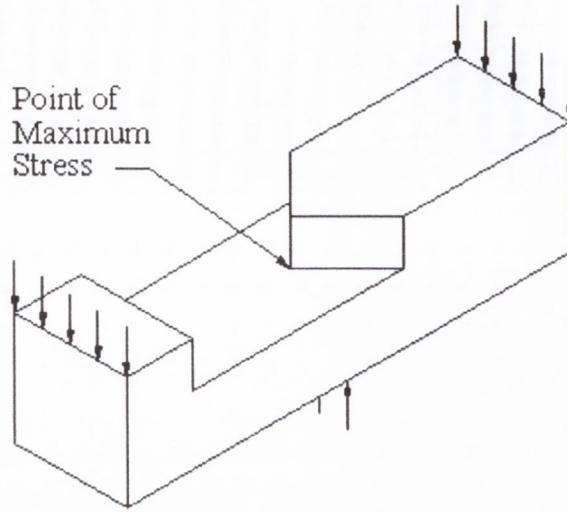
## A.2.5 Discussion

The results presented above show that the fatigue predictions for the Fillet-A specimen were very conservative, with error factors of 2 or greater. Furthermore, none of the geometrical variations considered improved the predictions. Hence it was concluded that the analysis methods are inadequate to analyse this type of specimen.

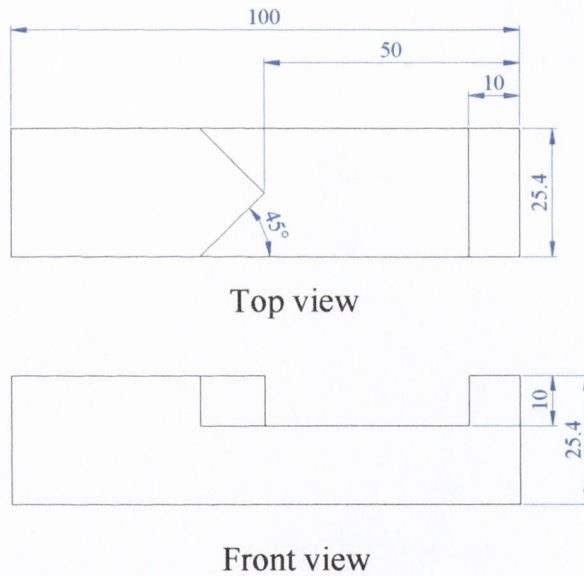
## A.3 The Model-E specimen

### A.3.1 The specimen

The Model-E specimen is shown below in Figures A.28 and A.29. As discussed in Chapter 5, section 5.3.2, this specimen was chosen for investigation, to test the fatigue prediction methods for a non-welded, complex three-dimensional stress concentration. This work was done in collaboration with Ezio Mazzi [2000].



*Fig. A.28 - Schematic of the Model-E specimen*



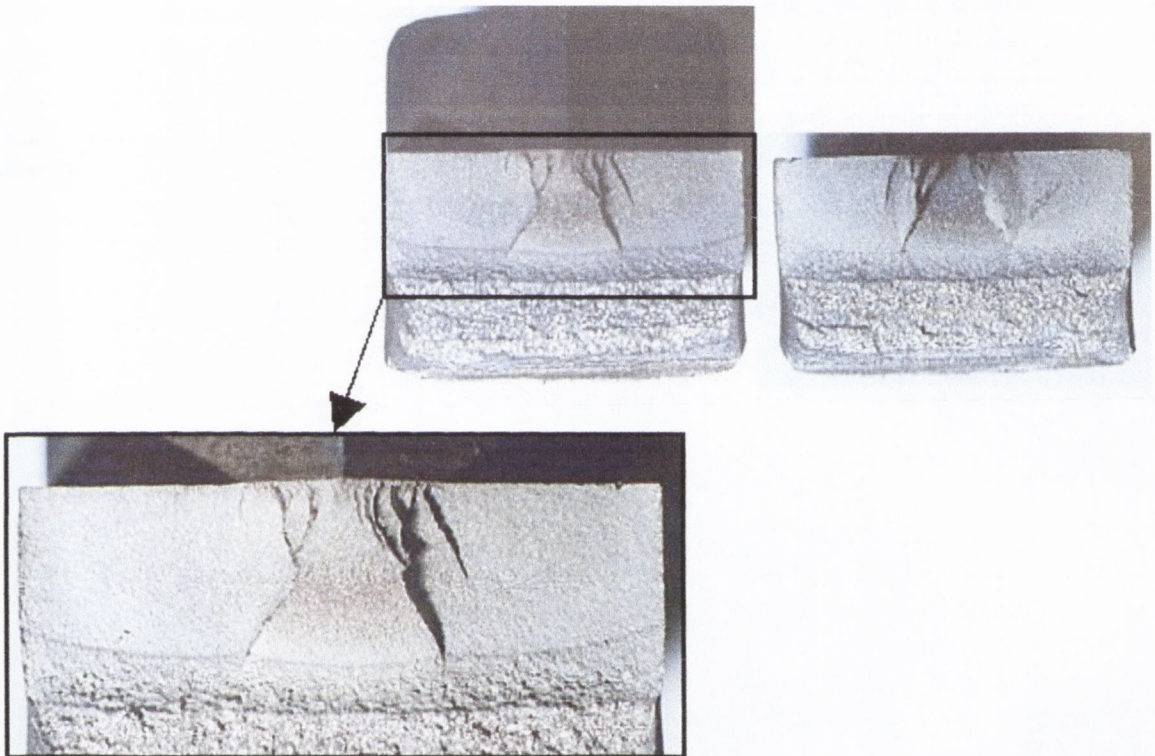
*Fig. A.29 - Dimensions of the Model-E specimen in mm*

### A.3.2 Material properties

The Model-E specimen was machined from the structural steel discussed in section A.1 above. For this material the plain specimen fatigue limit was determined in both bending and tension, consequently two sets of (fatigue) material properties were obtained. These are summarised in Table A.1 above.

### A.3.3 Experimental results

As shown in Figure A.28 above, the specimen was tested in three-point bending at an R-ratio of 0.1. Figure A.30 is a picture of both halves of a typical failure, with a detail, at increased magnification, of one of the sides. It can be seen that the failure surfaces are very complex and non-planar in the region of the stress-concentration. Also, the fatigue regions can clearly be distinguished from the fast fracture regions.



*Fig. A.30 - The failure surface*

The experimental data and the S-N curve obtained for this specimen are shown in Table A.12 and Figure A.31 below.

Table A.12 - Summary of experimental results for the Model-E specimen

Test No	R-ratio	Load Range (kN)	No. of cycles	Comment
1	0.103	5.47	3.12E+06	Failure
2	0.103	8.19	1.14E+06	Failure
3	0.106	7.26	1.95E+06	Failure
4	0.098	6.44	2.08E+06	Failure
5	0.101	4.54	5.08E+06	Run out
6	0.093	5.34	4.09E+06	Failure
7	0.098	15.49	7.20E+04	Failure

Note: Error factor is defined as the ratio of the Experimental fatigue strength to the predicted fatigue strength

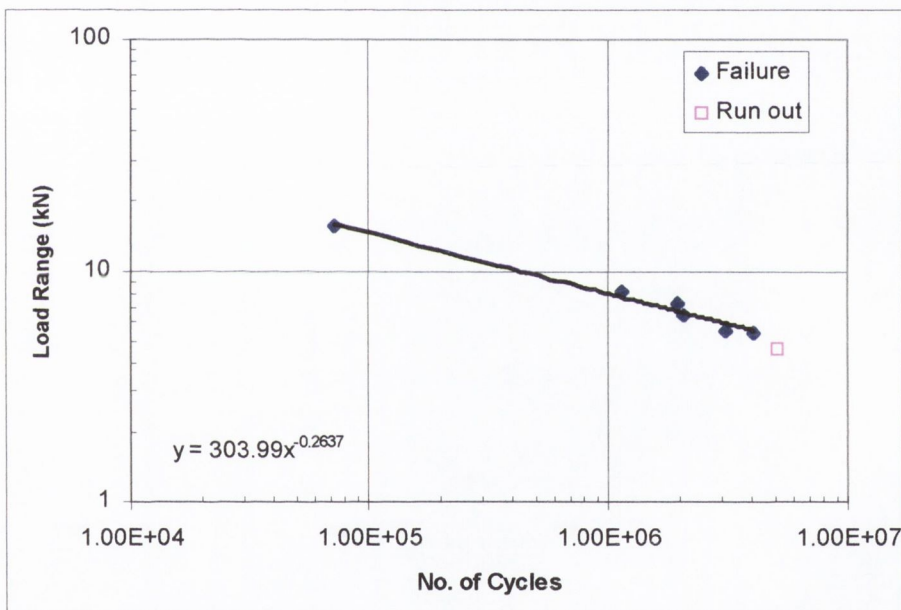
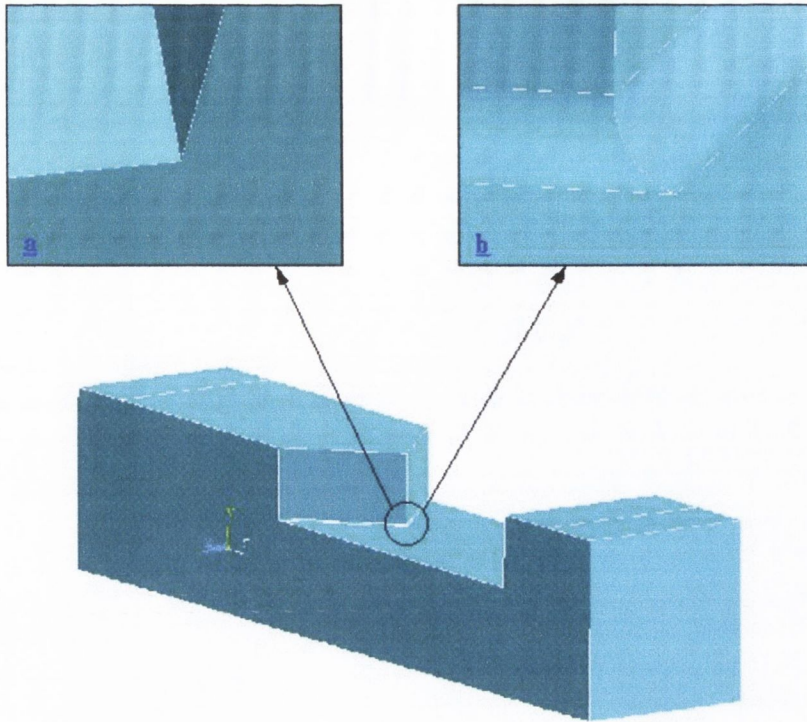


Fig. A.31 - S/N curve obtained for the Model-E specimen

The fatigue strength was determined to be an applied load range of 6.6 kN at  $2 \times 10^6$  cycles.

#### A.3.4 Stress and fatigue assessments

Two finite element models were built to investigate this geometry. One contained a root radius at the failure location, which was equal to the average measured value of 0.2mm. This specimen was called Model-E2. The other had a zero root radius of zero (it was designated Model-E1). This is demonstrated in Figure A.32.



*Fig. A.32 - Finite element models of the Fillet-A specimen (a) Model-E1 - no root radius  
 (b) Model-E2 - the root radius equals 0.2mm*

#### A.3.4.1 Selection of the focus path

For this specimen, the plane of symmetry simplifies the selection of the focus path, as it is intuitively obvious that the focus path should lie on the plane of symmetry. Hence only one criterion is needed. In this case, the plane of crack growth (and consequently the focus path) is assumed to be perpendicular to the maximum principal stress at the hotspot. The direction of the focus path, for each of the models, is summarised in Figure A.33 and Table A.13 below.

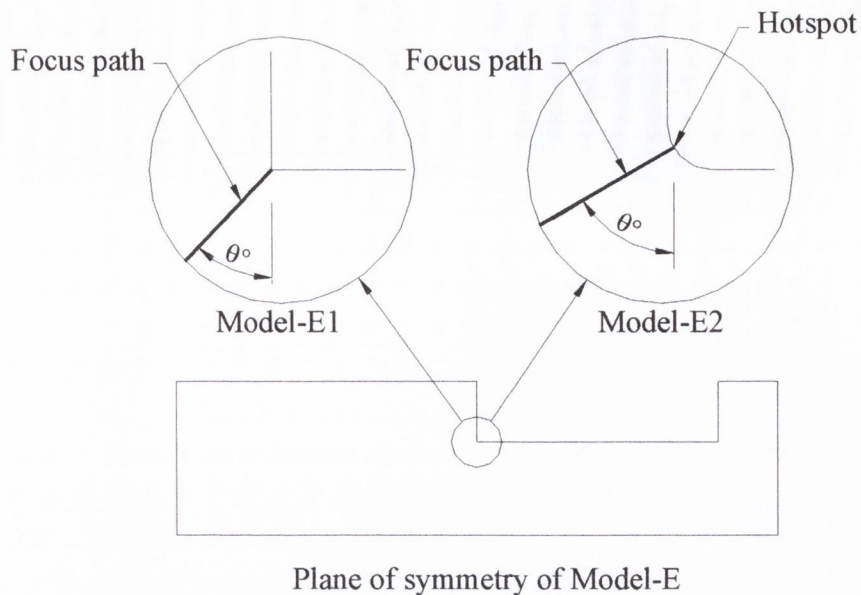
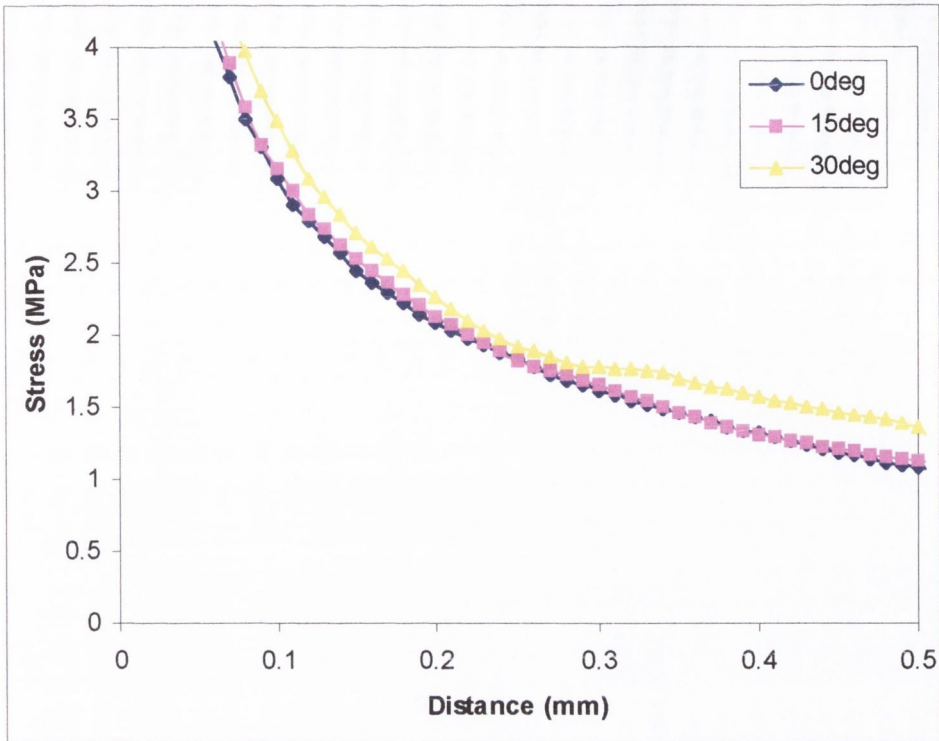


Fig. A.33 - Orientation of the focus path, Model-E

Table A.13 - The orientation of the focus path, Model-E

	Angle $\theta$ (The direction of the focus path relative to the vertical)
Model-E1	46.9°
Model-E2	60.3°

In order to check the assumption that the focus path should lie on the plane of symmetry, the stress-distance curves for various angles within the assumed plane of crack growth are compared in Figure A.34 below. It can be seen that the zero degree curve (or the curve on the plane of symmetry) is characterised by the highest stress gradient. Hence, this direction represents the direction of minimum crack growth potential and is the correct choice for the focus path according to the criteria given in Chapter 2, section 2.2.2.2.2.



*Fig. A.34 - The stress distance curves for Model-E1 for various angles within the assumed plane of crack growth*

#### A.3.4.2 Summary of results

Table A.14 below is a summary of the fatigue assessment results for the model-E specimen. It can be seen that for each assessment method there are four separate results. This because the analysis has been done for both finite element models (i.e. with and without the root radius) and for both sets of fatigue material properties (as discussed in section A.1.4 above).



Table A.14 - Summary of results for the Model-E

	$\Delta\sigma_o _{\text{bending}} (a_o = 0.205\text{mm})$		$\Delta\sigma_o _{\text{tension}} (a_o = 0.288\text{mm})$	
	<b>Model-E1</b> ( $\rho=0\text{mm}$ )	<b>Model-E2</b> ( $\rho = 0.2\text{mm}$ )	<b>Model-E1</b> ( $\rho=0\text{mm}$ )	<b>Model-E2</b> ( $\rho = 0.2\text{mm}$ )
<b>Experimental</b>	6.6 kN at $2 \times 10^6$ cycles			
<b>Point method</b> (Error factor)	2.99 kN (2.21)	2.52 kN (2.62)	3.09 kN (2.14)	2.56 kN (2.58)
<b>Line method</b> (Error factor)	3.06 kN (2.16)	3.04 kN (2.17)	3.19 kN (2.07)	3.05 kN (2.16)
<b>Area method</b> (Error factor)	3.35 kN (1.97)	3.14 kN (2.10)	3.65 kN (1.81)	3.25 kN (2.03)
<b>Volume method</b> (Error factor)	3.70 kN (1.78)	4.21 kN (1.57)	3.65 kN (1.81)	4.07 kN (1.62)
<b>CMM</b> (Error factor)	4.56kN (1.45)	3.78 kN (1.75)	4.65 kN (1.42)	3.83 kN (1.72)
<b>Stress-life meth.</b> (Error factor)		1.25 kN (5.28)		1.06 kN (6.23)

Note: Error factor is defined as the ratio of the *Experimental fatigue strength* to the *predicted fatigue strength*

### A.3.5 Discussion

It can be seen from Table A.14 that the result for the point, line and area methods are very conservative, with error factors ranging between 1.81 and 2.62. Also, only a very small difference can be observed between the results obtained using the two sets of material properties.

It can be seen that there is quite a large difference between the results for the volume method, depending on which finite element model is used. This is because the root radius in the Model-E2 model (which is the same order of magnitude as the critical radius) causes a large part of the semi-spherical critical volume to be outside the specimen. Hence a smaller than expected volume, characterised by higher stresses is obtained. Consequently the average stress is higher and the predicted fatigue limit is less conservative. It is believed that for this reason the result obtained for the volume method using the Model-E2 model is erroneous and should be disregarded.

Furthermore, from Table A.14 it can be seen that the difference between the CMM and the CDMs, is quite significant. A probable explanation for this can be found by examining the Kitagawa diagram (see Figure A.35). This shows that for short cracks the real fatigue limit is lower than that predicted by standard fracture mechanics methods and subsequently the

CMM. Previous experience suggests that the CDMs are more able to predict the behaviour of short cracks. Hence, if there is a large difference between the predictions made using the Critical Distance Methods and the Crack Modelling Methods (where the CMM is overestimating the fatigue limit), the former should be taken as being more accurate. Reference to Figure A.35 shows that if the length of a crack is less than  $a_0$ , short crack behaviour can be expected and the CMM will overestimate the fatigue limit. In this case  $a_0$  is between 0.2mm and 0.3mm, which is very similar to the root radius of Model-E. This suggests that the stress concentration of Model-E is short crack-like.

If the above is accepted then it can be seen that the fatigue methods result in very conservative predictions, with error factors ranging between 1.4 and 2.0. From this it was concluded that the methods are inadequate to assess the behaviour of complex 3D stress concentrations.

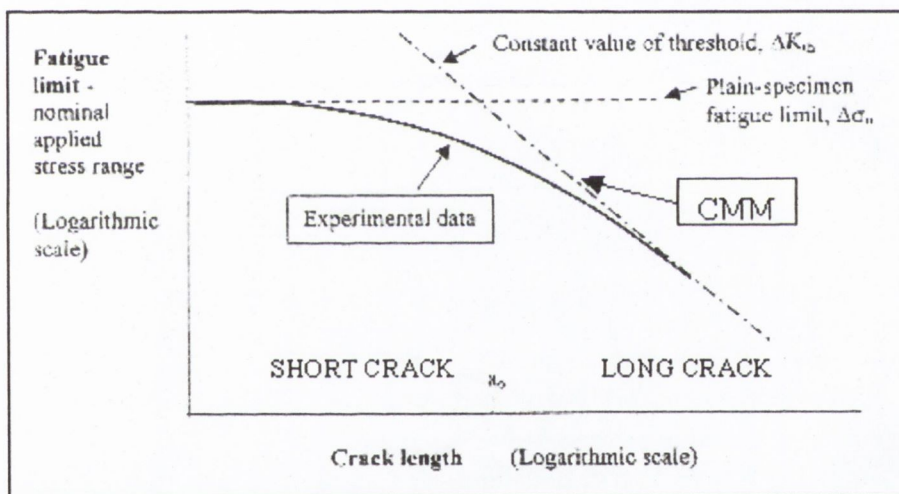


Fig. A.35 - The Kitagawa diagram, describing short crack behaviour

#### A.4 The Model-T specimen

##### A.4.1 The specimen

The second solid steel specimen investigated is shown in Figures A.36 and A.37 below. The specimen is a sharply notched bar loaded in three-point-bending, but the notch is orientated vertically relative to the direction of the applied load so that the fatigue crack is forced to initiate at the top of the specimen, at the notch root. As discussed in Chapter 5, section 5.3.3 this specimen was chosen for investigation because it is a slightly more

complex stress concentration than a pure two-dimensional case. The bending gradient causes the fatigue crack to grow from the notch root at the top of the specimen. Furthermore the fatigue crack will have a semi-elliptical shape, which was hoped, we would be able to measure. The work on this specimen, which is designated Model-T, was done in collaboration with Thomas Pircher [2001].

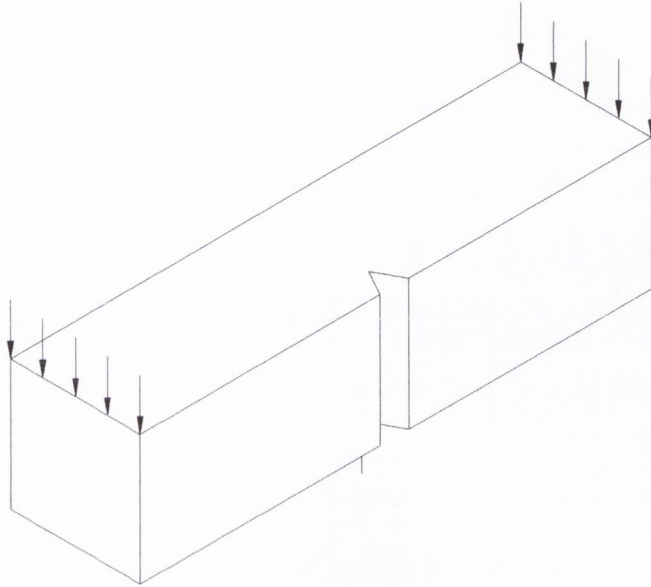


Fig. A.36 - Schematic of the Model-T specimen

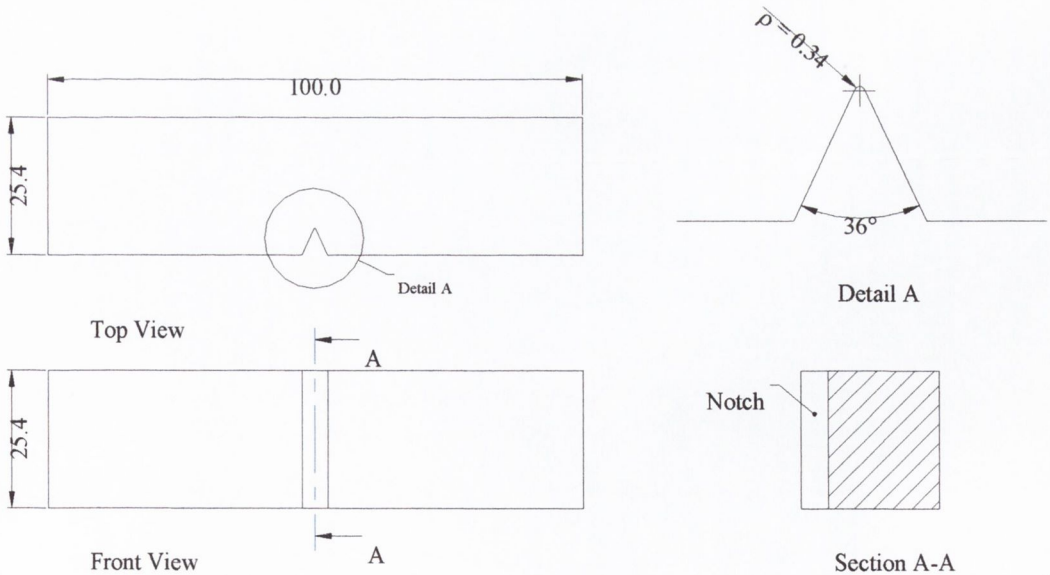


Fig. A.37 - Dimensions of the model-T specimen in mm

#### A.4.2 Material properties

As per the Model-E specimen, Model-T was machined from the structural steel discussed in section A.1 above. For this material the plain specimen fatigue limit was determined in both bending and tension, consequently two sets of (fatigue) material properties were obtained. These are summarised in Table A.4 above.

#### A.4.3 Experimental results

The experimental data and S-N curve obtained for this specimen are shown in Table A.15 and Figure A.38 below.

*Table A.15 - Summary of experimental results, Model-T*

R-ratio	Load Range (kN)	No. of cycles	Comment
0.1	22.5	1.42E+05	Failure
0.1	22.5	1.42E+05	Failure
0.1	18	3.70E+05	Failure
0.1	15	7.21E+05	Failure
0.1	12.35	1.30E+06	Failure
0.1	10.04	2.55E+06	Failure
0.1	10.88	3.08E+06	Failure
0.1	10.8	2.27E+06	Run out
0.1	9.02	1.07E+07	Run out
0.1	7.65	1.00E+07	Run out
0.1	7.2	1.00E+07	Run out

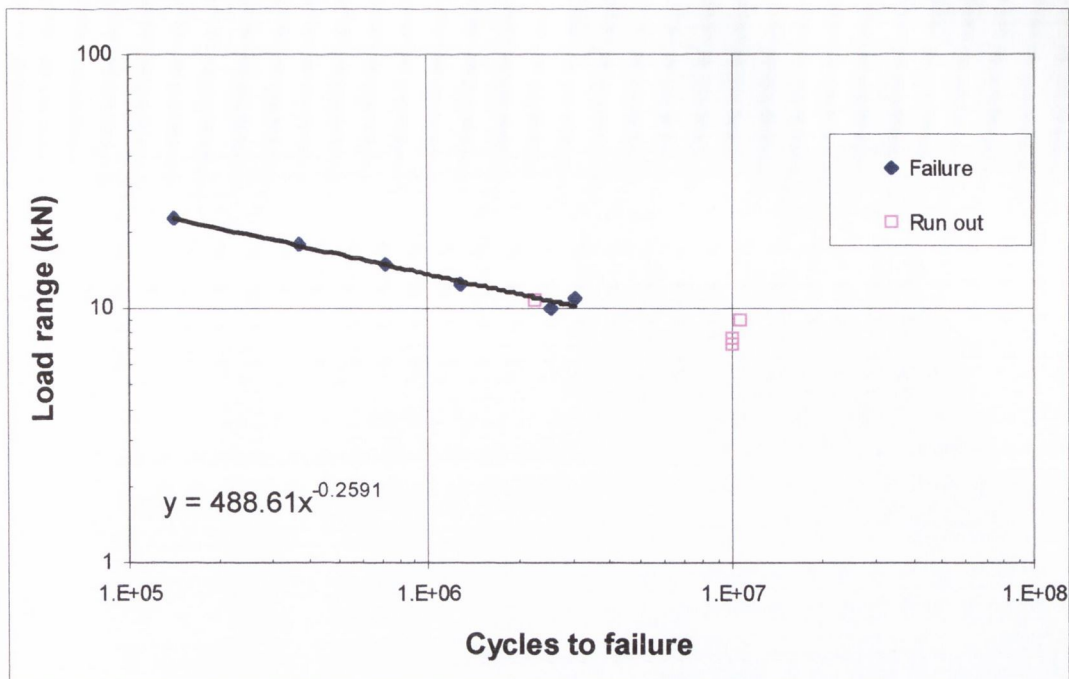


Fig. A.38 - S-N curve obtained for the Model-T specimen

The fatigue strength was determined to be a load range of 11.4kN at  $2 \times 10^6$  cycles.

#### A.4.3.1 Crack shape observation and measurement

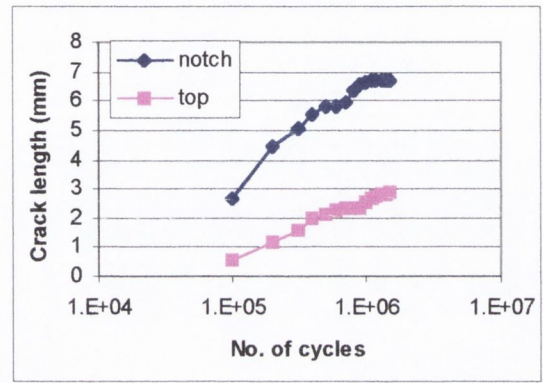
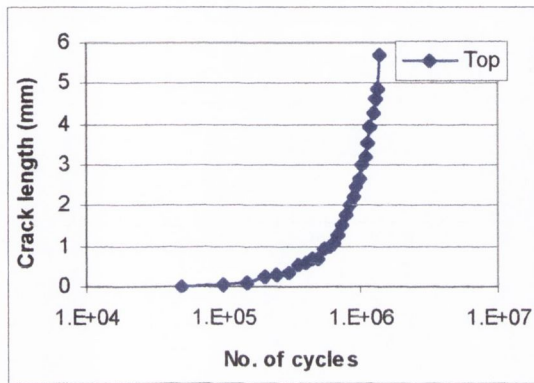
In order to observe the evolution of the fatigue crack shape, three different methods were tried. The first approach was to apply periodic overloads during the fatigue test in order to *mark* the crack front at various crack lengths. It was hoped that we could achieve a failure surface characterised by *beach-marks* as per typical in-service failures. Two different overload values were tried, but unfortunately neither result was satisfactory as nothing different could be observed on the failure surface even under an electron microscope.

The second method was direct visual observation of the crack, through a travelling microscope. Acetate replica tape was also used to measure crack growth along the top surface. Measurements of the crack length, along the top surface and along the notch root, as a function of the number of cycles were recorded. The results of this investigation are presented in the section immediately below.

The third approach was to grow a small fatigue crack, then cut and open the specimen to allow direct observation of the crack. This was done for two specimens and the resulting failure surfaces were examined using a scanning electron microscope (SEM).

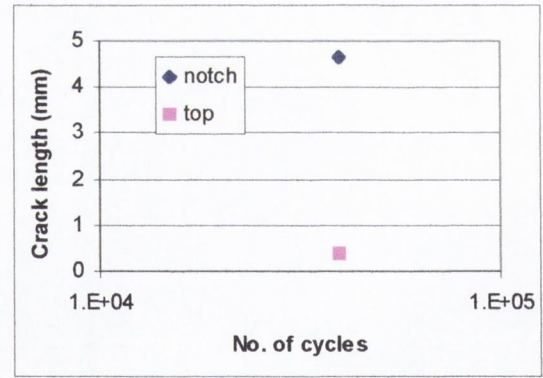
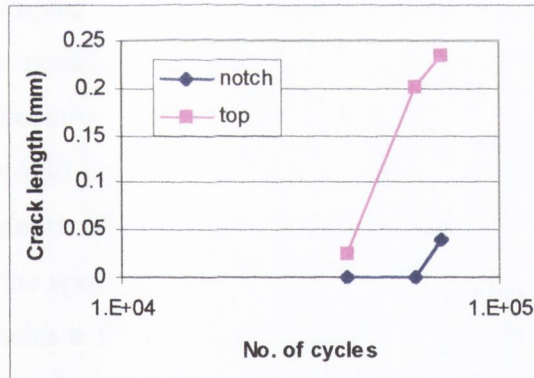
### A.4.3.1.1 Crack growth measurements

The results of the crack growth measurements are presented in Figure A.39 below and summarised in Figure A.40. In each of the graphs, the measured crack length along the top surface and the notch root are plotted against the number of cycles. The applied load range was 15 kN at an R-ratio of 0.1.



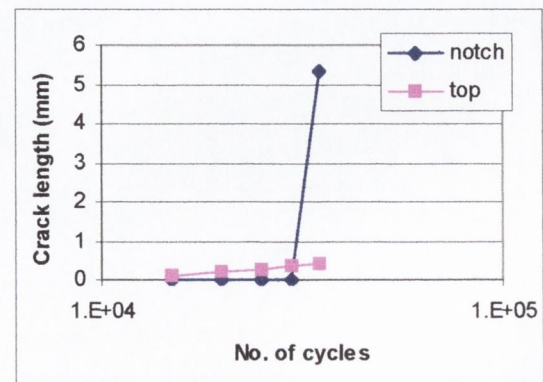
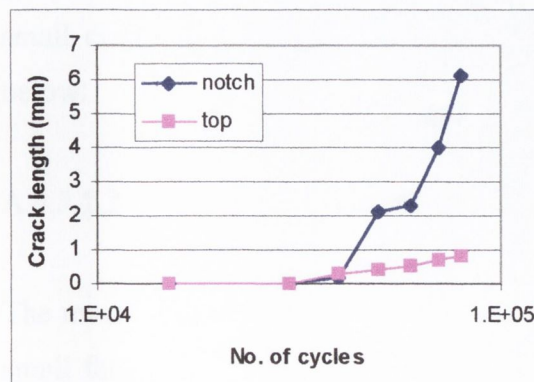
(a)

(b)



(c)

(d)



(e)

(f)

Fig. A.39 - Results of the crack shape measurement tests

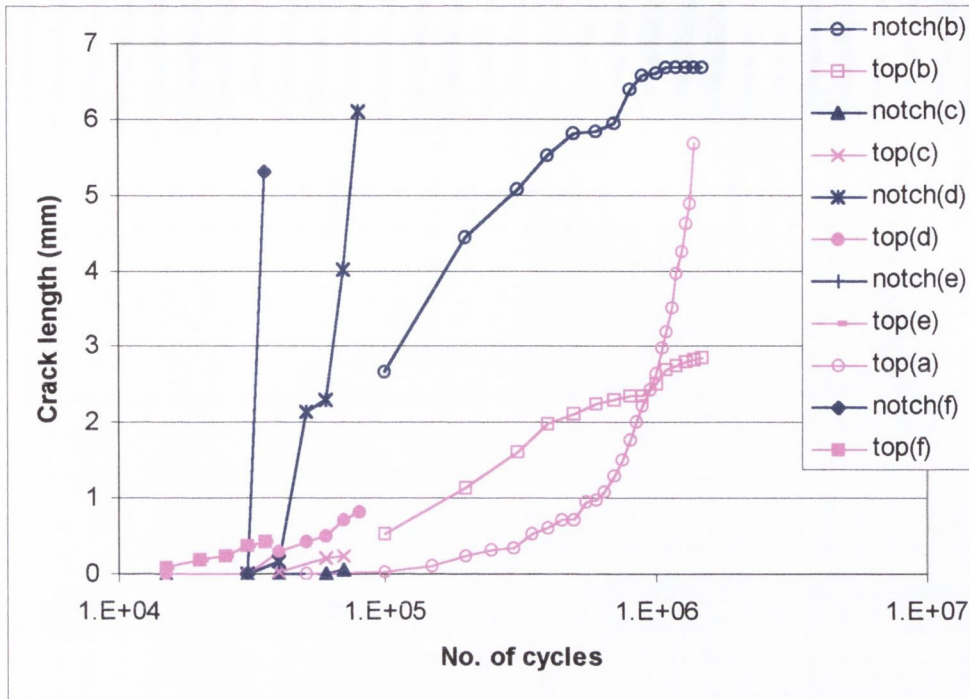


Fig. A.40 - Comparison of the crack shape experiments

Figure A.40 shows all of the measured data plotted together. It can be seen that the repeatability is not very good, especially for the measurements along the notch. This is because it was very difficult to observe the crack length in this direction, as replica tape could not be used, and the travelling microscope was difficult to use because of its small depth of field. Also, heat-treating of the specimens to relieve residual stresses resulted in the specimens being covered by a thin oxide layer, which had to be removed via polishing with a fine grain sand paper. This was difficult to achieve along the notch root and the resulting surface when viewed under the microscope was not optimal for observing crack growth. For these reasons the measurements in the direction of the notch, especially for small crack lengths, must be viewed with suspicion. This is highlighted in the section below.

#### A.4.3.1.2 SEM observations of the crack shape

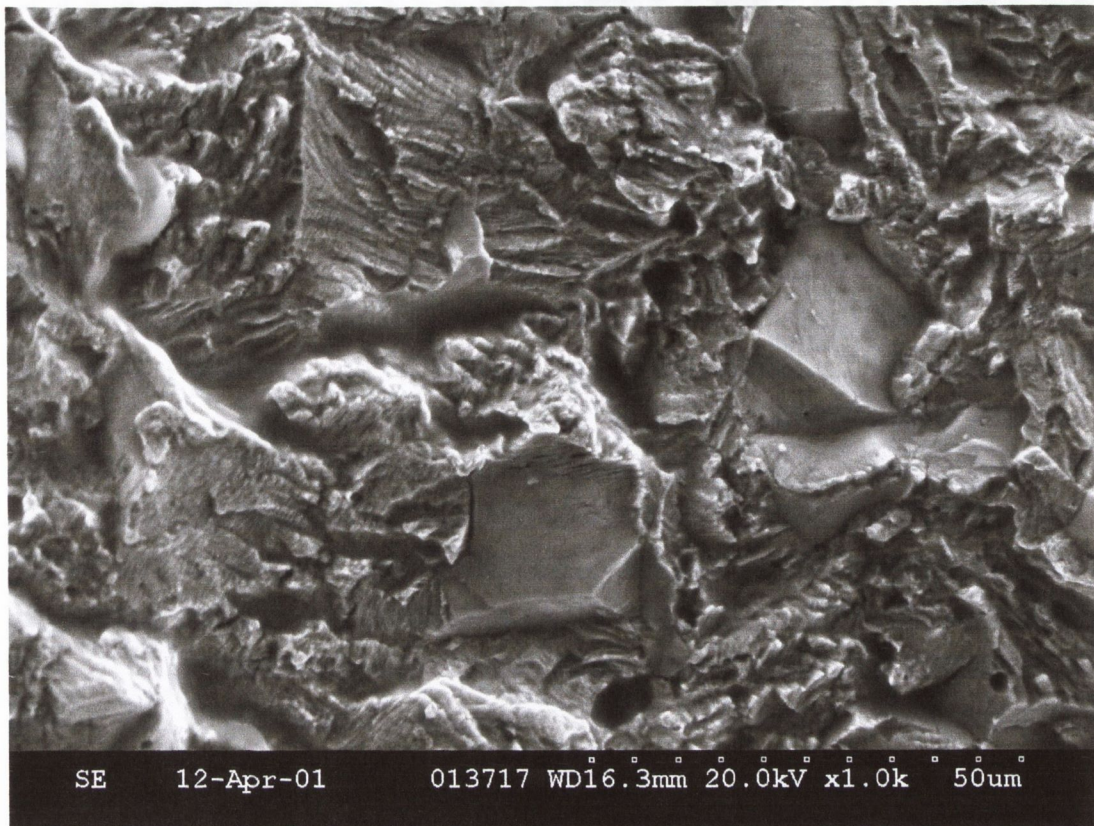
The most successful approach to observe the crack shape for this specimen was to grow a small fatigue crack, then cut through the majority of the specimen cross-section (without destroying the fatigue crack) so that an impact caused the remaining cross-section to failure via fast fracture. Using a scanning electron microscope (SEM) it was then possible

to differentiate between the different parts of the failure surface (i.e. fatigue and fast fracture). This was done for two specimens, which are referred to as crack-and-open specimens 1 and 2.

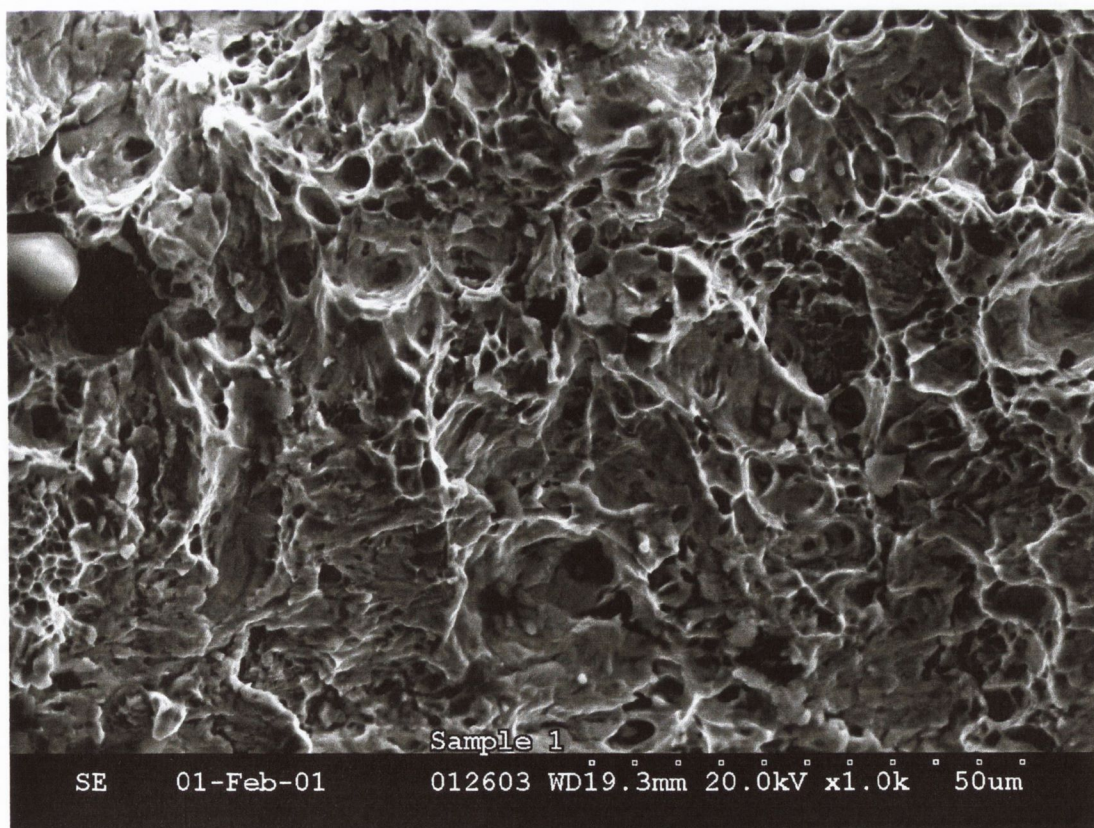
In order to determine what the different parts of the failure surfaces look like, a failed specimen used to produce the S-N curve, in which the different regions were visibly obvious, was examined. Figure A.41 below shows a typical *fatigue* failure surface and Figure A.42 shows a typical *fast fracture* surface. It can be seen that they are very different. The majority of the fatigue failure surface is characterised by linear striations or ridges typical of fatigue. Some smooth regions are also apparent; these are most probably fractured grains. The fast fracture surface on the other hand is characterised by a dimpled surface.

Figures A.43 and A.44 show the failure surface of the first crack-and-open specimen at a fairly low resolution. The specimen is orientated so that the notch is aligned with the bottom of the figure. An approximately elliptical shape, with the major axis orientated along the notch, is immediately obvious. The dimensions of the ellipse are approximately 1.6mm along the notch and 0.3mm perpendicular to the notch. In these figures the surface is divided into three zones (A, B and C). The following three figures show the failure surface of these three zones at higher resolution. It can be seen that zones A and B (Figures A.45 and A.46) are fatigue failure surfaces. Although it appears that a certain amount of rubbing between opposing crack faces has occurred. Zone C on the other hand (see Figure A.47) is clearly fast fracture. Hence, it is concluded that shape of the fatigue crack is highly elliptical with the major axis orientated along the notch.

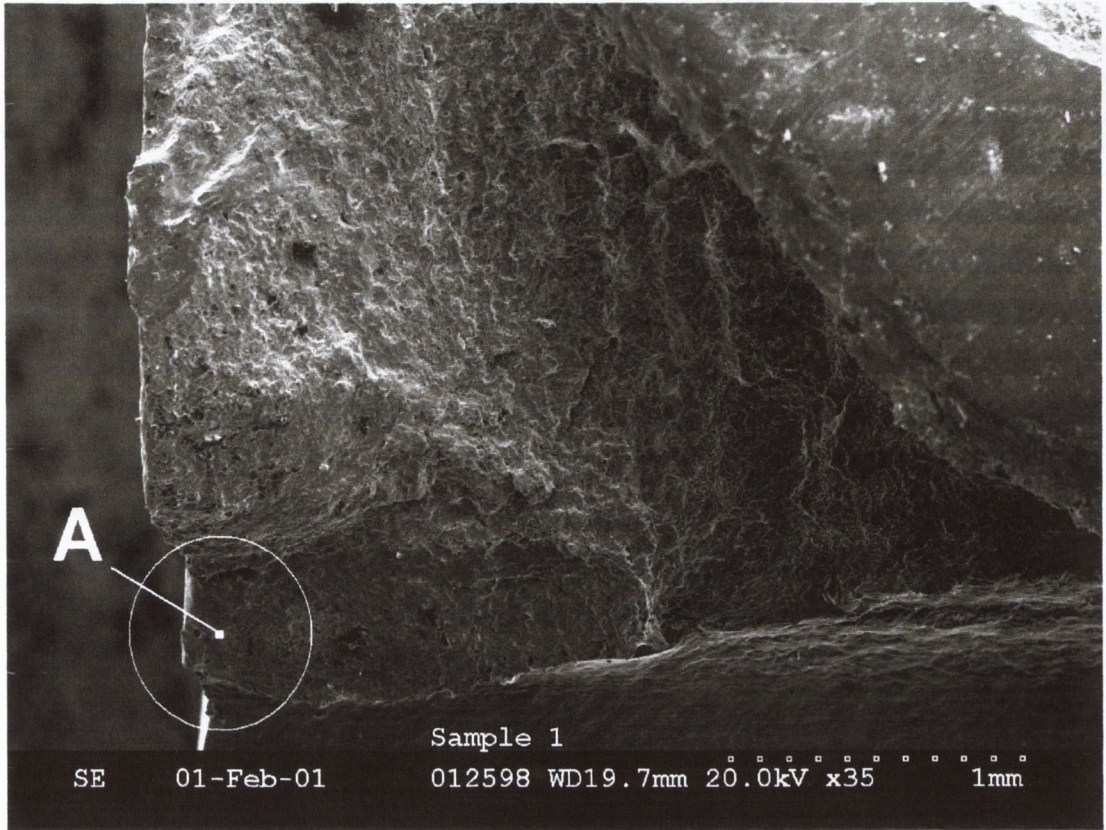




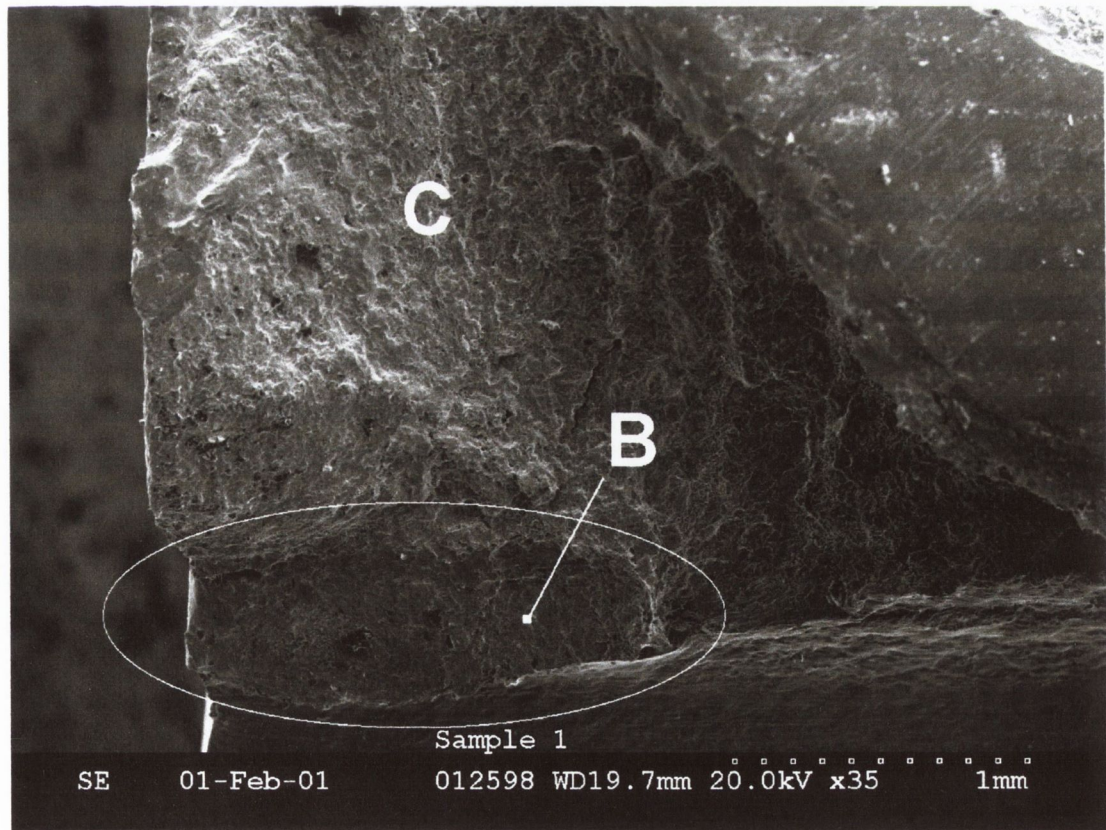
*Fig. A.41 - Typical fatigue failure surface*



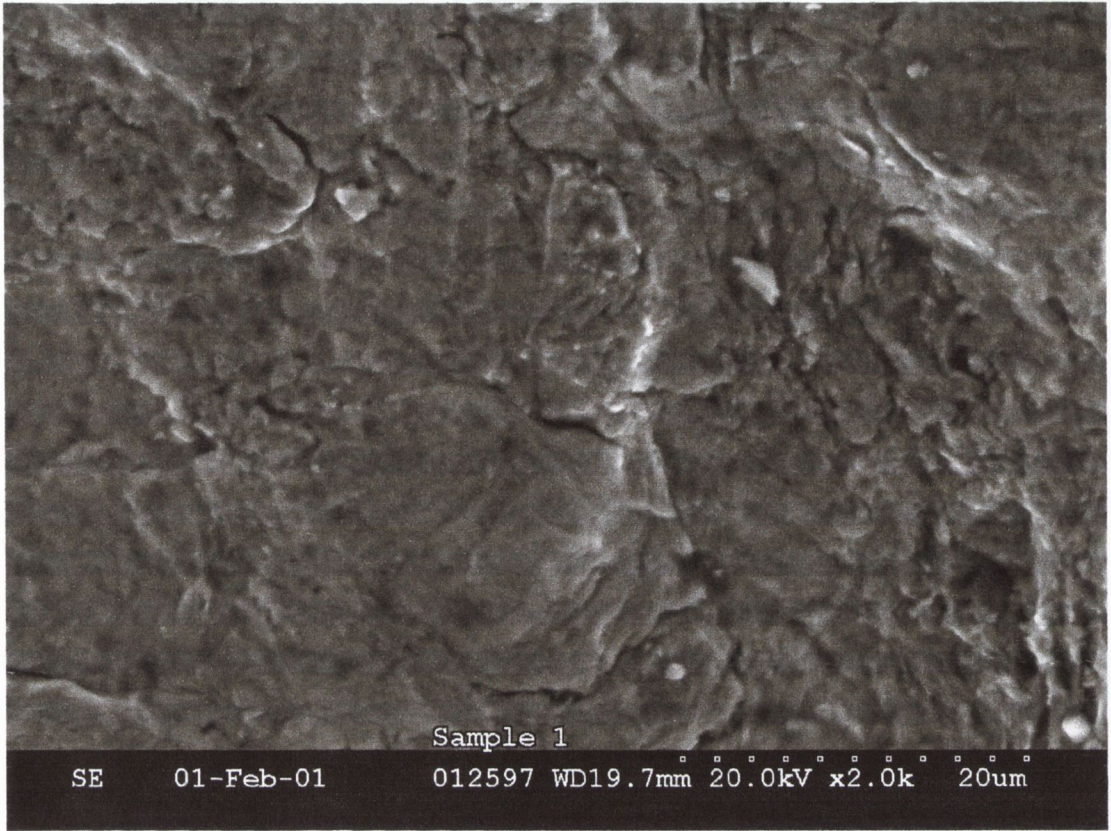
*Fig. A.42 - Typical fast fracture failure surface*



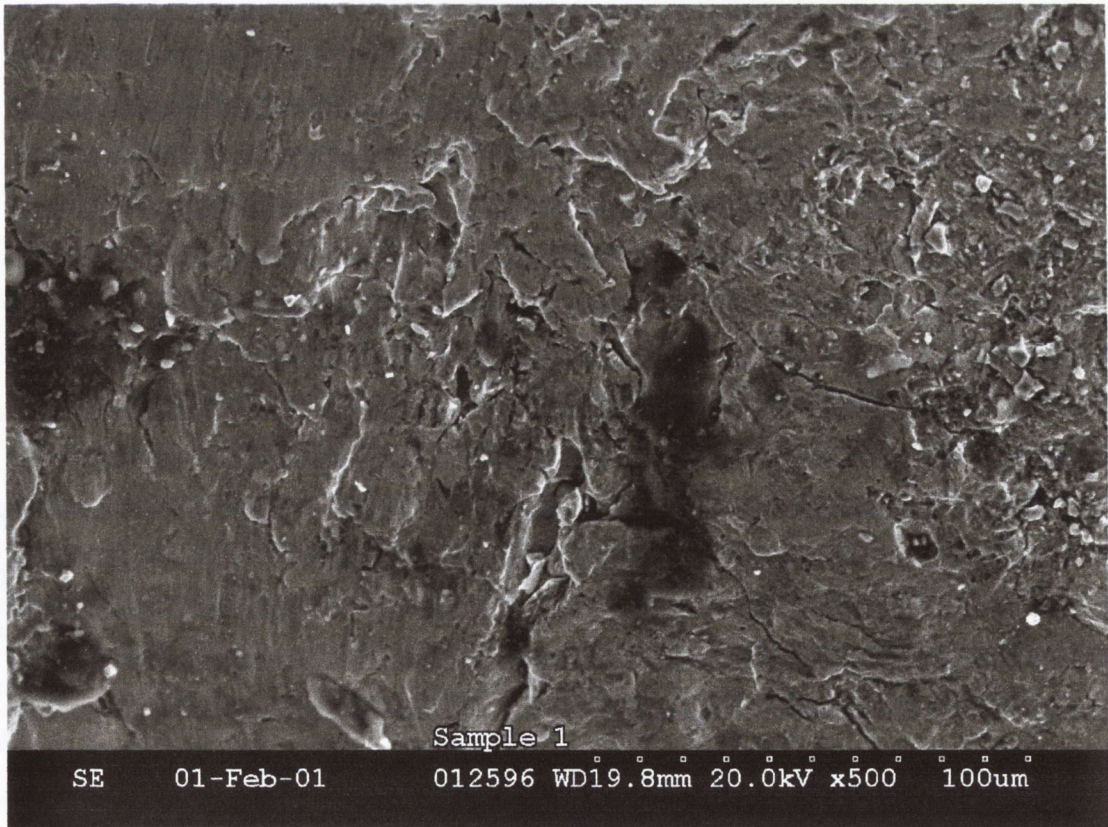
*Fig. A.43 - First crack-and-open specimen - showing zone A*



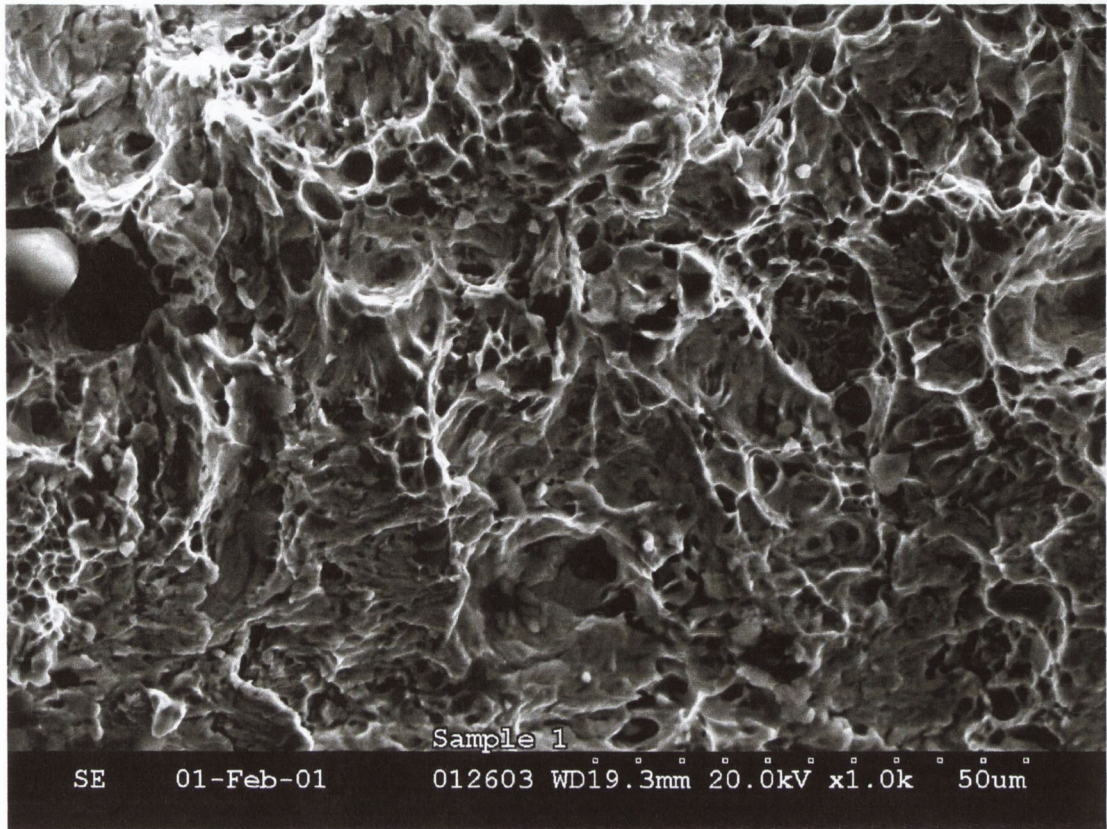
*Fig. A.44 - First crack-and-open specimen - showing zones B and C*



*Fig. A.45 - First crack-and-open specimen - zone A*



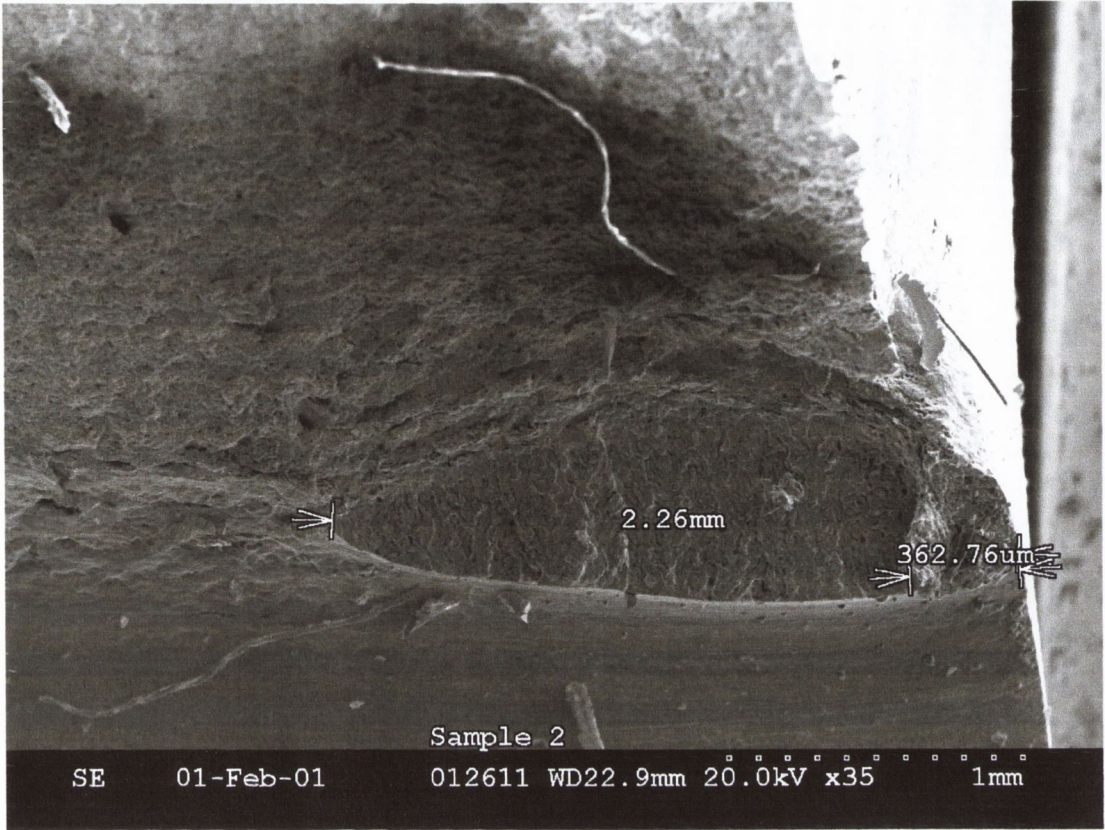
*Fig. A.46 - First crack-and-open specimen - zone B*



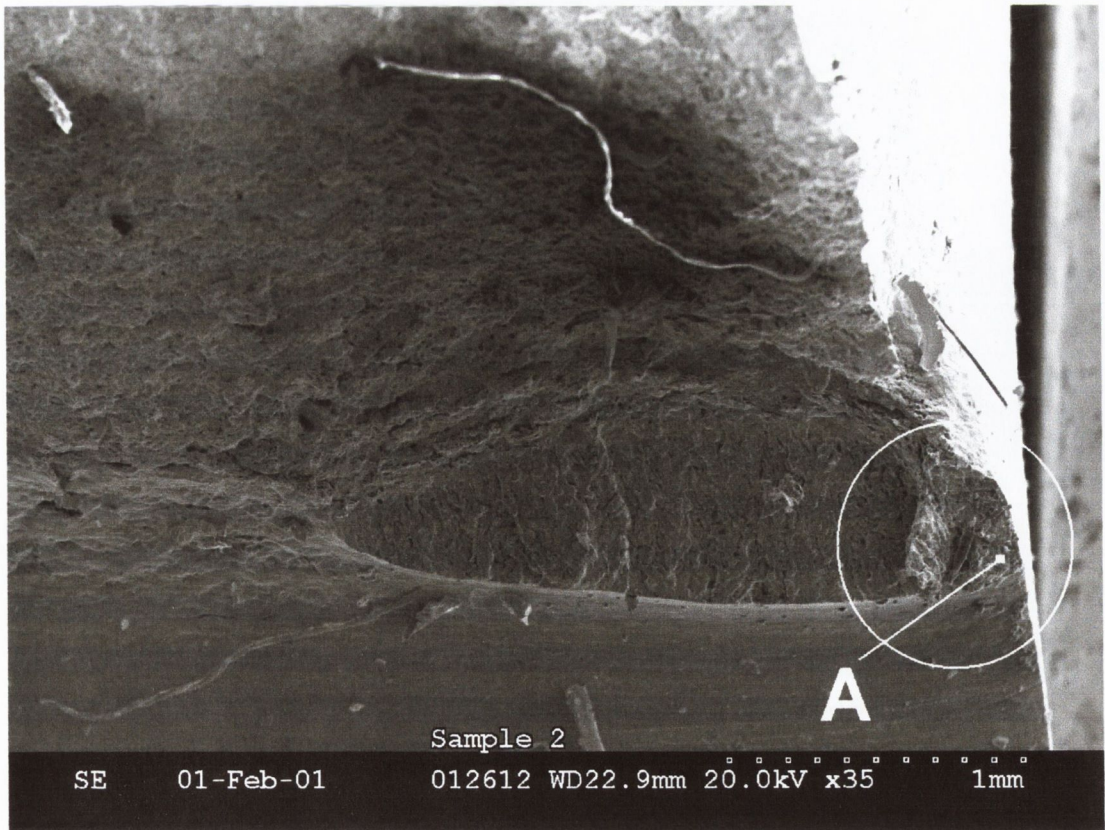
*Fig. A.47 - First crack-and-open specimen - zone C*

It should be noted that for this specimen the growth of the fatigue crack was also measured using the travelling microscope and replica tape as per the procedure outlined in section A.4.3.1.1 above. In fact, the measurements given in Figure A.39(c) are for this specimen. It can be seen that the maximum length measured along the notch, using the travelling microscope, was 0.04mm. This is woefully inaccurate compared to the actual value of 1.6mm measured using the SEM. This underlines the comments made above, concerning the accuracy of the measurements made using the travelling microscope.

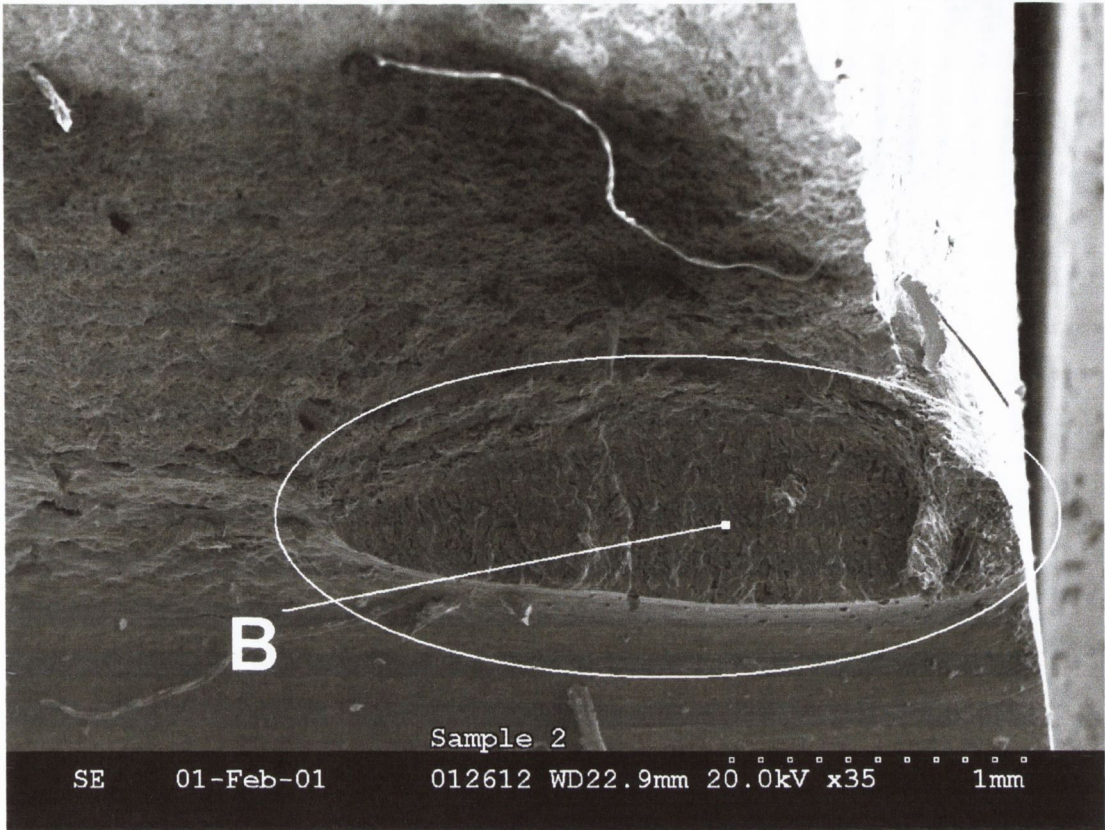
The second crack-and-open specimen is shown in Figure A.48 below. The notch is again orientated along the bottom of the figure and again a very distinctive elliptical shape can be seen. The dimensions of the ellipse are approximately 2.26mm along the notch and 0.5mm perpendicular to the notch. However, the right end of the ellipse appears to be slightly different. Therefore, the failure surface has been divided into two zones (A and B) as shown in Figures A.49 and A.50. Higher resolution views of the failure surfaces in these two zones are given in Figures A.51 and A.52.



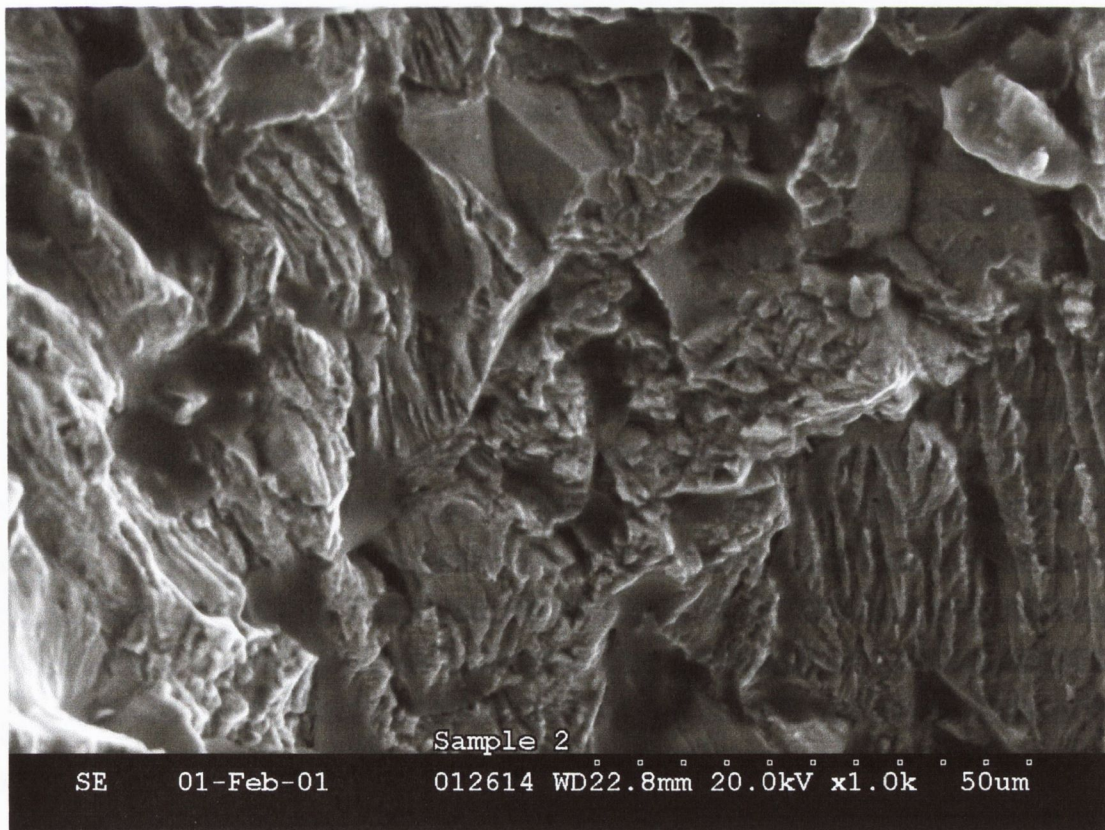
*Fig. A.48 - Second crack-and-open specimen*



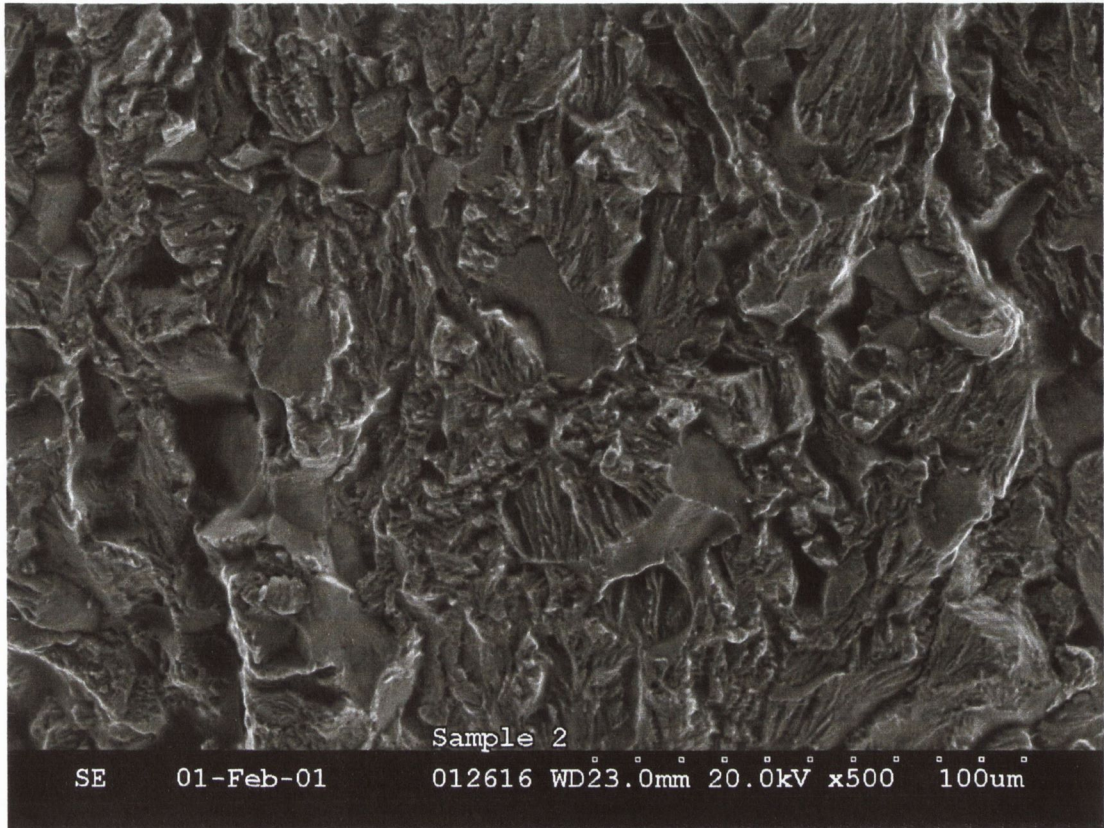
*Fig. A.49 - Second crack-and-open specimen - showing zone A*



*Fig. A.50 - Second crack-and-open specimen - showing zone B*



*Fig. A.51 - Second crack-and-open specimen - zone A*



*Fig. A.52 - Second crack-and-open specimen - zone B*

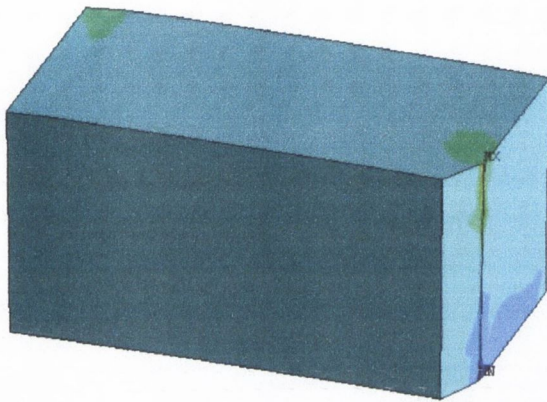
Figures A.51 and A.52 show that both zones A and B are characterised by fatigue failure. Hence, it is concluded that fatigue cracks developed at the Model-T stress concentration are highly elliptical with the major axis orientated along the notch. The elliptical ratio appears to be approximately 0.2.

#### A.4.4 Stress and fatigue assessments

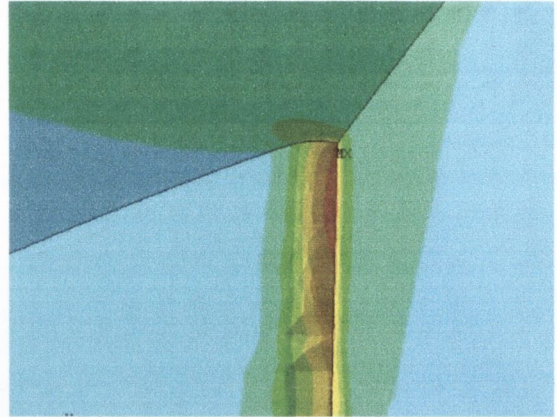
In order to determine the stress distribution within the specimen, a linear Elastic finite element analysis, of the component was undertaken. Due to the symmetry of the problem, it was possible to utilise a half model (see Figure A.53(a)).

Again, the mesh refinement criteria suggested by Wang [1999] was used. That is, approximately 5 elements were placed within a distance  $a_0$  from the hotspot. This resulted in a very fine mesh (element size  $\sim 0.04\text{mm}$ ) at the failure location.

Due to this fine mesh size, an unexpected phenomenon was observed. That is, the hotspot did not occur at the top surface of the specimen, where normal bending theory would predict. Instead, it was located a very small distance, approximately 0.17mm, down the notch (see Figure A.53(b)).



(a) FEM of Model-T



(a) Detail of the hotspot

Fig. A.53 - The finite element analysis of the Model-T specimen

It is believed that this is a real effect, and is explained as below. Figure A.54 shows the X, Y and Z stresses, plotted along the root of the notch. Note that the X, Y and Z stresses correspond to the principal stress for this specimen. It can be seen that the stress in the X-direction (or maximum principal stress) takes its maximum value approximately 0.17mm down the notch root. Also from this diagram, it is possible to observe that the Y and Z stresses are zero at the top of the specimen (i.e. Distance=0mm) and then increase. This is because at a free surface it is impossible to have a normal force, which is not externally applied.

Figure A.55 below shows the stress states that exist at the top of the notch and short distance along the notch root by considering two elemental volumes at these locations. The element at the top surface is free to contract in both the Y and Z directions (i.e. stress is relaxed). The element below the top surface is however constrained in the Z direction; hence at this location a stress is developed in that direction.



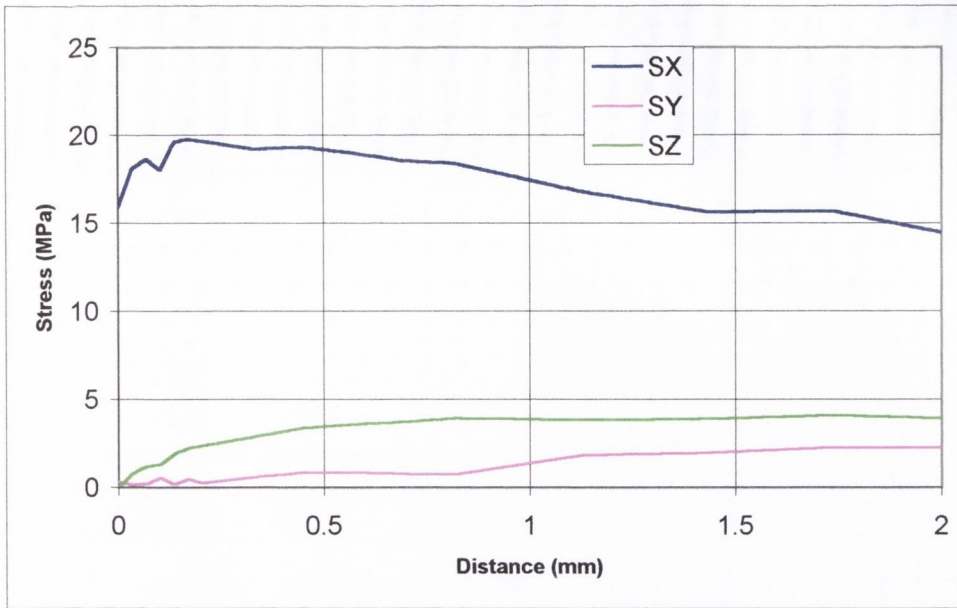


Fig. A.54 - The X, Y and Z stresses plotted along the root of the notch

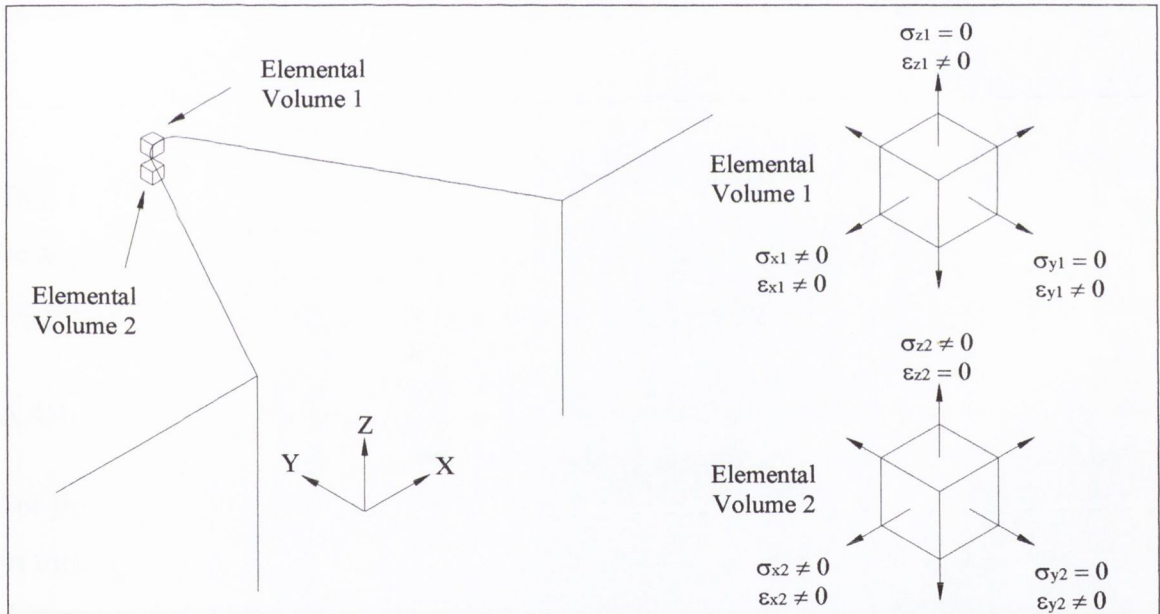


Fig. A.55 - The stress states of two-elemental volumes at the notch root. One at the top surface of the specimen and one slightly below

Given that Hooke's law, describing the relationship between normal stresses and strains, is:

$$\epsilon_x = \frac{1}{E}(\sigma_x - \nu(\sigma_y + \sigma_z))$$

$$\epsilon_y = \frac{1}{E}(\sigma_y - \nu(\sigma_x + \sigma_z))$$

$$\epsilon_z = \frac{1}{E}(\sigma_z - \nu(\sigma_x + \sigma_y))$$

(A-13)

Given that the strain in the Z direction is equal to zero for the lower elemental volume (No. 2), the relationship between stress in the X direction and the Z direction, at this location, is:

$$\varepsilon_{z2} = \frac{1}{E}(\sigma_{z2} - \nu\sigma_{x2}) = 0 \Rightarrow \sigma_{z2} = \nu\sigma_{x2} \quad (\text{A-14})$$

If it is assumed that the strain in the x-direction, for both elemental volumes, must be approximately the same, then:

$$\varepsilon_{x1} = \frac{\sigma_{x1}}{E} \quad (\text{A-15})$$

$$\varepsilon_{x2} = \frac{1}{E}(\sigma_{x2} - \nu\sigma_{z2}) = \frac{\sigma_{x2}}{E}(1 - \nu^2) \quad (\text{A-16})$$

Hence:

$$\sigma_{x1} = (1 - \nu^2)\sigma_{x2} \cong 0.91\sigma_{x2} \quad (\text{A-17})$$

That is, the X direction stress (or the maximum principal stress) at the top surface should be slightly lower than the stress a short distance along the notch root. This is approximately the difference observed in Figure A.54 above.

#### A.4.4.1 Direction of the focus path

For this specimen the plane of crack growth is obviously the plane of symmetry, which is in turn the plane perpendicular to the maximum principal stress at the hotspot. In order to determine the direction of the focus path, within the plane of crack growth, the stress-distance curves, for various directions within this plane are compared in Figure A.57 below. The direction of the angle is defined as per Figure A.56. Note that the paths begin at the hotspot (just below the top surface of the specimen). The zero degree path is therefore parallel to the surface of the specimen and the 90 degree path is along the notch root.

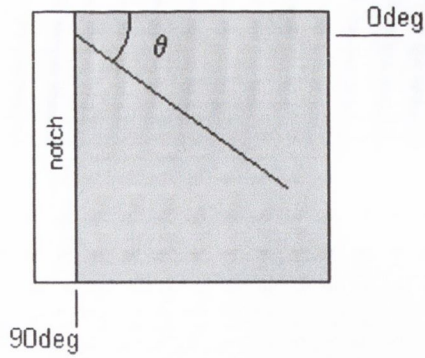


Fig. A.56 - Definition of the focus path angle, within the plane of crack growth

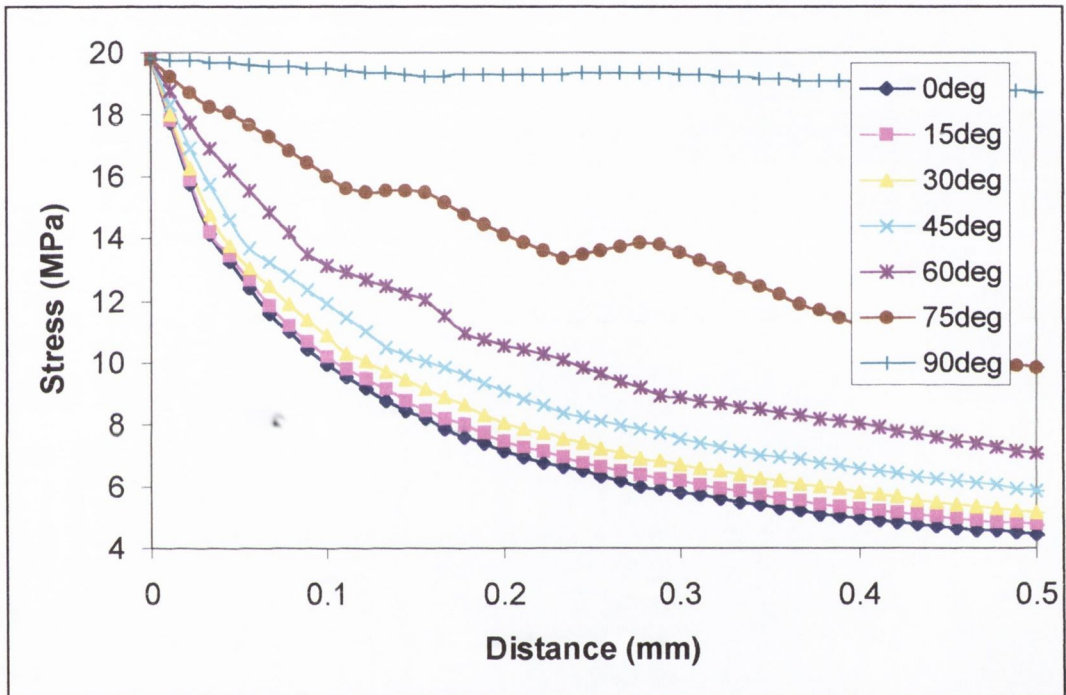


Fig. A.57 - Stress-distance curves for various angles within the plane of crack growth

It can be seen that the zero degree path has the steepest stress gradient and therefore represents the path of minimum crack growth potential. This path is used in the following for the fatigue analyses.

#### A.4.4.2 Summary of results

Table A.16 below shows the results obtained for the various fatigue analyses using the focus path described above. Note that the analyses are done using two different sets of (fatigue) material properties (see section A.1.4).

Table A.16 - Summary of results for the Model-T

	$\Delta\sigma_o _{\text{bending}} (a_o = 0.205\text{mm})$	$\Delta\sigma_o _{\text{tension}} (a_o = 0.288\text{mm})$
<b>Experimental</b>	11.4 kN at $2 \times 10^6$ cycles	
<b>Point method</b> (Error factor)	11.48 kN (0.99)	11.4 kN (1.00)
<b>Line method</b> (Error factor)	13.56 kN (0.84)	13.34 kN (0.85)
<b>Area method</b> (Error factor)	12.72 kN (0.90)	12.7 kN (0.90)
<b>Volume method</b> (Error factor)	13.9 kN (0.82)	14.25 kN (0.80)
<b>CMM</b> (Error factor)	13.64 kN (0.85)	13.8 kN (0.83)
<b>Stress-life meth.</b> (Error factor)	5.72 kN (1.99)	4.86 kN (2.35)

Note: Error factor is defined as the ratio of the *Experimental fatigue strength* to the *predicted fatigue strength*

#### A.4.5 Discussion

The predictions for the Model-T specimen are in general quite good, and if anything, slightly non-conservative. Indeed the point method is almost perfect. The line, area and volume methods result in slightly higher predictions with error factors between 0.8 and 0.9. These are still considered acceptable.

The CMM and the CDM's give considerably more accurate results than the *stress-life* method, which is very conservative. With reference to the Smith and Miller diagram (see Figure A.10), this implies that the stress concentration is indeed crack-like.

Also, it can be seen that the error is not greatly affected by the material properties used. That is, the material properties obtained using the plain specimen fatigue strength determined in bending or tension, as discussed in section A.1.4.4 above.

#### A.5 Concluding remarks

The purpose of this appendix was to present the experimental work and subsequent fatigue analyses done as part of this project in a concise but thorough manner. It expands on the work presented in Chapter 5 and as such the concluding remarks made there are equally as valid here.

## Appendix B: Application of other fatigue methods

---

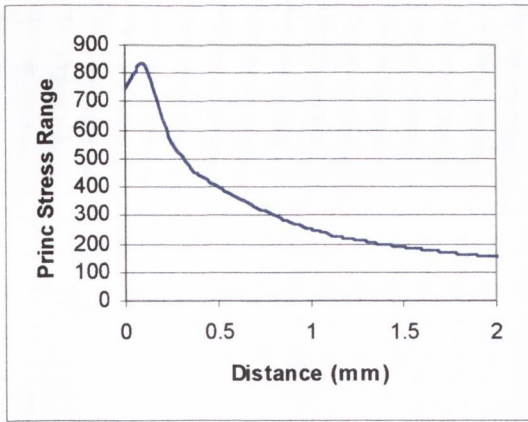
Within the body of this work the main fatigue analysis methods used are the critical distance methods [Taylor, 1999], the crack modelling method [Taylor, 1996] and the stress-life method. The purpose of this appendix is to present the results of other analyses methods when applied to the various specimens discussed throughout this work. It was not convenient to do this within the body of the text because the specimens were presented at different stages.

### **B.1 The Pluvinage method**

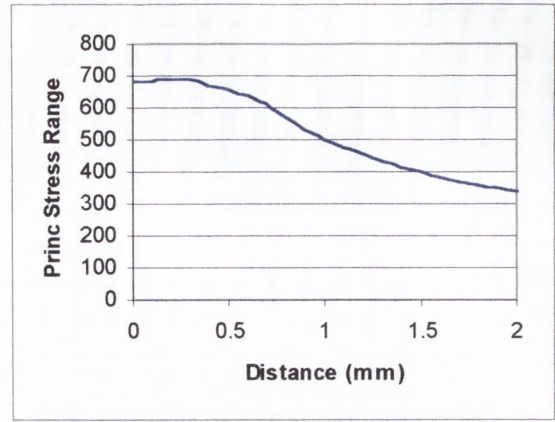
As discussed in Chapter 2, section 2.2.2.3, the Pluvinage approach is a critical distance method implemented using the elastic-plastic stress distribution, which takes into account the stress gradient via a weighting function. Here, the method has been implemented as per Qyalfku *et al.* [1999]. This is essentially a two-dimensional approach that considers the stress distribution plotted on a line ahead of the stress concentration. It should be noted however that the authors have recently updated the method to be a volumetric approach, which takes into account the hydrostatic stress [Qyalfku *et al.*, 2001].

In order to obtain the stress distribution, an elastic-plastic finite element analysis, using the cyclic stress-strain curve, discussed in Appendix A section A.1.2, has been undertaken for each of the specimens. In each case the experimentally determined load at the fatigue limit has been applied at the correct R-ratio.

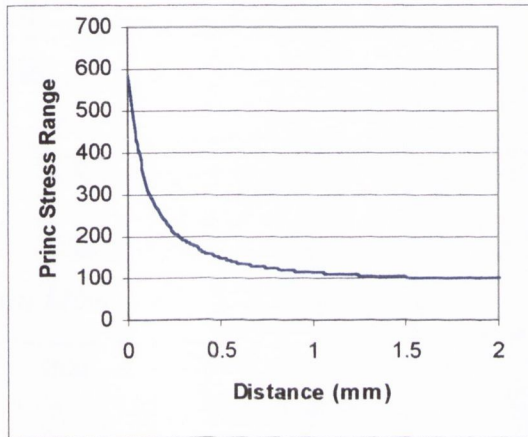
As no guidelines have been given regarding the choice of the focus path, the criteria described in Chapter 2, section 2.2.2.2.2 were used. The elastic-plastic stress-distance curve for the Model-E, Model-J, Model-T and Fillet-A specimens are shown in Figure B.1 below.



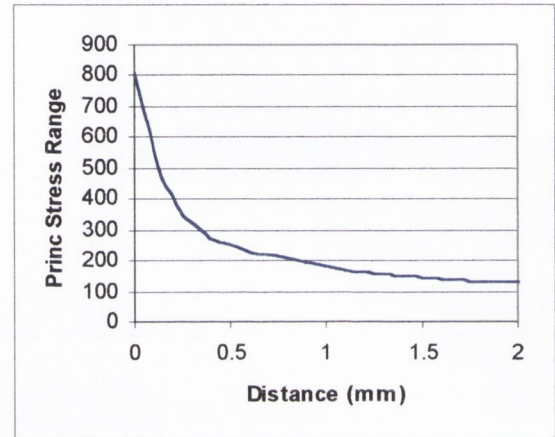
(a) Model-E



(b) Model-J



(c) Model-T



(d) Fillet-A

Fig. B.1 - Elastic-plastic stress distributions

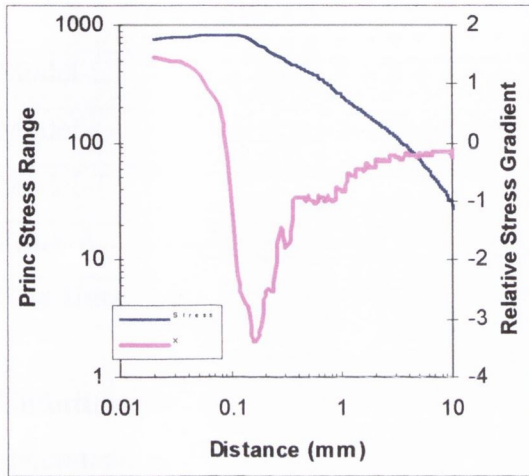
The stress-distance curves for the Model-E and Model-J specimens (Figures B.1(a) and (b) respectively) show the expected relationship. That is, the maximum stress occurs a small distance along the path, inside the specimen. Also, it can be seen that the maximum stress is higher in the Model-E specimen, implying a higher degree of constraint, or less plastic relaxation.

This behaviour is not observed for the Model-T and Fillet-A specimens (Figures B.1(c) and (d) respectively), in which the maximum stress occurs at the very beginning of the path. It was expected that this would happen for the Fillet-A specimen, which has no root radius at the failure location, but is not fully understood for the Model-T specimen.

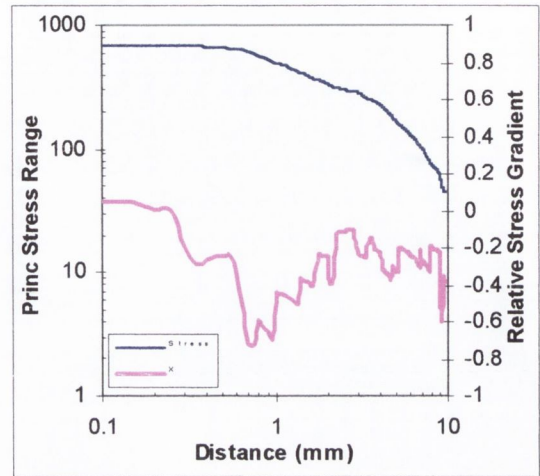
The next step in the analysis is to determine the relative stress gradient. This is defined as per equation B-1 and is plotted in Figure B.2, for the various specimens. A little bit of

numerical instability can be seen, however this is simply due to the nature of the numerical integration.

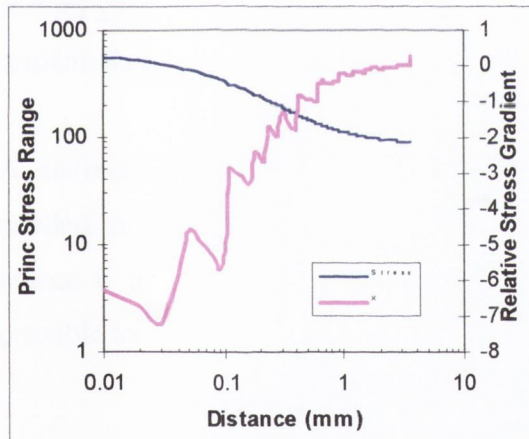
$$\chi = \frac{1}{\sigma(x)} \frac{d\sigma(x)}{dx} \tag{B-1}$$



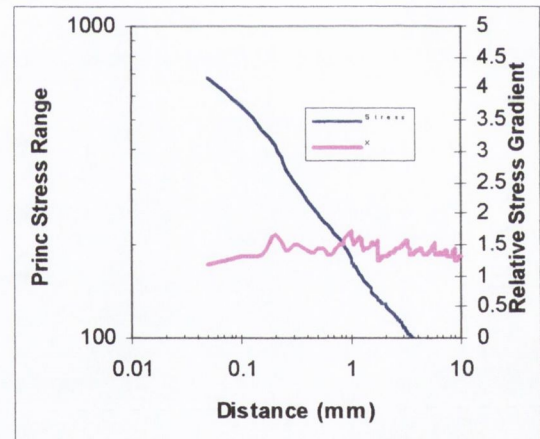
(a) Model-E



(b) Model-J



(c) Model-T



(d) Fillet-A

Fig. B.2 - The relative stress gradient, Model-E

In accordance with the methodology the critical distance,  $x_{ef}$ , coincides with the point of minimum relative stress gradient. It can be seen from Figure B.2 that this is only clearly defined for the Model-E and Model-J specimens. The resulting critical distances are given in Table B.1 below.

Once the critical distance is known, the predicted fatigue strength is given as per equation B-2. The results are also summarised in Table B.1.

$$\Delta\sigma_{FI} = \frac{1}{x_{ef}} \int_0^{x_{ef}} \Delta\sigma_1 (1 - \chi x) dx \quad (B-2)$$

Table B.1 - Summary of results from the Pluvinage approach

	Critical distance, $x_{ef}$ (mm)	$\Delta\sigma_{FI}$ (MPa)	Error factor*
Model-E	0.16	999.9	2.29
Model-J	0.8	898.1	2.06
Model-T	Undetermined	Undetermined	
Fillet-A	Undetermined	Undetermined	

Note: Using the plain specimen fatigue limit determined in bending,  $\Delta\sigma_{ol \text{ bending}} = 435$  MPa

Unfortunately it was not possible to determine the results for the Model-T and Fillet-A specimens, as the critical distance could not be determined. However, it can be seen that the results for the Model-E and Model-J specimens are very conservative, with error factors greater than two. In this respect, the Pluvinage method shows the same trend as the critical distance methods and the crack modelling method.

A distinct disadvantage of this approach, aside from the time and computer resources needed to do the elastic-plastic FEA, is the fact that an elastic-plastic FEA is non-linear. Hence if the result of the analysis is inaccurate, as per the predictions above, it is not possible to simply scale the result to determine the predicted failure load.

## B.2 The Neuber and Peterson methods

As discussed in Chapter 2, section 2.2.2.1 application of the Neuber and Peterson methods requires the presence of a root radius at the stress concentration feature being analysed. Hence, it was only possible to analyse three specimens using these methods, Model-E, Model-T and Model-J. Fortunately, all of these specimens were machined from the same steel, for which the Peterson and Neuber material constants are calculated as per the equations below.

The Peterson material constant for steels, given by Stephens *et al.* [2000]:



$$a_p = 0.0254 \left( \frac{2070}{\sigma_{uts}} \right)^{1.8} = 0.468 \text{ mm} \quad (\text{B-3})$$

The Neuber material constant [Neuber, 1958]

$$\rho^* = 624.8 \times 10^{-6} \exp(-0.0034 \sigma_{uts}) = 0.155 \text{ mm} \quad (\text{B-4})$$

For each of the three specimens investigated, the way in which the nominal stress range,  $\Delta\sigma_{nom}$ , and the elastic stress concentration factor,  $K_t$  was determined is shown in Figures B.3, B.4 and B.5 below. Note that some data from the finite element analyses has been used. The results of the analyses are summarised in Table B.2 below.

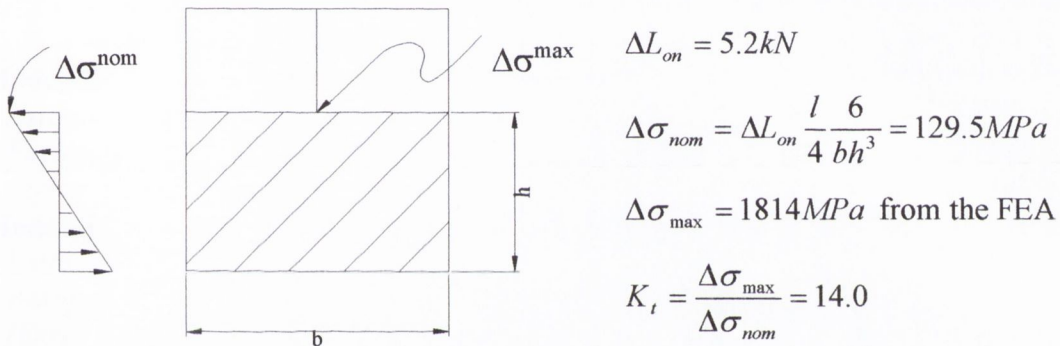


Fig. B.3 - Definition of the elastic stress concentration factor for the Model-E specimen

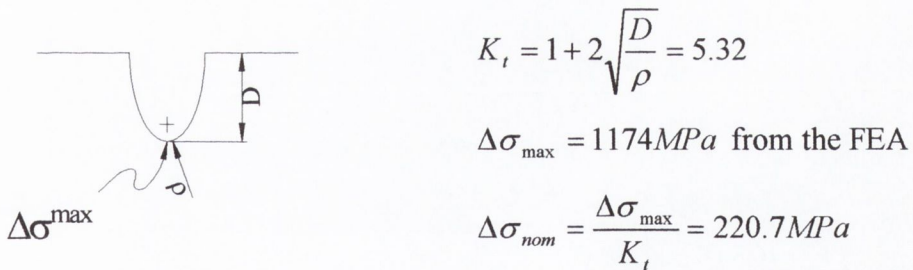
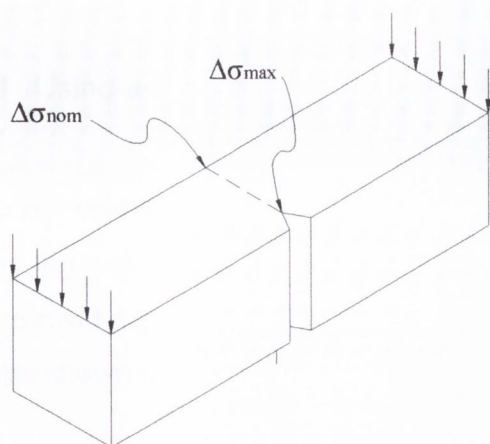


Fig. B.4 - Definition of the elastic stress concentration factor for the Model-J specimen



$$\Delta\sigma_{\max} = 867.1 \text{ MPa from the FEA}$$

$$\Delta\sigma_{\text{nom}} = 109.6 \text{ MPa from the FEA}$$

$$K_t = \frac{\Delta\sigma_{\max}}{\Delta\sigma_{\text{nom}}} = 7.91$$

Fig. B.5 - Definition of the elastic stress concentration factor for the Model-T specimen

Table B.2 - Summary of results for the Neuber and Peterson methods

	Neuber method	Peterson method	Experimental result
<b>Model-E</b> Estimated fatigue strength Fatigue reduction factor (Error factor)	2.21 kN $K_f = 7.92$ (2.36)	3.57 kN $K_f = 4.893$ (1.46)	5.2 kN
<b>Model-J</b> Estimated fatigue strength Fatigue reduction factor (Error factor)	1.09 kN $K_f = 4.178$ (2.12)	1.11 kN $K_f = 4.108$ (2.08)	2.32 kN
<b>Model-T</b> Estimated fatigue strength Fatigue reduction factor (Error factor)	8.83 kN $K_f = 5.125$ (1.29)	11.58 kN $K_f = 3.907$ (0.98)	11.4 kN

Note: This analysis uses the plain specimen fatigue limit determined in bending,  $\Delta\sigma_{o| \text{ bending}} = 435 \text{ MPa}$

It can be seen that the Peterson and Neuber methods also show the same trends as the critical distance methods and the crack modelling method. That is, the results for the Model-E and Model-J specimens are very conservative while relatively good predictions are obtained for the Model-T specimen.

### B.3 The strain life method

As discussed in Chapter 2, section 2.4.1, the strain-life method has been implemented below in two ways. The first approach uses the strains obtained via an elastic-plastic finite element analysis. The second way is to use the Neuber rule [1961] to estimate the notch tip strains.

### B.3.1 Using an elastic-plastic FEA

Table B.3 below is a summary of the notch tip stresses and strains obtained via the elastic-plastic finite element analyses, in which the applied loads were equal to the experimentally determined fatigue limits. The strain-distance curves, plotted along the various focus paths, are also shown in Figure B.6 below.

Table B.3 - Summary of notch tip stresses and strains obtained from FEA

	Max. values	Min. values	Amplitude	Mean
<b>Model-E</b>	$\sigma_{\max} = 370.1 \text{ MPa}$ $\epsilon_{\max} = 0.016128$	$\sigma_{\min} = -376.4 \text{ MPa}$ $\epsilon_{\min} = 0.006238$	$\sigma_{\text{amp}} = 373.3 \text{ MPa}$ $\epsilon_{\text{amp}} = 0.00494$	$\sigma_{\text{mean}} = -3.15 \text{ MPa}$ $\epsilon_{\text{mean}} = 0.0011183$
<b>Model-J</b>	$\sigma_{\max} = 337.1 \text{ MPa}$ $\epsilon_{\max} = 0.007811$	$\sigma_{\min} = -341.6 \text{ MPa}$ $\epsilon_{\min} = 0.001894$	$\sigma_{\text{amp}} = 339.4 \text{ MPa}$ $\epsilon_{\text{amp}} = 0.0029585$	$\sigma_{\text{mean}} = -2.25 \text{ MPa}$ $\epsilon_{\text{mean}} = 0.0048525$
<b>Model-T</b>	$\sigma_{\max} = 333.0 \text{ MPa}$ $\epsilon_{\max} = 0.0044567$	$\sigma_{\min} = -253.7 \text{ MPa}$ $\epsilon_{\min} = 0.001918$	$\sigma_{\text{amp}} = 293.4 \text{ MPa}$ $\epsilon_{\text{amp}} = 0.00126935$	$\sigma_{\text{mean}} = 39.65 \text{ MPa}$ $\epsilon_{\text{mean}} = 0.00318735$
<b>Fillet-A</b>	$\sigma_{\max} = 424 \text{ MPa}$ $\epsilon_{\max} = 0.0147$	$\sigma_{\min} = -383.5 \text{ MPa}$ $\epsilon_{\min} = 0.0047913$	$\sigma_{\text{amp}} = 403.75 \text{ MPa}$ $\epsilon_{\text{amp}} = 0.00495435$	$\sigma_{\text{mean}} = 20.25 \text{ MPa}$ $\epsilon_{\text{mean}} = 0.00974565$

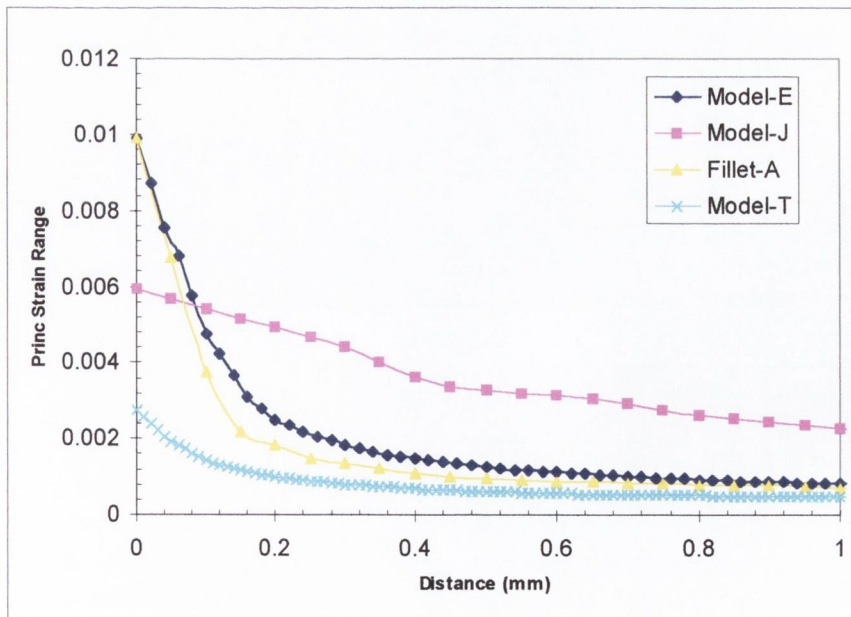
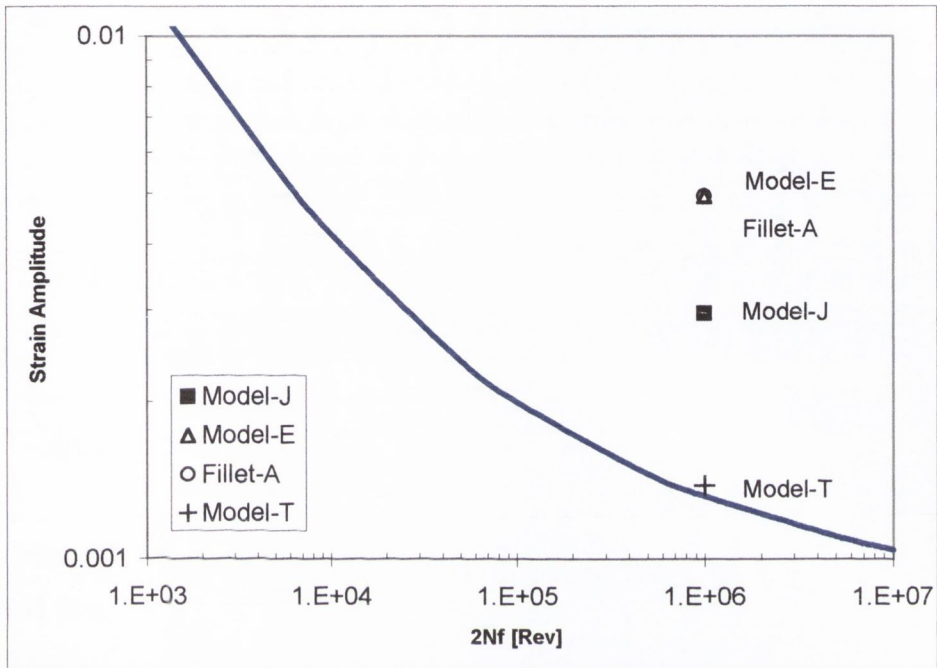


Fig. B.6 - The strain-distance curves (maximum principal, total strain)

Once this data is available, the maximum strain amplitude, for each specimen, can then be plotted on the strain-life curve. These data points are shown in Figure B.7 below, it can be seen that they correspond to  $2N_f = 1 \times 10^6$  cycles. The solid line is the strain-life curve discussed in Appendix A, section A.1.2. This curve is effectively the prediction, for the maximum allowable strain amplitude, made using the strain-life method.



*Fig. B.7 - The strain-life curve showing the strain amplitude of the various specimens, determined using the FEA data*

It must be noted however, that the above does not take into account the effect of mean strain. As discussed in Chapter 2, section 2.4.1.2 this can be done through the use of the Smith, Watson and Topper parameter,  $P_{SWT}$ . The resulting life curve is shown in Figure B.8 below, in which the values for the various models are also shown.

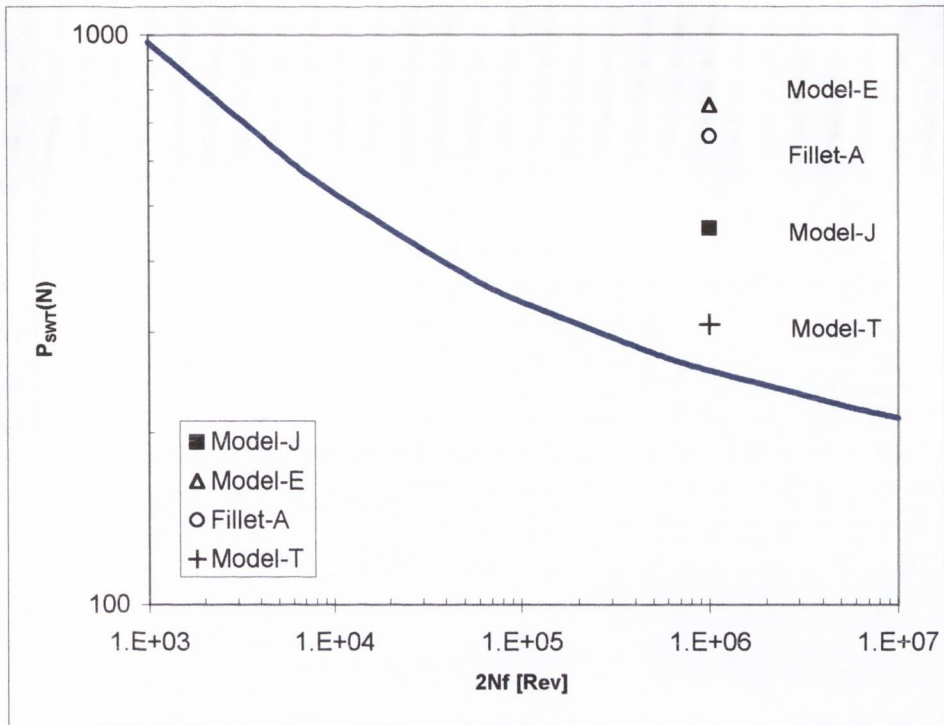


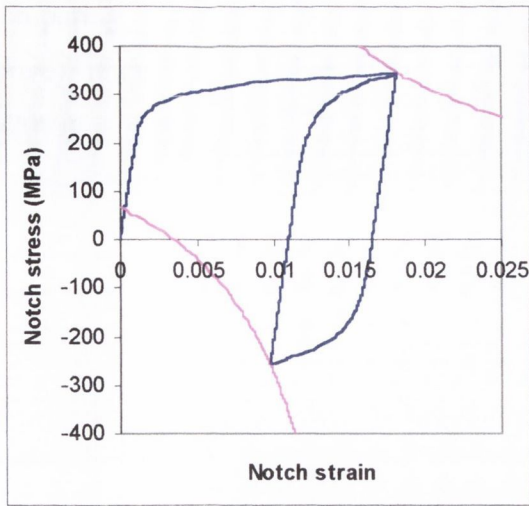
Fig. B.8 - Application of the Smith, Watson and Topper parameter (using the FEA data)

It can be seen that the lives predicted for the specimens are all quite conservative. Indeed, this method predicts that the Model-E specimen should only survive approximately 1000 cycles. The results for the other three specimens are less conservative to various degrees, with the Model-T specimen giving the best predictions. Hence, the trends seen for the critical distance methods are again observed here.

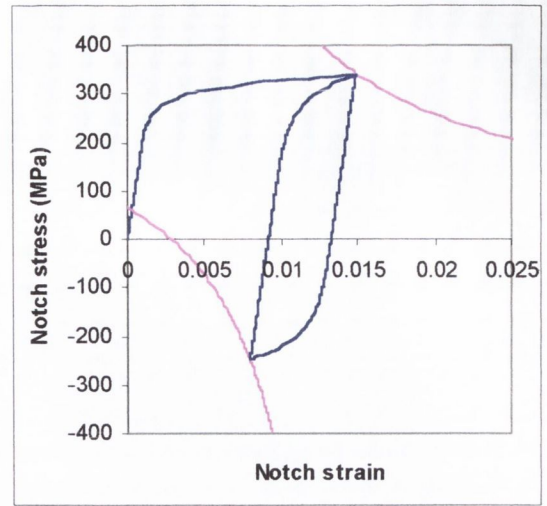
### B.3.2 Using the Neuber rule

As discussed in Chapter 2, section 2.4.1.1, in order to use the Neuber rule to estimate the local notch tip stresses and strains, you must be able to define the elastic stress concentration factor,  $K_t$ , and the fatigue reduction factor,  $K_f$ . Hence, this approach could only be applied to three specimens, for which these values are given in section B.2 above.

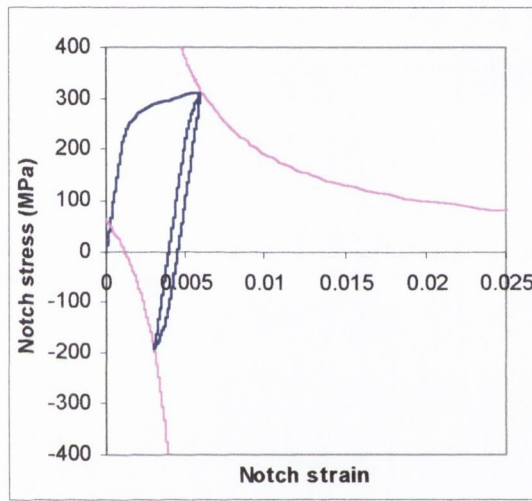
Figure B.9 below shows the estimated stress-strain relationship at the notch tip for the Model-E, Model-J and Model-T specimens. These values are summarised in Table B.4.



(a) Model-E



(b) Model-J



(c) Model-T

Fig. B.9 - The estimated stress-strain relationship at the notch tip

Table B.4 - Summary of estimated notch tip stresses and strains using the Neuber rule

	<b>Max. values</b>	<b>Min. values</b>	<b>Amplitude</b>	<b>Mean</b>
<b>Model-E</b>	$\sigma_{\max} = 344 \text{ MPa}$ $\epsilon_{\max} = 0.0182$	$\sigma_{\min} = -255.5 \text{ MPa}$ $\epsilon_{\min} = 0.00976$	$\sigma_{\text{amp}} = 299.8 \text{ MPa}$ $\epsilon_{\text{amp}} = 0.00422$	$\sigma_{\text{mean}} = 44.25 \text{ MPa}$ $\epsilon_{\text{mean}} = 0.01398$
<b>Model-J</b>	$\sigma_{\max} = 337.9 \text{ MPa}$ $\epsilon_{\max} = 0.01491$	$\sigma_{\min} = -248 \text{ MPa}$ $\epsilon_{\min} = 0.00796$	$\sigma_{\text{amp}} = 292.95 \text{ MPa}$ $\epsilon_{\text{amp}} = 0.003475$	$\sigma_{\text{mean}} = 44.95 \text{ MPa}$ $\epsilon_{\text{mean}} = 0.0111435$
<b>Model-T</b>	$\sigma_{\max} = 311 \text{ MPa}$ $\epsilon_{\max} = 0.00602$	$\sigma_{\min} = -192 \text{ MPa}$ $\epsilon_{\min} = 0.00303$	$\sigma_{\text{amp}} = 251.5 \text{ MPa}$ $\epsilon_{\text{amp}} = 0.001495$	$\sigma_{\text{mean}} = 59.5 \text{ MPa}$ $\epsilon_{\text{mean}} = 0.004525$

Comparing the values above with the strain amplitudes obtained via FEA (see Table B.3 above), it can be seen that, for these specimens, the Neuber rule is relatively accurate ( $\pm 20\%$ ).

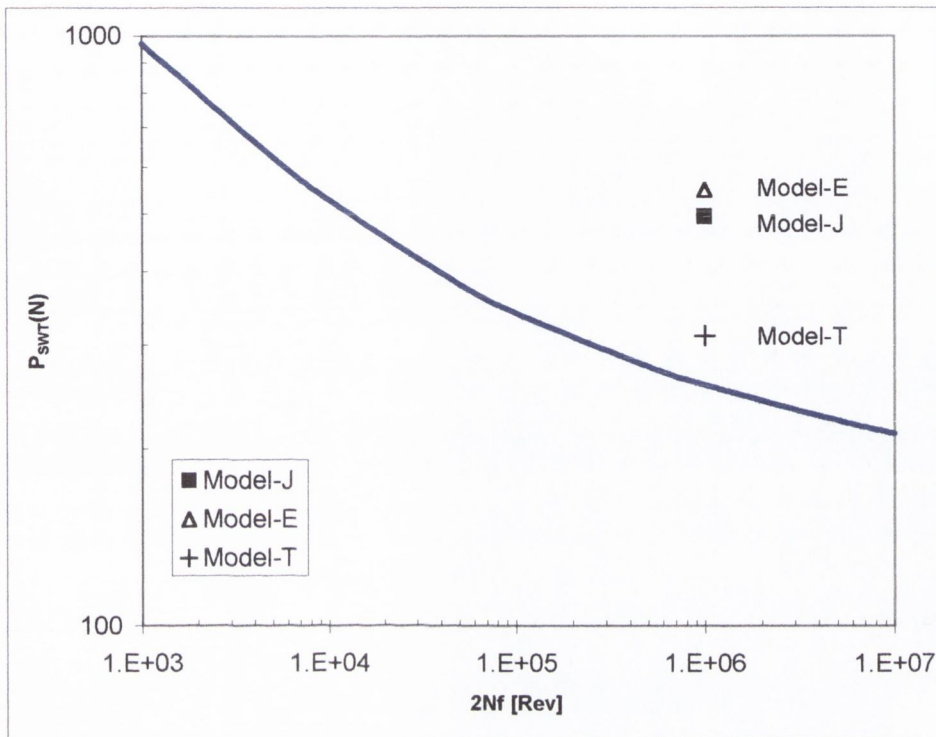


Fig. B.10 - Application of the Smith, Watson and Topper parameter (using the Neuber rule)

As per the section above, once the notch tip stresses and strains are known the fatigue prediction can be made using the Smith, Watson and Topper parameter,  $P_{SWT}$ . The resulting life curve is shown in Figure B.10 above, on which the values for the various models are also shown.

As expected the results are very similar to those obtained using the FEA data. That is, the predictions for all of the specimens are conservative, with Model-E being the most conservative and Model-T being the least conservative.

#### ***B.4 Concluding remarks***

It has been shown above that the predictions of the Pluvinage method, the traditional approaches of Neuber and Peterson and the strain-life method (implemented using FEA data and the Neuber rule) all show similar trends to the critical distance methods and the crack modelling method. That is, very conservative predictions were obtained for the Fillet-A, Model-E and Model-J specimens, while the Model-T specimen enjoyed more accurate predictions. From this it was concluded that the critical distance methods and the crack modelling methods are not unique in being unable to predict the fatigue behaviour of certain complex three-dimensional stress concentrations.



# Appendix C: ANSYS macros

---

## C.1 The area method macro

### C.1.1 Methodology

The area method is implemented via a numerical integration done within an ANSYS macro, which makes use of the *ANSYS - path operations* commands. Essentially, the area being considered is discretised by multiple paths onto which the stress is plotted, radiating from the hotspot as shown in Figure C.1 below.

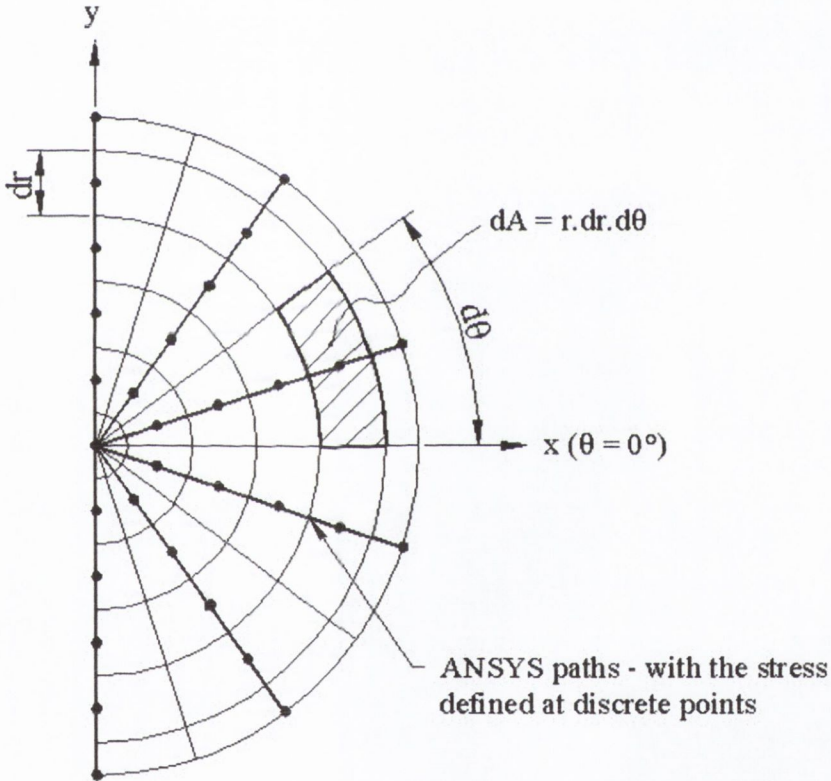


Fig. C.1 - The area method macro methodology

### C.1.2 Running the Area Method macro

In order to run the macro, the user must make sure that two files, (*AreaMeth.mac* and *AreaMethStart.mac*) are either in the working directory of the current ANSYS model or in the ANSYS docu subdirectory (C:\Program Files\Ansys Inc\ANSYS57\docu).

If these two files are present, simply type, *AreaMethStart* in the command prompt. The following dialogue box will appear and wait for user input.

**Multi-Prompt for Variables**

**AreaMeth**  
For calculating the average stress in a circular Area

**Number of the Hotspot Node**  
CenNd

**Number of a Node on the x-axis**  
xNd

**Number of a Node in the x-y plan**  
xyNd

**Maximum Angle**  
MaxAng

**Number of Paths**  
NoPaths

**Radius of the Circular Area**  
Rc

**Number of Points on the Paths**  
NoPoints

**The Stress Component**  
StrType

*Fig. C.2 - User interface for the Area Method macro*

### C.1.3 Inputs

#### *CenNd, xNd and xyNd*

The first three inputs are node numbers, which define a cylindrical coordinate system. The first node defines the centre of the area and is generally taken to be the hotspot node. The second node is a node on the x-axis or the zero degree direction and the third is simply any node in the x-y plane. (Note: it is sometimes necessary to copy the hotspot node in order to create a node along the x-axis).

### *MaxAng*

The fourth input defines the angle of the circular sector considered. This is usually  $180^\circ$ , which implies a semi-circle.

### *NoPaths*

The fifth input is the number of ANSYS paths that are used to divide the area (see Figure C.1). This number should be increased until solution convergence has been achieved.

### *Rc*

The sixth input is the radius of the circular sector being considered. As discussed in Chapter 3, Section 3.1.2, this is usually taken to be  $1.32 a_0$ .

### *NoPoints*

The seventh input is the number of divisions into which the ANSYS paths are divided. Again, this value should be increased until solution convergence has been achieved.

### *StrType*

The last input defines the stress component that is averaged inside the circular sector. This defaults to the first principal stress.

## **C.2 The volume method macro**

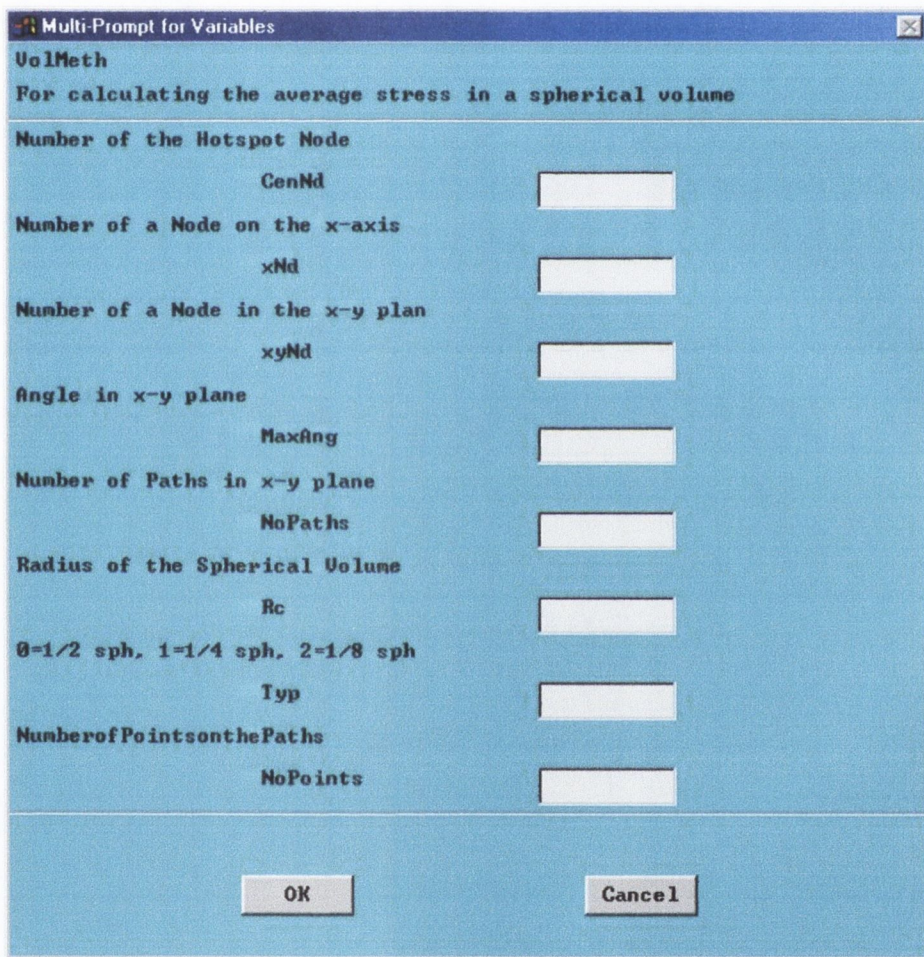
### **C.2.4 Methodology**

The volume method is implemented in a very similar manner as per the area method discussed above. Except in this case the numerical integration is carried out within a spherical volume using a spherical coordinate system.

## C.2.5 Running the Volume Method macro

In order to run the macro, the user must make sure that two files, (*VolMeth.mac* and *VolMethStart.mac*) are either in the working directory of the current ANSYS model or in the ANSYS docu subdirectory (C:\Program Files\Ansys Inc\ANSYS57\docu).

If these two files are present, simply type, *VolMethStart* in the command prompt. The following dialogue box will appear and wait for user input.



The dialog box is titled "Multi-Prompt for Variables" and contains the following text and input fields:

**VolMeth**  
For calculating the average stress in a spherical volume

Number of the Hotspot Node  
CenNd

Number of a Node on the x-axis  
xNd

Number of a Node in the x-y plane  
xyNd

Angle in x-y plane  
MaxAng

Number of Paths in x-y plane  
NoPaths

Radius of the Spherical Volume  
Rc

$\theta=1/2$  sph,  $1=1/4$  sph,  $2=1/8$  sph  
Typ

Number of Points on the Paths  
NoPoints

OK Cancel

Fig. C.3 - User interface for the Volume Method macro

## C.2.6 Inputs

### *CenNd, xNd and xyNd*

The first three inputs are node numbers, which define a spherical coordinate system. The first node defines the centre of the area and is generally taken to be the hotspot

node. The second node is a node in the x-direction or on the  $\theta = 0^\circ$  line and the third is simply any node in the x-y plane. (Note: it is sometimes necessary to copy the hotspot node in order to create nodes in the appropriate directions).

#### *MaxAng*

The fourth input defines the enclosed angle in the x-y plane. This is usually  $180^\circ$ , which implies a semi-circle.

#### *NoPaths*

The fifth input is the number of ANSYS paths (in each plane) that are used to divide the volume. This number should be increased until solution convergence has been achieved.

#### *Typ*

The sixth input defines the shape in which the average volume is calculated. Three different shapes are possible; a half sphere, a quarter sphere and one eights of a sphere. For these the *Typ* input should be 1, 2 or 3 respectively.

#### *Rc*

The seventh input is the radius of the circular sector being considered. As discussed in Chapter 3, Section 3.2.1, this is usually taken to be  $1.54 a_0$ .

#### *NoPoints*

The final input is the number of division into which the ANSYS paths are divided. Again, this value should be increased until solution convergence has been achieved.

## Appendix D: Application of PM to rotating bending data

---

The purpose of this appendix is to present the application of the point method [Taylor, 1999] to a large amount of experimental data which demonstrates the size effect observed in the fatigue strength of rotating steel bending specimens. The data, given in Table D.1 below, has been produced by various authors but was compiled by Heywood [1962].

Twenty-eight different steels, of various chemical composition and strength, are included. The point method has been applied to each material separately (see Figure D.1 below), by choosing the value of  $a_o$ , which results in the best fit with the experimental data. The best fit was chosen on the basis of visual inspection. Based on this  $a_o$  value the threshold stress intensity factor,  $\Delta K_{th}$ , for the material was then estimated using the El Haddad equation. That is:

$$\Delta K_{th} = \Delta \sigma_o \sqrt{\pi a_o} \quad (D-1)$$

The intention is to determine if the point method is suitable to predict the size effect observed in this data.

### ***D.1 The Data***

The experimental data is reported in Table D.1 below.

Table D.1 - Size effect data for plain steel specimens testing in bending

Data set	Material	UTS (MPa)	Yield strength (MPa)	Elongation %	Diameter (mm)	Fatigue limit (MPa)
1	0.44% C, 0.6% Mn	563.3	301.3	32	1.27	240.6
					6.86	246.2
					11.94	229.6
					25.40	216.5
					50.80	218.6
2	0.42% C, 0.6% Mn, 0.15% Si, hot rolled	508.9	256.5	34	1.27	232.4
					6.86	220.6
					11.94	220.6
					25.40	231.0
3	0.57% C, 0.6% Mn, 0.26% Si, H.T.	703.3	462.0	20	1.27	331.0
					11.94	337.9
4	0.45% C	-	-	-	1.27	217.2
					12.70	220.6
					50.80	224.1
5	0.19% C	-	-	-	1.27	179.3
					7.62	191.0
					25.40	168.9
6	0.46% C, 0.66% Mn, 0.2% Si, 3.3% Ni, (SAE 2345 H.T.)	865.3	686.1	22.7	3.18	484.0
					4.06	487.5
					6.35	459.9
					7.62	482.7
					12.70	458.5
					22.10	441.3
7	0.2% C, 0.5% Mn (SAE 1020, strain relieved)	413.0	240.6	37	38.10	458.5
					4.06	200.0
					6.35	200.0
					12.70	193.1
					25.40	193.1
8	0.39% C, 0.7% Mn, 1.7% Ni, 0.7% Cr, 0.35% Mo (SAE 4340 H.T.)	1037.0	917.7	18.2	47.50	193.1
					2.54	586.1
					7.62	552.3
					9.40	558.5
9	0.08% C, 0.4% Mn, 0.7% Ni, 0.07% Mo (H.T. 50, as rolled)	458.5	335.1	32	11.94	520.6
					2.54	303.4
					7.62	317.9
					9.40	315.1
					11.94	289.6

Table D.1 (continued) - Size effect data for plain steel specimens testing in bending

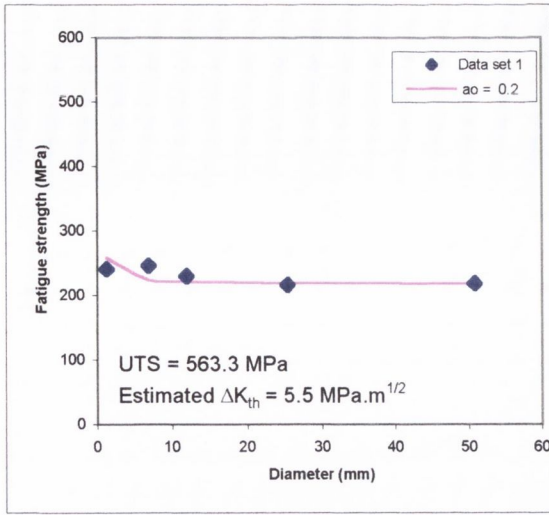
Data set	Material	UTS (MPa)	Yield strength (MPa)	Elongation %	Diameter (mm)	Fatigue limit (MPa)
10	0.31% C, 0.5% Mn, 1.1% Cr, 0.2% Mo (SAE X4130 H.T.)	977.7	797.1	17	3.05	513.7
					6.35	481.3
					12.70	448.2
					22.10	448.2
					38.10	448.2
11	0.22% C, 0.5% Mn, 0.2% Si (SAE 1020, as rolled)	427.5	222.7	28	3.05	227.5
					6.35	217.2
					12.70	186.2
					25.40	193.1
					50.80	193.1
12	0.34% C, 0.8% Mn, 0.24% Si (SAE 1035, as rolled)	604.0	325.4	25	3.05	268.9
					6.35	268.9
					12.70	244.8
					25.40	244.8
					44.45	237.9
13	0.34% C, 0.8% Mn, 0.24% Si (SAE 1035, polished and annealed in <i>vacuo</i> )	535.1	299.2	27.5	3.05	241.3
					6.35	234.4
					12.70	217.2
14	0.14% C, 0.5% Mn, 3.1% Ni, 0.9% Cr (H.T.)	818.4	-	27	3.56	479.2
					7.11	401.3
15	0.46% C, 0.7% Mn, 0.2% Si, 0.12% Mo	617.1	-	31	2.03	266.1
					7.62	274.4
					25.40	248.2
					50.80	236.5
16	(SAE X4340-A)	-	-	-	7.62	551.6
					25.40	496.4
					50.80	496.4
17	0.38% C, 0.8% Mn, 1.8% Ni, 0.7% Cr, 0.25% Mo (SAE 4340 H.T.)	1128.7	-	16	3.05	568.8
					6.35	558.5
					12.70	537.8
					25.40	510.2
					44.45	510.2
18	0.17% C, 0.7% Mn, 0.2% Si, normalised	462.0	299.9	40	2.54	265.5
					4.06	265.5
					6.35	265.5
					12.70	244.1



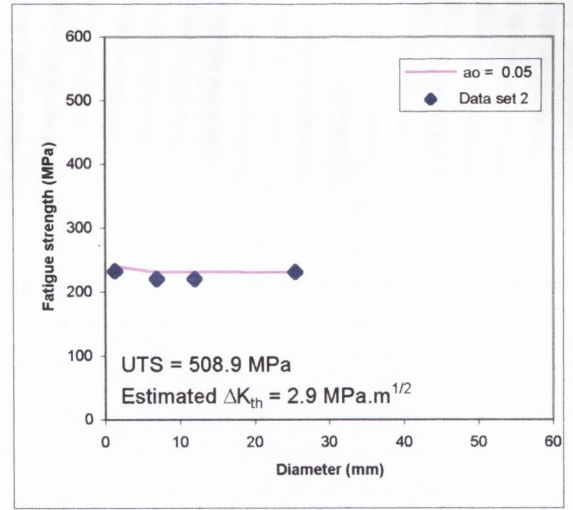
Table D.1 (continued) - Size effect data for plain steel specimens testing in bending

Data set	Material	UTS (MPa)	Yield strength (MPa)	Elongation %	Diameter (mm)	Fatigue limit (MPa)
19	0.04% C	379.2	-	-	1.02	298.6
					2.03	271.7
					4.06	275.8
					7.87	275.8
20	0.41% C	448.2	-	-	1.02	210.3
					2.03	186.2
					4.06	186.2
					7.87	186.2
21	0.35% C (Mechanically polished)	609.5	-	25	2.03	280.6
					4.06	264.8
					7.87	256.5
					16.00	242.0
					32.00	219.3
					56.13	225.5
22	0.35% C (Electrolytically polished)	609.5	-	25	2.03	229.6
					4.06	220.6
					7.87	207.5
					16.00	202.7
					32.00	216.5
23	Ni-Cr steel, H.T.	1130.8	1028.7	11	7.62 27.43	588.1 509.5
24	1% C, normalized	830.8	374.4	12	7.62 27.43	323.4 294.4
25	1% C, annealed	638.5	279.2	13.5	7.62 27.43	294.4 264.8
26	0.1% C	406.8	255.8	29.5	7.62	259.3
					17.27 27.43	255.1 244.8
27	0.3% C	553.7	327.5	24	7.62	288.9
					17.27 27.43	284.1 269.6
28	0.17% C, 0.35% Cr	528.8	-	26	7.62	313.7
					27.43	294.4

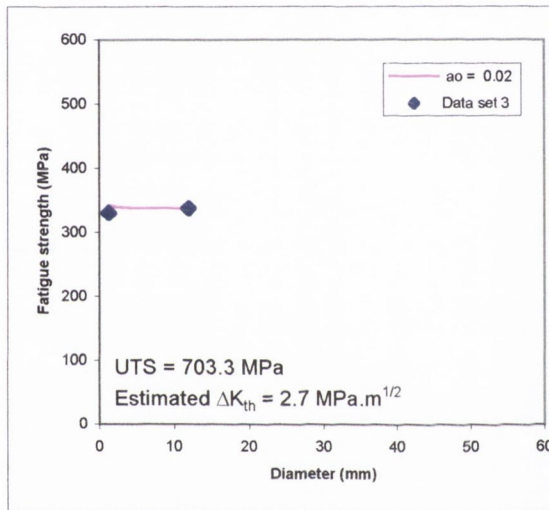
## D.2 Application of the point method



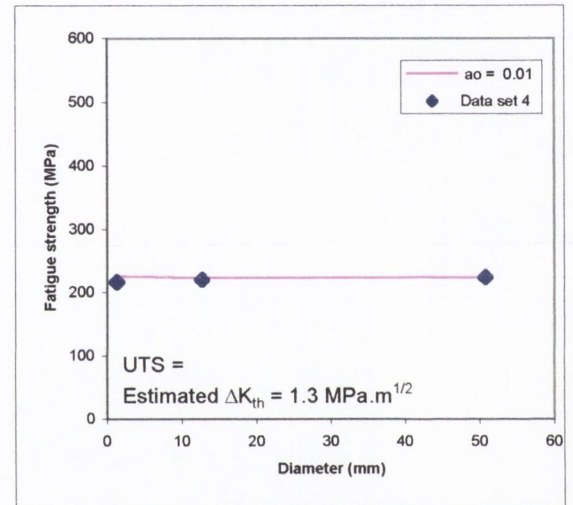
(a) Data set 1



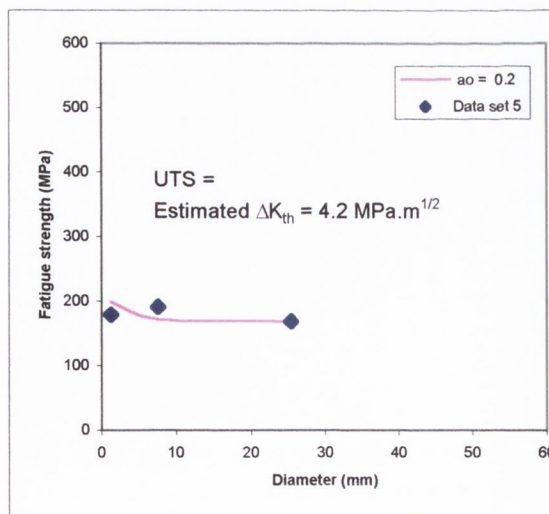
(b) Data set 2



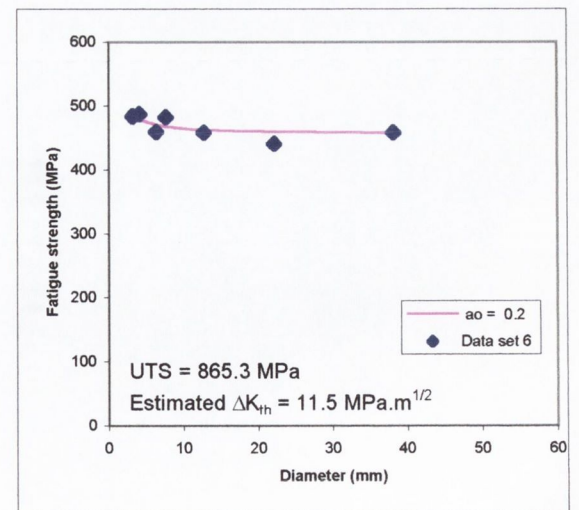
(c) Data set 3



(d) Data set 4

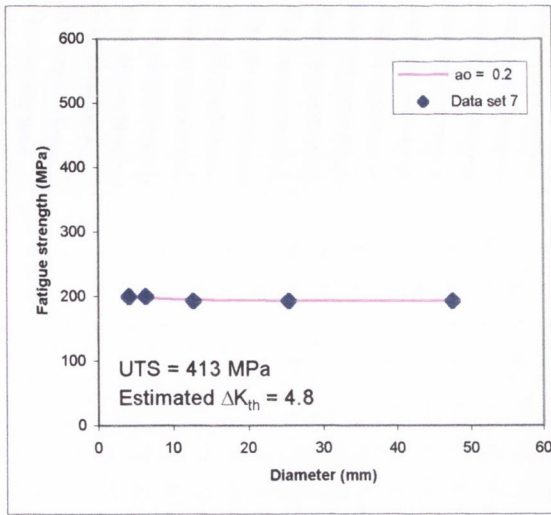


(e) Data set 5

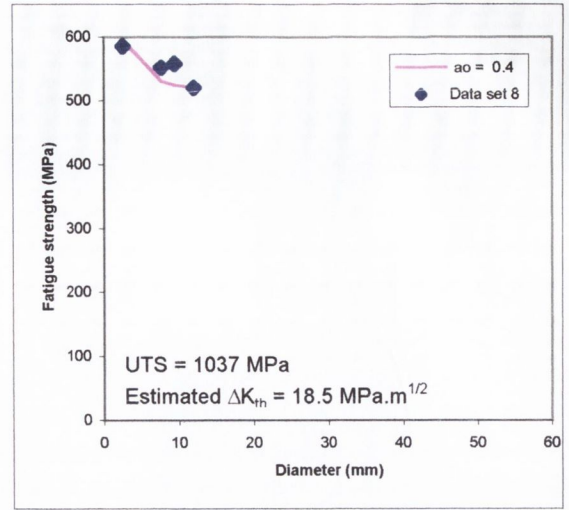


(f) Data set 6

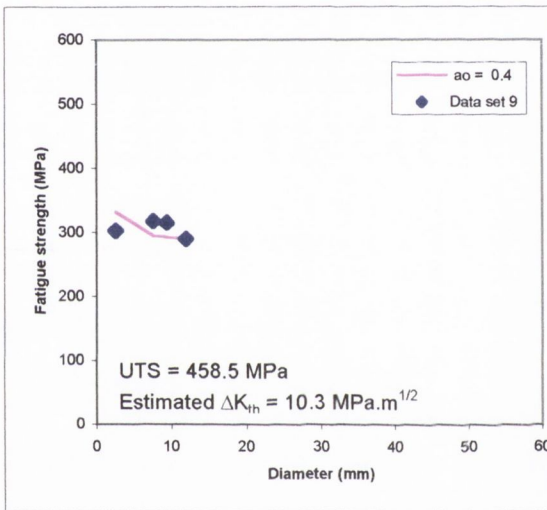
Fig. D.1 - Application of the point method to size effect data for rotating steel specimens



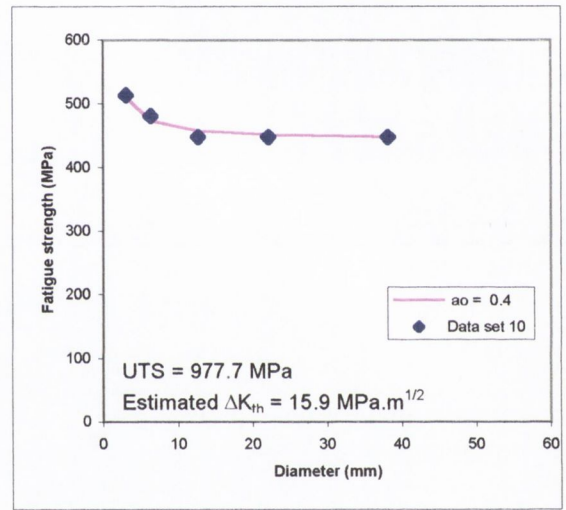
(g) Data set 7



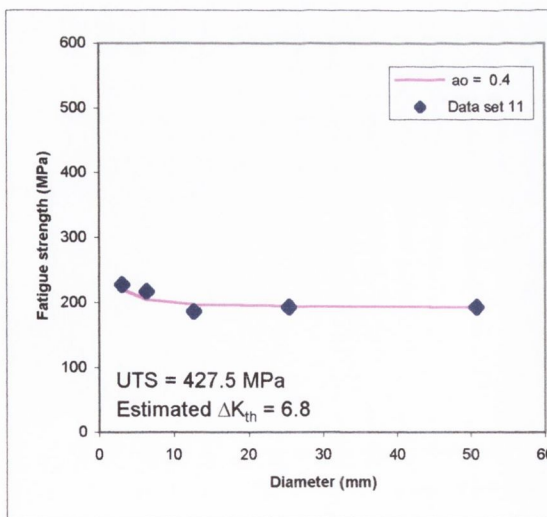
(h) Data set 8



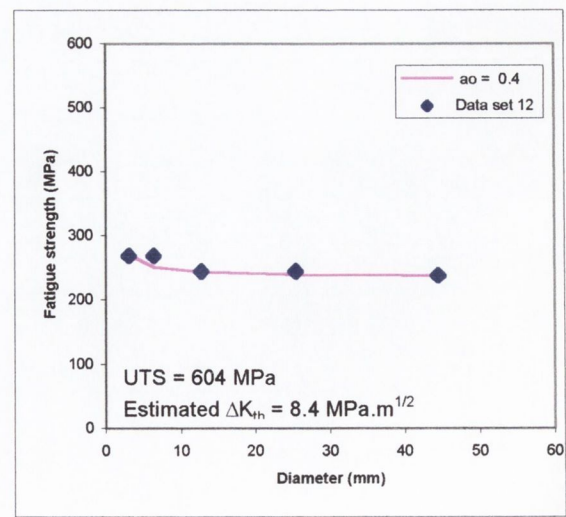
(i) Data set 9



(j) Data set 10

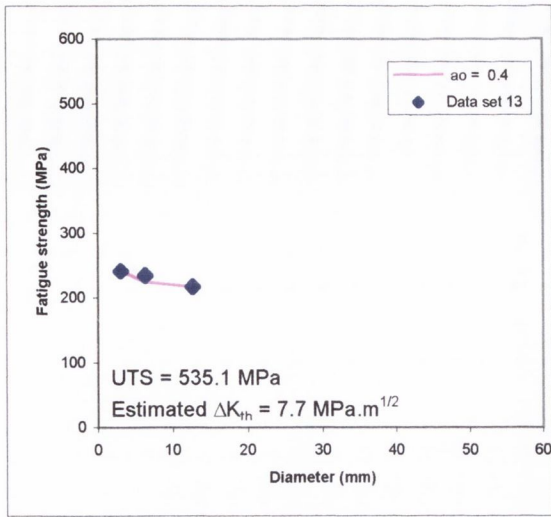


(k) Data set 11

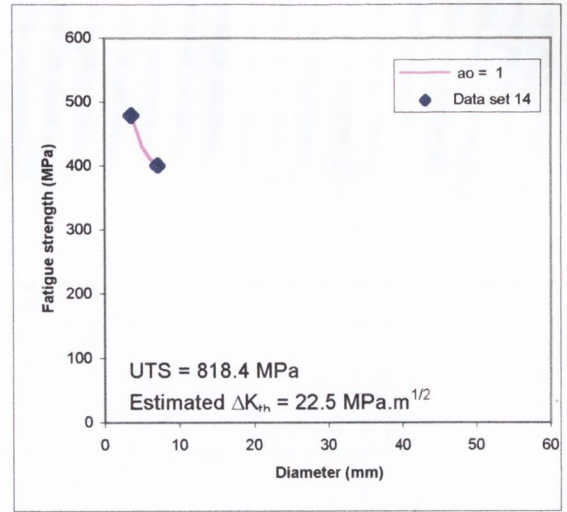


(l) Data set 12

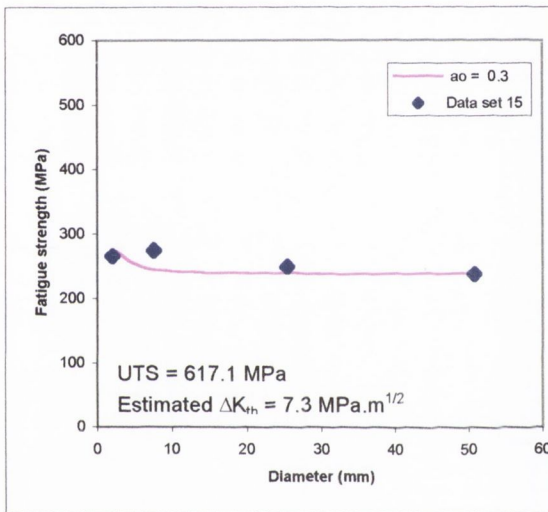
Fig. D.1(cont) - Application of the PM to size effect data for rotating steel specimens



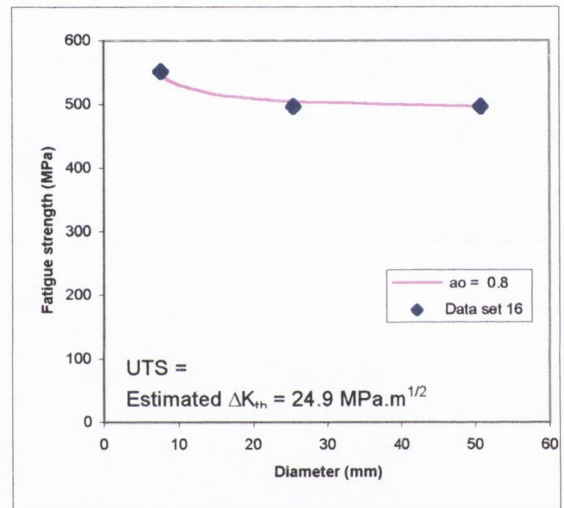
(m) Data set 13



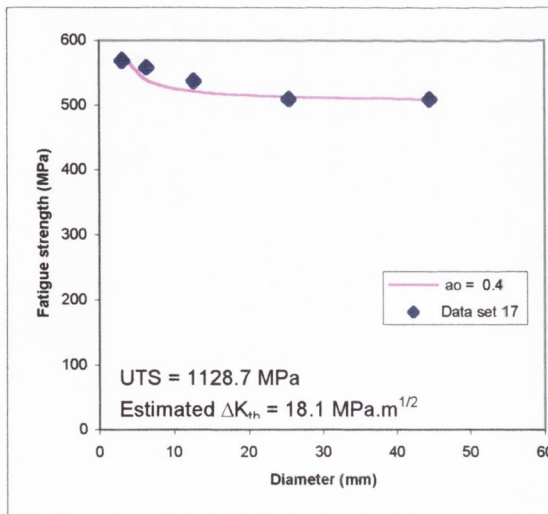
(n) Data set 14



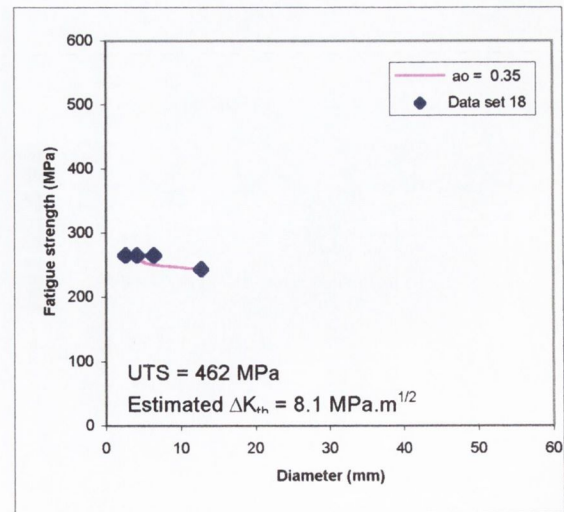
(o) Data set 15



(p) Data set 16

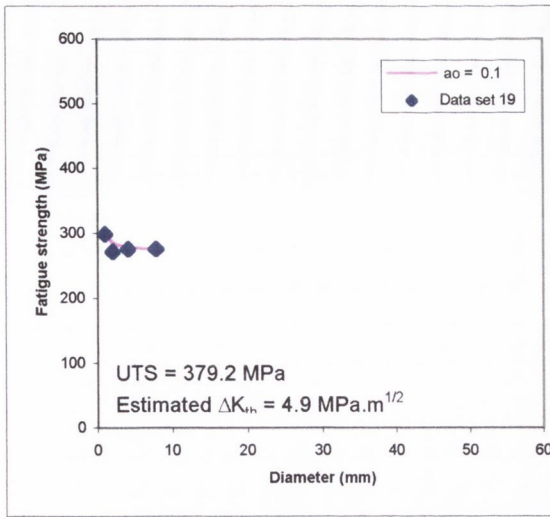


(q) Data set 17

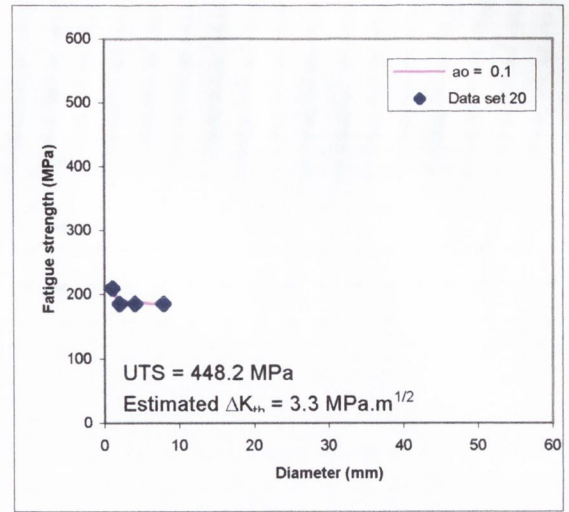


(r) Data set 18

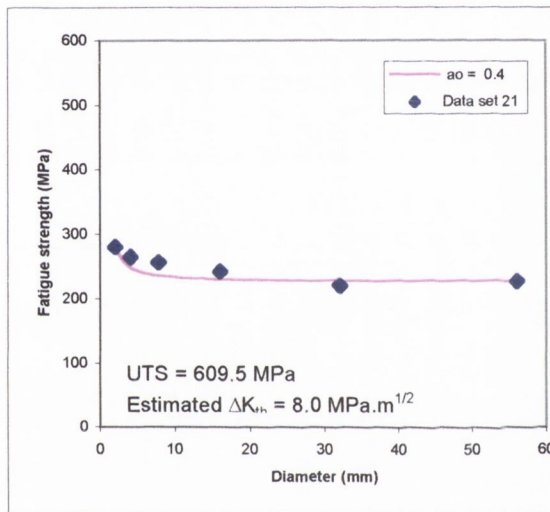
Fig. D.1(cont) - Application of the PM to size effect data for rotating steel specimens



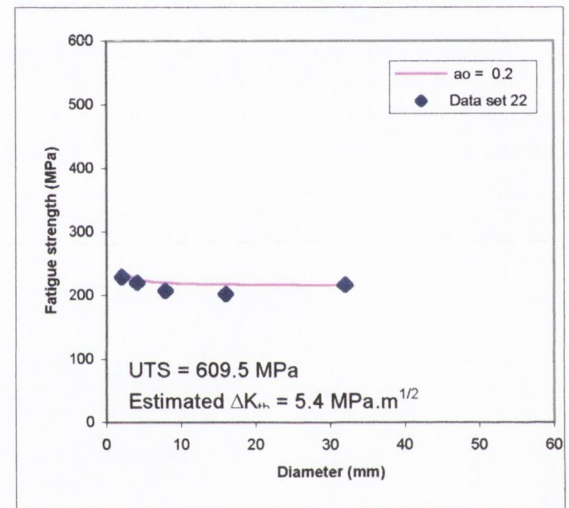
(s) Data set 19



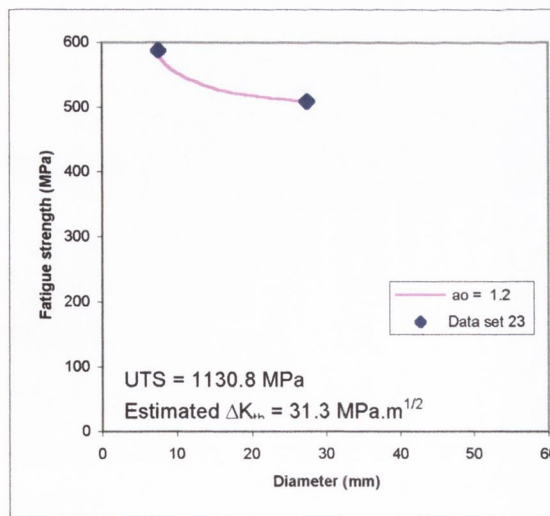
(t) Data set 20



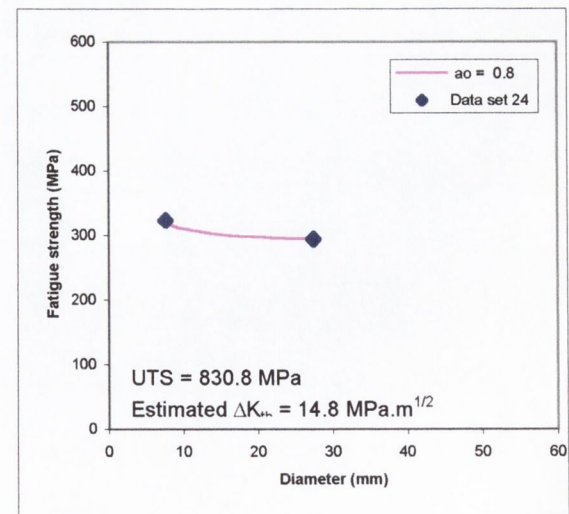
(u) Data set 21



(v) Data set 22

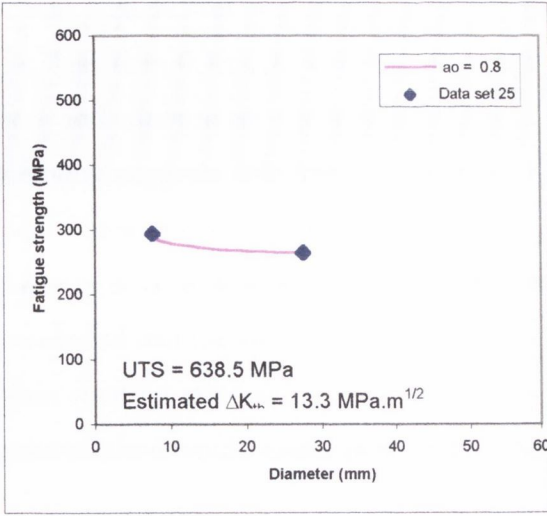


(w) Data set 23

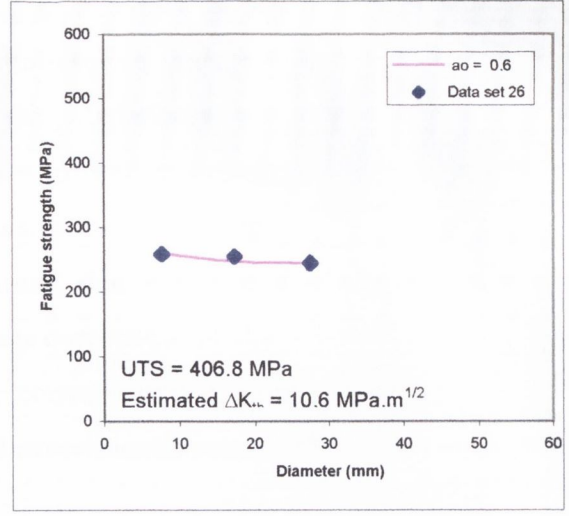


(x) Data set 24

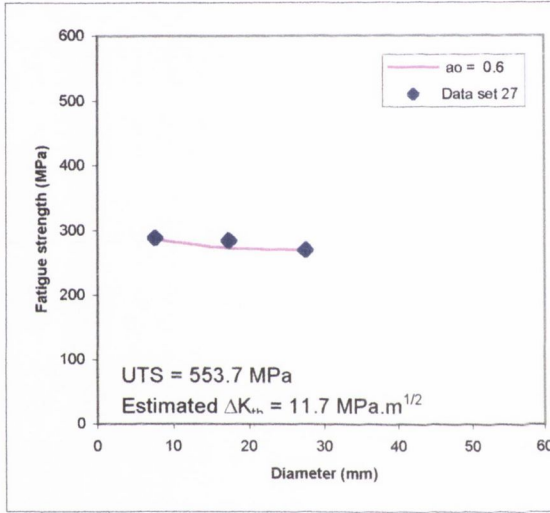
Fig. D.1(cont) - Application of the PM to size effect data for rotating steel specimens



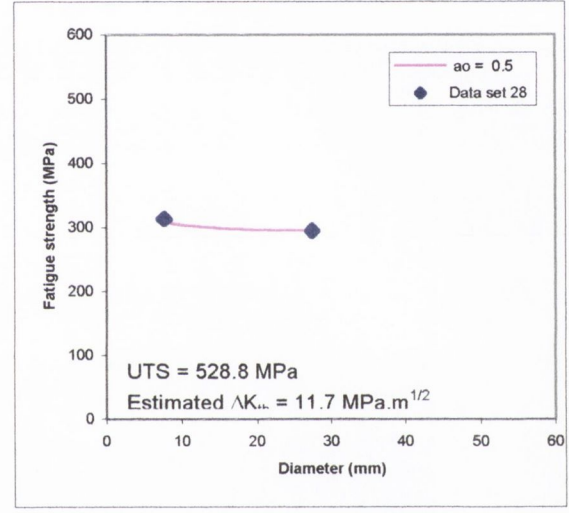
(y) Data set 25



(z) Data set 26



(aa) Data set 27



(bb) Data set 28

Fig. D.1(cont) - Application of the PM to size effect data for rotating steel specimens

### D.3 Discussion

As expected there is quite a lot of scatter in the experimental results presented above. Therefore, data sets for which there are only two or three data points should be treated with suspicion. Nevertheless, it can be seen from the above, that for each material, there is a value of  $a_0$  that can be used in conjunction with the point method, which results in good correlation with the experimental data. The question is: are these  $a_0$  values and subsequent  $\Delta K_{th}$  values realistic?

A very general rule-of-thumb is that high strength materials usually have small  $a_0$  values (i.e. less than 0.1mm), while  $a_0$  is typically quite large in low strength materials like cast iron and aluminium (greater than 1mm). In fact, experience with the critical distance methods suggests that the  $a_0$  values used above to predict the experimental data are, in most cases, too high. Furthermore, it can be seen that the greater the  $a_0$  value, a bigger difference is predicted between large and small diameter specimens. Therefore it is concluded that the point method does make some correction for the size effect observed in plain rotating steel specimens, however if the correct material properties were used, the point method would under-predict the observed experimental result.